Damage Tolerance
in
Aircraft Structures

DAMAGE TOLERANCE
IN AIRCRAFT STRUCTURES

A symposium
presented at the
Seventy-third Annual Meeting
AMERICAN SOCIETY FOR
TESTING AND MATERIALS
Toronto, Ontario, Canada, 21–26 June 1970

ASTM SPECIAL TECHNICAL PUBLICATION 486

List price $19.50
04-486000-30

Foreword

The Symposium on Damage Tolerance in Aircraft Structures was conducted in two sessions at the Seventy-third Annual Meeting of the American Society for Testing and Materials, held in Toronto, Ontario, Canada, 21–26 June 1970. The symposium was sponsored by ASTM Committee E-9 on Fatigue. M. S. Rosenfeld, of the Naval Air Development Center, served as symposium chairman, with P. C. Paris, Del Research Corp., Hellertown, Pa., and R. J. Hebert, Canadair, Ltd., Montreal, Ontario, presiding as chairmen of the first and second sessions, respectively.

Related
ASTM Publications

Structural Fatigue in Aircraft, STP 404 (1966), $18.50

Fatigue at High Temperature, STP 459 (1969), $11.25

Effects of Environment and Complex Load History on Fatigue Life, STP 462 (1970), $22.00

Contents

Introduction

In the past aircraft were designed for maximum performance, with particular attention given to range, altitude, speed, and pay load. Structural concepts and materials which provided minimum weight were used with little consideration for damage tolerance or, in the case of military aircraft, structural vulnerability. The current emphasis on safety, with longer intervals between maintenance periods to increase aircraft availability, has required more intensive consideration on the part of the designer of crack propagation characteristics and residual strength of flight structures.

Information on the growth of cracks in engineering structures and the residual strength of cracked structures is necessary for the prediction of service lives of structures subjected to fatigue loading and for the establishment of safe inspection intervals. This symposium provided an effective means of exchanging technological advances in fatigue crack propagation and fracture theory. The specific objectives of the symposium were

1. To review the state of aircraft structural analysis for structures with propagating cracks.

2. To present recent advancements in research into basic mechanisms of crack propagation and residual strength of aircraft structures.

3. To provide a review of fracture mechanics as applied to the assessment of structural vulnerability and residual strength of materials and structures.

Because of the limited time available in a symposium of this nature, emphasis was placed on discussions of theoretical considerations that influence damage tolerance design of aircraft structures. Although material characteristics can influence crack growth behavior and residual strength of structures, this aspect of the problem was not emphasized. The role of material in the attainment of damage tolerant structures should be the subject of a separate symposium.

The papers presented can be separated into four distinct categories: (1) basic concepts in fatigue crack propagation, (2) effects of panel geometry, (3) influence of panel stiffeners, and (4) application of fracture mechanics and crack propagation to the design and test of aircraft structures.

In the first category, Elber considers the effect of crack closure on crack propagation, Barsom reviews crack propagation laws and concludes that the primary factor affecting fatigue crack growth behavior is the strain energy release rate, and Brussat presents a semiprobabilistic approach for predicting fatigue crack growth under variable amplitude uniaxial cyclic loading.

In the second category, the effects of geometry are discussed in papers by Allen, who discusses the effect of panel thickness, by Adams, who considers

the influence of panel curvature on the stress intensity at the tip of a crack, and by Feddersen, who considers the residual strength of center cracked tension panels. Feddersen also proposes a simple and direct empirical method for relating gross stress, stress intensity factor, and crack length over the full range of crack lengths and panel widths. This method defines the residual strength characteristics of panels using a minimum of experimental data.

Moving further up the ladder of increasing structural complexity, Poe and Liu and Ekvall discuss the effects of stiffener strength, geometry, stiffness, and spacing on the crack propagation characteristics of flat panels.

The fourth category of papers deals with the application of fracture mechanics and crack propagation concepts to the design of modern aircraft structures. Graziano and Fitch discuss the crack growth behavior in a wing designed with no consideration given to fatigue and crack growth, and Swift discusses the extensive analytical and experimental considerations being given crack growth in the design of a commercial transport of the immediate future.

Further, Jensen presents the results of investigations into the ballistic damage characteristics and ballistic damage tolerance of various panel configurations used for tension skins in multispar wing boxes. In a related paper not presented at the symposium, Rich discusses the propagation of cracks in helicopter rotor blades.

Grateful acknowledgment is made of the contributions of the authors, the session chairmen, those who reviewed papers prior to the meeting, the Toronto coordinator, and the discussion participants.

M. S. Rosenfeld
research aerospace engineer
Aero Structures Department
Naval Air Development Center
Warminster, Pa. 18974
symposium chairman

J. M. Barsom[1]

The Dependence of Fatigue Crack Propagation on Strain Energy Release Rate and Crack Opening Displacement

ABSTRACT: Information on the growth of fatigue cracks in engineering structures is necessary for the prediction of service lives of structures subjected to fatigue loading. Thus, considerable work has been done to develop fatigue crack propagation laws. To determine the primary material parameters affecting fatigue crack growth, a review and analysis of existing fatigue crack propagation data were conducted.

The results show that the primary factor affecting fatigue crack growth rates in high yield strength steels, titanium, and aluminum is the applied energy release rate range, $\Delta \mathcal{G}_I$, in psi ·inches. The stress intensity factor, K_I, can be related to $\mathcal{G}_I$ by using the modulus of elasticity; consequently, crack growth rates usually are expressed in terms of ΔK_I for a particular material. However, the primary factor affecting fatigue crack growth rate is $\Delta \mathcal{G}_I$. Crack growth rates also can be expressed in terms of the crack opening displacement range, $\Delta \delta$, because $\mathcal{G}_I$ can be related to δ. By using a critical strain, crack extension criterion, analysis of crack propagation behavior for these metals suggests that a change to accelerated crack growth rates occurs when δ reaches a value of 1.6×10^{-3} in.

KEY WORDS: cracking (fracturing), crack propagation, strain energy methods, fatigue (materials), corrosion fatigue, stress corrosion, cyclic loads, stress cycle, ductility, tensile properties, yield strength, pressure vessels, structural steels, titanium alloys, aluminum alloys

Engineering structures that are subjected to repeated loads often develop subcritical cracks during the life of the structure. If these subcritical cracks form during fabrication (a common occurrence for heavily constrained welded structures), the useful life of a structure will be governed by the fatigue crack propagation behavior of the steel comprising it. Therefore, to predict the service life of structures that may have subcritical cracks, as well as to establish safe inspection intervals, an understanding of the rates of fatigue crack propagation in steels is required.

[1] Applied Research Laboratory, U.S. Steel Corp., Monroeville, Pa. 15146.

The correlation of a considerable amount of fatigue crack growth data [1–6][2] in terms of a power law [7] indicates that the rate of subcritical crack propagation is related to the stress intensity factor, K_I, raised to the nth power and can be expressed as follows:

$$da/dN = A(\Delta K_I)^n \dots\dots\dots\dots\dots\dots\dots(1)$$

where

$$da/dN = \text{crack growth per loading cycle, in./cycle,}$$
$$\Delta K_I = \text{stress intensity factor range, } ksi\sqrt{in.}, \text{ and}$$
$$A \text{ and } n = \text{constants.}$$

However, neither the value of the constant A nor of the exponent n has been defined as a fixed value for all metal alloys or as a function of material properties. Furthermore, n has been shown to vary [5, 6, 8] for tests conducted in a room temperature air environment, that is, under conditions where environmental effects normally are minimal. Carman and Katlin [6] have pointed out that failure to account for such changes in the value of the exponent n in design applications can lead to a dangerous overestimation of the fatigue life of a structure. Thus, the exact value of the constants A and n should be determined and the conditions causing an increase in n (accelerated crack growth rate) explained so that the empirical laws established by laboratory investigations can become useful design tools.

Existing fatigue crack propagation laws were reviewed to establish the necessary relations for predicting the fatigue life of structural steels. These laws were compared with the results of crack propagation tests of high yield strength structural steels tested at room temperature in air [5]. By using linear, elastic, fracture mechanics concepts, these test results [5] were compared with existing information on the crack growth behavior of steels, titanium alloys, and aluminum alloys. This report describes the results of this analysis and presents a fatigue crack propagation law that is expressed in terms of material properties and that seems to predict the fatigue crack propagation rates in high yield strength steels, titanium, and aluminum.

Review of Previous Fatigue Crack Propagation Laws

In the past few years several fatigue crack propagation laws have been proposed. For the simple case of a through-thickness crack of length $2a$ in an infinite plate subjected to uniform stress σ, most of these laws [1, 4, 9–13] can be represented approximately as

$$da/dN = A\sigma^n a^m \dots\dots\dots\dots\dots\dots\dots(2)$$

---

[2] Italic numbers in brackets refer to the list of references at the end of this paper.

where

$$da/dN = \text{crack growth per loading cycle, in./cycle,}$$
$$\sigma = \text{fluctuating stress, ksi,}$$
$$a = \text{crack length, in., and}$$
$$A, n, \text{ and } m = \text{constants.}$$

Equation 2 suggests that fatigue crack propagation rates are dependent on the magnitude of the alternating stress and on the crack length. However, both σ and a (combined) can be represented by the stress intensity factor K; thus, Paris [1] reasoned that the rate of crack propagation should be controlled by the stress intensity factor range ΔK_I (ΔK under opening-mode load conditions). Consequently, for a zero to tension load range, the rate of crack propagation can be represented by the equation

$$da/dN = f(K_I). \dots\dots\dots\dots\dots\dots\dots\dots\dots(3)$$

For a through-thickness crack of length $2a$, the stress intensity factor is given by the equation [13]

$$K_I = \sigma\sqrt{\pi a}. \dots\dots\dots\dots\dots\dots\dots\dots(4)$$

Equations 2 and 3 would be in agreement only when $2m = n$.

Using dimensional analysis, Frost and Dugdale [10] and Liu [11, 12] concluded that the crack propagation rate should depend linearly on crack length, that is,

$$da/dN = Ba. \dots\dots\dots\dots\dots\dots\dots\dots\dots(5)$$

where B is a function of the applied stress.

To fit their experimental data (limited), Frost and Dugdale concluded that B is proportional to σ^3, which means that their results would not agree with Eq 3. On the other hand, by using an energy approach to fatigue crack propagation, Liu [12] reasoned that B is proportional to σ^2, which is in agreement with both Eq 2 and Eq 3. Furthermore, Paris and Erdogan [14] showed that when the crack tip radius is small compared with the crack length, the fatigue crack propagation law proposed by McEvily and Illg [4] is equivalent to the law advanced by Paris [1, 14, 15], Eq 3.

Thus, the fatigue crack propagation laws suggested by Paris, by McEvily and Illg, and by Liu all state that the rate of crack propagation depends on the stress intensity factor, K_I. Whereas the laws of Paris and of McEvily and Illg do not define the exact form of this functional dependence, Liu proposes that the crack propagation rate is a function of the stress intensity factor raised to the second power ($n = 2$, Eq 1). (As described later, Barsom et al [5] found n to be 2.25 for high yield strength steels.)

On the basis of extensive fatigue crack propagation data on thin sheets of 2024-T3 and 7075-T6 aluminum alloy [2, 3, 4, 14], Paris and Erdogan [14] suggested that the crack propagation rate is a function of the stress intensity

factor raised to the fourth power. However, recently, Paris [16] has indicated that the data used in their analysis included environmental effects that may have resulted in an elevated value of n.

Development of an Empirical Crack Propagation Law for Low K_I Values

To establish a valid crack propagation law for high yield strength constructional steels, Barsom et al [5] investigated fatigue crack growth in high, yield strength steels in a room temperature air environment. These results, Fig. 1, show that the fatigue crack propagation rates in the steels tested at low stress intensity factors ($K_I < 100$ ksi$\sqrt{\text{in.}}$) fall within a narrow band. Furthermore, these results suggest that a conservative estimate of fatigue crack growth in high yield strength steels may be expressed as follows:

$$da/dN = 0.66 \times 10^{-8}\,(\Delta K_I)^{2.25} \dots\dots\dots\dots\dots\dots(6)$$

where ΔK_I is the stress intensity factor range ($K_{I\,(\text{max})} - K_{I\,(\text{min})}$), ksi$\sqrt{\text{in.}}$

Paris and Erdogan [14] have pointed out that determining the exponents n and m in Eq 2 "from a limited quantity of data is a doubtful practice. That is to say that plotting data from single test specimens on a logarithmic or semilogarithmic graph on which laws such as Head's, Frost's, and Liu's predict straight line relationships is not a reasonable test of the validity of a crack propagation law."

Equation 6 has been verified for 19 steels studied by Barsom et al [5], Wei et al [17], Clark [18–20], Carman and Katlin [6], and Schwab [21]. All of the tests were conducted under zero-to-tension or tension-to-tension sinusoidal loading. The specimen types used by these investigators included a wedge opening loading (WOL) specimen, a center notched specimen under constant load, a center notched specimen under either constant load or constant K_I, and a tapered, double cantilever beam specimen. The stress intensity factor range, ΔK_I, for these tests varied from 5 to 150 ksi$\sqrt{\text{in.}}$ [5]. This range of ΔK_I values produced a change of four orders of magnitude in crack growth rate, Fig. 1. Consequently, on the basis of considerable experimental evidence, Eq 6 can be considered a valid crack propagation law for high yield strength steels for zero-to-tension or tension-to-tension sinusoidal loading.

The data presented in Fig. 1 and Ref 5 clearly show that, at a low stress intensity factor range, that is, $K_I < 100$ ksi$\sqrt{\text{in.}}$, the crack propagation rate in high yield strength steels conforms more closely to a second power law than to a fourth power law. Furthermore, the crack propagation rates for the various steels investigated seem to be independent of yield strength. These observations, coupled with the observations of Anderson [7] and Bates and Clark [22] that on a log-log plot crack propagation rates for various metals fall in a single band when plotted against the ratio $\Delta K_I/E$, suggest the possibility that, neglecting second order effects, Eq 2 may be written in the following general form for various metals:
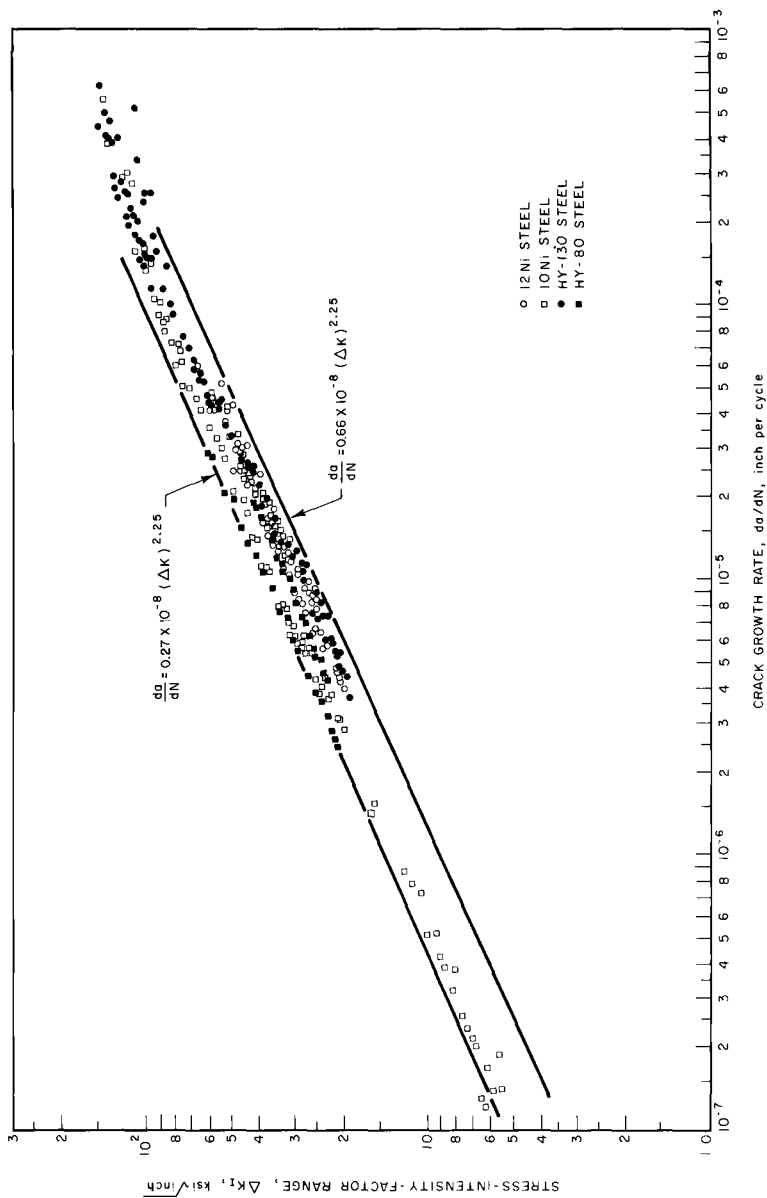
$$da/dN = D(\Delta \mathcal{G}_I) \dots\dots\dots\dots\dots\dots\dots(7)$$

FIG. 1—Summary of fatigue crack growth data for high strength steels [5].

where

D = a constant and

$\Delta \mathcal{G}_{I} = [\mathcal{G}_{I\,(max)} - \mathcal{G}_{I\,(min)}]$, the cyclic, strain energy release rate range, psi·inches per cycle, which is related to the cyclic stress intensity factor range, ΔK_{I}, for tension-to-tension loading by the equations

$$\Delta \mathcal{G}_{I} = \frac{(\Delta K_{I})^2}{E} \qquad \text{plane stress} \dots \dots \dots \dots \dots \dots (8)$$

$$\Delta \mathcal{G}_{I} = \frac{(1 - \nu^2)}{E} (\Delta K_{I})^2 \qquad \text{plane strain} \dots \dots \dots \dots \dots (9)$$

where

E = Young's modulus and
ν = Poisson's ratio.

It should be noted that for zero-to-tension loading $\Delta \mathcal{G}_{I}$ and ΔK_{I} are equal to $\mathcal{G}_{I\,(max)}$ and $K_{I\,(max)}$, respectively. Moreover, for completely reversed cyclic loading, one assumes that there is no crack opening displacement during the compression stroke of the cycle. Consequently, under completely reversed cyclic loading, $\Delta \mathcal{G}_{I}$ and ΔK_{I} are calculated by neglecting the compressive component of the applied stress.

Because Young's modulus and Poisson's ratio are constant for steels, Eqs 7 and 6 essentially are identical. However, the crack propagation law in the form given by Eq 7 includes the material properties E and ν (for plane strain), which vary from one metal to another. Consequently, although the applicability of the above crack propagation law, Eq 7, to steels is apparent from the data presented in Fig. 1, the applicability of Eq 7 to other metals must be shown.

The general validity of the proposed crack propagation law was tested by using Bates and Clark's [22] data on 7079-T6 and 5456-H321 aluminum alloys and a Ti-6A1-4V titanium alloy. For Eq 7 to be valid, a log-log plot of crack propagation rate versus the ratio of the stress intensity range to the square root of Young's modulus should produce a linear relation between these parameters, because of the form of Eq 7. Furthermore, the data for steel, aluminum, and titanium should fall within a narrow scatterband. Figure 2 presents Bates and Clark's data for aluminum and titanium alloys superimposed on the line I suggested for predicting crack propagation rates in high strength steels. The separation of the data for aluminum, titanium, and steel, Fig. 2, does not indicate necessarily lack of agreement with Eq 7. That is, although steels have the highest value for the modulus of elasticity, compared with titanium and aluminum, the suggested crack propagation line for steels falls between the lines for the other two metals. Thus, the reasons for the data separation may be attributed to slight second order
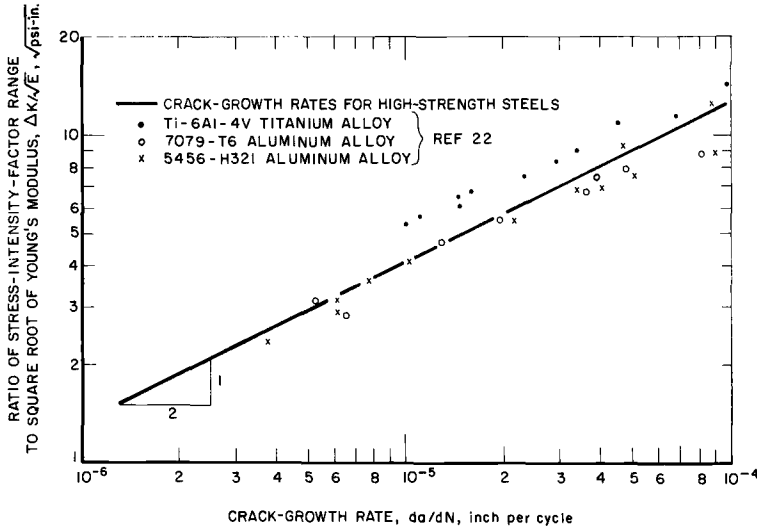
FIG. 2—*Correlation of fatigue crack growth rate with $\Delta K / \sqrt{E}$ for high strength steels, one titanium alloy, and two aluminum alloys.*

effects (corrosion, strain aging, etc.), to experimental error, to the fact that the values used for the modulus of elasticity were not measured but were assumed to be 30×10^6 psi for steel, 10.6×10^6 psi for aluminum, and 15.8×10^6 psi for titanium, or combinations of the above. Hence it may be concluded that at low stress intensity factor ranges, crack propagation rates for various steel, aluminum, and titanium alloys can be predicted to a first order approximation from the equation

$$da/dN = D(\Delta \, \mathcal{G}_I) \dots\dots\dots\dots\dots\dots\dots(7)$$

where D is constant for steel, aluminum, and titanium and is equal to 5×10^{-7} (Fig. 2) when a is in inches and $\mathcal{G}_I$ is in psi·inches.

Analysis of Crack Propagation Behavior by Crack Opening Displacement

In the previous section, a crack propagation law, Eq 7, was deduced on the basis of continuum mechanics to predict the macroscopic growth rates of cracks in various metals. In the present section, an attempt is made at using continuum mechanics relations to rewrite the equation in terms of crack opening displacement (the opening at the crack tip, Fig. 3) and material properties.

The strain energy release rate, $\mathcal{G}_I$, is related to the crack opening displacement at the leading edge of the crack, δ, by the equations [23, 24]

$$\mathcal{G}_I = \delta \sigma_y \quad \text{and} \quad \Delta \, \mathcal{G}_I = (\Delta \delta) \, \sigma_y \dots\dots\dots\dots\dots(10)$$
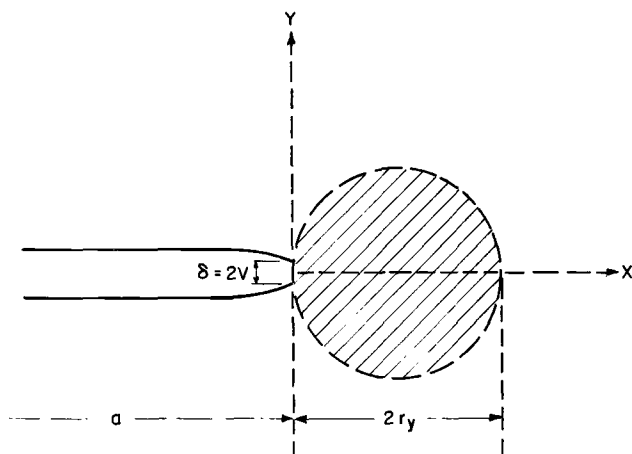
FIG. 3—*Plastic zone at the leading edge of a crack.*

where

  $\mathcal{G}_I$ = strain energy release rate, psi·in.,
  δ = crack opening displacement, in.,
  σ_y = 0.2 percent offset tensile yield strength, and
  Δ represents the range per cycle in both $\mathcal{G}_I$ and δ.

Substituting this expression for $\mathcal{G}_I$ into Eq 7, the crack propagation law for low stress levels takes the form

$$da/dN = D[\Delta(\delta)\,\sigma_y]\dots\dots\dots\dots\dots\dots(11)$$

where D has been shown to be constant for all materials and is approximately 5×10^{-7} when a is in inches and $\mathcal{G}_I$ is in psi·inches.

Transition from Low to High Rates of Crack Propagation

The crack propagation laws presented in Eq 7 or 11 have been applied to the region with low stress intensity factor, K_I, and for applied stresses which are small compared with the yield strength of the material. For high yield strength steels this region was generally defined by $K_I < 100$ ksi$\sqrt{\text{in.}}$; however, there is ample evidence in the literature [5, 6, 8, 18] to suggest that fatigue crack propagation rates increase markedly as the stress intensity approaches the critical value, K_{Ic}, for the material. The onset of acceleration of fatigue crack propagation is called, in this paper, the "fatigue rate transition." Clark and Wessel [8] observed that in 5456-H321 aluminum alloy the fatigue rate transition occurred at a stress intensity level of approximately 25 ksi$\sqrt{\text{in.}}$ On the basis of metallographic examinations by the electron microscope, they associated the onset of accelerated fatigue crack growth rates (the fatigue rate transition) with the superposition of a ductile fracture

mechanism onto the fatigue mechanism (that is, the mechanism of cyclic, subcritical crack extension which leaves fatigue striations on the fracture surface). This superposition of a ductile fracture mechanism onto the fatigue mechanism most probably will occur at different stress intensity levels for different materials.

A knowledge of the variables affecting the onset of accelerated fatigue crack growth rates is essential for predicting the service life of a structure and for establishing inspection requirements. Using a critical strain criterion for crack growth (presented in the Appendix) and from analysis of the experimental data on fatigue crack growth, it is suggested that the acceleration of fatigue crack propagation occurs at an essentially constant value of $\Delta\delta$. Figure 4 presents data on 5456-H321 aluminum [8] which clearly show the fatigue rate transition occurring at $\Delta K_I = 25$ ksi$\sqrt{\text{in.}}$ (or $\Delta \mathcal{G}_I = 62$ psi·in.) approximately. Substituting this value of $\Delta \mathcal{G}_I$ and the yield strength of the material ($\sigma_y = 37$ ksi) into Eq 10 gives $\Delta\delta_T = 1.6 \times 10^{-3}$ in., where $\Delta\delta_T$ represents the crack opening displacement range at the onset of accelerated fatigue crack growth rates and is equal to $\delta_{T(\max)}$ for zero-to-tension loading. For 10Ni-Cr-Mo-Co steel (yield strength 190 ksi), HY-130 steel (yield strength 140 ksi), and HY-80 (yield strength 84 ksi), substituting this value of δ_T into Eqs 9 and 10 predicts that the fatigue rate transition should occur at stress intensity levels approximately equal to 95 ksi $\sqrt{\text{in.}}$, 85 ksi$\sqrt{\text{in.}}$, and 64 ksi$\sqrt{\text{in.}}$, respectively. These values are shown in Figs. 5, 6, and 7, respectively, and agree well with the experimental data. This behavior is confirmed further by the fatigue crack propagation data obtained by Hertzberg and Nordberg [25] on A514-F steel (yield strength 110 ksi), Fig. 8. Thus, it appears
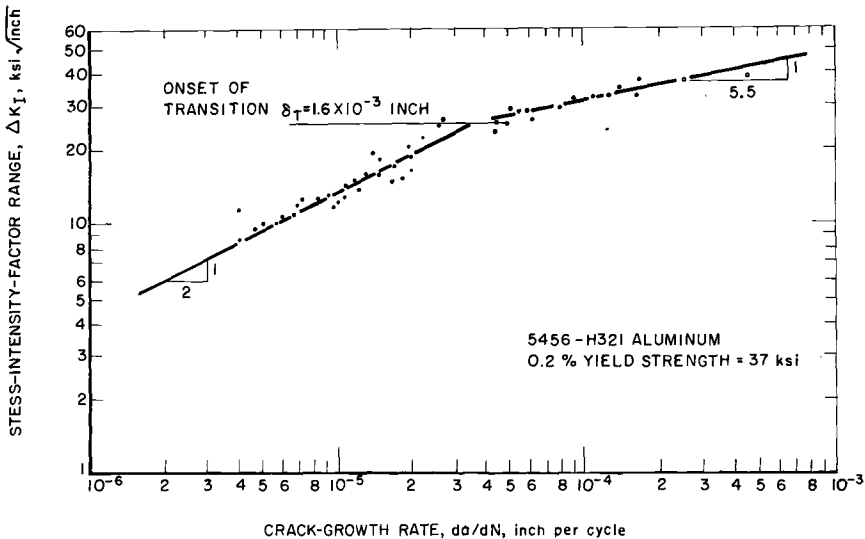

FIG. 4—*Fatigue crack growth rate as a function of stress intensity for 5456-H321 aluminum.*

that a critical strain, fracture initiation criterion is applicable to prediction of the onset of accelerated fatigue crack propagation rates in steels having yield strengths greater than 80 ksi and that the fatigue rate transition occurs at an approximately constant value of the crack opening displacement range, $\Delta\delta_T = 1.6 \times 10^{-3}$ in.
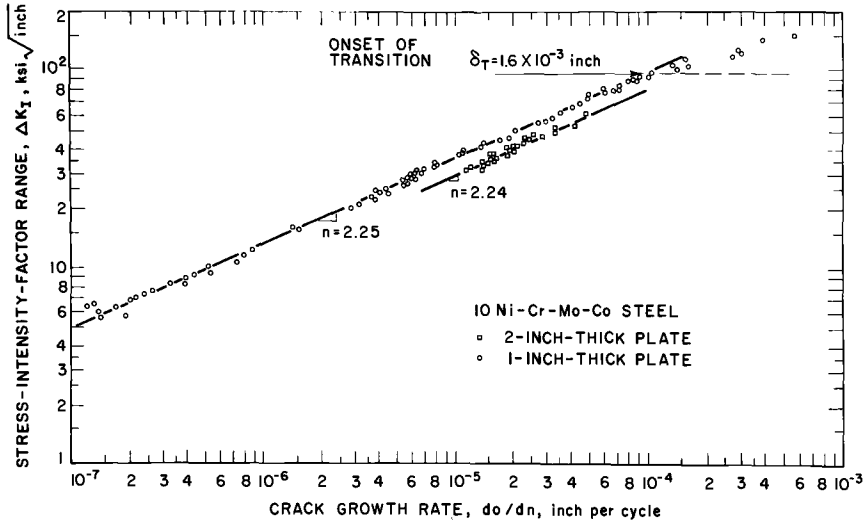

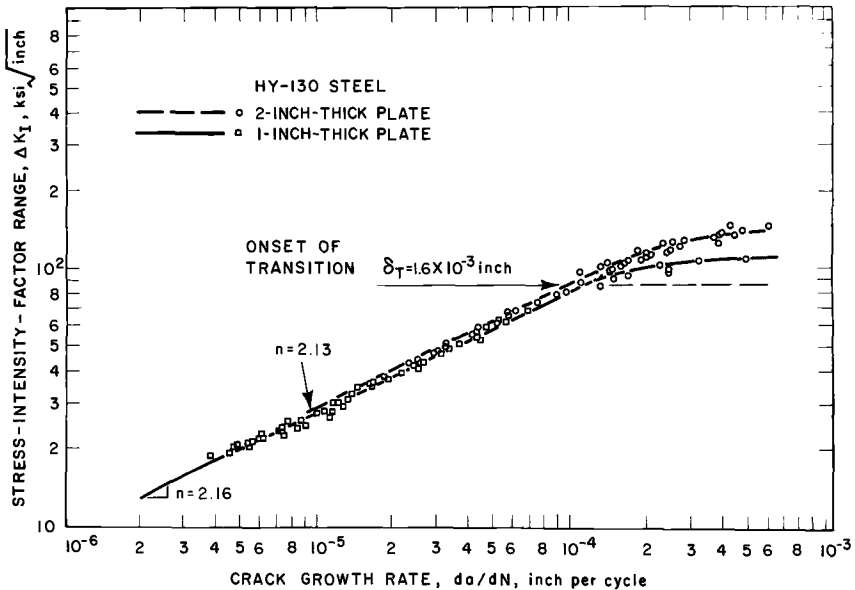FIG. 5—Onset of accelerated fatigue crack growth rate for 10Ni-Cr-Mo-Co steel.

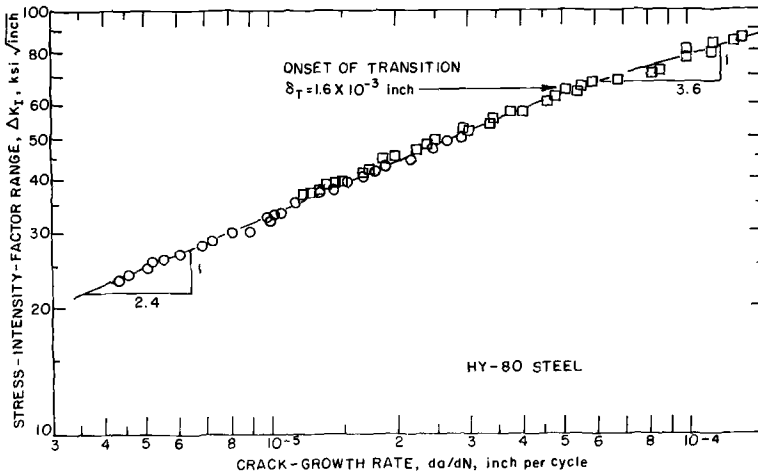FIG. 6—Onset of accelerated fatigue crack growth rate for HY-130 steel.

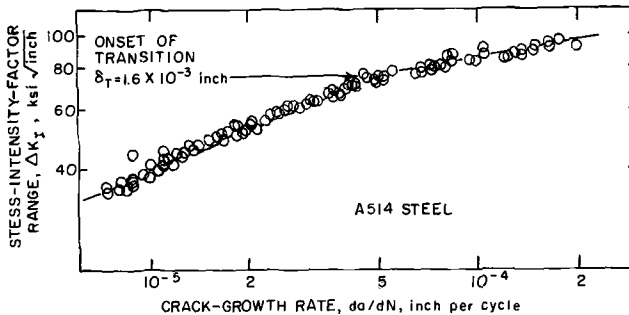FIG. 7—*Onset of accelerated fatigue crack growth rate for HY-80 steel.*

FIG. 8—*Onset of accelerated fatigue crack growth rate for A514 steel.*

Some Practical Implications

The results of the previous analysis indicate that fatigue crack growth rates in metals subjected to applied stresses low in comparison with the yield strength are related linearly to the strain energy release rate range, $\Delta \mathcal{G}_I$. However, at applied stresses approaching yield stress, fatigue crack growth is accelerated by the superposition of a tensile, ductile tear mechanism onto the fatigue mechanism. This acceleration was found to occur when the crack opening displacement range, $\Delta\delta$, was greater than 1.6×10^{-3} in.

Acceleration of fatigue crack growth rates at $\delta_T \geq 1.6 \times 10^{-3}$ in. suggests that cyclic proof testing of pressure vessels may be detrimental to the useful life of the vessel, especially when these vessels are subjected to cyclic stresses corresponding to crack opening displacements greater than 1.6×10^{-3} in. It is possible, however, that in one-cycle proof testing, sufficient crack blunting may occur to prevent subcritical crack growth at stresses corresponding to

$\delta > 1.6 \times 10^{-3}$ in. Further work is needed to establish the conditions necessary and sufficient to avoid subcritical crack growth in a one-cycle proof test of pressure vessels.

In investigating the corrosion fatigue behavior of a metal, the acceleration of subcritical crack growth by a ductile tear mechanism should be separated from the possible acceleration caused by electrochemical mechanisms, that is, by environmental effects. For example, 10Ni-Cr-Mo-Co steel has a K_{Iscc} value, in 3 percent sodium chloride solution, greater than 170 ksi$\sqrt{\text{in.}}$, whereas acceleration in the fatigue crack growth in air environment occurs at a stress intensity level of about 100 ksi$\sqrt{\text{in.}}$ Thus acceleration of corrosion fatigue crack growth rates at above $K_I = 100$ ksi$\sqrt{\text{in.}}$ could be attributed incorrectly to susceptibility of the steel to environmental effects.

Although there are no K_{Iscc} values for 5456-H321 aluminum alloy, it is accepted generally that this material is not susceptible to stress corrosion cracking. For a 1000-h runout time, the K_{Iscc} values for 10Ni-Cr-Mo-Co steel and for HY-130 steel in room temperature, 3 percent solution of sodium chloride are greater than 170 ksi$\sqrt{\text{in.}}$ and 135 ksi$\sqrt{\text{in.}}$, respectively [26]. These values are about twice the stress intensity factor values at which acceleration in fatigue crack growth occurs in room temperature air environment for these steels (95 and 85 ksi$\sqrt{\text{in.}}$, respectively). Consequently, for the materials investigated, the transition in crack growth rate is not induced environmentally. However, for materials highly susceptible to stress corrosion cracking, it is conceivable that an environment enhanced transition in fatigue crack growth rates might occur at stress levels below the transitional value calculated at $\delta_T = 1.6 \times 10^{-3}$ in. Similarly, acceleration in the fatigue crack growth rate may occur at δ values less than 1.6×10^{-3} in. when the crack opening displacement at failure, that is, δ corresponding to K_{Ic} or K_c, of the material is less than 1.6×10^{-3} in. These effects must be incorporated in fracture control plans for structures subjected to fluctuating loads.

Summary

The results of this investigation can be summarized as follows:

1. The primary factor affecting fatigue crack growth rates in steel, titanium, and aluminum is the cyclic, applied energy release rate range, Δg_I, in psi·inches.

2. An estimate of fatigue crack propagation rates for high yield strength steel, aluminum, and titanium alloys tested in a room temperature air environment can be obtained from the following equation:

$$da/dN = 5 \times 10^{-7} (\Delta g_I)$$

where g_I is in psi·inches and a is in inches.

Because g_I and K_I can be related by using the modulus of elasticity, E, crack growth rates usually are expressed in terms of ΔK_I for a particular

material. However, the primary factor affecting fatigue crack growth rate is $\Delta \mathcal{G}_I$, where

$$\Delta \mathcal{G}_I = \frac{(1 - \nu^2)(\Delta K_I)^2}{E}$$

in plane strain.

3. Because $\mathcal{G}_I$ can also be related to the crack opening displacement, δ, crack propagation rates also can be expressed in terms of $\Delta\delta$ where $\Delta \mathcal{G}_I = (\Delta\delta)\, \sigma_y$.

4. By using a critical strain, crack extension criterion, analysis of crack propagation behavior for high yield strength steel, aluminum, and titanium alloys suggests that a transition to accelerated crack propagation rates occurs when the crack opening displacement range, $\Delta\delta$, is equal to an approximately constant value $(1.6 \times 10^{-3}$ in.).

5. Cyclic proof testing at stress levels corresponding to a crack opening displacement, δ, of about 1.6×10^{-3} in. may cause accelerated subcritical crack extension, thereby decreasing the useful life of the structure.

In general, the results of this investigation have shown that the primary factor affecting fatigue crack growth behavior is the strain energy release rate range, $\Delta \mathcal{G}_I$, which can be related to either the stress intensity factor range, ΔK_I, or the crack opening displacement range, $\Delta\delta$, and that acceleration in fatigue crack growth occurs when $\Delta\delta$ is equal to an approximately constant value $(1.6 \times 10^{-3}$ in.).

APPENDIX

Critical Strain Criterion of Crack Growth

To establish the fatigue rate transition behavior of materials subjected to cyclic stresses, assume a critical strain criterion of crack growth [27–31]. The material ahead of the crack tip can be approximated by adjacent tensile ligaments of length l and width w, Fig. 9. At sufficiently high stresses the ligament adjacent to the crack tip breaks, thus causing crack extension [27].

Under slow loading conditions and cyclic loading conditions, failure of the first ligament may cause the failure of the remaining ligaments, thus generating unstable crack extension. On the other hand, stable crack extension occurs when failure of the first ligament does not result in fracture of the remaining ligaments.

Under plane strain conditions, the length of the ligament, l, is taken to be equal to the thickness of the zone of plastic deformation, Fig. 9, which, in turn, is of the order of the crack tip diameter, 2ρ. Consequently, the crack opening displacement, δ, can be written as

$$\delta = 2\rho\epsilon \dots\dots\dots\dots\dots\dots\dots\dots\dots\dots\dots\dots(12)$$

where ϵ is the axial unit strain (under plane strain conditions) [32] in the ligament adjacent to the crack tip.
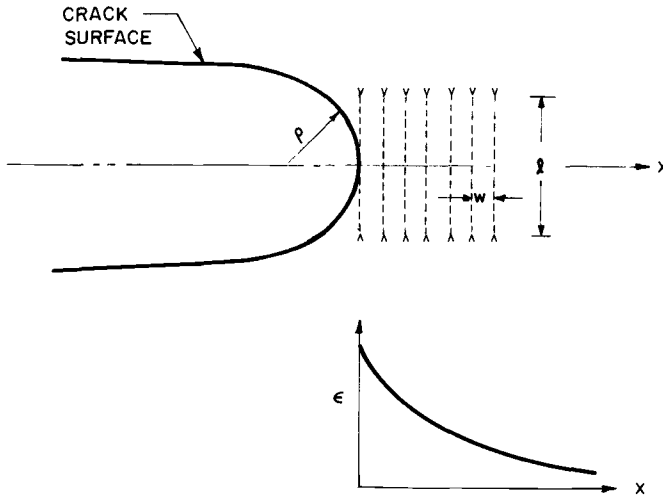
FIG. 9—*The material ahead of the crack represented as a series of tensile ligaments* [31].

When the axial unit strain, ϵ, in the first ligament equals the fracture, plane strain ductility, $\epsilon_{F,P\text{-}ST}$ [*32, 33*], the ligament fractures. Thus, crack extension is assumed to occur when the strain at the crack tip reaches a critical value, $\epsilon_{F,P\text{-}ST}$, or when the crack opening displacement at the crack tip reaches a critical value, δ_F. This crack extension criterion is represented by the equation

$$\delta_F = 2\rho\epsilon_{F,P-ST}\dots\dots\dots\dots\dots\dots\dots\dots\dots\dots(13)$$

Hahn and Rosenfield [*28*] have shown that a similar criterion applies for fracture initiation in plane stress tensile loading.

The ductile, dimple fracture mechanism superimposed onto the fatigue mechanism [*34*] (that is, the mechanism of cyclic, subcritical crack extension which leaves fatigue striations on the fracture surface) can be thought of as a superposition of stable, subcritical crack extension governed by the above-discussed fracture criterion and Eq 13. Consequently, by using this critical strain model and from analysis of the experimental data on fatigue crack growth, it is suggested that the transition of fatigue crack growth to higher rates occurs at a critical value of the crack opening displacement.

References

[*1*] Paris, P. C., *Proceedings*, Tenth Sagamore Army Materials Research Conference, Syracuse University Press, 1964.

[*2*] Donaldson, D. R. and Anderson, W. E. in *Proceedings*, Crack Propagation Symposium, Carnfield, England, Vol. 2, 1969, p. 375.

[*3*] Martin, D. E. and Sinclair, G. M. in *Proceedings*, Third U.S. National Congress of Applied Mechanics, 1958, p. 595.

[*4*] McEvily, A. J. and Illg, W., "The Rate of Crack Propagation in Two Aluminum Alloys," NACA Technical Note 4394, 1958.

[*5*] Barsom, J. M., Imhof, E. J., Jr., and Rolfe, S. T., "Fatigue-Crack Propagation in High-Strength Steels," AD846 127 L, 20 Dec. 1968 (available from Defense Documentation Center).

[*6*] Carman, C. M. and Katlin, J. M., "Low Cycle Fatigue Crack Propagation of High-Strength Steels," ASME Paper No. 66-MET-3, April 1966.

[7] Johnson, H. H. and Paris, P. C., *Journal of Engineering Fracture Mechanics*, Vol. 1, No. 1, 1968, p. 3.

[8] Clark, W. G., Jr., and Wessel, E. T., "Interpretation of the Fracture Behavior of 5456-H321 Aluminum with WOL Toughness Specimens," Scientific Paper 67-1 D6-BTLFR-P4, Westinghouse Research Laboratory, Sept. 1967.

[9] Head, A. K., *Philosophical Magazine*, PHMAA, Vol. 44, Series 7, 1953, p. 925.

[10] Frost, N. E. and Dugdale, D. S., *Journal of the Mechanics and Physics of Solids*, JMPSA, Vol. 6, No. 2, 1958, p. 92.

[11] Liu, H. W., *Journal of Basic Engineering*, ASME Transactions, Series D, JBAEA, Vol. 83, No. 1, 1969, p. 23.

[12] Liu, H. W., "Fatigue Crack Propagation and Applied Stress Range—An Energy Approach," ASME Paper No. 62-MET-2, 1962.

[13] Irwin, G. R. in *Handbuch der Physik*, Vol. VI, Springer, 1958, pp. 551–590.

[14] Paris, P. C. and Erdogan, F., *Journal of Basic Engineering*, ASME Transactions, Series D, JBAEA, Vol. 85, No. 3, 1963, p. 528.

[15] Paris, P. C., Gomez, M. P., and Anderson, W. E., *Trend in Engineering*, TREEA, Vol. 13, 1961, p. 9.

[16] Paris, P. C., "Application of Fracture Mechanics to Subcritical Crack Growth," presented at Westinghouse Nuclear Energy Systems, Nuclear Fuel Division, Forest Hills, Pittsburgh, Pa., 6 March 1969.

[17] Wei, R. P., Talda, P. M., and Li, Che-Yu in *Fatigue Crack Propagation, ASTM STP 415*, American Society for Testing and Materials, 1967, p. 460.

[18] Clark, W. G., Jr., *Journal of Engineering Fracture Mechanics*, Vol. 1, No. 2, 1968, p. 385.

[19] Clark, W. G., Jr., *Materials Evaluation*, MAEVA, Vol. 25, No. 8, Aug. 1967.

[20] Clark, W. G., Jr., "Influence of Temperature and Section Size on Fatigue Crack Growth Behavior in Ni-Mo-V Alloy Steel," presented at the National Symposium on Fracture Mechanics, Lehigh University, June 1968.

[21] Schwab, R. C., "The Use of Tapered Double-Cantilever-Beam Specimens for Fatigue-Crack Growth Studies," Report No. 2689, Naval Ship Research and Development Center, July 1968.

[22] Bates, R. C. and Clark, W. G., Jr., "Fractography and Fracture Mechanics," Scientific Paper No. 68-1D7-RDAFC-P1, Westinghouse Research Laboratory, Sept. 1968.

[23] Irwin, G. R., *Journal of Engineering Fracture Mechanics*, Vol. 1, No. 2, Aug. 1968, p. 245.

[24] Wells, A. A., *British Welding Journal*, MCBWA, Vol. 15, No. 5, May 1968, p. 221.

[25] Hertzberg, R. W. and Nordberg, N., "Fatigue Crack Propagation in A514 Steel," Fritz Engineering Laboratory Report No. 358.7, Lehigh University, Bethlehem, Pa., Nov. 1969.

[26] Connor, L. P., Porter, L. F., and Rolfe, S. T., "Fourth Progress Report: Development of an HY-180/210 Weldment," AD 835 686 L, 20 Sept. 1968 (available from Defense Documentation Center).

[27] Cottrell, A. H., *Proceedings of the Royal Society*, PRSLA, Vol. 285, 1965, p. 10.

[28] Hahn, G. T. and Rosenfield, A. R., *Acta Metallurgica*, AMETA, Vol. 12, 1965, p. 293.

[29] McClintok, F. A., *Journal of Applied Mechanics*, ASME Transactions, Series E, Vol. 25, 1958, p. 282.

[30] Bilby, B. A., Cottrell, A. H., and Swinden, K. H., *Proceedings of the Royal Society*, PRSLA, Vol. A272, 1963, p. 304.

[31] Tetelman, A. S. and McEvily, A. J., Jr., *Fracture of Structural Materials*, John Wiley and Sons, New York, 1967, p. 60.

[32] Clausing, D. P., "Effect of Plane-Strain Sensitivity on the Charpy Toughness of Structural Steels," AD836 314 L, 15 May 1968 (available from Defense Documentation Center).

[33] Barsom, J. M. and Rolfe, S. T., "K_{Ic} Transition-Temperature Behavior of A517-F Steel," AD 846 124 L, 29 Nov. 1968 (available from Defense Documentation Center).

[34] Clark, W. G., Jr., and Wessel, E. T., "Interpretation of the Fracture Behavior of 5456-H321 Aluminum with WOL Toughness Specimens," Scientific Paper 67-1D6-BTLFR-P4, Westinghouse Research Laboratory, Sept. 1967.

F. C. Allen[1]

Effect of Thickness on the Fracture Toughness of 7075 Aluminum in the T6 and T73 Conditions

ABSTRACT: The objectives of the investigation described were to find the variation of fracture toughness with thickness for 7075-T6 and 7075-T73 materials and to provide data upon which a theory could be established for the variation of fracture toughness with thickness. A test program was conducted on 60 centrally cracked specimens varying in thickness from 0.05 to 0.75 in.

Analysis of the results showed that the two materials displayed substantially different characteristics. This is attributed to the fact that, owing to the low proportional limit of the T73 material, the net section stress was in the plastic range for most specimens, whereas for the T6 material the net section stress was always in the elastic range.

It was noted that during slow crack growth, the crack grew faster in the center than at the surface of the material. A generally parabolic shaped crack front, therefore, existed at failure. It was hypothesized that the crack shape corresponded to the development of plane stress at its boundaries and that fracture toughness based on final crack length would be constant. This appeared to be true for the T6 material, within the range tested, but could not be proved for the T73 material.

A lumped parameter, redundant force analysis of three plates of varying thickness was made. The results show the development of plane strain conditions with increased thickness. Although correlation with the test results was not established, extension of the work may provide explanation of the phenomena observed in tests.

An appendix provides theoretical load-deflection relationships for centrally cracked plates which include the effects of plasticity.

KEY WORDS: failure, fractures (materials), cracking (fracturing), crack propagation, toughness, damage, tolerance (mechanics), aircraft, plates (structural members), metal sheets, aluminum alloys, fracture tests, stress analysis

Nomenclature

a One-half crack length

E Young's modulus of elasticity

l_c Crack length at start of fast fracture

---

[1] Assistant technical manager, Structural Mechanics Methods/R&D Group, Douglas Aircraft Co., McDonnell Douglas Corp., Long Beach, Calif. 90801.

l_{c_0} Crack length at start of final load application
R Ratio of maximum to minimum stress in fatigue loading
t Thickness of plate
v Vertical displacement of a point on the y axis due to application of stress σ (one half of compliance measurement)
w Width of plate
x, y, z Transverse, longitudinal, and thickness coordinates, respectively, of the cracked plate (Fig. 1)
Y Yield stress for ideal elastoplastic material
Z Function of complex variable ζ
$\bar{Z}$ Defined by $Z = (d/d\zeta)\, \bar{Z}$
ζ Complex variable $x + iy$
μ Poisson's ratios
ρ Plastic zone size measured along x axis
σ Stress in plate at a point far removed from crack (gross stress)
σ_{pl} Material proportional limit stress
σ_{net} Stress on the net section of the cracked plate
σ_{yp} Material yield stress
τ Shear stress

As airplanes increase in size, the gages of the skin material increase correspondingly so that damage tolerant design calculations require a knowledge of the fracture toughness of sheets which can no longer be considered thin. Considerable work has been done by many investigators to determine the plane stress and plane strain fracture toughness of commonly used materials. The plane stress fracture toughness is applicable to thin sheets and the plane strain toughness to very thick plates; however, inadequate data are available on plates of intermediate thickness. Furthermore, no theory exists for the calculation of the fracture toughness of intermediate thickness plates given the plane stress and plane strain values.

The investigation described herein was undertaken for the dual purpose of supplying data on the two materials and developing a theory which could assist in calculating the variation of fracture toughness with thickness for materials generally. It will be noted that at this stage of the investigation, the objectives are not by any means completely attained; however, it is hoped that the results and observations presented herein will prove useful to other investigators in this field.

The Test Program

Specimen Configuration and Preparation

Figure 1 shows the general configuration and nomenclature of the specimens tested. All panels were centrally cracked and had a length, including provision for attachments, equal to three times the width. In all specimens the grain was parallel to the direction of loading.

Table 1 shows the number of specimens and their nominal geometry. The majority were 8 in. wide; however, additional widths were investigated with the T73 material at thicknesses of 0.312 and 0.600 in. Crack length was varied on specimens 0.10, 0.312, and 0.600 in. thick.

TABLE 1—*Nominal geometry of specimens tested.*

Thickness, t, in.	l_c/w	Width, w, in.			
		2	8	22	32
0.05.......	0.2	...	XO	...	...
0.10.......	0.1	...	XO	...	...
	0.2	...	XO	...	...
	0.3	...	XO	...	...
0.2........	0.2	...	XO	...	...
0.312......	0.1	...	XO	...	...
	0.2	O	XO	O	O
	0.3	...	XO	...	...
0.45.......	0.2	...	XO	...	...
0.6........	0.1	...	XO	...	...
	0.2	O	XO	...	O
	0.3	...	XO	...	...
0.75.......	0.2	...	XO	...	...

NOTE—Two specimens were tested for each configuration and material except as follows:

W	t	No. of Specimens
8	0.05	6
8	0.45	1
8	0.75	1
22	0.312	1
32	0.312	1

X = 7075-T651
O = 7075-T7351

All specimens were machined from 0.75-in.-thick raw stock. All material came from the same heat and was heat treated at the same time.[2] Two sets of three 0.05-in.-thick by 8-in.-wide specimens of each material were cut from the stock plate at different positions through the thickness (see Fig. 2). These were used to determine whether the plane stress fracture toughness of the material was a function of position relative to the surface.

The cracks were developed from starter notches by unidirectional fatigue loading ($R = 0.1$). The gross stress level, σ, as the crack approached the desired length was 10,000 psi. Crack length versus number of cycles and load level were recorded.

[2] All material was received as 7075-T651 (heat treated by producer). Portions of the stock were subsequently heat treated by the user to the T73 condition. The designation T6 is used herein interchangeably with T651 and T73 with T7351 regardless of minor technical differences.
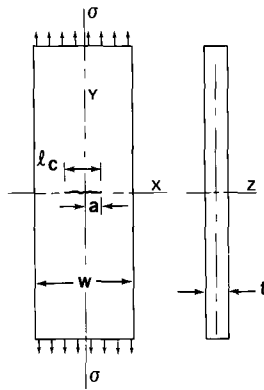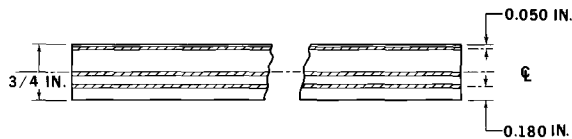
FIG. 1—*Specimen general configuration.*

FIG. 2—*Location of the 0.05-in.-thick specimens relative to the surface.*

Test Procedure

The test specimens were pulled to failure on an appropriate test machine at a loading rate of approximately 20,000 psi/min. All tests were at room temperature. Buckling restraint was provided on the 0.05-in.-thick specimens only.

Compliance measurements and close range crack photographs were taken on approximately half of the specimens. The photographs were taken with a 35-mm camera at intervals which became more rapid as the failure load was approached. These photographs were coordinated with load by means of a Beckman recorder, which also recorded the output of the compliance gage.

After failure the fracture faces were examined in detail for failure mode and evidence of slow crack growth. The actual fatigue crack length was measured from the surface markings. At this time it was noted that more or less well defined parabolic shaped chevron marks were visible ahead of the fatigue crack. Assuming that these were evidence of slow crack growth, their dimensions were recorded for later correlation with compliance measurements. To further corroborate the fact that the chevron marks were, in fact, an indication of slow crack growth, one 0.75-in. specimen was loaded to 90 percent of its failing load. It was then X-rayed and sectioned as described later to determine the extent of internal crack growth.

Longitudinal and transverse tension specimens were cut from the failed halves of most of the fracture toughness specimens. Tensile yield and ultimate strength were obtained. Several full range stress-strain diagrams also were recorded.

Results

Material Properties—The variation of material properties obtained from the numerous tension specimens cut from the failed halves of the fracture toughness specimens is shown in Fig. 3. It will be noted that, in spite of efforts to obtain a uniform material, variations comparable to those obtained from random sampling of material existed.

Residual Strength Data—A compilation of residual strength data is presented in Table 2. The yield and ultimate strength obtained from the tension specimens cut from each fracture toughness specimen are included where available.

TABLE 2—*Residual strength data.*

Specimen No.[a]	Thickness, t, in.	Width, w, in.	l_{c_0}, in.	l_{c_0}/w	Failing Load, lb	Gross Stress, psi	σ_{yp} Long.	σ_{yp} Trans.
A-.05–1	0.0520	8.000	1.616	0.202	14 150	34 000	80 100	77 100
A-.05–2	0.0530	7.999	1.610	0.201	14 150	33 400	79 400	76 400
A-.05–3	0.0475	7.990	1.606	0.201	12 200	32 200	80 800	77 600
A-.05–4	0.0525	8.000	1.606	0.201	15 750	37 500	75 000	72 900
A-.05–5	0.0530	8.000	1.615	0.202	15 400	36 300	76 700	73 300
A-.05–6	0.0515	8.000	1.604	0.200	15 600	37 900	77 500	74 400
A-.1–3	0.1005	7.998	0.799	0.100	36 500	45 400	...	...
A-.1–4	0.1027	7.996	0.813	0.102	38 200	46 500	...	...
A-.1–2	0.1028	7.995	1.610	0.201	27 200	33 100	...	...
A-.1–5	0.1036	7.997	1.607	0.201	27 750	33 500	...	...
A-.1–6	0.1016	7.998	2.415	0.302	23 610	29 100	...	...
A-.1–7	0.1013	7.997	2.437	0.305	23 150	28 600	78 300	76 300
A-.2–1	0.2010	7.999	1.636	0.205	51 250	31 900	77 000	75 900
A-.2–2	0.2000	7.989	1.597	0.200	50 750	31 800	75 600	74 900
A-.3–4	0.3142	7.973	0.736	0.092	118 000	47 100	80 900	77 800
A-.3–5	0.3150	8.010	0.765	0.096	115 000	45 600	80 600	77 000
A-.3–1	0.3132	7.997	1.553	0.194	87 500	34 900	...	...
A-.3–2	0.3156	8.012	1.594	0.199	86 000	34 000	...	...
A-.3–3	0.3159	8.012	2.355	0.294	74 000	29 200	...	...
A-.3–6	0.3156	7.947	2.309	0.291	72 200	28 800	82 100	77 400
A-.45–1	0.4530	7.995	1.662	0.208	125 900	34 800	81 300	78 800
A-.6–6	0.6029	8.016	0.754	0.094	171 200	35 400	80 600	78 100
A-.6–7	0.6028	8.014	0.757	0.094	171 200	35 400	78 400	77 100
A-.6–2	0.6023	8.008	1.583	0.198	137 200	28 400	...	...
A-.6–3	0.6016	7.995	1.619	0.203	134 250	27 900	...	...
A-.6–4	0.6032	8.006	2.443	0.305	109 750	22 700	80 500	77 200
A-.6–5	0.6027	8.000	2.450	0.306	107 250	22 200	78 200	76 200
A-.75–1	0.7627	7.995	1.578	0.197	141 800	23 300	77 500	76 800
B-.05–1	0.0538	7.991	1.606	0.201	19 800	46 100	...	67 200
B-.05–2	0.0535	7.991	1.609	0.201	19 900	46 600	67 700	66 200
B-.05–3	0.0535	7.989	1.610	0.201	17 350	40 600	70 500	70 000

TABLE 2 (continued)

Specimen No.[a]	Thickness, t, in.	Width, w, in.	l_{c_0}, in.	l_{c_0}/w	Failing Load, lb	Gross Stress, psi	σ_{yp} Long.	σ_{yp} Trans.
B–.05–4.......	0.0531	7.999	1.608	0.202	18 000	42 400	69 100	69 000
B–.05–5.......	0.0545	7.990	1.638	0.205	18 700	42 900	68 800	69 500
B–.05–6.......	0.0545	7.990	1.620	0.203	19 700	45 200	69 400	68 800
B–.1–1........	0.1005	8.004	0.815	0.102	46 350	57 600	...	...
B–.1–2........	0.1036	8.005	0.818	0.102	44 825	54 100	...	...
B–.1–3........	0.1040	8.005	1.621	0.202	39 225	47 100	...	...
B–.1–4........	0.1045	8.005	1.617	0.202	37 200	44 500	62 900	63 900
B–.1–5........	0.1038	8.001	2.419	0.302	32 300	38 900	...	...
B–.1–6........	0.1012	8.001	2.412	0.301	30 000	37 100	...	...
B–.2–1........	0.2001	7.999	1.631	0.204	70 750	44 200	69 900	69 100
B–.2–2........	0.2010	7.991	1.641	0.205	63 000	39 200	68 300	68 000
B–.3 × 2–1....	0.3151	2.000	0.390	0.195	33 250	52 800	...	...
B–.3 × 2–2....	0.3187	2.001	0.432	0.215	32 500	51 000	...	...
B–.3–1........	0.3119	7.947	0.763	0.096	127 000	51 200	67 900	66 000
B–.3–2........	0.3164	7.949	0.770	0.097	127 600	50 700	68 400	68 400
B–.3–4........	0.3135	8.004	1.565	0.196	104 400	41 600	...	...
B–.3–5........	0.3159	8.000	1.589	0.199	108 000	42 700	...	...
B–.3–3........	0.3130	8.000	2.373	0.297	85 000	33 900	...	...
B–.3–6........	0.3168	8.000	2.371	0.296	87 000	34 300	69 200	71 900
B–.3 × 22–1...	0.313	22.0	4.43	0.201	216 000	31 400	70 850	69 600
B–.3 × 32–1...	0.311	32.0	6.42	0.201	285 000	28 600	67 150	68 100
B–.45–1.......	0.4575	7.995	1.627	0.204	148 200	40 500	70 600	69 700
B–.6 × 2–1....	0.5973	2.002	0.334	0.167	68 400	57 200	...	...
B–.6 × 2–2....	0.6020	2.003	0.307	0.153	66 000	54 700	...	...
B–.6–5........	0.6020	8.002	0.820	0.102	223 500	46 400	66 800	66 800
B–.6–6........	0.6050	8.000	0.785	0.098	220 750	45 600	63 600	65 800
B–.6–3........	0.5990	8.002	1.588	0.198	183 000	38 200	...	...
B–.6–4........	0.6018	8.008	1.613	0.201	177 250	36 800	...	...
B–.6–1........	0.5985	7.994	2.387	0.299	141 000	29 500	66 900	66 600
B–.6–2........	0.6000	7.993	2.421	0.303	141 500	29 500	66 700	65 800
B–.6 × 32–1...	0.6166	32.0	6.45	0.202	419 000	21 200	...	...
B–.6 × 32–2...	0.6152	32.0	6.40	0.200	465 000	23 600	...	...
B–.75–1.......	0.7635	7.992	1.614	0.202	171 400	28 100	68 300	69 000

[a]A = 7075-T651 material.
B = 7075-T7351 material.

Slow Growth Data—Slow crack growth is obtainable from crack photographs in the case of thin (0.05 and 0.10 in.) specimens, from compliance measurements coupled with a suitable calibration curve on tests where valid compliance measurements were obtained, and from interpretation of the markings on the failed surfaces. Slow growth obtained from crack photographs is not valid above $t = 0.1$ because of the tendency for cracks to grow faster in the interior of thick plates than on the surface. Figure 4 shows the surface markings on two specimens.

Use of the surface markings required some justification inasmuch as this is an unconventional procedure. Proof of the internal crack growth is provided by Figs. 5 and 6. Figure 5 is an X-ray of a 0.75-in. cracked plate loaded to 100
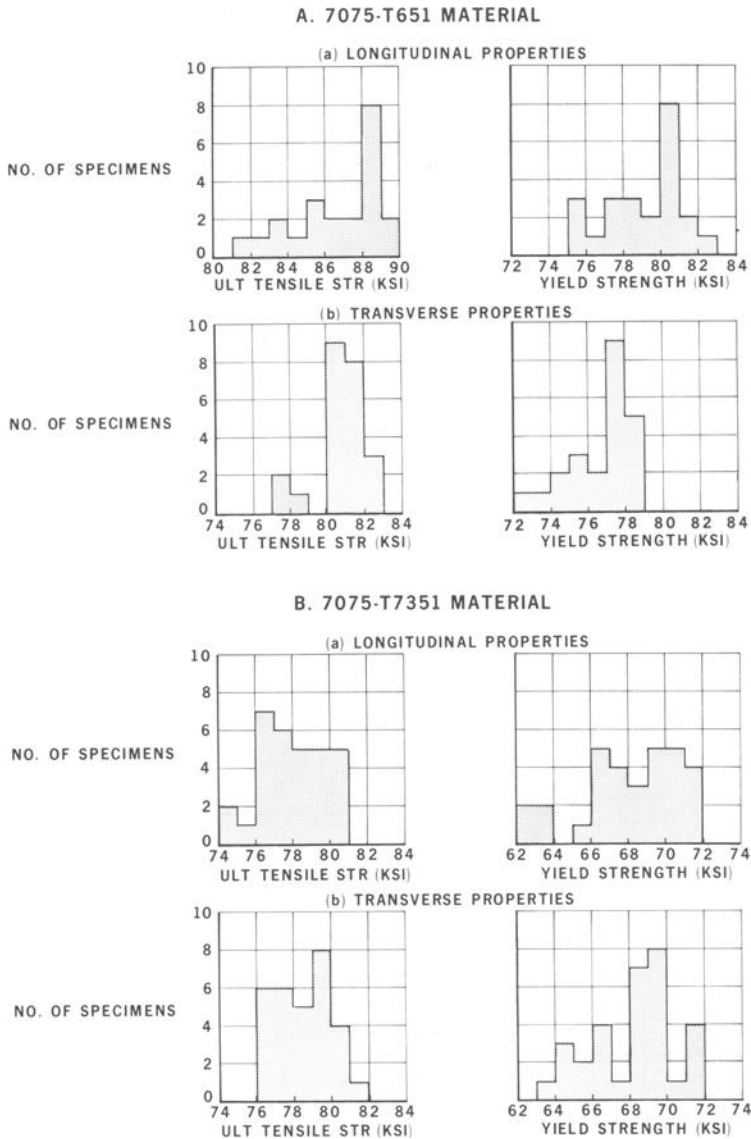
A. 7075-T651 MATERIAL

FIG. 3—*Variation of material properties.*

kip after having previously been loaded to 150 kip (approximately 90 percent of its failing load). The internal extension of the crack is evident. The same specimen subsequently was sectioned as shown in Fig. 6a, polished, and subjected to a penetrating dye; the results are shown in Fig. 6b. Evidence of internal growth again is apparent.
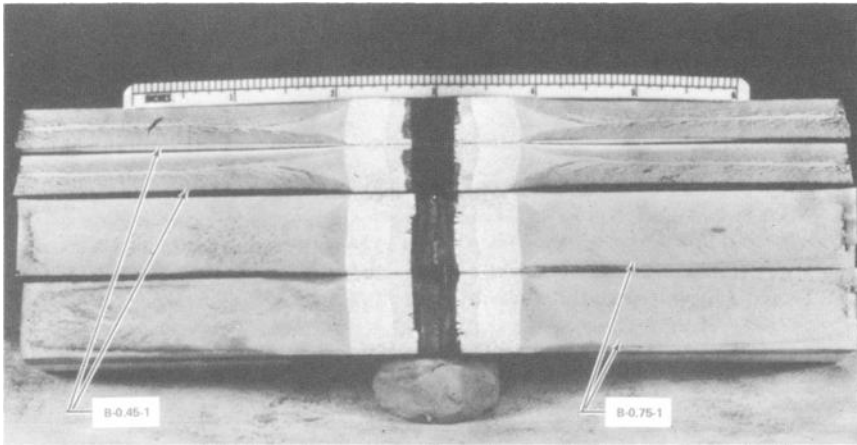
FIG. 4—*Surface markings on two specimens.*

The final crack length was computed from compliance measurements and compared to the final crack length obtained from surface markings. The results are shown in Fig. 7, where it can be seen that reasonable consistency is obtained with this technique. The calibration curve used for converting the compliance readings to crack length is derived in the Appendix. It will be noted that the derivation accounts for the effects of plasticity in accordance with the assumptions of Dugdale. An extension of published procedures is provided inasmuch as the effect of finite plate width is considered to the extent that the derivation is provided for a plate with a series of colinear, equally spaced cracks.

Table 3 provides the slow growth data for all specimens on which the growth could be determined. Voids in the data exist generally in the intermediate thicknesses where the surface markings were not clear and compliance measurements were not made. It is worthy of special note that the crack length recorded when the data were obtained from surface markings was the average of the crack front, as indicated by the sketch at the bottom of the table.
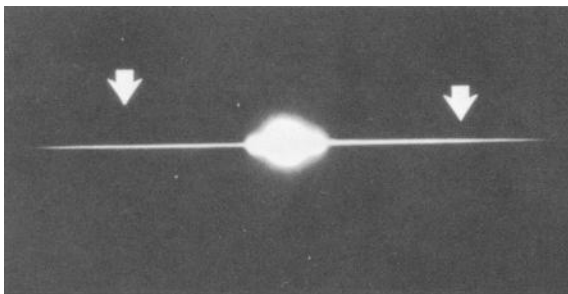

FIG. 5—*X-ray of cracked specimen under load (arrows denote limits of visible crack).*

TABLE 3—*Slow crack growth data.*

Specimen No.	Width, w, in.	Thickness, t, in.	$\dfrac{l_{c0} + \Delta l_c}{w}$
A–.05–1	8.000	0.0520	0.223
A–.05–2	7.999	0.0530	0.231
A–.05–3	7.990	0.0475	0.243
A–.05–4	8.000	0.0525	0.264
A–.05–5	8.000	0.0530	0.234
A–.05–6	8.000	0.0515	0.241
A–.2–1	7.999	0.2010	0.250
A–.2–2	7.989	0.2000	0.287
A–.3–4	7.973	0.3142	0.146
A–.3–5	8.010	0.3150	0.177
A–.3–1	7.997	0.3132	0.258
A–.3–2	8.012	0.3156	0.238
A–.3–3	8.012	0.3159	0.384
A–.3–6	7.947	0.3156	0.386
A–.45–1	7.995	0.4530	0.325
A–.6–6	8.016	0.6029	0.256
A–.6–7	8.014	0.6028	0.258
A–.6–2	8.008	0.6023	0.384
A–.6–3	7.995	0.6016	0.409
A–.6–4	8.006	0.6032	0.485
A–.6–5	8.000	0.6027	0.488
A–.75–1	7.995	0.7627	0.42
B–.05–1	7.991	0.0538	0.264
B–.05–2	7.991	0.0535	0.276
B–.05–3	7.989	0.0535	0.269
B–.05–4	7.999	0.0531	0.289
B–.05–5	7.990	0.0545	0.257
B–.05–6	7.990	0.0545	0.270
B–.2–1	7.999	0.2001	0.300
B–.2–2	7.991	0.2010	0.294
B–.3 × 2–1	2.000	0.3151	0.335
B–.3 × 2–2	2.001	0.3187	0.376
B–.3–1	7.947	0.3119	...
B–.3–2	7.949	0.3164	...
B–.3–3	8.004	0.3135	...
B–.3–4	8.000	0.3159	0.230
B–.3–5	8.000	0.3130	...
B–.3–6	8.000	0.3168	...
B–.3 × 22–1	22.0	0.313	0.248
B–.3 × 32–1	32.0	0.311	0.318
B–.45–1	7.995	0.4575	0.288
B–.6 × 2–1	2.002	0.5973	0.205
B–.6 × 2–2	2.003	0.6020	0.205
B–.6–5	8.002	0.6020	0.181
B–.6–6	8.000	0.6050	0.185
B–.6–3	8.002	0.5990	0.304
B–.6–4	8.008	0.6018	0.280
B–.6–1	7.994	0.5985	0.367
B–.6–2	7.993	0.6000	0.400
B–.6 × 32–1	32.0	0.6166	0.206
B–.6 × 32–2	32.0	0.6152	0.204
B–.75–1	7.992	0.7635	0.294

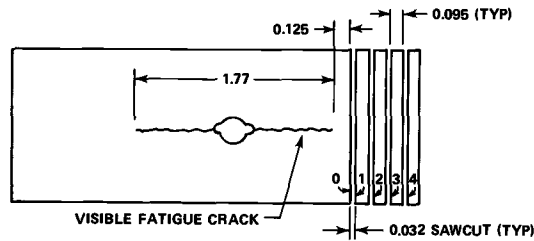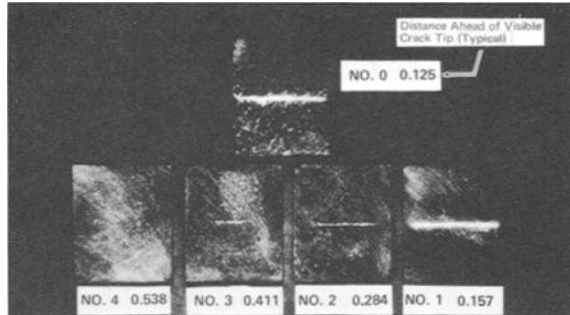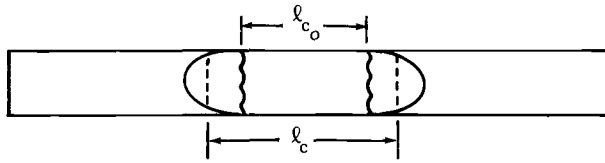NOTE—See Table 2 for l_{c0}.

TABLE 3 (continued)

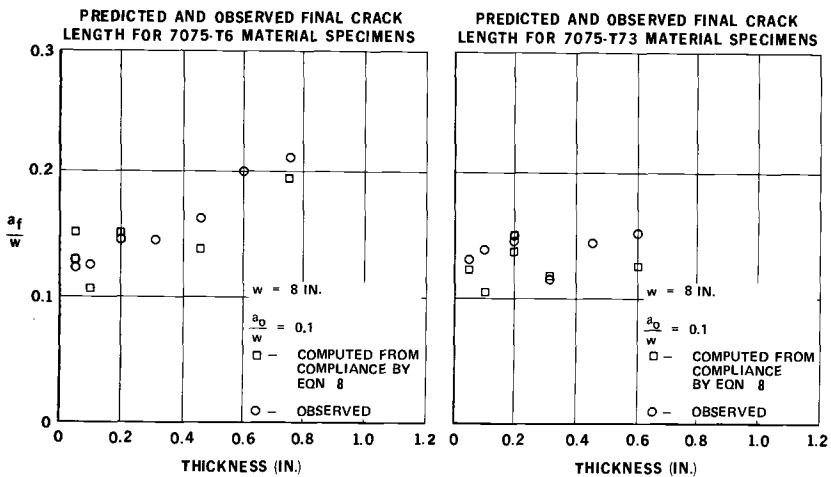FIG. 6—*Internal crack growth as determined from sections cut from a ¾-in. cracked plate.*

FIG. 7—*Computed and observed final crack length.*

Analysis of Data—In order to isolate the effects of thickness on fracture toughness, the data are reduced in the manner prescribed for thin plates. Differences between the fracture toughness of thick and thin plates can be designated then as thickness effects.

The classical equation for fracture toughness is the crack tip stress intensity factor of Irwin:

$$K_c = \sigma \sqrt{w \tan{(\pi a/w)}} \dots\dots\dots\dots\dots\dots\dots\dots(1)$$

where

σ = the gross area stress,
w = the plate width, and
a = one half the crack length.

Previous work [1][3] has shown that greater consistency is obtained with thin plate data if the following equation is used:

$$K_c' = \sigma \left[1 - \left(\frac{\sin{(\pi a/w)}}{\sin{\{(\pi/w)[a + (1/2\pi)]\}}} \right)^2 \right]^{-1/2} \dots\dots\dots\dots(2)$$

Both equations give a value of K which is numerically equal to the stress at a point $\frac{1}{2}\pi$ in. in front of the crack. However, in deriving Eq 1 it is assumed that the distance r in front of the crack, at which the stress is measured, is very small in relation to a, the one-half crack length. In practice, this does not appear to be a valid assumption when the crack length is small. As an example, Fig. 8 shows 7075-T6 thin plate data reduced on the basis of both equations. The value of K_c' remains essentially constant whereas K_c reduces with crack length. As a matter of interest, if r^2/a^2 is assumed small relative to unity, the following equation is obtained for the $\frac{1}{2}\pi$ stress:

$$K_c' = \sigma \sqrt{w \tan{(\pi a/w)} + 1} \dots\dots\dots\dots\dots\dots(3)$$

This is a close approximation of Eq 2. Ignoring the 1 under the radical produces the error in plates with short cracks. This fact was recognized by Kuhn [2] although he approached the problem in a somewhat different fashion. It also is recognized that better results are obtained if the half crack length includes the slow crack growth induced during loading to failure; however, because of the difficulty involved in measuring slow crack growth, results are often plotted on the basis of original crack length.

When thin, centrally cracked plate data are reduced correctly, curves such as those appearing in Fig. 9 are produced. These generally have a constant portion representing stability failure in the elastic range. At the lower values of crack length or plate width, the curves experience a cutoff caused by gross yielding on the net section (Fig. 9a). Materials with exceptionally high toughness will not fail prior to the development of yielding on the net section. Data

---

[3] Italic numbers in brackets refer to the list of references at the end of this paper.
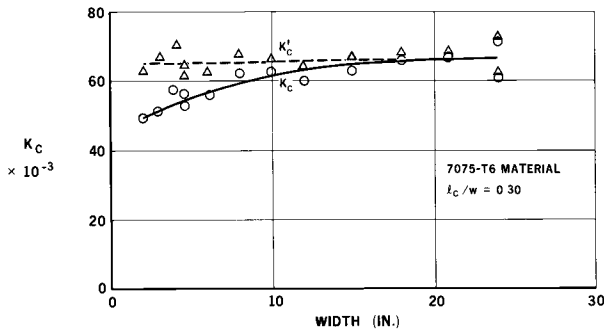
FIG. 8—*Variation of* K_c *and* K_c' *with plate width.*

from these materials appear as in Fig. 9b. If a material has a definite non-linearity below the yield, the proportional limit may be a limiting factor rather than the yield point as shown in Fig. 9c. It will be noted in the following pages that 7075-T6 material behaves according to Fig. 9a, the T73 material according to Fig. 9c.

Data Uncorrected for Slow Crack Growth—Figure 10 shows the variation of K_c and K_c' with crack length for material thicknesses of 0.1, 0.3, and 0.6 in. As mentioned above, K_c tends to reduce as crack length is reduced while K_c' tends to remain constant. Figure 11 shows the variation of fracture toughness with thickness for the 8-in.-wide specimens having l_{c0}/w equal to approximately 0.2. These curves are extrapolated to their respective K_{Ic} values. It is seen that the fracture toughness of 7075-T6 varies little up to a thickness of 0.45 in. and that the plane strain value is reached with both materials at a thickness of approximately 1 in.

Figure 12 shows that K_c and K_c' for the 7075-T73 material vary considerably with plate width. K_c varies more than K_c' and the difference again is attributed to the inability of Eq 1 to correctly analyze plates with short cracks. Figure 13 shows the variation of fracture toughness through the thickness of the stock 0.75-in. plate as obtained from the 0.05-in.-thick specimens. The toughness is
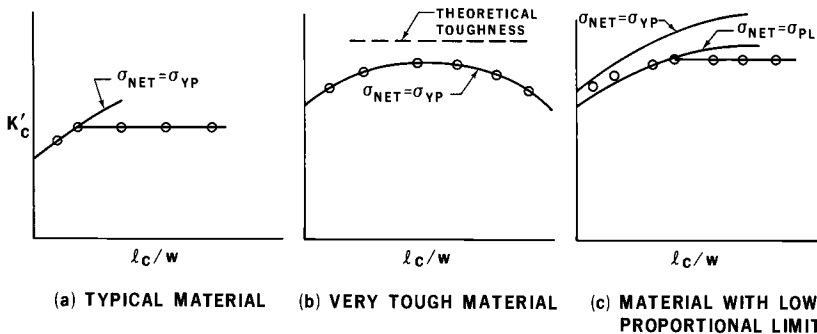

(a) TYPICAL MATERIAL   (b) VERY TOUGH MATERIAL   (c) MATERIAL WITH LOW
PROPORTIONAL LIMIT

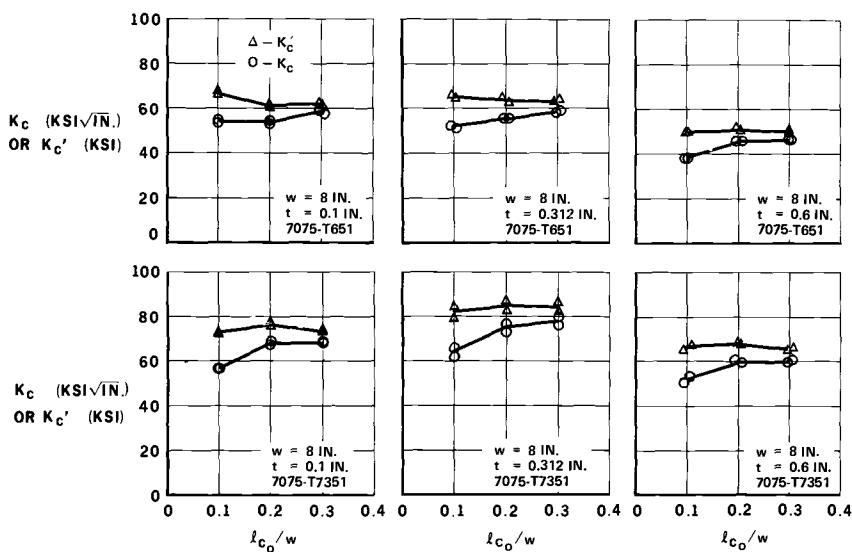FIG. 9—*Schematic plots of thin plate data.*

FIG. 10—*Variation of fracture toughness with crack length (uncorrected for slow growth)*.
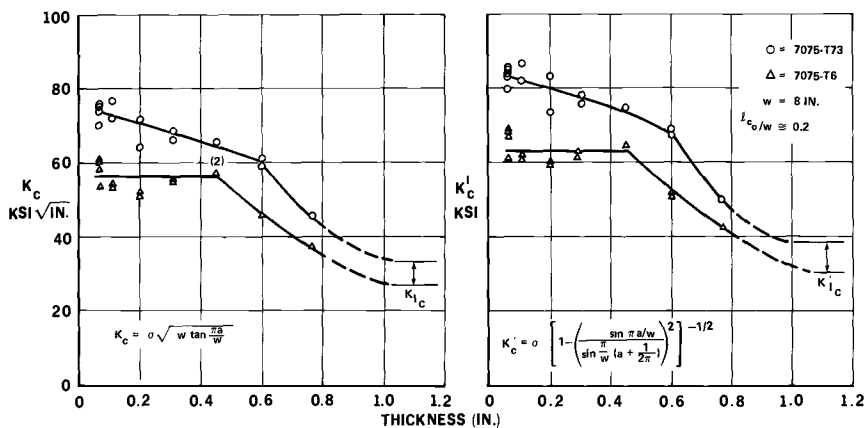

FIG. 11—*Variation of fracture toughness with thickness (8-in.-wide specimens—uncorrected for slow crack growth)*.

lower at the center than near the surface by approximately 10 percent. The toughness varies inversely with the yield strength of the material.

Data Reduced on the Basis of Final Crack Length—General reasoning leads to the conclusion that the crack front will assume the shape which is most stable, and this corresponds to the development of plane stress at its boundaries. It is expected, therefore, that the fracture toughness should be constant when it is calculated on the basis of final crack length.

The variation of fracture toughness with crack length for the 8-in.-wide specimens is shown in Fig. 14; the variation with thickness is shown in Fig. 15.

There is a tendency for the fracture toughness to be constant within experimental scatter, although a downward trend with thickness is noticeable with 7075-T73.

Figure 16 shows plots of fracture toughness versus plate width. Because of the limited amount of wide plate data available from the current program, the plot includes data from another source. It appears from examination of the 7076-T6 data in Figs. 14, 15, and 16 that the fracture toughness constant is independent of thickness and width within the range investigated.

The fracture toughness of the T73 material varies considerably with width. The values of K_c' corresponding to net section stresses of σ_{yp} and σ_{pl} are plotted on Fig. 16, from which it can be seen that for all except the thickest
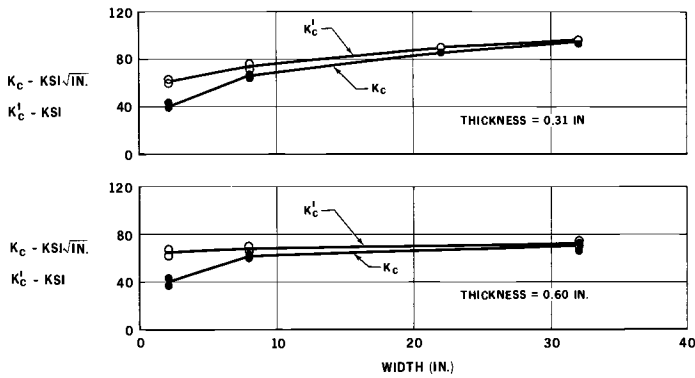

FIG. 12—*Variation of fracture toughness with plate width for 7075-T73 material (uncorrected for slow crack growth).*
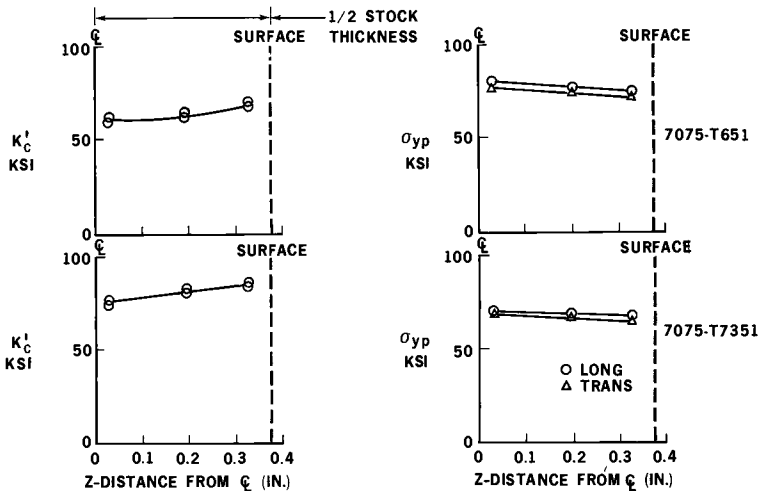

FIG. 13—*Variation of fracture toughness through the thickness as obtained from 0.05-in.-thick specimens (uncorrected for slow crack growth).*
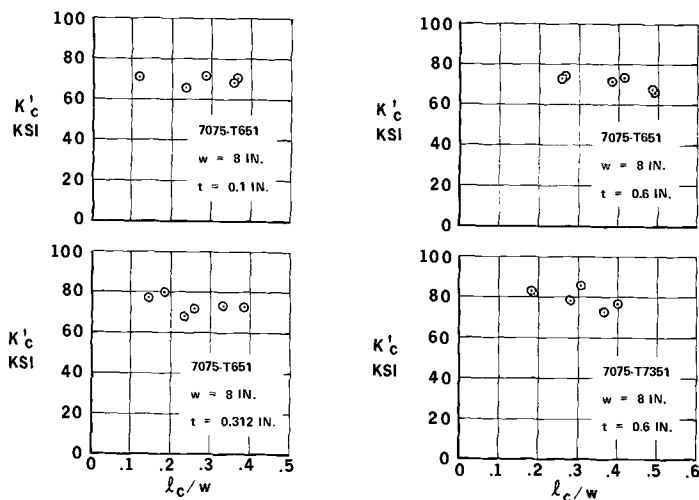
FIG. 14—*Variation of fracture toughness with thickness (8-in.-wide specimens—corrected for slow crack growth.)*

specimens the net stresses were between the proportional limit and the yield. Thus, the data from the 0.312-in.-thick specimens follow previously noted behavior for thin specimens. The loss of fracture toughness noted for the 0.6 and 0.1-in.-thick specimens represents an effect of thickness which is currently unpredictable.

Conclusions—The results of these tests have shown that the fracture toughness characteristics of 7075-T6 and 7075-T73 are substantially different. The
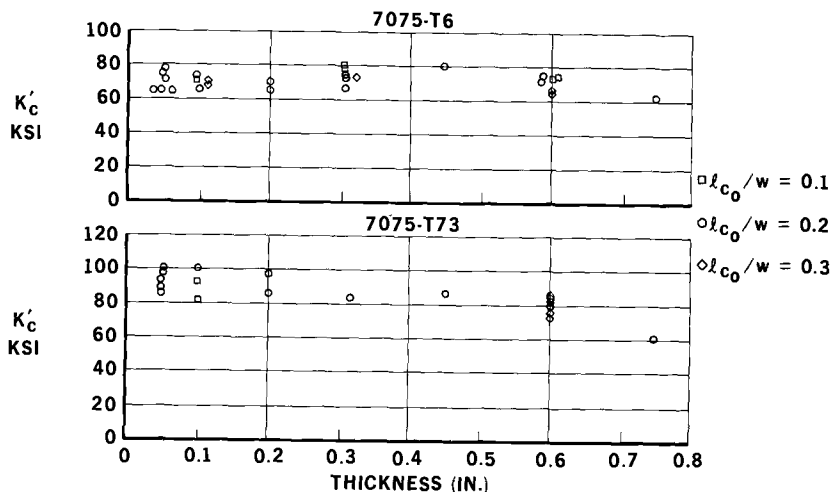

FIG. 15—*Variation of fracture toughness with thickness (8-in.-wide specimens—corrected for slow crack growth).*
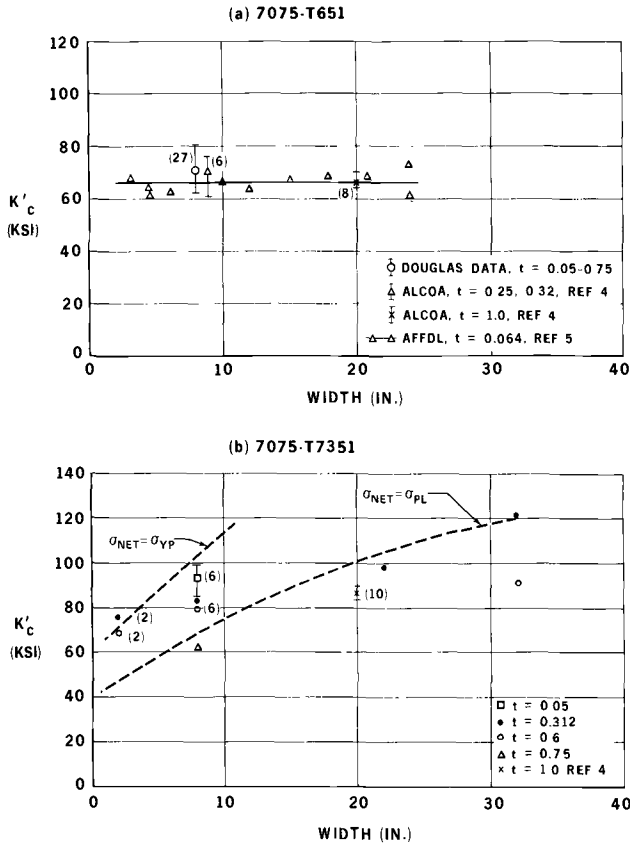
(a) 7075-T651

(b) 7075-T7351

FIG. 16—*Variation of fracture toughness with plate width (corrected for slow crack growth).*

fracture toughness of the 7075-T6 material when computed on the basis of final crack length appears to be independent of thickness or width. The fracture toughness of the T73 material shows a variation with both.

It has been hypothesized that the crack front will develop a shape during slow loading which is most stable and that this corresponds to the development of plane stress at its boundaries. It was expected, therefore, that fracture toughness based on final crack length should be constant. This theory was borne out by the results of the 7075-T6 tests, but not by the tests on 7075-T73.

The variation of fracture toughness with width of the 0.312-in.-thick T73 material follows the pattern described in Fig. 9c and is attributed to the fact that various amounts of gross yielding on the net section occur with the thinner specimens. It can be concluded that the true plane stress fracture toughness of the T73 is above 100 ksi and that plate widths greater than 32 in. are needed to determine the value accurately. In this regard the material is similar to 2024-T3.
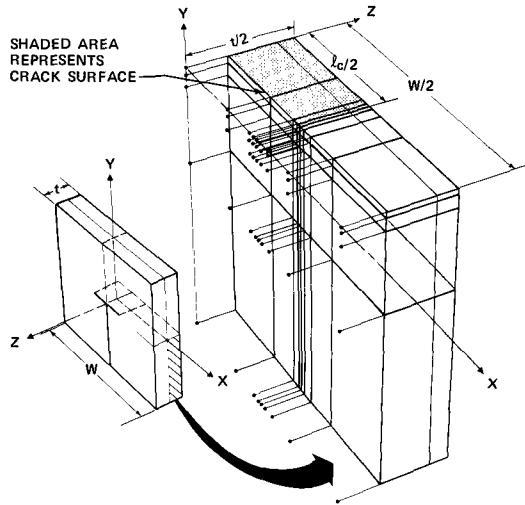
FIG. 17—*Structural model for lumped parameter analysis.*

On the basis of rather meager data it appears that a rapid loss in fracture toughness of the T73 occurs with wide specimens at thicknesses above 0.312 in. (see Fig. 16). This loss is unexplainable at this time and will require further investigation.

The Analytical Program

Calculation of the stress distribution in three centrally cracked plates of varying thickness was performed by a lumped parameter, redundant force
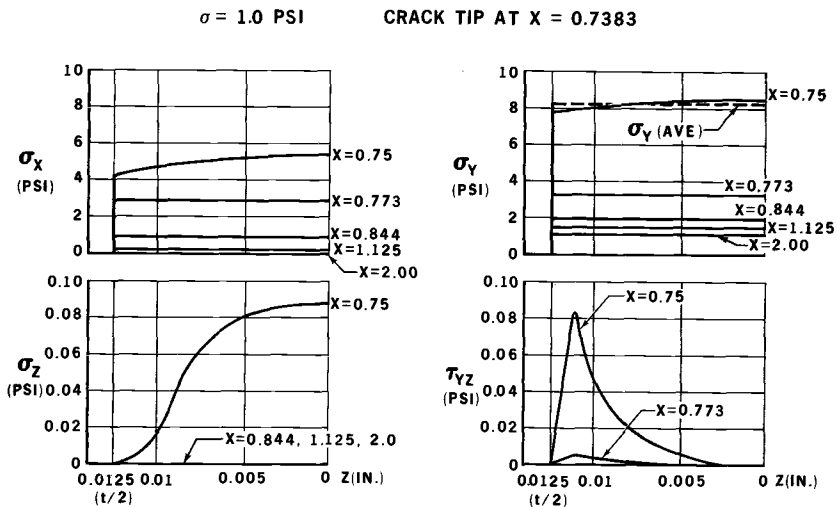

FIG. 18—*Stress distribution through the thickness in the crack plane in a 0.025-in.-thick plate.*
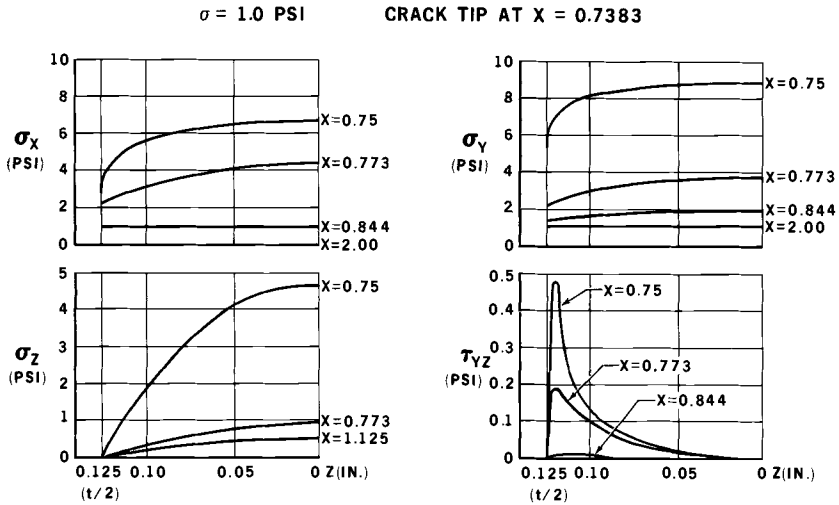
σ = 1.0 PSI   CRACK TIP AT X = 0.7383

FIG. 19—*Stress distribution through the thickness in the crack plane in a 0.25-in.-thick plate.*

analysis using the FORMAT (Fortran matrix abstraction technique) system. Previous work on single layered thin sheets provided results that were in reasonable agreement with classical theory.

The current analysis was a three-dimensional elastic analysis which included the Poisson ratio effects on the formulation of a 1049 by 1049 flexibility matrix. The plates were modeled as shown in Fig. 17. Conditions of symmetry permitted the analysis to be performed on one eighth of the total plate. Thicknesses of 0.025, 0.250, and 0.500 in. were analyzed. The plate width was
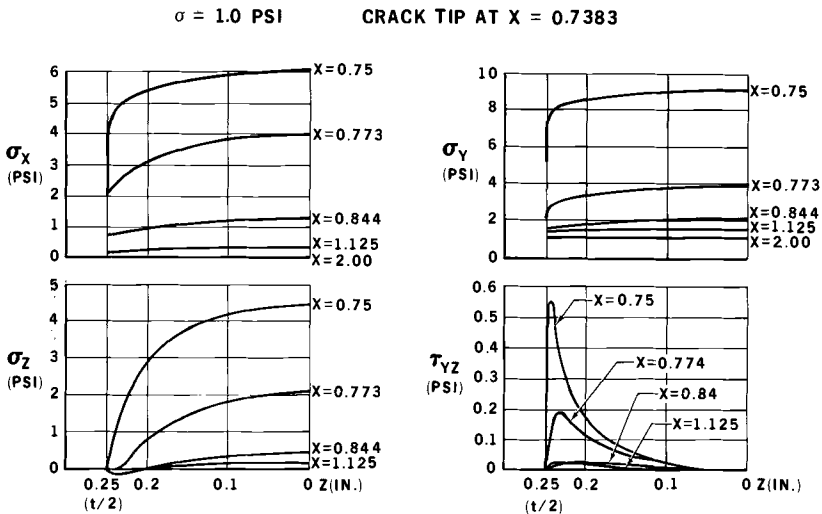
σ = 1.0 PSI   CRACK TIP AT X = 0.7383

FIG. 20—*Stress distribution through the thickness in the crack plane in a 0.50-in.-thick plate.*

W = 4.0 IN.
ℓ_c = 1.4766 IN.
x − a = 0.0117 IN.
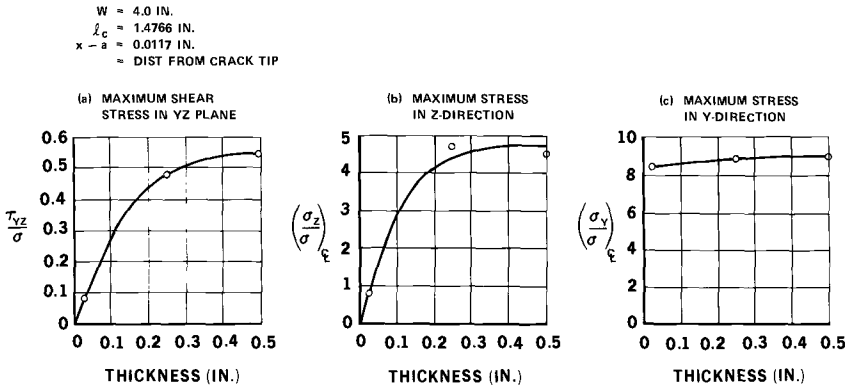   = DIST FROM CRACK TIP

FIG. 21—*Variation of stresses near tip of crack with thickness of plate.*

4 in. and the crack aspect ratio was 0.370 in all cases. Three layers per side were used. Although the model appears to simulate the plate in a rather gross manner, the complexity was such as to strain the capacity of the computing machine. Each solution required 2.5 h running time on the IBM 360 computer. There were 236 redundant forces.

The results of the analysis are shown in Figs. 18, 19, and 20 in terms of stresses in the crack plane through the thickness at various distances from the plate center line. Because of the sparsity of points considerable judgment was involved in fairing these curves; therefore, they should be viewed qualitatively. The distributions at $x = 0.75$ in. ($r = 0.0117$ in.) correspond to the assumptions involved in the conventional stress intensity factor, namely, an elastic analysis and $r \rightarrow 0$. At this station, the distributions vary considerably with thickness. Of considerable interest are the increases in σ_z and τ_{xz} which accompany increased thickness. These are displayed more simply in Fig. 21, where it can be seen that plane strain effects are nearly completely developed at a thickness of 0.25 in. On the basis of such an analysis, one would expect that the fracture toughness would attain its K_{Ic} value in plates of 0.25-in. thickness. It has been shown in the test program that K_{Ic} is attained at a thickness of approximately 1 in. The difference is attributed to the fact that the analysis does not consider plasticity or slow crack growth.

The final objective of this work was to obtain stress distributions including the effects of plasticity. However, the complexity of the problem and budget limitations have deterred effort in this area. Some such analysis is considered necessary, however, to explain the fracture characteristics of plates of intermediate thickness.
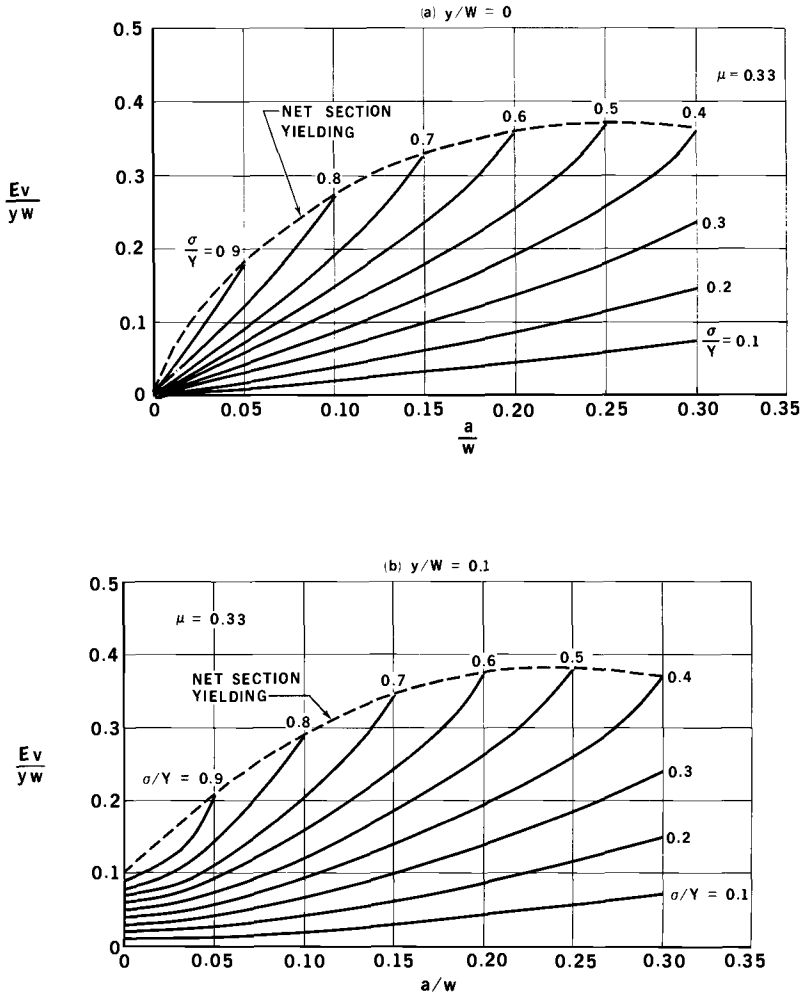
FIG. 22—*Deflection curves for centrally cracked panels.*

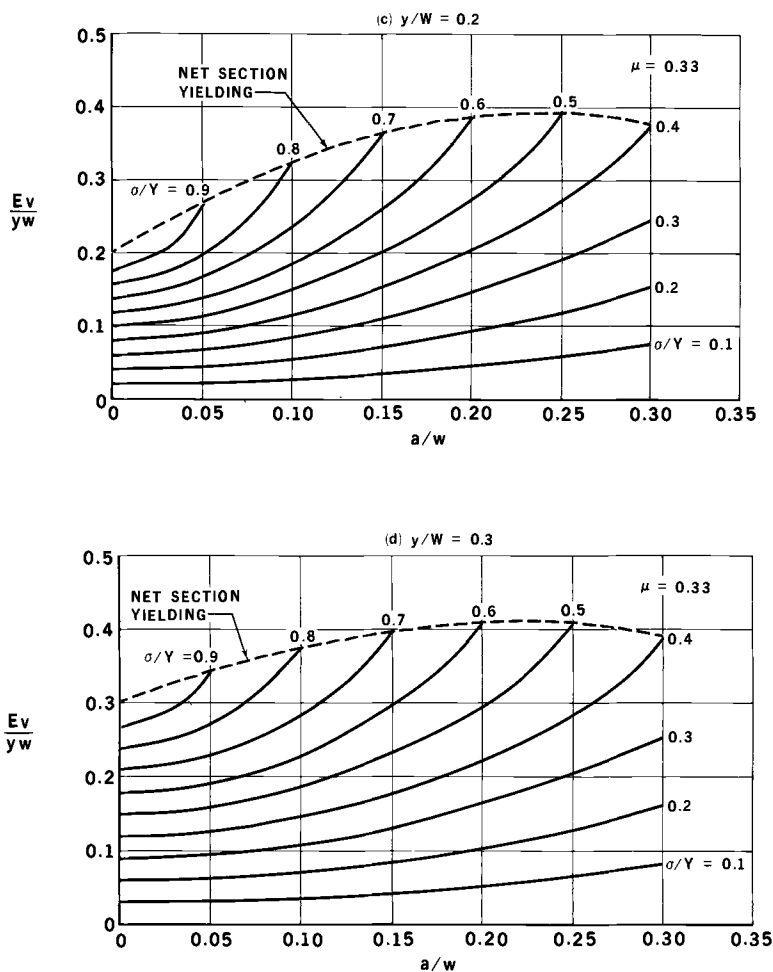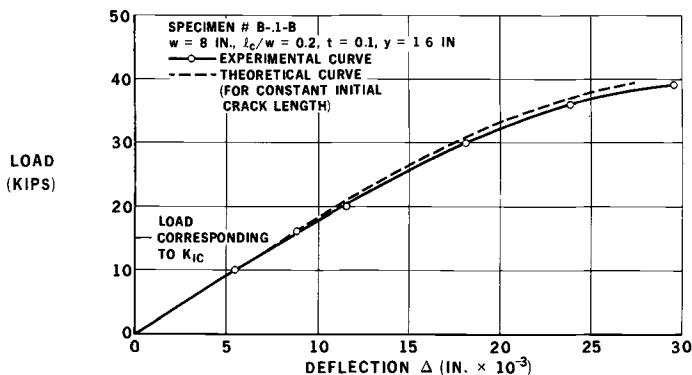## Acknowledgments

FIG. 22—*Continued.*

FIG. 23—*Experimental and theoretical load-deflection diagrams for a 7075-T73 specimen.*

APPENDIX

Load-Deflection Relationships for Centrally Cracked Plates Including the Effects of Plasticity

The load-deflection relationships of centrally cracked plates is derived for the case of an infinite plate with a series of colinear cracks equally spaced w inches apart. The effects of plasticity are included in accordance with the assumptions of Dugdale, namely, that the material is ideally elastoplastic and a uniform stress, $\sigma_{yp} = Y$, exists in the plastic zone.

The Westergaard stress function for a biaxially loaded plate described above is

$$Z(\zeta) = Y \left\{ 1 - \frac{2}{\pi} \tan^{-1} \left[\frac{1 - \left(\frac{\sin (\pi/w)(a + \rho)}{\sin (\pi/w)\, \zeta} \right)^2}{\left(\frac{\sin (\pi/w)(a + \rho)}{\sin (\pi/w)\, a} \right)^2 - 1} \right]^{1/2} \right\}$$

$$- Y \left[1 - \frac{2}{\pi} \sin^{-1} \left(\frac{\sin (\pi a/w)}{\sin (\pi/w)(a + \rho)} \right) \right] \left[1 - \left(\frac{\sin (\pi/w)(a + \rho)}{\sin (\pi/w)\, \zeta} \right)^2 \right]^{-1/2}$$

$$+ \sigma \left[1 - \left(\frac{\sin (\pi/w)(a + \rho)}{\sin (\pi/w)\, \zeta} \right)^2 \right]^{-1/2} \quad \ldots\ldots\ldots\ldots\ldots\ldots (4)$$

where $Z(\zeta)$ is a function of the complex variable

$$\zeta = x + iy$$

and ρ is the plastic zone size.

The plastic zone size for this geometry has been derived by Smith [3] using the technique of Dugdale, which requires that the extended crack tip stress be finite and equal to Y. This condition is attained when the coefficients of the singular terms sum to zero. The plastic zone size is given by

$$\rho = \frac{w}{\pi} \sin^{-1} \left[\sin \frac{\pi a}{w} \sec \frac{\pi}{2} \frac{\sigma}{Y} \right] - a \ldots\ldots\ldots\ldots\ldots (5)$$

When the plastic zone size is defined by Eq 5, Eq 4 reduces to

$$Z(\zeta) = Y \left\{ 1 - \frac{2}{\pi} \tan^{-1} \left[\frac{1 - \left(\frac{\sin (\pi/w)(a + \rho)}{\sin (\pi/w)\, \zeta} \right)^2}{\left(\frac{\sin (\pi/w)(a + \rho)}{\sin (\pi/w)\, a} \right)^2 - 1} \right]^{1/2} \right\} \quad \ldots\ldots\ldots (6)$$

For uniaxial tension and plane stress conditions, the vertical displacement at any point in the plate is given by

$$v = \frac{2}{E} \text{Im}\{\bar{Z}\} - \frac{1 + \mu}{E} y \, \text{Re}\{Z\} + \frac{\mu y \sigma}{E} \ldots\ldots\ldots\ldots\ldots (7)$$

where Re and Im are the real and imaginary parts of the noted functions and

$$Z = (d/d\zeta) \bar{Z}$$

Substituting Eq 6 into Eq 7, the following is obtained for the displacement:

$$
v = \frac{Y}{E\pi} \int_0^{a+\rho} \ln \left(\frac{1+\phi}{1-\phi}\right)^2 dx + y \left[\frac{(1-\mu)}{E} y + \frac{\mu}{E}\sigma\right]
$$
$$
- \frac{4Y}{\pi E} \int_0^y \tan^{-1}\left[\frac{1}{B}\sqrt{1+\left(\frac{\sin(\pi/w)(a+\rho)}{\sinh(\pi y/w)}\right)^2}\right] dy
$$
$$
+ \frac{2(1+\mu)yY}{\pi E}\tan^{-1}\left[\frac{1}{B}\sqrt{1+\left(\frac{\sin(\pi/w)(a+\rho)}{\sinh(\pi y/w)}\right)^2}\right] \dots\dots\dots\dots(8)
$$

where

$$
\phi = \sqrt{\frac{\left(\dfrac{\sin^2(\pi/w)(a+\rho)}{\sin^2(\pi/w)\,x}-1\right)}{\left(\dfrac{\sin^2(\pi/w)(a+\rho)}{\sin^2(\pi a/w}-1\right)}}
$$

and

$$
B = \sqrt{\left(\frac{\sin(\pi/w)(a+\rho)}{\sin(\pi a/w)}\right)^2 - 1}
$$

The solution for the displacement v was obtained by numerical integration of Eq 8 and the results are presented in graphical form in Fig. 22. The load-deflection curve for a specific case may be obtained from a vertical cross plot of the pertinent figure. An example is shown in Fig. 23 where a comparison is made with experimental data.

References

[1] Allen, F. C., "*Stress Analysis of Centrally Cracked Plates*," Douglas Aircraft Company Engineering Paper 5513, March 1969.
[2] Kuhn, Paul, "*Residual Strength in the Presence of Fatigue Cracks*," NASA unnumbered publication presented to Structures and Materials Panel, Advisory Group for Aeronautical Research and Development, North Atlantic Treaty Organization (AGARD), April 1967.
[3] Smith, E., "*Fracture at Stress Concentrations*,"Proceedings of the First International Conference on Fracture, Sendai, Japan, 1965.
[4] Feddersen, C. E. and Hyler, W. S., "*Compilation of Fracture Data for Aluminum Alloys*," DMIC Technical Note, Defense Metals Information Center, Battelle Memorial Institute, Columbus, Ohio, 1 Nov. 1965.
[5] Forman, R. G., "*Experimental Program to Determine the Effect of Crack Buckling and Specimen Dimensions on Fracture Toughness of Thin Sheet Materials*," AFFDL-TR-65-146, Air Force Flight Dynamics Laboratory, Wright-Patterson Air Force Base, Dayton, Ohio, Jan. 1966.

N. J. I. Adams[1]

The Influence of Curvature on Stress Intensity at the Tip of a Circumferential Crack in a Cylindrical Shell

ABSTRACT: The validity of a nondimensional curvature parameter, relating discontinuity size to shell radius and thickness, used to express the effect of curvature on stress intensification at a discontinuity in a cylindrical shell, has been substantiated within a limited range. Fatigue crack growth tests were conducted on flat and curved axially loaded specimens to examine the influence of curvature on stress intensity in cylindrical shells. Using crack growth rates, a curvature correction is obtained which can be used to apply a stress intensity analysis in flat sheets to cylinders. The influence of curvature on stress intensity is found to be similar to that of sheet buckling in flat sheets containing cracks.

KEY WORDS: metal sheets, aluminum alloys, fatigue (materials), cracking (fracturing), crack propagation, structural design, curvature, cylindrical shells, loads (forces), stresses, axial strain, static tests, fatigue tests

Nomenclature

a Half length of discontinuity (crack, ellipse, circle), in. (m)

a_c Half length of crack in curved sheet, in. (m)

a_f Half length of crack in flat sheet, in. (m)

b Minor axis of ellipse, in. (m)

C Buckling correction factor, $1 + 20(\delta/a)^2$

C_c Curvature correction factor, $\sqrt{a_f}/\sqrt{a_c}$, for equal stress intensity

C_W Finite width correction factor, $\sec \sqrt{\pi a/W}$

D Modulus of rigidity, $Eh^3/\sqrt{12(1 - \nu^2)}$

E Young's modulus of elasticity, psi (MN/m²)

h Shell thickness, in. (m)

i Complex number

[1] Resident research associate, National Academy of Sciences, NASA Langley Research Center, National Aeronautics and Space Administration, Hampton, Va. 23365.

K_{cyl} Stress intensity factor for a crack in a cylindrical shell, $\text{ksi}\sqrt{\text{in.}}$ $(\text{MN/m}^{3/2})$

K_{flat} Stress intensity factor for a crack in a flat sheet, $\text{ksi}\sqrt{\text{in.}}$ $(\text{MN/m}^{3/2})$

N Number of cycles

R Shell radius, in. (m)

S Stress at "infinity," ksi (MN/m^2)

W Sheet width, in. (m)

w Radial deflection, in. (m)

α Curvature parameter, a^2/Rh

δ Out-of-plane deflection of crack edge, in. (m)

δ_c Radial distance from crack tip to crack center, in a cylindrical shell in. (m)

$\epsilon_\theta, \epsilon_\infty$ Strain

σ Axial stress at "infinity," psi (MN/m^2)

σ_η Stress (elliptic coordinates), psi (MN/m^2)

ν Poisson's ratio

φ Force function

The application of a fail-safe design philosophy can be greatly enhanced by an improved understanding of the resistance of structures and structural materials to failure in the presence of a discontinuity. Data relating to material failure at a discontinuity in a highly stressed structure generally are based on testing flat sheet specimens in fatigue or monotonic loading conditions. Such data are used frequently in the design of structures which make use of curvature to achieve greater structural efficiency. The effect of curvature on stress states at a discontinuity had received little attention [1][2] until recently [2–6].

The purpose of the present investigation was to examine, experimentally, the influence of curvature on stress intensification at a discontinuity in an axially loaded circular cylindrical shell. Results are presented of static and fatigue tests which were conducted on flat and cylindrical specimens weakened by a circular hole or circumferential crack. A curvature correction factor was obtained experimentally which permitted the theoretical analysis of a flat sheet containing a crack to be applied to a cylindrical shell which contains a crack.

Theoretical Background

The state of stress in a cylindrical shell is dependent upon two variables: a force function which defines the in-plane stress state and a displacement function which defines the bending stresses present in the shell. These two

---

[2] Italic numbers in brackets refer to the list of references at the end of this paper.

functions are coupled by the following governing equations for shallow cylindrical shells:

$$\left.\begin{array}{c} \dfrac{1}{Eh}\,\nabla^4\varphi + \dfrac{1}{R}\,\dfrac{\partial^2 w}{\partial x^2} = 0 \\[4mm] D\nabla^4 w - \dfrac{1}{R}\,\dfrac{\partial^2\varphi}{\partial x^2} = 0 \end{array}\right\} \dotfill(1)$$

When the governing equations are expressed in elliptic coordinates, a solution can be obtained for an axially loaded cylindrical shell containing an elliptic cutout [7]. When the major axis is normal to the loading direction, the maximum stress concentration on the midplane of the shell is given by

$$\frac{\sigma_\eta}{\sigma} = \left(1 + \frac{2a}{b}\right) + \frac{\alpha\pi\sqrt{3(1 - \nu^2)}}{16}\left(\frac{a}{b} + \frac{b}{a}\right) \dotfill(2)$$

The first part of this equation is the familiar flat plate solution and the second part introduces the effect of curvature. When $a = b$ the solution for a circular hole is obtained, and as $b \to 0$ the solution for a crack is obtained. This solution was chosen as an example because, with the ratio a/b held constant, it demonstrates that concentration effects due to curvature depend only on the nondimensional curvature parameter

$$\alpha = a^2/Rh \dotfill(3)$$

which is a function of the shell radius, thickness, and half length of the discontinuity (see Fig. 1).

The solutions [2–7] are all in terms of α, but their application is restricted to a particular range of α. This range is governed by the assumptions made in satisfying the boundary conditions and governing equations.
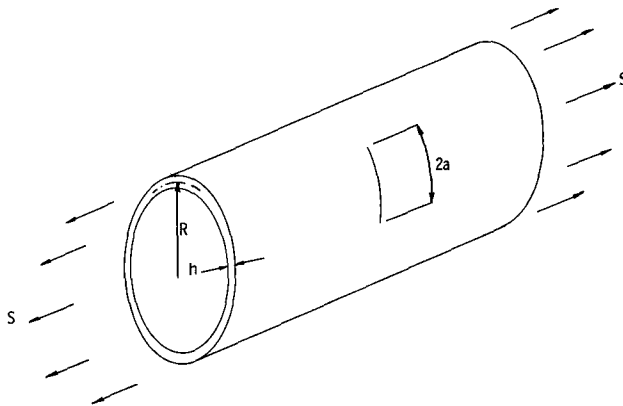

FIG. 1—*Shell geometry and loading.*

Experimental Work

The experimental work was divided into two parts. The first dealt with static tests on cylinders, to confirm the validity of the curvature parameter α as a means of expressing curvature effects on stress intensification at a discontinuity. The second part consisted of tension-tension fatigue crack growth tests on flat and curved specimens. From these tests the influence of curvature on crack growth rate was determined.

Static Experiments

One cylinder and one cylindrical panel with approximately equal values for the curvature parameter α, but different dimensions, as shown in Table 1, were tested statically. The cylinder was made of mild steel and had a radius: thickness ratio of 10.5, which is close to the lower limit of thin shell theory. This cylinder was tested in compression. The second specimen was a cylindrical panel made of aluminum and had a radius:thickness ratio of approximately 140. This specimen was tested by loading in tension in the same manner as the fatigue specimen (see Fig. 2). In both cases strain gages were used to measure strains in the hole on the midplane of the shell and the strains on the surface remote from the hole, that is, at "infinity." Several tests were made on each specimen, and prior to each test adjustments were made to the shell end fittings in an attempt to improve the distribution of strain around the shell remote from the hole.

Fatigue Experiments

Fatigue crack growth tests were conducted on flat panels and panels having a radius of curvature, perpendicular to the axis of loading, of 4 in. (102 mm) and 5 in. (127 mm). The flat and developed width of the curved specimens was 8 in. (204 mm). The specimens were manufactured from L72 (2014-T4) aluminum sheet 0.036 in. (0.9 mm) thick. To obtain consistent material properties, all the specimen blanks were annealed. Those to be of cylindrical form were pressed to about 6-in. (151-mm) radius, and then rolled to obtain a 4-in. (102-mm) or 5-in. (127-mm) radius. The flat and curved specimens were then aged artificially, according to material manufacturer's specifications (160 C for 7 h).

Repeated axial loading with a maximum gross stress of 8 ksi (55 MN/m²)— ratio of minimum to maximum stress, 0.5—was applied. Fatigue crack growth was monitored automatically using multistrand, foil crack propagation gages [8]. The gages were attached to the specimen at both ends of a central starter notch, made by the electric discharge process. To simplify loading of the curved specimen, one test panel and one dummy panel were bolted back to back on circular end fittings (see Fig. 2). The dummy panel contained a large, circular hole in place of the starter notch. This arrangement produced an approximately equal load distribution between the panels. The same maximum remote stress and stress range were applied to both the flat and curved specimens to simplify comparison of the results.
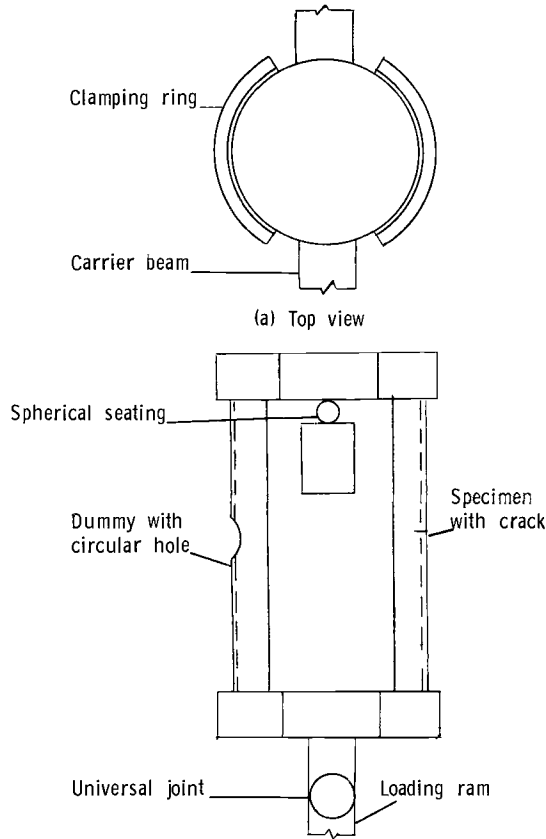
FIG. 2—*Testing arrangement for cylindrical static and fatigue specimen.*

Results and Discussion

The experimental results for the static tests were analyzed and compared with theoretical predictions. Crack growth rate and stress intensity analysis for flat plates were used to determine a curvature correction factor C_c for stress intensity in curved panels, and the result compared with existing theory.

Static Results

From the measurements the strain concentration factor $\epsilon_\theta/\epsilon_\infty$ was determined. The theoretical strain varies less than 0.5 percent from the maximum value for the gage length used to measure the strain in the hole. Thus, within the elastic range it is possible to compare the experimentally determined elastic strain concentration factor with the force concentration factor predicted theoretically. The experimental results and theoretical predictions are shown in Table 1. The experimental values represent analysis of the results based on three tests. The theoretical results were obtained from Eq 2 for the case $a = b$. Results of strain measurements are presented in greater detail in Ref 6.

The results shown in Table 1 confirm that for circular holes, in shells having dimensions within the range examined, the theoretical prediction of the effect of curvature on stress concentration can be expressed in terms of the nondimensional parameter α. In view of the good agreement between the experimental results and theoretical predictions, together with the fact that α appears in theoretical solutions for cylindrical shells containing cracks, it was felt that α was a valid parameter to use in the analysis of crack propagation results for cylindrical shells.

TABLE 1—*Theoretical and experimental strain gage results.*

Cylinder Material, Mild Steel

R = 2.625 in. (67 mm), h = 0.25 in. (6.35 mm), a = 1.006 in. (25.6 mm), α = 1.542

Test	Experimental Strain Concentration Factor	Theoretical Stress Concentration Factor
1	3.89	. . .
2	3.97	4.0
3	4.14	. . .

Cylinder Material, Aluminum Alloy L72

R = 5.018 in. (127 mm), h = 0.036 in. (0.9 mm), a = 0.5 in (12.7 mm), α = 1.383

Test	Experimental Strain Concentration Factor	Theoretical Stress Concentration Factor
1	3.63	. . .
2	3.81	3.89
3	3.83	. . .

Fatigue Results

The results of the crack propagation tests are presented in Fig. 3 as nondimensional crack length, $2a/W$, plotted against cycles, N. The points represent the averages of data collected for both crack tips from tests on four panels of each type.

Stress intensity can be related to fatigue crack propagation rates, and this fact is used to determine experimentally a stress intensity curvature correction factor to be applied to flat plate analysis. The assumption used was that equal crack growth rates in flat and curved specimens $(da_f/dN = da_c/dN)$ were indicative of equal stress intensity $(K_{flat} = K_{cyl})$.

For a selected crack growth rate, the crack lengths in both the flat and curved specimens were determined. The crack length for the flat specimen was used to calculate the stress intensity from the following expression

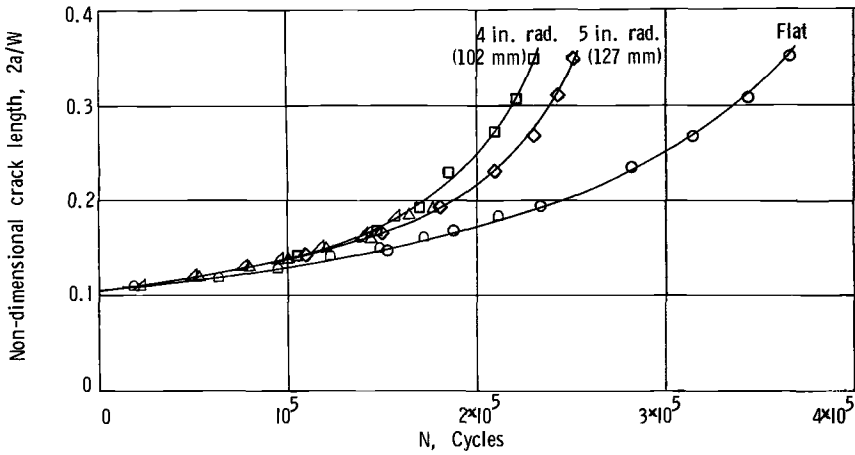$$K_{flat} = S\sqrt{a_f} \times C_W \dots\dots\dots\dots\dots(4)$$

FIG. 3—*Fatigue crack propagation curves for flat and curved specimens.*

where C_W is the finite width correction for a flat, center cracked sheet [9]. Applying the assumption that stress intensity is the same for equal crack growth rates, and using the crack lengths appropriate to the curved specimen,

$$K_{\text{cyl}} = S\sqrt{a_{\text{c}}} \times C_W \times C_c \ldots\ldots\ldots\ldots\ldots\ldots(5)$$

where C_c is defined as the curvature correction factor and from Eqs 4 and 5 is given by

$$C_c = \frac{\sqrt{a_f}}{\sqrt{a_{\text{c}}}} \frac{K_{\text{cyl}}}{K_{\text{flat}}} \frac{C_W}{C_W} \ldots\ldots\ldots\ldots\ldots\ldots(6)$$

(the C_W fraction cancels only when $2a_f/W = 2a_c/W$); therefore

$$C_c = \frac{\sqrt{a_f}}{\sqrt{a_{\text{c}}}} \frac{C_W}{C_W} \quad \text{when} \quad K_{\text{cyl}} = K_{\text{flat}}$$

and

$$C_c = \frac{K_{\text{cyl}}}{K_{\text{flat}}} \quad \text{when} \quad a_f = a_{\text{c}}$$

A number of crack growth rates were chosen to obtain curvature correction factors for values of α up to 6. These results are shown plotted against the curvature parameter in Fig. 4. The linear relationship between curvature correction and curvature parameter predicted by Eq 2 when $b \rightarrow 0$ is not shown by the experimental results. The nonlinear effect of curvature on stress intensity observed in Fig. 4 has been predicted theoretically [10]; however, the value of C_c differs by a factor of approximately 2 from the present experimental results, see Fig. 5. To provide a simple curvature correction that fits
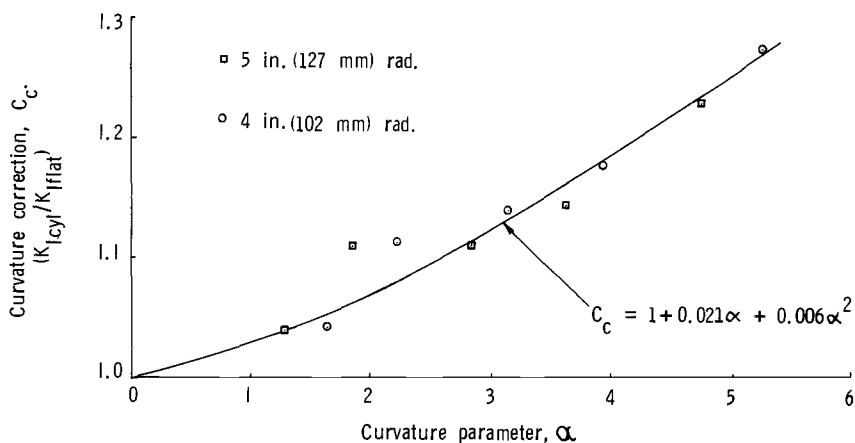
FIG. 4—*Curvature correction for stress intensity determined from fatigue crack growth tests.*

the present experimental data, a three-term polynomial function of α,

$$C_c = 1 + 0.021\alpha + 0.006\alpha^2 \ldots\ldots\ldots\ldots\ldots\ldots(7)$$

was fitted to the data of Fig. 4 by the method of least squares.

Figure 5 presents results obtained experimentally in the present work together with those of Ref *11*. The results of Ref *11* were obtained in fracture tests on curved panels, and, although limitations of thickness, fracture mode, and crack length measurement technique exist in applying fracture analysis to those results, they do give support to the trend of the present results. In addition, the theoretical predictions of Refs *4, 7,* and *10* are shown. The first two are modified solutions for the case of an internally pressurized cylinder. The solution presented in Ref *10* is closest in agreement with the present experimentally determined results.
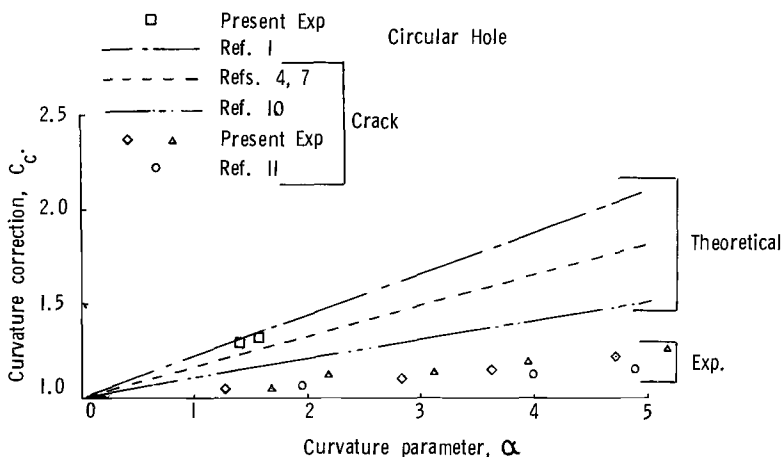

FIG. 5—*Variation of curvature correction with curvature parameter.*

From a comparison of the theoretical solutions for a cylindrical shell weakened by a circular hole or crack as shown in Fig. 5, it can be seen that the effect of curvature on stress concentration is more severe for a circular hole than for a crack. This is verified to a limited extent in the present experimental study as shown by the data points in Fig. 5. This difference would appear to be due to the increase in local stiffness at the point of maximum stress when a crack is present.

Comparison with Crack Buckling

As seen in the two previous sections, curvature causes a higher stress intensity at a discontinuity in a cylindrical shell than is found in a flat plate. The increase in stress intensity due to curvature is similar to that produced at a crack tip in a flat sheet, when the area of the sheet containing the crack buckles out of its plane (see Fig. 6). Forces normal to the plane of the sheet are set up, and this results in additional strains in the midplane of the sheet. The increase in stress intensification caused by buckling around the crack was expressed in Ref 12 as

$$C = 1 + 20(\delta/a)^2 \dots\dots\dots\dots\dots\dots\dots(8)$$

(a) Flat sheet

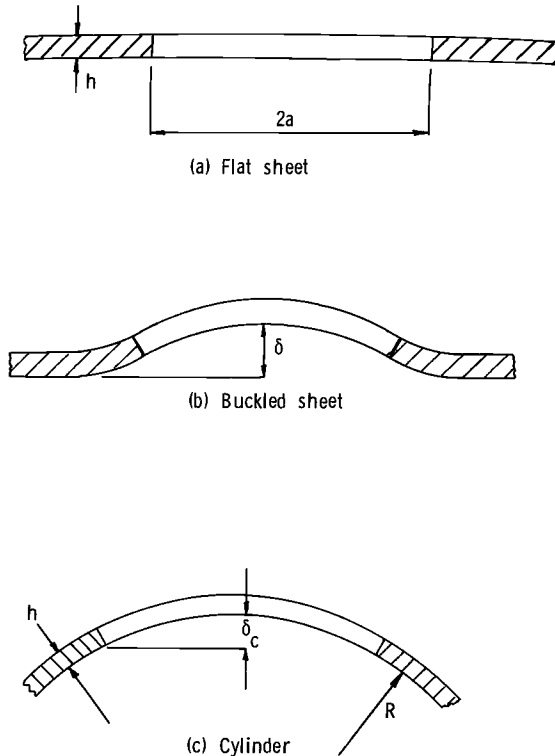(b) Buckled sheet

(c) Cylinder

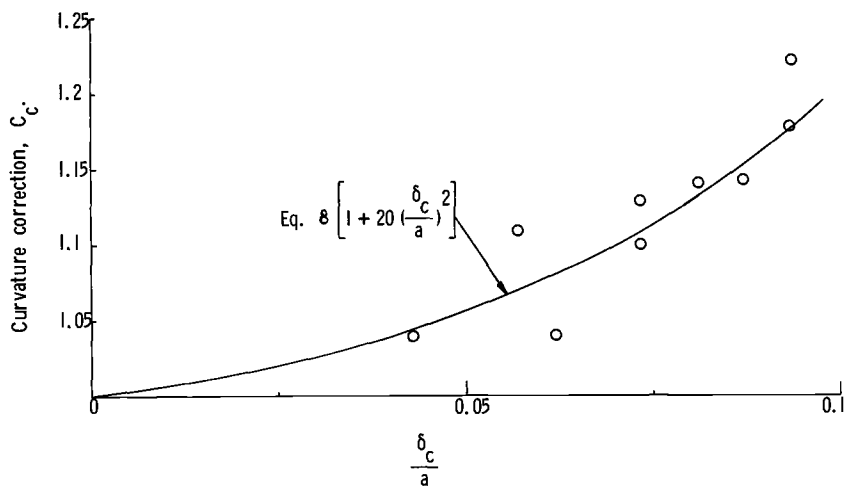FIG. 6—*Geometrical relationship between buckling and curvature.*

FIG. 7—*Comparison of experimentally determined and theoretically predicted curvature correction factors based on a buckling parameter.*

where C was the correction factor and δ was the out-of-plane deflection (see Fig. 6b). If shell curvature were considered equivalent to buckling, then δ could be replaced by δ_c, as defined in Fig. 6c. The values of curvature correction determined experimentally in the present work are shown plotted against δ_c/a in Fig. 7. The curve in this figure represents Eq 7 with δ replaced by δ_c and a good fit with the data is obtained. The results suggest that curvature and buckling have much in common and that δ_c could replace α as a curvature parameter. However, δ_c does not have the generality of α as a curvature parameter, since it does not include thickness effects.

Concluding Remarks

The influence of curvature on stress intensification at a discontinuity in an axially loaded cylindrical shell has been examined. A previously proposed, nondimensional curvature parameter, in terms of which curvature effects could be expressed, has been substantiated experimentally for a circular hole in a cylindrical shell, within a limited range.

The same nondimensional curvature parameter has been used to correlate crack propagation data from tests on cylindrical panels. The influence of curvature on stress intensity was determined by considering equal crack growth rates in flat and curved specimens to indicate equal stress intensity. The influence of curvature on stress intensity determined by this method is presented in terms of a curvature correction factor as a function of the nondimensional curvature parameter. The increase in stress intensity due to curvature that was determined experimentally was compared with, and found to be considerably smaller than, present theoretical predictions.

The increase in stress intensification due to curvature at a crack tip is less than that for a circular hole. The increase in stress intensity due to curvature was found to be comparable to that due to buckling of a flat sheet containing a crack.

References

[1] Lurie, A. I., *Prikladnaia Matematika I Mekhanika*, PMAMA, Vol. 10, 1946, pp. 397–406.

[2] Folias, E. S., *International Journal of Fracture Mechanics*, IJFMA, Vol. 1, No. 1, 1965, pp. 20–46.

[3] Folias, E. S., *International Journal of Fracture Mechanics*, IJFMA, Vol. 1, No. 2, 1965, pp. 104–113.

[4] Folias, E. S., *International Journal of Fracture Mechanics*, IJFMA, Vol. 3, No. 1, 1967, pp. 1–11.

[5] Eringen, A. C., Naghdi, A. K., and Thiel, C. C., *Welding Research Council Bulletin*, WRCBB, No. 102, 1965.

[6] Adams, N. J. I., Ph.D. thesis, University of Southampton, England, 1969.

[7] Murthy, M. V., *Technical Report*, National Aeronautical Laboratory, India, NALRA, 1967.

[8] Adams, N. J. I. and Munro, H. G., *Strain*, STRAB, Vol. 5, No. 2, 1969, pp. 68–73.

[9] *Plane Strain Crack Toughness Testing of High Strength Metallic Materials, ASTM STP 410*, American Society for Testing and Materials, 1966.

[10] Erdogan, F. and Ratwani, M., "Fatigue and Fracture of Cylindrical Shells Containing Circumferential Cracks," Rept. under NASA Grant NGR 39-007-011, Lehigh Univ., Sept. 1969.

[11] Houghton, D. S. and Rothwell, A., Symposium on Non-Classical Shell Problems, International Association for Shell Structures, Warsaw, 1963.

[12] Dixon, J. R. and Strannigan, J. S. in *Fracture 1969*, Proceedings of 2nd International Conference on Fracture, Brighton, England, pp. 105–118.

C. E. Feddersen[1]

Evaluation and Prediction of the Residual Strength of Center Cracked Tension Panels

ABSTRACT: The residual strength of center cracked tension panels is considered from a phenomenological perspective. A simple, direct analysis technique is derived from experimental observations and stress intensity factor concepts. A smooth, continuous stress-flaw size curve is generated over the full range of crack lengths and panel widths. Plasticity and finite width effects are accommodated in a manner simpler and more consistent for engineering purposes than the iterative procedures implicit in current theoretical models. The technique is verified by an analysis of data from a variety of sources. It is concluded that toughness indexes, in the form of stress intensity factors, are reliable indicators of fracture instability, as well as other damage levels. They can be analyzed and interpreted on an elementary format. It also is shown that width can be uncoupled as a parameter in cracked panel behavior.

KEY WORDS: aircraft panels, damage, fractures (materials), crack propagation, notch sensitivity, toughness, fatigue (materials), strains, stresses, residual stress, yield strength, ultimate strength, tensile properties, plastic properties, aluminum, tension tests

A simple, direct residual strength analysis technique for center cracked tension panels is derived from experimental observations and stress intensity factor concepts. The procedures developed are applicable for describing crack behavior in center cracked tension panels over the full range of crack lengths and panel widths. The major points to be made are that

1. The stress intensity factor can be utilized effectively in an elementary format to generate a smooth and continuous stress-flaw size relation.

2. The stress intensity factor is an accurate and consistent measure of crack damage, not only for fracture instability but also for other levels of crack damage severity, provided the damage is consistently specified and detected.

3. Panel width can be uncoupled as an independent parameter in crack behavior data.

[1] Senior research engineer, Structural Materials Engineering, Columbus Laboratories, Battelle Memorial Institute, Columbus, Ohio 43201.

50

Before proceeding with the main discussion, it is important to recall a bit of technical philosophy intrinsic to the study of crack behavior. As an initial premise, it is assumed that basic toughness indexes (be they stresses, strains, energies, or whatever) do exist and that they can characterize the cracking sensitivity of a material independent of the structure in which the crack is contained. To be useful in practical applications, measures of material toughness must serve two purposes. They must (1) provide a comparative rating of materials and (2) be directly relatable to structural design dimensions. This duality in the nature and function of a toughness measure is a basic criterion for a truly useful fracture characterization technique.

It is the goal of this paper to demonstrate that the elementary stress intensity factor concept can be applied in a rational and straightforward manner to center cracked tension panels, maintaining both the utility and generality of K and the simplicity of an elementary stress-flaw size relationship.

The value of the stress intensity factor concept is that a mathematical relationship can be established between stress, flaw size, and a characteristic material toughness value, K_x. While this concept has been applied successfully to material configurations exhibiting plane strain stress states, its application to plane stress and transitional stress states, typified by thin-section materials, has been disputed for some time.

The discussion opens with a brief review of the background of residual strength analysis. Then, the physical phenomenon of crack behavior is discussed. Next, the development of the analytical method is presented and verified in terms of a single panel width. Finally, the discussion is generalized to accommodate multiple panel widths.

Background

For more than a decade there has been extensive interest in characterizing the residual strength of center cracked tension panels. One of the first approaches to this problem area was the "effective width technique" [1].[2] In this method, a zone of material at the crack tip, uniformly stressed at the tensile yield strength, TYS, was assumed to carry the redistributed portion of the panel load, which was cut by the crack. The zone size was determined empirically, which necessitated the testing of many crack and panel size combinations. Subsequently, in the "notch resistance method" [2], this concept was modified to account for the localized stress gradient defined by the Westergaard [3] stress distribution. A zone at the crack tip, uniformly stressed at the tensile ultimate strength, TUS, was equated to the integral of the idealized Westergaard stress over that zone. The resultant parameter also was determined empirically. Then, from a different perspective, the "notch strength analysis" [4] and "crack strength analysis" [5] procedures were developed to characterize local material behavior at the root of a notch, or crack. These techniques defined a crack sensitivity parameter somewhat

[2] Italic numbers in brackets refer to the list of references at the end of this paper.

related to an "inverse" stress intensity factor. More recently, the concept of a fracture index [6] has been introduced as a direct tool for stress analysis.

These and still other engineering models of fracture behavior evolved as a result of disparities in the original stress intensity factor approaches of linear, elastic fracture mechanics. Each approach has some merit depending on the specific application; however, the real question is, What technique has the *broadest* usefulness in materials selection and design application? The first four methods mentioned above center about indexes or parameters which are artificial in regard to the physical quantities normally determined in mechanical testing. While each quantity is adequate within the context of its own individual method, it does not have an immediately apparent physical significance for greater generalization. In short, there are no ready transformations to other structural geometries other than "brute force" correlations. Herein lies the real potential of the stress intensity factor concept, if properly interpreted. It is founded in the mathematical concepts of elasticity and can be related immediately to a variety of flaw and structural forms by conventional techniques of stress analysis. Furthermore, the physical quantity of a stress intensity factor (or its parent, the strain energy release rate) has a more plausible physical significance. A simpler, more direct utilization of this concept is the goal of the following development.

Crack Behavior in the Rising Load Test

Consider the center cracked panel illustrated in Fig. 1. In a rising load test, this panel responds in a linear and elastic fashion until some combination of crack tip plasticity and slow crack growth introduce the nonlinearities shown in the typical load-deformation record of Fig. 2. As the loading continues, a slow, but stable, extension of the crack is observed along with an enlargement of the plastic zone at the crack tip. Eventually, a critical instability is achieved where a sudden, rapid, and unstable extension of the crack severs the panel.

At least three significant bench marks, as illustrated in the crack growth curve of Fig. 3, are apparent in this crack behavior. Point *0* marks the onset of nonlinear behavior and is important because it denotes the threshold of irreversible damage to the panel or test specimen. Although precise discrimination between the effects of plasticity and slow crack growth is difficult, visual observations, photographic records, or graphical offsets on load records can provide means of separating these nonlinear processes. Point *1* marks the point (or region) of critical instability where fracture is imminent. Point *N* relates initial crack length to maximum load in accord with the original notch concept of fracture. It is a first approximation to the actual dynamic slow crack growth traced by the segment *0–1* between points *0* and *1*.

The determination of point *1*, critical instability, is elusive. Consider the critical flaw conditions interfacing slow tear and rapid crack propagation illustrated in Fig. 4. As the critical fracture condition is approached at the
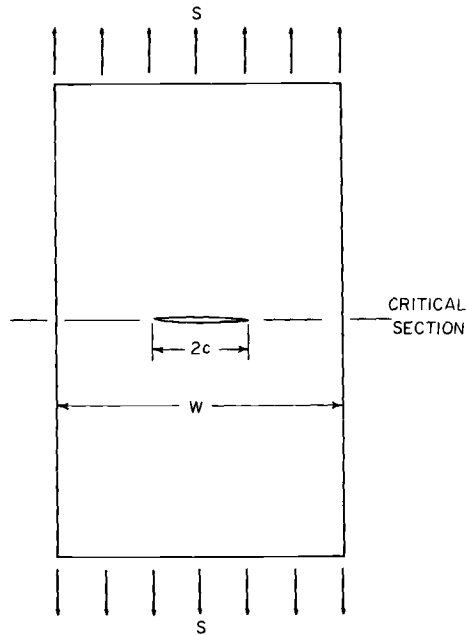
FIG. 1—*Center cracked tension panel.*
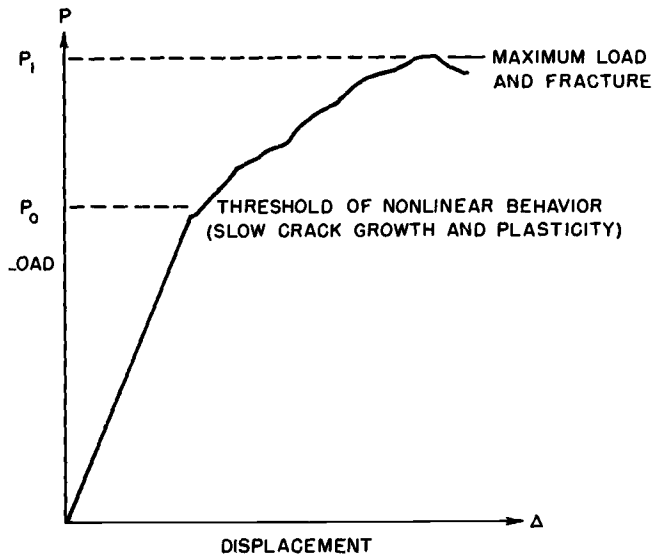
FIG. 2—*Typical load-deflection record.*
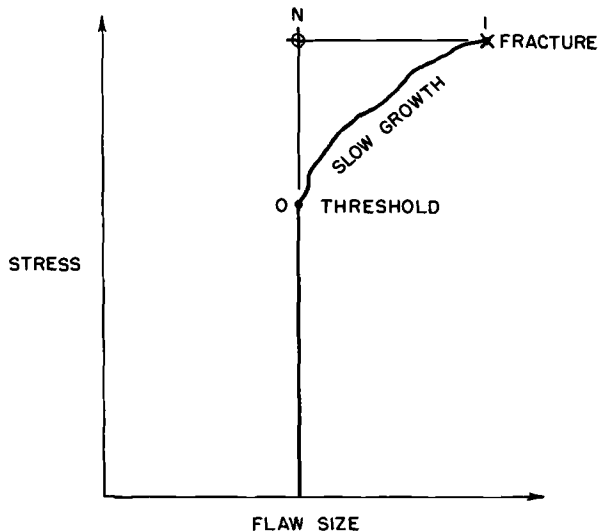
FIG. 3—*Crack growth curve.*
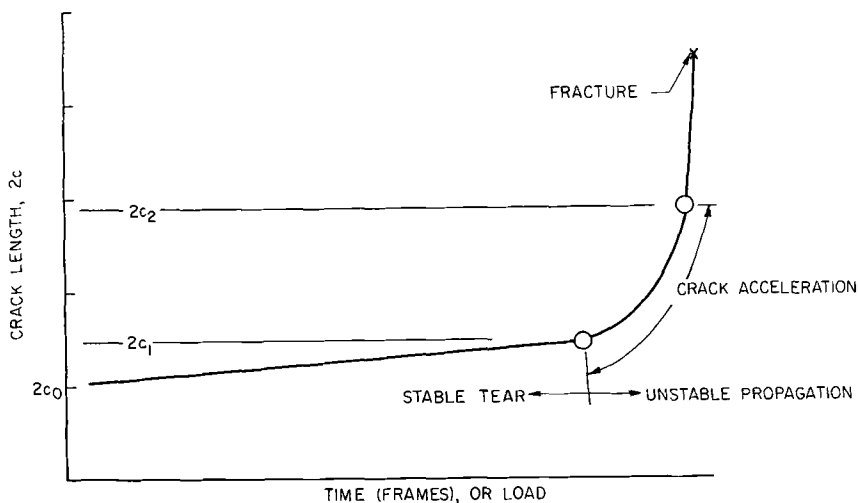
FIG. 4—*Typical crack growth behavior.*

termination of slow crack growth, the unique designation of a specific, critical crack length is difficult owing to the acceleration pulse. Although an instability analysis could be proposed to identify this point, it appears adequate for the present to bracket this critical regime by more readily identifiable measures. If photographic records are made of this event, it can be noted that two crack lengths, $2c_1$ and $2c_2$, the fore and aft tangency points (that is, departure from and onset of linearity), respectively, to the apparent acceleration pulse can be used to bracket the critical areas.

CRACK LENGTH, 2 c
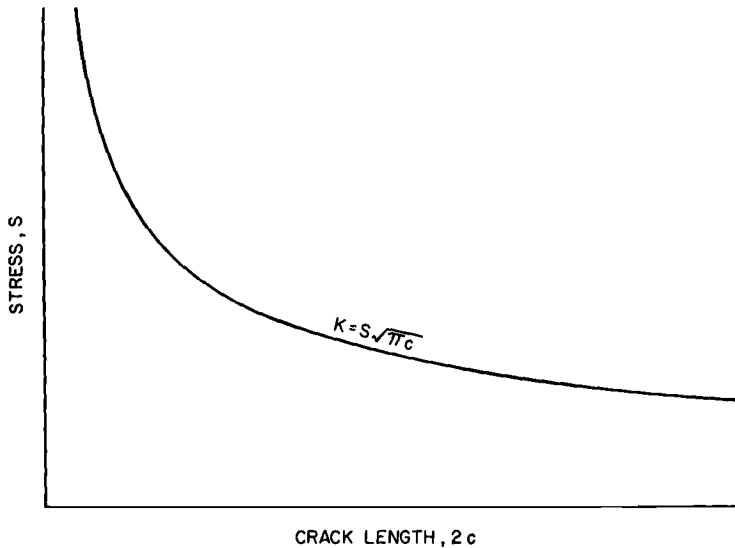
FIG. 5—*Ideally elastic fracture behavior.*

From this discussion it should be realized that there are several discrete damage levels of interest, each of which can be characterized by a toughness index. The next section describes the analytical method by which these damage levels can be modeled.

Analytical Development

Results of experimental observations at Battelle, especially those of a recent study [7] of fracture and fatigue crack propagation on 7075-T73 aluminum alloy sheet and plate (-T7351), have motivated a reconsideration of the basic analyses of center cracked tension panel fracture behavior. Observations on these data suggested a major simplification of data analysis. Subsequent review of the data of other investigations supported this new approach and implied that it had significant potential for design applications. The evolution of this rationale is presented in the following discussion.

Basic Considerations

The idealized inverse relationship between stress S and crack length $2c$ for elastic fracture behavior is illustrated in Fig. 5. This relationship [8] is derived from the analysis of a panel of infinite size in which a uniform stress field exists remote to the crack. The curve pictured represents one of a family of curves, parametric on K, covering the entire quadrant.

However, real panels and real materials have finite limits to their size and strength. In the stress dimension, they are elastically limited by the tensile yield strength, TYS. In the crack length dimension, they are limited by the finite width W. In an actual structural panel, these constraints define a net
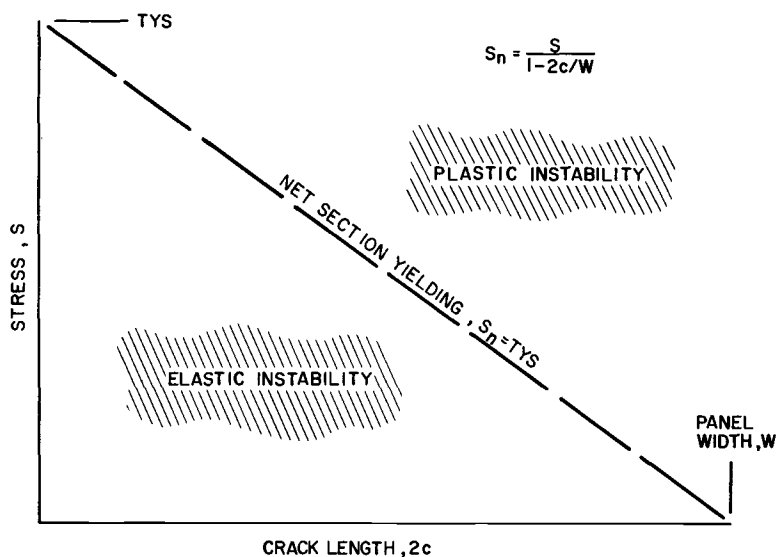
FIG. 6—*Natural limits on elastic behavior.*

section yield limit, *NSY*, shown as the diagonal dashed line on Fig. 6. Here it is appropriate to note that any diagonal straight line passing through the panel width limit on the crack length axis and intersecting the gross stress axis is a line of constant net section stress. It is the locus of points whose respective gross stress and crack length provide the same net section stress on the remaining cross section of the panel. The net section stress value for a particular diagonal corresponds to the gross stress intercept of that diagonal. Thus, the *NSY* line is so called because it intersects the stress axis at *TYS*.

The diagonal *NSY* limit may be used to separate fracture behavior into two basic categories. Data points which fall above and to the right of the limit represent fracture conditions with extensive (if not total) plasticity on the net section. Hence, the regime is identified as *plastic instability* in Fig. 6. The data points which appear below and to the left of the *NSY* limit, that is, within the stress-flaw size quadrant, reflect considerable elastic behavior on the critical net section. This area is identified as *elastic instability*. Now we can compare these analytical concepts with some experimental observations.

Practical Observations

It is generally observed that fracture data occur in two general categories as shown in Fig. 7. Thin-sheet fracture data which fall into the plastic in- stability region appear to form linear bands at or above the *NSY* limit. Such behavior implies that a net section stress, or "flow stress" between *TYS* and the tensile ultimate strength, *TUS*, has merit as a plastic instability criterion. In contrast, the study of thin-sheet fracture data occurring in the regime of elastic instability reveals that these data do indeed tend to follow the saddle

shaped central portion of the idealized elastic instability behavior. However, when the elastic instability studies are extended to the extremes of stress and flaw size, in other words, to the intersections of the elastic instability line and the *NSY* limit, the data deviate from the idealized behavior of either mode.

The shaded areas of Fig. 8 illustrate the interaction zones or intersections of the elastic and plastic instability modes and are the primary regions of data deviation and dispersion. The deviations noted at the left-hand intersection, at high stress levels, are termed the plasticity or plastic zone effects. The deviations at the right-hand intersection at relatively long crack lengths are termed finite width or boundary effects. Many theoretical analyses have been developed and utilized to account for both of these effects; however, they have not significantly consolidated the data into a meaningful form over the *full* range of stress and flaw size. Thus, there remains the goal of reducing experimental results to a simple, yet general, form for engineering applications.

A Data Model

The linear lower bounds to the shaded areas of Fig. 8 are more than schematic constructions. In the previously cited Battelle research program, it was observed that the data behaved in a linear fashion at the extremes of both stress and flaw size. This suggested the use of linear tangents to the idealized *K* curve as a method of establishing a smooth and continuous curve of fracture behavior over the full range of crack lengths.
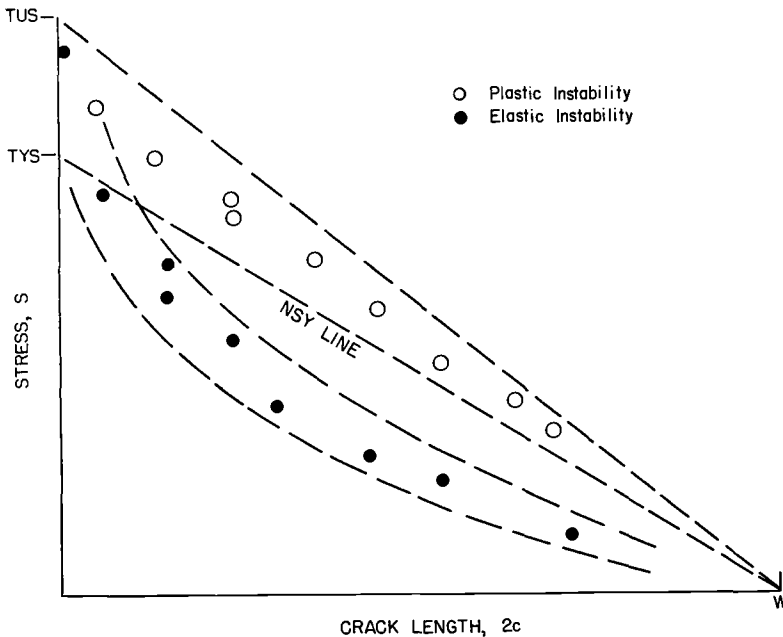
FIG. 7—*Typical instability data.*

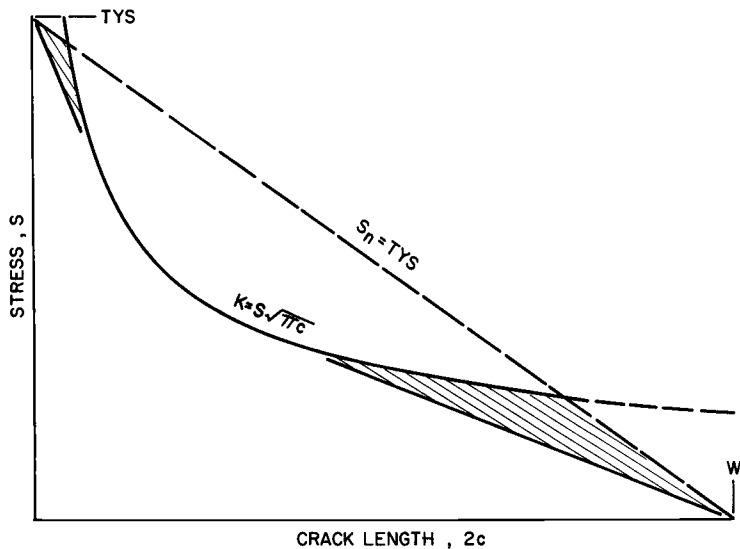FIG. 8—*Natural limits superimposed on ideally elastic fracture behavior.*
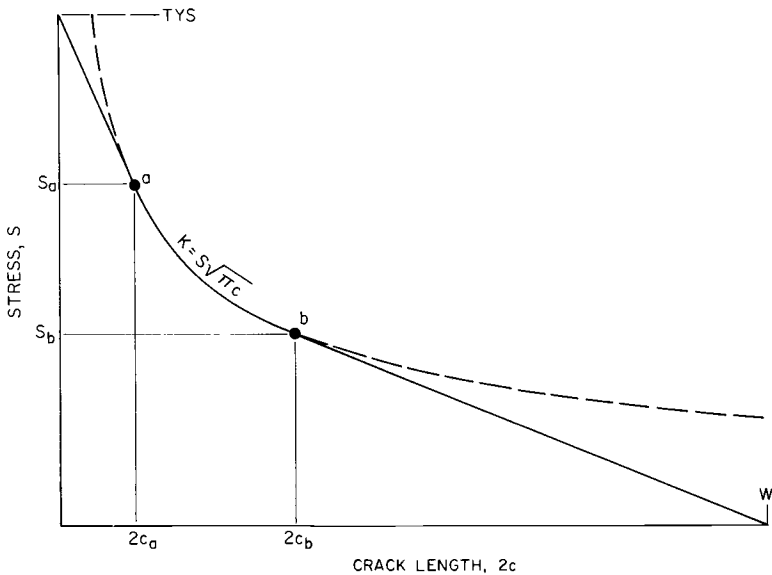

FIG. 9—*Tangency conditions.*

Tangency Conditions—The slope of the K curve at any point is

$$\frac{dS}{d(2c)} = \frac{d}{d(2c)}\left(\frac{K}{\sqrt{\pi c}}\right) = -\frac{S}{4c} \quad \dots \dots \dots \dots \dots (1)$$

This slope is equated to the slope of the linear tangents at points a and b as identified in Fig. 9.

At point a, the tangency condition is

$$\text{slope at } a = \left.\frac{dS}{d(2c)}\right|_a = -\frac{S_a}{4c_a} = -\frac{TYS - S_a}{2c_a} \quad \ldots\ldots\ldots\ldots(2)$$

which reduces to

$$S_a = \tfrac{2}{3}(TYS) \ldots\ldots\ldots\ldots\ldots\ldots\ldots\ldots(3)$$

This expression implies that the left-hand tangency point (a) always occurs at a stress level of two thirds of TYS. This stress level is the locus of points or the boundary which separates the data most appropriately represented by the left-hand linear tangent from the data better represented either by the central K curve or by the next tangency condition.

At point b, the second tangency condition is

$$\text{slope at } b = \left.\frac{dS}{d(2c)}\right|_b = -\frac{S_b}{4c_b} = -\frac{S_b}{W - 2c_b} \quad \ldots\ldots\ldots\ldots(4)$$

which reduces to

$$2c_b = W/3 \ldots\ldots\ldots\ldots\ldots\ldots\ldots\ldots(5)$$

In a manner similar to the first tangency condition, Eq 5 defines the locus of points or the boundary between the data most appropriately represented by the right-hand linear tangent and the data better represented by either the central K curve or the other linear tangent. This expression indicates that the right-hand tangency point always occurs at one third of the panel width. These conditions may now be transformed into screening criteria.

Screening Criteria—Equations 3 and 5 are important relations which must be carefully understood. These expressions define the boundary between zones of data which may be most appropriately represented by either the left-hand linear tangent, the central K curve, or the right-hand linear tangent. These zones within the elastic instability region are illustrated in Fig. 10 and are identified in the following table.

Zone	Screening Criterion	Data Modeled by
1	$S \geq \frac{2}{3} TYS$	left-hand linear tangent
2	$S \leq \frac{2}{3} TYS, 2c \leq \frac{W}{3}$	K curve
3	$2c \geq W/3$	right-hand linear tangent

For a given material TYS value and a given panel width, a unique left- and a unique right-hand linear tangent to each K curve may be drawn.

Rules of the Method

At this point it is appropriate to summarize the set of rules which define the three segments of the stress-flaw size curve. Referring back to Fig. 9, the equations become quite evident.
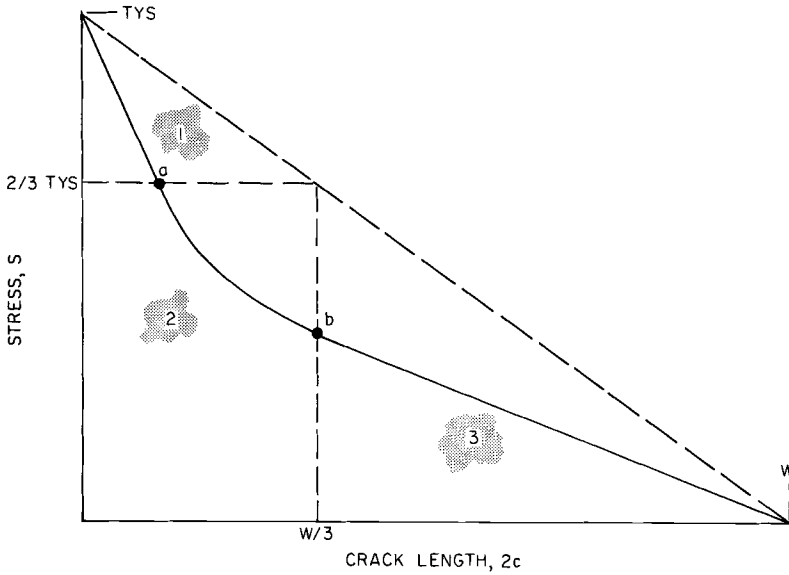
FIG. 10—*Data zones defined by screening criteria.*

In zone 1, the left-hand linear tangent is expressed as

$$S = TYS[1 - \tfrac{1}{3}(2c/2c_a)]. \dots \dots \dots \dots \dots (6)$$

between $(0, TYS)$ and $(2c_a, S_a)$.

In zone 2, the central K curve is expressed as

$$S = K/\sqrt{\pi c}. \dots \dots \dots \dots \dots (7)$$

between $(2c_a, S_a)$ and $(2c_b, S_b)$.

In zone 3, the right-hand linear tangent is expressed as

$$S = \tfrac{3}{2} S_b[1 - (2c/W)]. \dots \dots \dots \dots \dots (8)$$

between $(2c_b, S_b)$ and $(W, 0)$.

Substituting the control point values of Eqs 3 and 5 into the basic elastic instability expression,

$$K = S\sqrt{\pi c}. \dots \dots \dots \dots \dots (9)$$

yields

$$2c_a = (9/2\pi)(K/TYS)^2. \dots \dots \dots \dots \dots (10)$$

and

$$S_b = K\sqrt{(6/\pi W)}. \dots \dots \dots \dots \dots (11)$$

These expressions may now be used to either analyze data or predict fracture behavior in center cracked tension panels of a material with a specified *TYS*. Given a K value, the complete stress-flaw size curve can be constructed

with Eqs 6, 7, and 8. Or, conversely given a data point, that is, a coordinate $(2c, S)$ representing an experimentally derived point in the elastic instability region, the related K value, the K curve, and the pair of unique tangents can be back-calculated by using the expressions associated with the data zone in which it occurs.

Multiple Damage Levels

In the preceding analytical development, only a single damage condition, or K curve, implicitly that of fracture instability, has been described; however, these procedures and formulations can be applied to any or all of the damage levels pointed out in the earlier discussion of crack behavior in the rising load test. Furthermore, these can be combined in a multiple overlay of K curves. For example, a superposition of the threshold of stable tear and the two levels of crack damage bracketing critical instability is shown schematically in Fig. 11. The dashed crack growth curve is superimposed to clarify the relationship between the different damage levels and K curves.

Verification

The validity of this analytical method is best demonstrated by graphical displays of fracture data and the resultant computed curves. These are presented in Figs. 12–20 for a variety of aluminum center cracked tension panel data. In most cases, the computed curve provides an excellent fit to the experimental data. It should be noted that these data and the associated curves are presented on the basic format of stress and crack length, which is most fundamental for data evaluation.
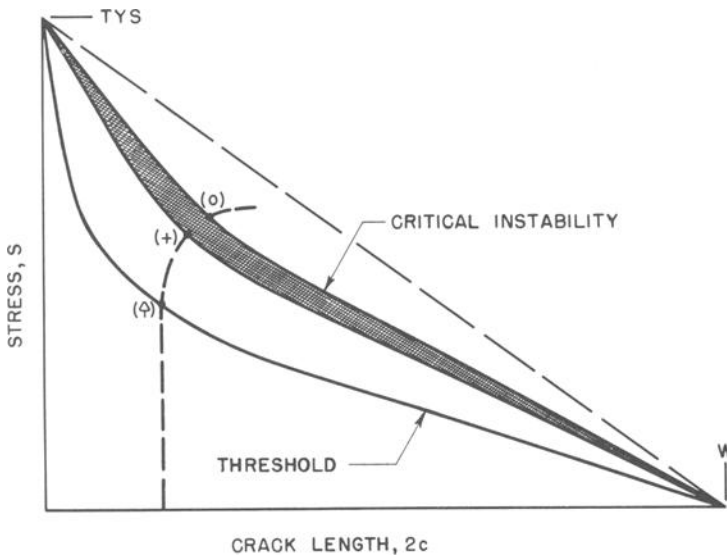
FIG. 11—*Superposition of multiple damage levels.*

The raw data are presented as reported by the investigator without further alteration. Several different damage levels, identified by various detection schemes, are presented in these illustrations. Thus, in verifying this analytical method, the important point is not the damage level itself but the fact that, when a consistent specification and identification of damage is used, the results indeed follow the K concept.

The K values indicated on the following figures are those associated with and computed from the zone 2 data, that is, within the K screening criteria. This has been done for simplicity, convenience, and proof of the concept. For a more rigorous analysis of design data, an extrapolation and weighing of the zone 1 and 3 data would be included.

The significant features of the data figures are described briefly in the following paragraphs. This sampling illustrates the applicability of this method to a broad spectrum of aluminum alloys. Equivalent validity in other materials has been observed in other Battelle programs.
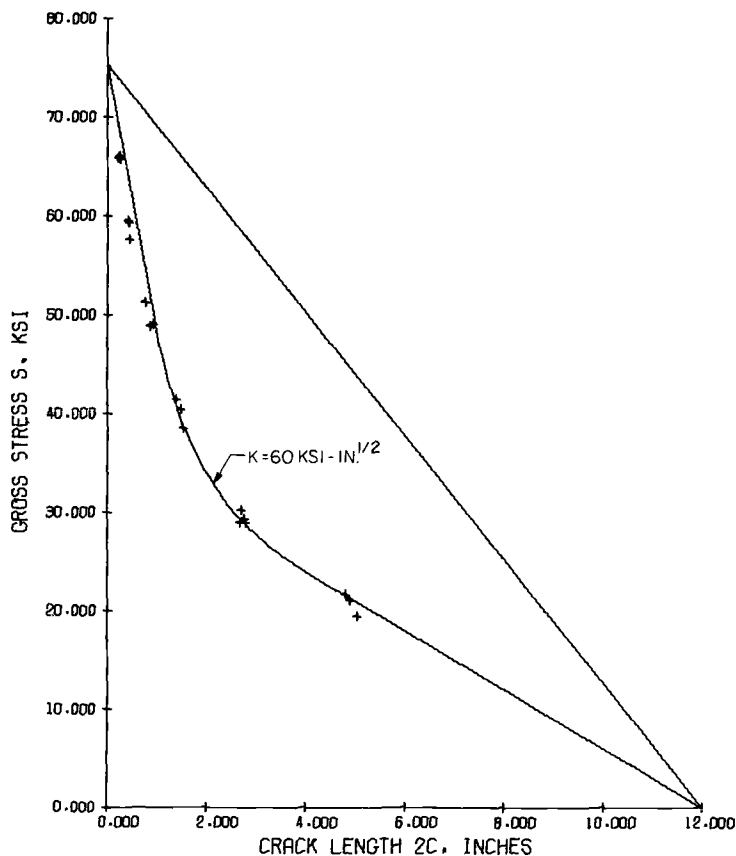
FIG. 12—*Computer plot of data and curve for critical instability of 0.060-in.-thick, 12-in.-wide 2014-T6 aluminum alloy sheet at —320 F* [9].

FIG. 13—*Computer plot of data and curves for threshold and critical instability of 0.040-in.-thick, 12-in.-wide 2024-T3 clad aluminum alloy sheet at room temperature* [10].

Critical instability data reported for cryogenic tests of 2014-T6 aluminum alloy sheet are presented in Fig. 12, along with the curve computed in accord with the rules of the method. The K value indicated on the figure is that associated with and computed from the zone 2 data, within the K screening criteria. However, as was previously pointed out, within the context of this specific method the tangents are related uniquely to the central K curve and also can be associated uniquely with that value.

Data and computed curves for 2024-T3 clad aluminum alloy sheet are presented in Figs. 13 and 14. Both threshold and critical instability data are presented. Both damage levels are distinctly different but appear to be relatable and identifiable with K concepts. Figure 13 represents a narrow panel in which the fracture instability was in the plastic regime. In contrast, Fig. 14, representing wider panel data, reveals a fracture instability within the elastic regime.
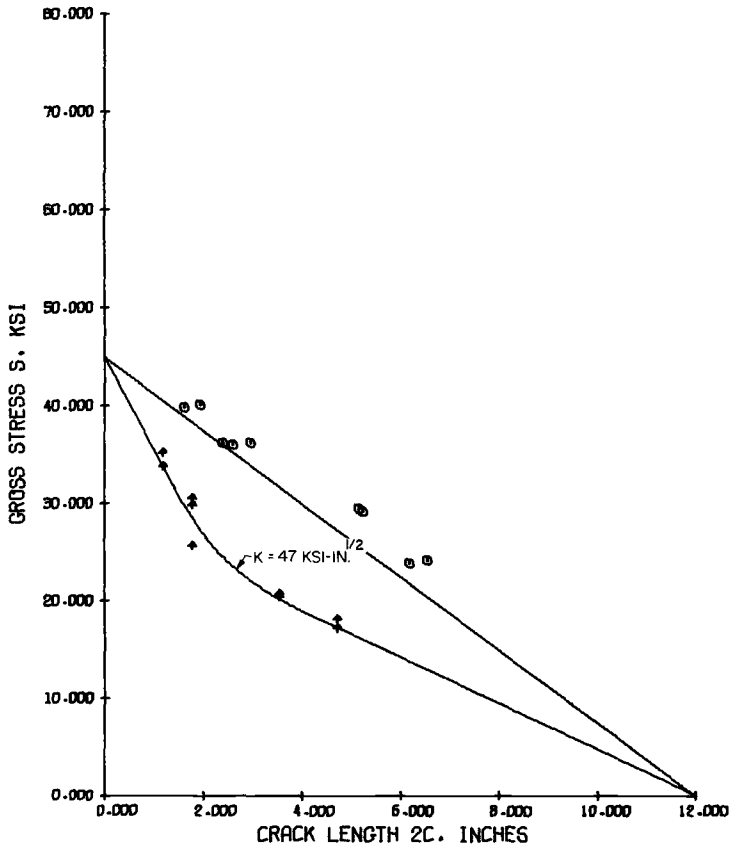
FIG. 14—*Computer plot of data and curves for threshold and critical instability of 0.040-in.-thick, 20-in.-wide 2024-T3 clad aluminum alloy sheet at room temperature* [10].

Figures 15 and 16 present the critical instability behavior of two different widths of 2219-T87 aluminum alloy sheet. In Fig. 15 it is interesting to note that the curve was determined by only one point, since these curves were developed considering only zone 2 data. However, the overall data fit is good. Figure 16 presents a similarly good data fit on wider panels. It is important to note the near equivalence of the K values for these two distinctly different size panels. This suggests that K may be a characteristic value of the zone 2 portion of a curve, which may yet differ markedly in zone 3 because of boundary effects. This observation is generalized in the next section.

For a contrast in alloys, 7075-T6 aluminum alloy data are presented for two different widths in the next two figures. Both critical instability and threshold of slow growth data are presented in Fig. 17. Again, the difference in the damage levels is distinct. In Fig. 18, from another source, only critical instability data are shown. However, the close correlation of the K values for these two figures indicates a distinct possibility of generalization.

Finally, in Figs. 19 and 20, threshold and fracture instability data for 7075-T7351 aluminum alloy plates are illustrated. These data are a sampling of those which motivated this development. Figure 19 indicates that in the ¼-in. thickness of this material an 8-inch-wide panel is not adequate to produce critical instability in the elastic region. In contrast, Fig. 20 reveals that both threshold and critical instability K values are depressed by increased thickness.

The good fit of data and narrow scatterbands which are evident in the preceding data are confirmation of the validity of this development. The extension of this technique and its broader implications are carried forward in the following sections.

Generalization of the Method

From the preceding development, it is but a short step to a generalization of this method. Observations among the previous data indicate that nearly
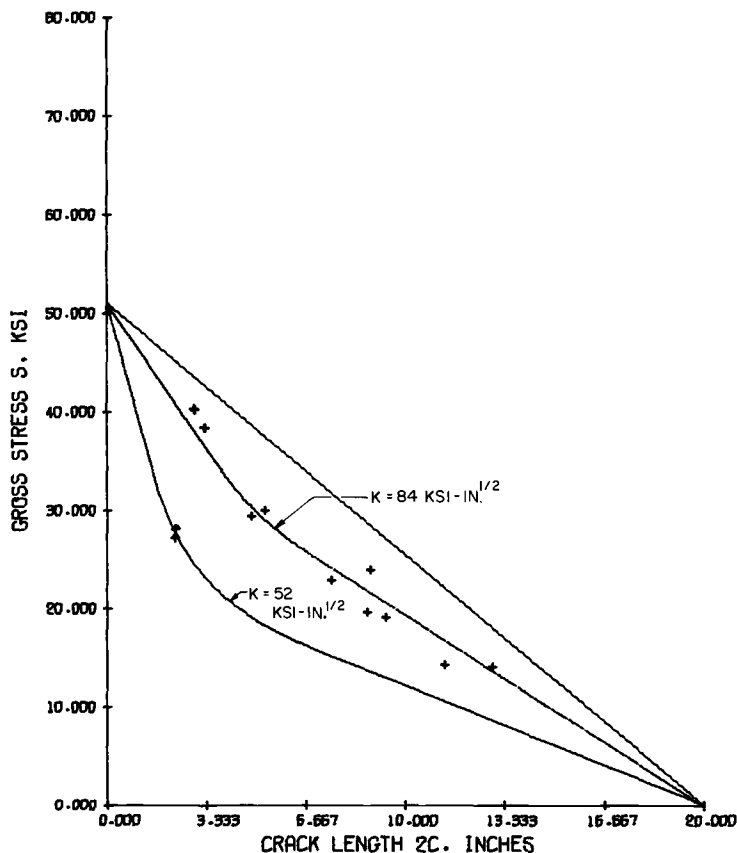

FIG. 15—*Computer plot of data and curve for critical instability of 0.100-in.-thick, 24-in.-wide 2219-T87 aluminum alloy sheet at room temperature* [11].

FIG. 16—*Computer plot of data and curve for critical instability of 0.100-in.-thick, 48-in.-wide 2219-T87 aluminum alloy sheet at room temperature* [11].

equivalent K values exist for equivalent damage levels in specimens which differ only in panel width. Thus, it appears that this method provides a consistent means of determining K values regardless of panel width and that it effectively uncouples width effects within the crack behavior data.

Width Uncoupled

Consider an overlay of several curves generated for the same *TYS* and K values but for different panel width dimensions as shown in Fig. 21. Here the idealized K curve is extended to the right without limit, representing the infinite plate solution,

$$K = S\sqrt{\pi c}$$

The right-hand linear tangents to the K curve intersecting the crack length axis at their respective panel widths provide the finite width cutoffs or the boundary corrections necessary in real panels. The idealized K curve becomes

a characteristic value for a given material and thickness range. Its existence beyond one third of the largest, real panel width is only of hypothetical value; nonetheless, its concept is important for establishing the linear tangents. Following a verification of this procedure, some important size requirements which are implied by this development will be pointed out.

Verification

That such an overlay of multiple panel width data can be achieved is illustrated in the next two figures. Figure 22 illustrates the 2219-T87 aluminum alloy data of Figs. 15 and 16 plus other panel widths. Figure 23 illustrates the 7075-T6 aluminum alloy data from several widths in addition to those of Figs. 17 and 18. The close correlation of the data points to their adjacent right-hand linear tangent is an obvious confirmation of this generalization. And here again, it is not the absolute value of the critical instability definition that is being emphasized but, rather, the consistency within the data which have been derived in a specified manner.

FIG. 17—*Computer plot of data and curves for threshold and critical instability of 0.090-in.-thick, 12-in.-wide 7075-T6 aluminum alloy sheet at room temperature* [12].
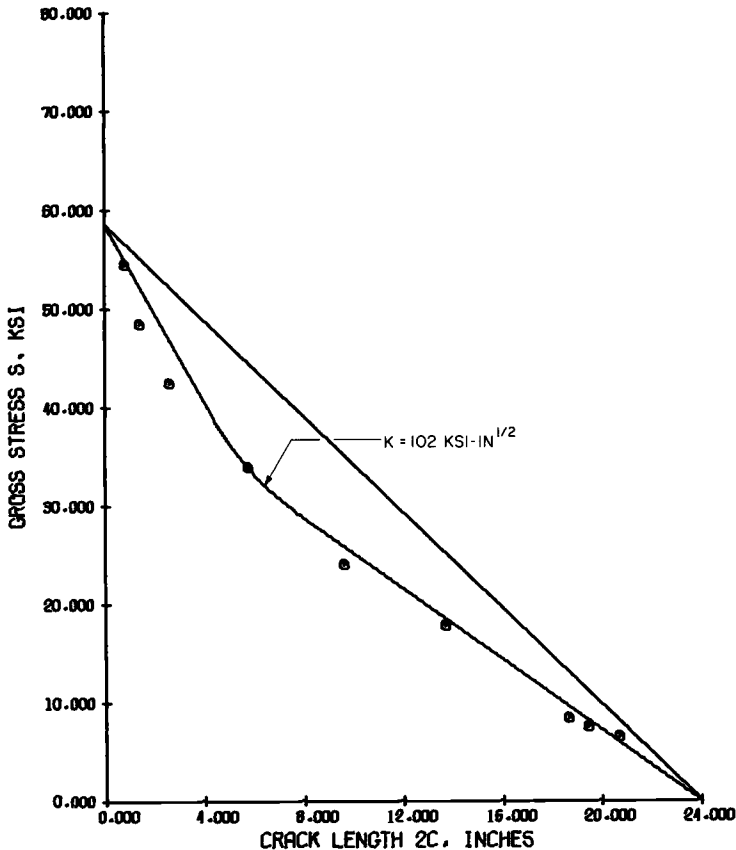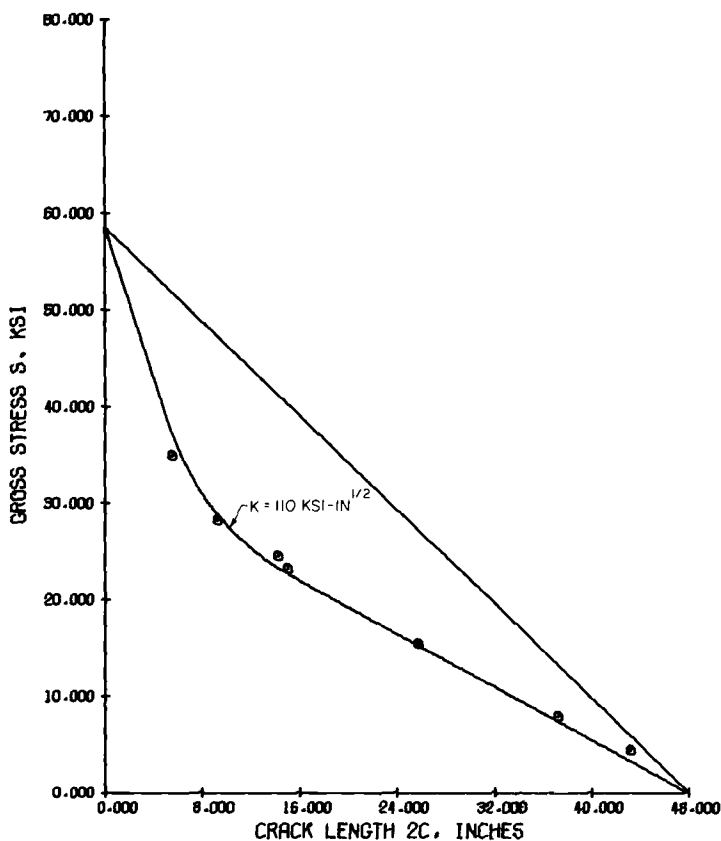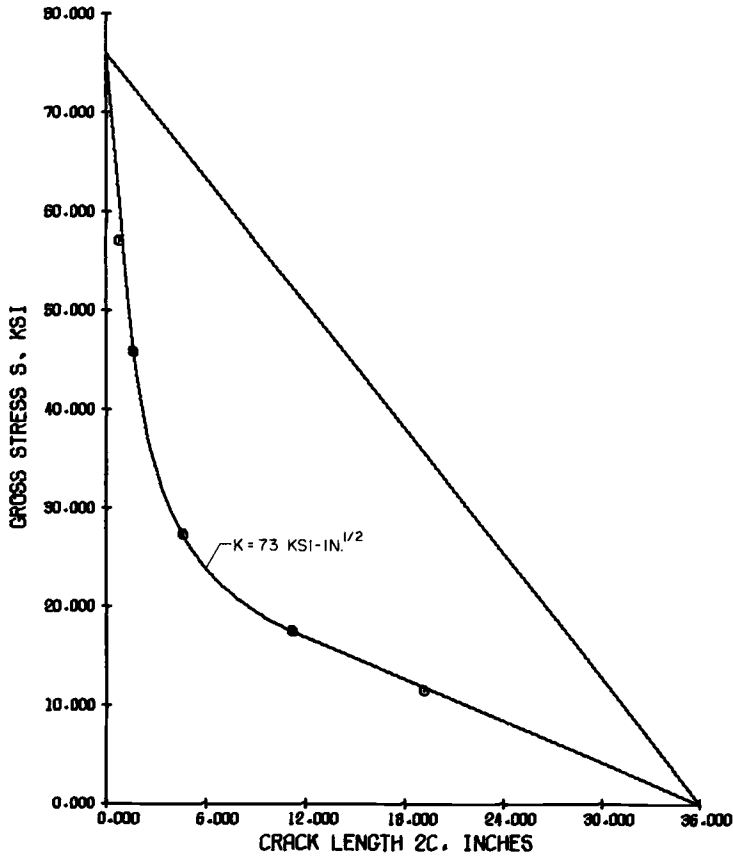
FIG. 18—*Computer plot of data and curve for critical instability of 0.100-in.-thick, 36-in.-wide 7075-T6 aluminum alloy sheet at room temperature* [11].

Minimum Width Panels

A characteristic of this phenomenological development is the limiting negative slope of the left-hand linear tangent shown in Fig. 21. Projecting this slope to the crack length axis yields an intercept W_{min}. Net section yield stress lines for panel widths less than W_{min} will not intersect the elastic instability curve. Physically, this implies that for panel widths less than W_{min} failures will be manifested as plastic instability. The dimension W_{min} represents the minimum panel width in which elastic instability can occur. In order to obtain "detectable" elastic instability, in other words, to be assured that the net section stresses are distinctly below TYS, a panel width at least 50 percent greater would be required.
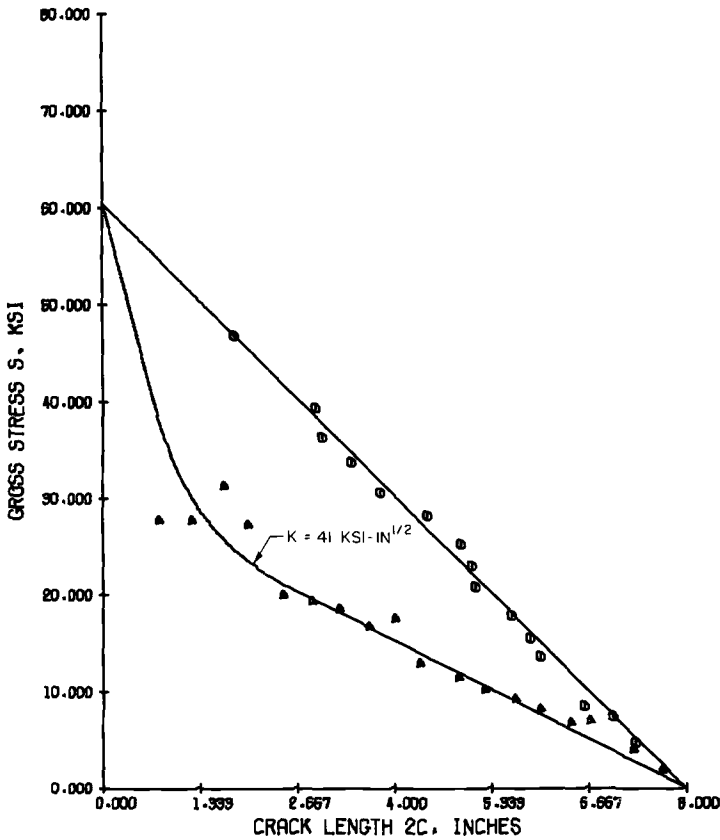
FIG. 19—*Computer plot of data and curves for threshold and critical instability of 0.250-in.-thick, 8-in.-wide 7075-T7351 aluminum alloy plate at room temperature* [7].

The value of W_{min} can be evaluated from the expressions presented in the subsection on rules of the method or directly from Fig. 21 where similar geometric triangles imply

$$\frac{W_{min}}{2c_a} = \frac{TYS}{TYS - S_a} \dots\dots\dots\dots\dots\dots\dots(12)$$

From Eqs 3 and 10

$$W_{min} = 6c_a = \frac{27}{2\pi}\left(\frac{K}{TYS}\right)^2 \dots\dots\dots\dots\dots\dots(13)$$

For the data of the preceding figures, Figs. 12–20, 22, and 23, the minimum panel widths have been determined in Table 1.

TABLE 1—*Determination of minimum panel widths.*

Alloy	Thick-ness, in.	Tem-perature, deg F	TYS, ksi	K, ksi $\sqrt{\text{in.}}$	W_{min}, in.	Minimum Specimen Width, 1.5 W_{min}, in.	Figure Reference
2014–T6......	0.060	−320	75	60	2.7	4	12
2024–T3 clad..	0.040	room	51	84	11.5	17	14
2219–T87.....	0.100	room	58	105	13.9	21	15, 16, 22
7075–T6......	0.090/ 0.100	room	75	70	3.7	6	17, 18, 23
7075–T7351...	1.00	room	61	52	2.4	4	20

It should be noted that these are minimum values as projected from a limited number of data. The investigator should stay significantly above these values to obtain meaningful elastic instability data. The major point is that test specimens below this size limit will not yield elastic instability information.
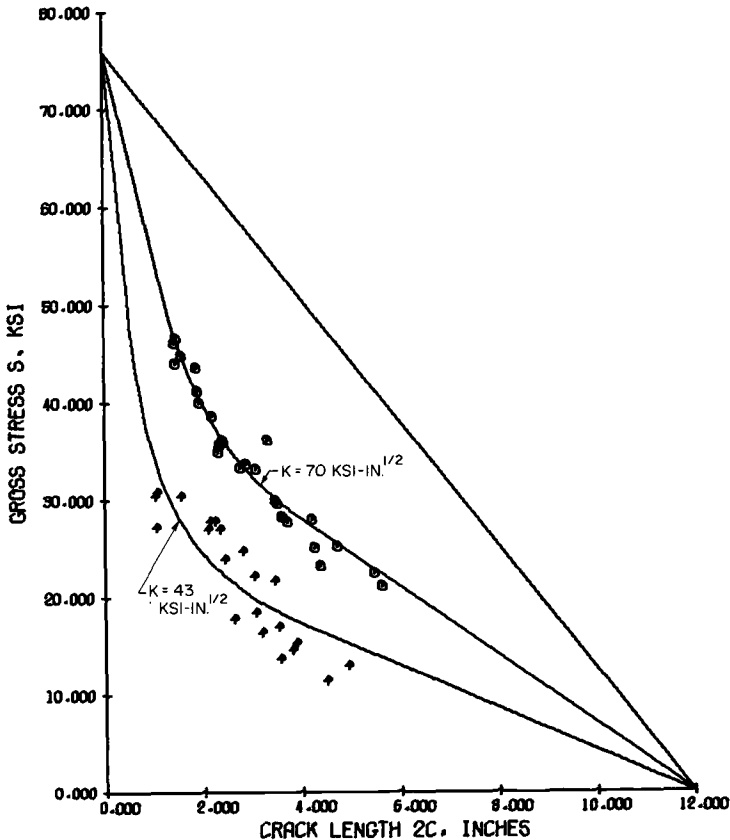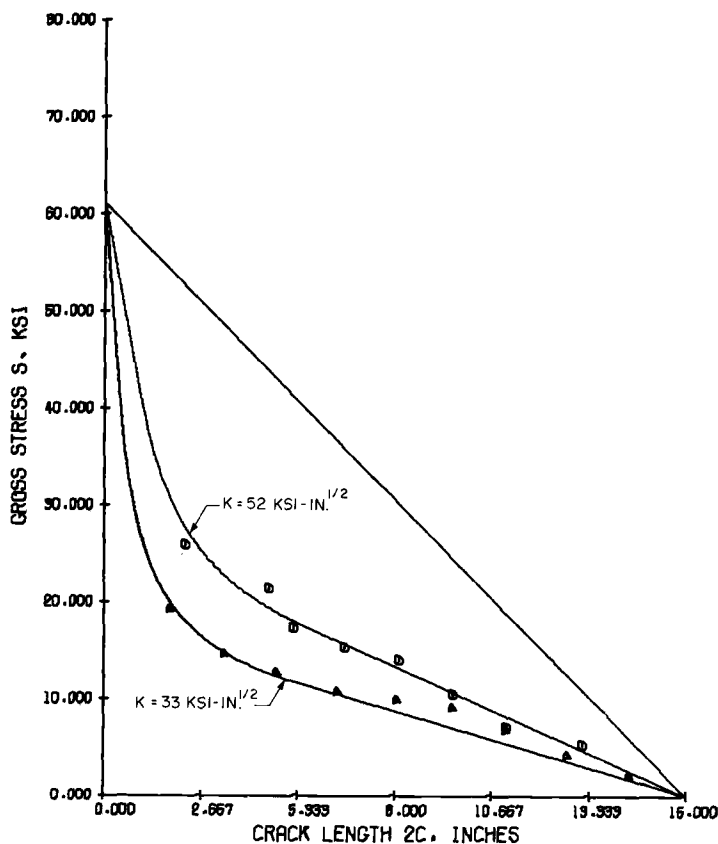

FIG. 20—*Computer plot of data and curves for threshold and critical instability of 1-in.-thick, 16-in.-wide 7075-T7351 aluminum alloy plate at room temperature* [7].
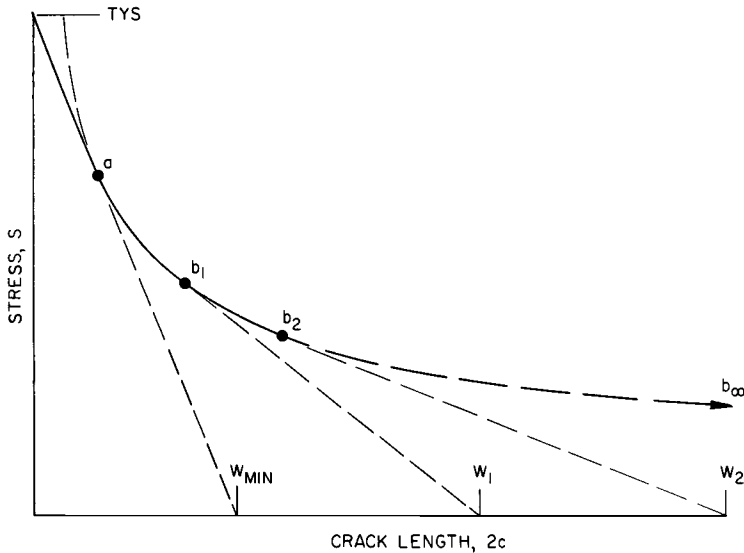
FIG. 21—*Generalization of the plot format.*

Crack Size Requirements

Also implicit in this development are some crack size limits between which elastic instability behavior is defined most rigorously. The minimum size crack for which predominantly elastic behavior may be expected is defined by Eq 10 as

$$2c_{min} = 1.43(K/TYS)^2 \dots\dots\dots\dots\dots\dots(14)$$

For crack lengths less than this value, the associated gross stress exceeds two thirds of TYS and is distorted by plasticity effects. The largest crack length compatible with ideal elastic behavior is

$$2c_{max} = W/3 \dots\dots\dots\dots\dots\dots\dots\dots(15)$$

since larger crack lengths will be increasingly affected by boundary influences.

Other Observations

The method which has been developed and verified in the previous sections has a simplicity and generality widely useful for design applications. Not only is the basic concept of associating crack damage levels with stress intensity factors retained but also a simple procedure for either analytical or graphical interpretation is provided. Furthermore, a detailed study of this procedure will reveal many other interesting insights to crack behavior and testing procedures. A few of these points are discussed in the following subsections.

Notch Concepts

In its original context, the term residual strength referred to the notch concept of evaluating the gross relationship of initial flaw or crack size, $2c_0$, to
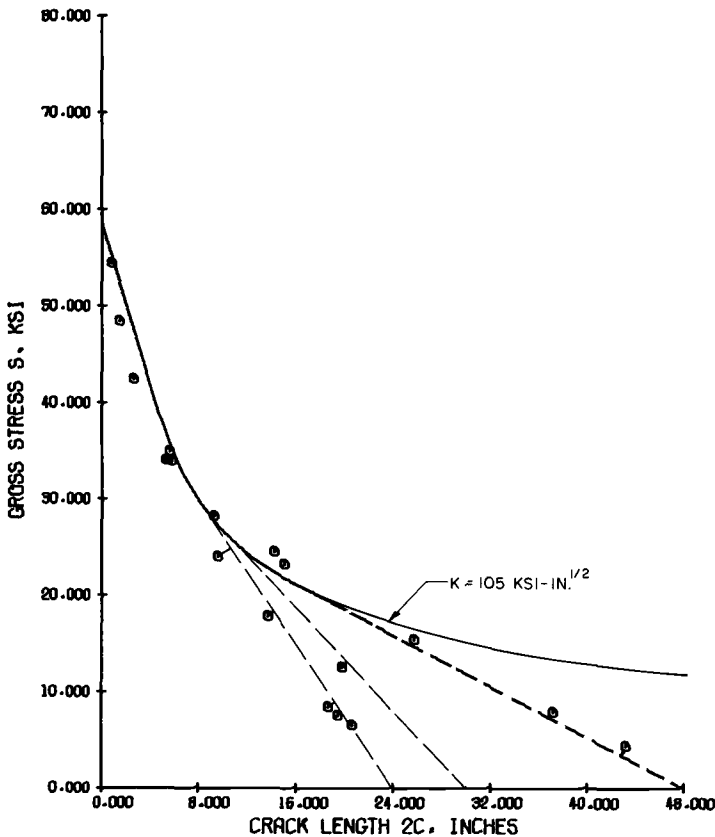
FIG. 22—*Computer plot of data and curve of critical instability of multiple widths of 0.100-in.-thick 2219-T87 aluminum alloy sheet at room temperature* [11].

the maximum load stress, S_1. This was a first approximation of crack response to loading and was an obvious and natural procedure. As knowledge of crack behavior has increased, the effort toward characterizing it also has increased. As a result, this presentation opened with an immediate recognition of two (or possibly three) general damage levels associated with the rising load fracture problem. While this additional refinement is useful and natural, the overall problem is still one of predicting or projecting the remaining (or residual) strength and structural life under specified service conditions.

The analysis which has been developed is still relevant to the notch concept. It should be noted that the representation of residual strength data by the earlier notch concept actually falls between the threshold and critical instability curves as shown in Fig. 24. For example, the data previously illustrated in Fig. 17 are reillustrated in Fig. 25 in terms of the notch concept. The resultant analysis of initial flaw-maximum stress data yields an apparent stress intensity factor which can be of some value in design. Since this value
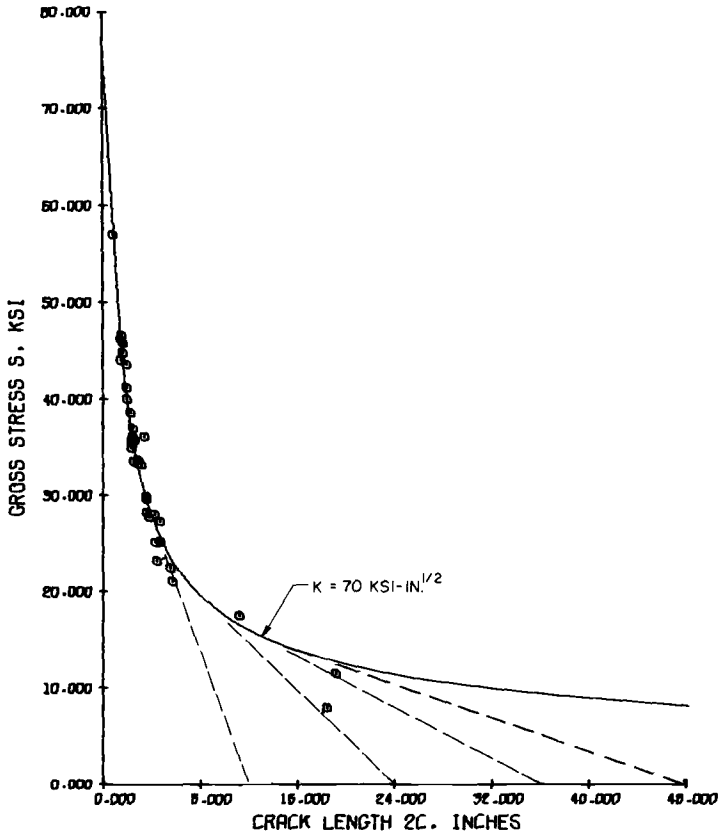
FIG. 23—*Computer plot of data and curve for critical instability of multiple widths of 0.090/0.100-in.-thick 7075-T6 aluminum alloy sheet at room temperature* [11, 12].

is less than that which might be associated with critical instability, it is conservative. However, it provides no reliable insight to the basic failure mode, elastic or plastic instability, since the slow tear process is masked over.

Other Elastic Limits

The *NSY* limit, as described by Fig. 6 and its associated discussion, was selected on the basis that *TYS* is a primary material strength value for practical engineering design. One could alternatively select the proportional limit stress; however, it is a more nebulous point to identify in the testing of materials and is not considered as relevant to the design procedure at hand.

It is interesting to note that an early, and still popular, criterion for the acceptability or validity of elastic fracture data is the relation

$$S_n \leq 0.8(TYS)$$

shown graphically in Fig. 26. This limit serves to screen out the problem areas (shaded) which are the very ones accommodated so well in this technique.
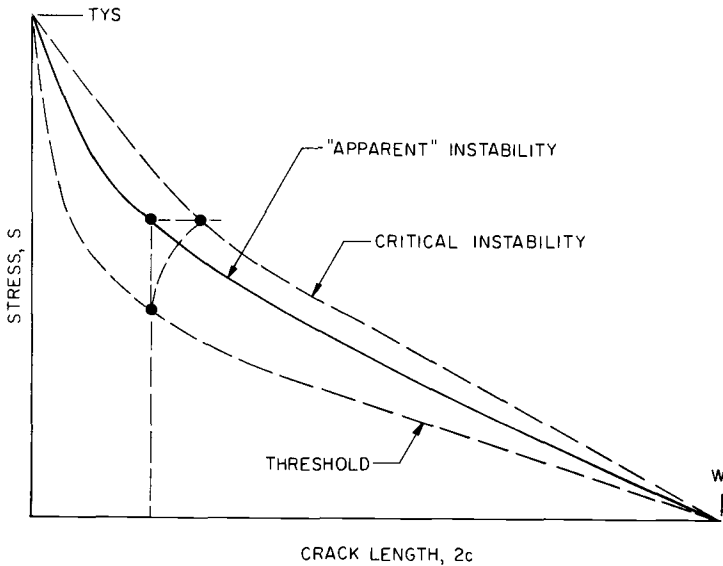
FIG. 24—*Notch concept of fracture behavior.*

Some Net Section Stress Limits

By its construction, the right-hand linear tangent is the minimum net section stress line for the particular damage level and panel width. This line touches the bottom of the saddle on the elastic instability curve. In terms of net section stress, this is a critical point. It implies that the associated crack length $W/3$ (at the tangency point, b) is the most sensitive flaw size relative to panel width for detecting elastic instability in a direct manner.

Since the use of a right-hand linear tangent is a phenomenological development, it appears that for a given panel width there does exist a lower limit on the net section stress. Although this limit tends to decrease as panel width increases, there is a finite limit to the width of practical panels such that an approximate criterion on net section stress limits could be established.

It also is interesting to note that this net section stress limit tends to approach a minimum in the area of $\frac{1}{2}TYS$ for many practical size panels. This behavior agrees well with the traditional observation that fatigue damage is not a problem at operating stresses one half or less of TYS.

Significance of the Linear Tangents

The linear tangents were selected because of their phenomenological representation of data behavior; thus, they may be considered to be empirical corrections to the basic stress intensity factor formulation. The mechanism of such behavior is beyond the scope of this paper; however, a conjecture can be made for each apparent correction. The left-hand linear tangent, or "plasticity corrected" curve, may be justifiable if the triggering mechanism is
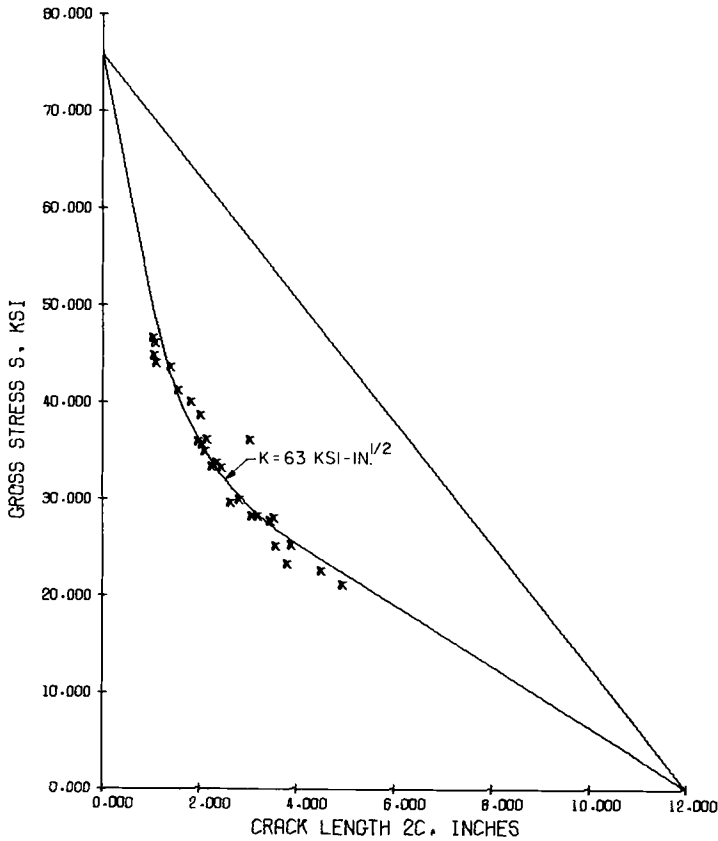
FIG. 25—*Computer plot of data and curve for apparent instability of 0.090-in.-thick, 12-in.-wide 7075-T6 aluminum alloy sheet at room temperature* [11].

indeed a flow stress. The right-hand linear tangent, or "width corrected" curve, may be due to an accentuation of the notch acuity due to boundary force transition or large deformations in the actual structural configuration.

Data Requirements

The stress-flaw size relationship which has been developed is a one-parameter curve (the parameter being K) for a given material yield strength and thickness range. From an analytical perspective, only one data point (one test) is required to determine the entire curve. Of course, practical aspects require a greater sampling of materials for confidence in the processing procedures. Nevertheless, the simplicity and directness of this technique allow a more rational selection and design of test specimens, as well as a more tangible means for interpreting the results.
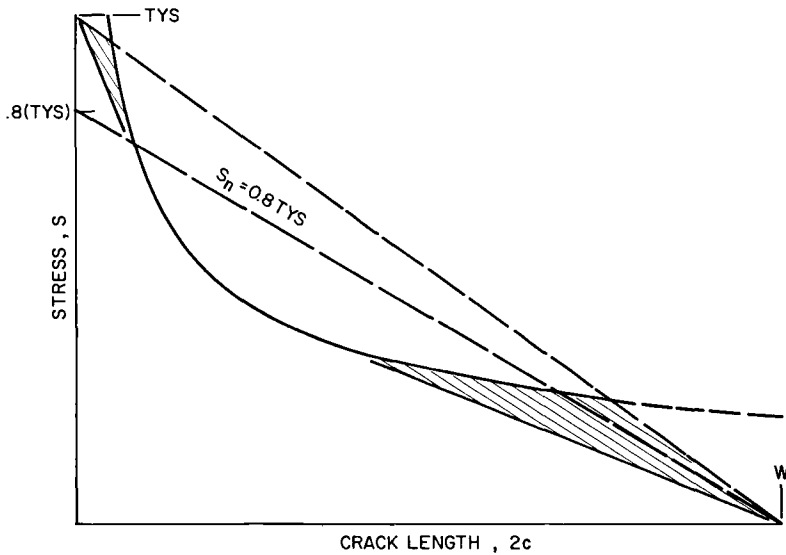
FIG. 26—*Comparison of elastic instability cutoffs.*

Nondimensional Format

The stress-flaw size format has been utilized to illustrate the basic details of this analytical development. If Eqs 6, 7, and 8 are ratioed to TYS, the procedures can be made nondimensionally parametric on $K/(TYS)\sqrt{W}$. The nondimensional coordinate system will have the stress ratio, S/TYS, as ordinate and the crack aspect ratio, $2c/W$, as abscissa.

Applications

The development, generalization, and observations of this residual strength analysis technique provide a framework for engineering definitions of toughness and damage tolerance. A few practical interpretations and their ramifications are mentioned in the following subsections.

Data Presentation

Since each curve is identified with a specific toughness index K, and since each curve is a specific mathematical construction, only a tabulation of the toughness index is needed to characterize a particular damage level in a given material thickness. That is, each curve could be reduced to a single entry in a data table. Then, the behavior of a crack length $2c$ in a panel width W would be determined from a calculation or graphical construction made according to the rules of the method.

The ultimate significance of this is illustrated in Fig. 27. A composite of fracture instability indexes and onset (or threshold) of flaw growth indexes is plotted versus panel thickness. The implied asymptotic trend to the right

suggests a plane strain limiting value of K_{Ic}. Each index represents the K value as determined from this technique and is valid for and derived from a full range of crack lengths and panel widths. Such a K versus t plot also could include temperature effects, environmental behavior, other damage levels, etc. This type of curve, along with a nondimensional stress ratio-crack aspect ratio plot, would be a significant design tool.

Testing Guidelines

Neglecting the uncertainties of materials processing, the implication of this one-parameter data representation is that a single, properly designed and conducted test (that is, a single datum point) is adequate to define a particular K index for a given material thickness range. In turn, this implies that more effective testing programs can be designed by considering the concepts set forth here.

While the absolute identification of damage levels has not been challenged, a more definite specification of them is needed. The consistency of curve fits in the data presentations illustrates that adequate detection means exist; however, more explicit standardization is needed.

Since, on a net section stress basis, maximum damage sensitivity is reached at a crack size of $W/3$ in center cracked tension panels, specimen design should reflect this for particular damage tests. For example, in critical instability studies, initial cracks of only $W/4$ in size may be necessary to accommodate the slow growth preceding failures at $W/3$.
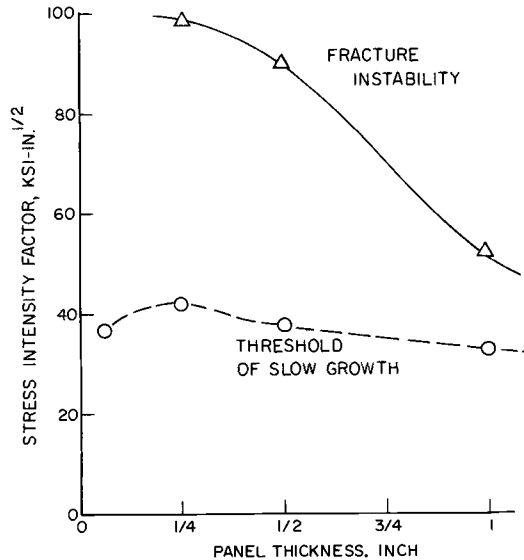
FIG. 27—*Effect of thickness on fracture criteria of centrally notched 7075-T7351 aluminum alloy panels* [7].

Conclusions

It has been demonstrated that the structural concept of residual strength can be related to the stress intensity factor, or K concept, in a simple and direct manner. The consistency and generality of the technique developed is functional for design. Furthermore, it has been illustrated that there exist detectable and distinctly different crack damage levels and that these can be modeled effectively by K concepts. This reinforces the potential of K as a general damage indicator.

The engineering rationale which has been developed is a basic framework for data analysis, design procedures, and test development related to structural damage tolerance. This work is being extended to establish design allowables, to consider other flaw configurations, and to relate to general flaw propagation behavior.

References

[1] Crichlow, W. J. in *Full Scale Fatigue Testing of Aircraft Structures*, Proceedings of the Symposium held in Amsterdam, June 1959, Pergamon Press, 1961, pp. 149–209.

[2] Christensen, R. H. and Denke, P. H., "Crack Strength and Crack Propagation Characteristics of High Strength Metals," ASD-TR-61-207, Douglas Aircraft Company, 1961.

[3] Westergaard, H. M., *Transactions*, American Society of Mechanical Engineers, TASMA, 1939, pp. A49–A53.

[4] Kuhn, P. and Figge, I. E., "Unified Notch-Strength Analysis for Wrought Aluminum Alloys," NASA TN-D-1259, National Aeronautics and Space Administration, 1962.

[5] Kuhn, P., "Residual Strength in the Presence of Fatigue Cracks," presented to the Structures and Materials Panel, Advisory Group for Aeronautical Research and Development, Turin, Italy, April 1967.

[6] Allen, F. C., "Stress Analysis of Centrally Cracked Plates," Paper 5513, Douglas Aircraft Company, presented to ASTM Committee E-24, 1969.

[7] Feddersen, C. E. and Hyler, W. S., "Fracture and Fatigue-Crack Propagation Characteristics of 7075-T7351 Aluminum Alloy Sheet and Plate," final report from Battelle Memorial Institute to Naval Air Development Center, Contract N00156-68-C-1344, 15 March 1970.

[8] Irwin, G. R., *Journal of Applied Mechanics*, JAMCA, Vol. 21, 1957, pp. 361–364.

[9] Orange, T. W., "Fracture Toughness of Wide 2014-T6 Aluminum Sheet at −320 F," NASA TN-D-4017, National Aeronautics and Space Administration, 1967.

[10] Broek, D., "The Effect of Sheet Thickness on the Fracture Toughness of Cracked Sheet," NLR Report TR M.2160, Netherlands National Aerospace Laboratory, 1966.

[11] Eichenberger, T. W., "Fracture Resistance Data Summary," Report No. D2-20947, Boeing Airplane Co., 1962.

[12] Hudson, C. M., "Effect of Stress Ratio on Fatigue-Crack Growth in 7075-T6 and 2024-T3 Aluminum Alloy Specimens," NASA TN-D-5390, National Aeronautics and Space Administration, 1969.

C. C. Poe, Jr.[1]

Fatigue Crack Propagation in Stiffened Panels

ABSTRACT: Rates of fatigue crack growth were measured in fatigue tests of stiffened panels constructed with bolted and integral stringers. The panels with bolted stringers were made from 2024-T3 aluminum alloy sheet with either aluminum alloy or steel stringers. The stringers were attached to the sheet with interference fit lock bolts. Stringer spacing and stiffness were varied systematically in the construction of the panels. The integrally stiffened panels were made from 7075-T6 aluminum alloy sheet extruded with outstanding stringers.

The stress intensity factor, calculated by a previously developed method, is used to predict the crack growth rates for the stiffened panels. Fatigue tests were conducted on unstiffened panels to determine the relationship between the stress intensity factor and crack growth rate.

In general, the stress intensity factor correctly predicts the crack growth rates in panels with bolted and with integral stringers except when the cracks are long. In these cases, the measured rates are slightly higher than the predicted rates. Furthermore, the stress intensity factor correctly predicts the rates to be lower in the panels with stiffer and more closely spaced stringers and to be equal in panels with steel and with aluminum alloy stringers of equal stiffness. The bolted stringers reduced the crack growth rate significantly below that for an equally stressed unstiffened panel, whereas the integral stringers had no significant effect.

KEY WORDS: aircraft, aircraft panels, joists, stiffening, fatigue (materials), cracking (fracturing), crack propagation, cyclic loads, axial stress, stress cycles, tensile properties, inspection, fatigue tests, aluminum alloys, structural steels

Nomenclature

a Half length of crack in sheet, measured from panel center line, in. (mm)

a_{st} Length of crack in integral stringer, in. (mm)

A Gross cross-sectional area of sheet, in.^{2} (m^2)

A_{st} Total gross cross-sectional area of stringers, in.^{2} (m^2)

b Spacing of stringers, in. (mm)

C Empirical constant

---

[1] Aerospace technologist, Fatigue Branch, Langley Research Center, National Aeronautics and Space Administration, Langley Station, Hampton, Va. 23365.

E Young's modulus of elasticity for sheet material, ksi (MN/m²)

E_{st} Young's modulus of elasticity for stringer material, ksi (MN/m²)

F Cumulative distribution function

K Stress intensity factor, ksi $\sqrt{\text{in.}}$ (MN/m³/²)

K_c Critical value of stress intensity factor, ksi $\sqrt{\text{in.}}$ (MN/m³/²)

K_{max} Stress intensity factor corresponding to maximum value of cyclic load, ksi $\sqrt{\text{in.}}$ (MN/m³/²)

ΔK Range of the stress intensity factor, $K_{max}(1 - R)$, ksi $\sqrt{\text{in.}}$ (MN/m³/²)

n Empirical constant

N Number of cycles of load

p Spacing of rivets, in. (mm)

r, θ Plane polar coordinates, in. (mm), deg

R Ratio of minimum to maximum values of cyclic load

S Gross stress in sheet, ksi (MN/m²)

S_{max} Maximum cyclic gross stress in sheet, ksi (MN/m²)

t_{st} Thickness of stringer material, in. (mm)

w Width of stringers, in. (mm)

W Width of unstiffened panel, in. (mm)

x, y Cartesian coordinates, in. (mm)

$(da/dN)_m$ Rate of growth of fatigue crack measured in panels without stringers, in./cycle (mm/cycle)

ϵ Exponential of error in method of least squares

μ Ratio of stringer stiffness to total stiffness

$\sigma_{xx}, \sigma_{xy}, \sigma_{zz}$ Normal stress components, ksi (MN/m²)

$\tau_{xy}, \tau_{xz}, \tau_{yz}$ Shearing stress components, ksi (MN/m²)

Long fatigue life and minimum structural weight are conflicting design requirements for aircraft structures. Because of the importance of low structural weight, allowable stresses cannot be lowered to eliminate totally the occurrence of fatigue cracks. For this reason, the structural integrity of a large portion of the commercial and military aircraft fleet today depends on some type of inspection procedure to detect fatigue cracks before they attain a critical length and cause catastrophic failure. If efficient and reliable inspection intervals are to be established, accurate analytical methods for predicting the rate of growth of a fatigue crack in an aircraft structure must be developed.

Numerous investigations have demonstrated that in a particular material the rate of fatigue crack growth for constant amplitude loading is related uniquely to the stress intensity factor (K-rate relationship). Figge and Newman [1][2] have demonstrated that stress intensity factor calculations and the K-rate relationship determined from tests of simple specimens can be used to predict fatigue crack growth rates in specimens subjected to various combinations of uniformly distributed and concentrated forces.

[2] Italic numbers in brackets refer to the list of references at the end of this paper.

The stiffened panel is representative of a large portion of aircraft construction and therefore has much practical importance. The stress intensity factor for a stiffened panel containing a crack in the sheet material and having riveted stringers of uniform size and spacing has been calculated and is presented in Ref 2. Stringer stiffness, stringer spacing, and rivet spacing were parameters in those calculations. The purpose of the present investigation is to demonstrate that the stress intensity factor calculated by the method in Ref 2 can be used to predict the rate of growth of a fatigue crack in a stiffened panel; thus, a comparison is made of measured and predicted crack growth rates in stiffened panels subjected to constant amplitude fatigue loading.

The specimens were constructed of 2024-T3 aluminum alloy sheet with bolted stringers of aluminum alloy or steel and of 7075-T6 aluminum alloy sheet extruded with integral stringers. The bolted stringers were attached with interference fit lock bolts. Stringer stiffness and stringer spacing were varied in the construction of the panels with bolted stringers. The K-rate relationships were determined from crack growth rates measured in unstiffened panels made from the same 2024-T3 and 7075-T6 materials. The method in Ref 2 also is extended to calculate the stress intensity factor for the panels with integral stringers.

Specimens

Panels with Bolted Stringers

Six stiffened panels were made with bolted stringers of various spacing, stiffness, and material as shown in Table 1. The stiffness of the stringers is given in terms of a dimensionless parameter μ where

$$\mu = \frac{A_{st}E_{st}}{AE + A_{st}E_{st}} \quad \dots\dots\dots\dots\dots\dots\dots\dots\dots(1)$$

which is the ratio of stringer stiffness to total panel stiffness. The panel material was 0.090-in. (2.29-mm)-thick 2024-T3 aluminum alloy sheet. The stringer materials were 2024-T3 and 2024-T4 aluminum alloys and AM350-CRT steel. The two panels with steel stringers were made with the stringer stiffness and spacing identical to two of the panels with aluminum alloy stringers. Figure 1 shows the basic configuration of the panels. The stringers were attached to the sheet material by $\frac{1}{4}$-in. (6.4-mm) lock bolts with a 1.00-in. (25-mm) pitch. Aluminum alloy bolts were used with the aluminum alloy stringers and steel bolts with the steel stringers. The sheet and stringer materials were match drilled for an interference fit with the bolts. Bolts were not installed along the transverse center line of the panels. The panels were made with the rolling direction of the sheet and stringer materials parallel to the longitudinal axis of the panels. A crack starter notch 0.50 in. (12.7 mm) long by 0.01 in. (0.24 mm) wide was made in the sheet material at the center
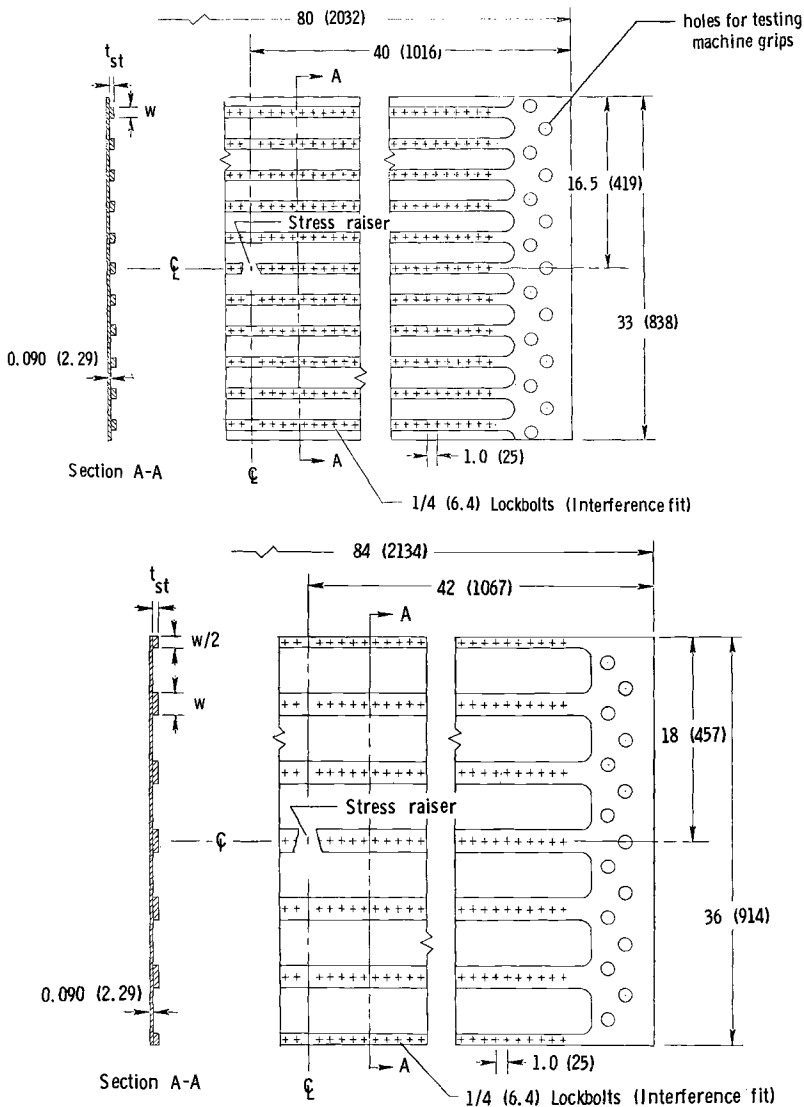
FIG. 1—*Panels with bolted stringers: top, 3-in. (76-mm) stringer spacing; bottom, 6-in. (152-mm) stringer spacing. Dimensions are in inches (millimeters).*

of each panel by an electrical discharge machining process. The tensile properties of the sheet and stringer materials were determined from standard ASTM tension specimens and are given in Table 2.

Panels with Integral Stringers

Three panels were fabricated from 7075-T6 sheets that had been extruded with integral stringers. The configuration of these panels is shown in Fig. 2.

TABLE 1—*Stiffened panels with bolted stringers.*

Stringer Material	Stringer Stiffness, μ	Stringer Spacing, b, in. (mm)	Stringer Thickness, t_{st}, in. (mm)	Stringer Width, w, in. (mm)
2024–T3..........	0.21	6.0 (152)	0.071 (1.80)	2.0 (51)
2024–T4..........	0.58	6.0 (152)	0.375 (9.53)	2.0 (51)
2024–T3..........	0.41	6.0 (152)	0.190 (4.83)	2.0 (51)
2024–T3..........	0.41	3.0 (76)	0.190 (4.83)	1.0 (25)
AM350–CRT......	0.41	6.0 (152)	0.050 (1.27)	2.5 (64)
AM350–CRT......	0.41	3.0 (76)	0.050 (1.27)	1.3 (32)

The stiffness ratio μ for these panels is 0.22. A crack starter notch 0.10 in. (2.54 mm) long by 0.01 in. (0.25 mm) wide was made in the center of each panel by an electrical discharge machining process. Rectangular aluminum blocks were adhesively bonded to the extruded panels at the ends to provide a firm and even surface for the testing machine grips. The tensile properties of these extrusions are given in Table 2.

Unstiffened Panels

Twelve unstiffened panels, 12 in. (300 mm) wide by 35 in. (890 mm) long, were made from the 0.090-in. (2.29-mm)-thick 2024-T3 aluminum alloy sheet. Two of these specimens were made from the remnant of each piece of material that had been used in making the sheet portion of the stiffened panels in Table 1.
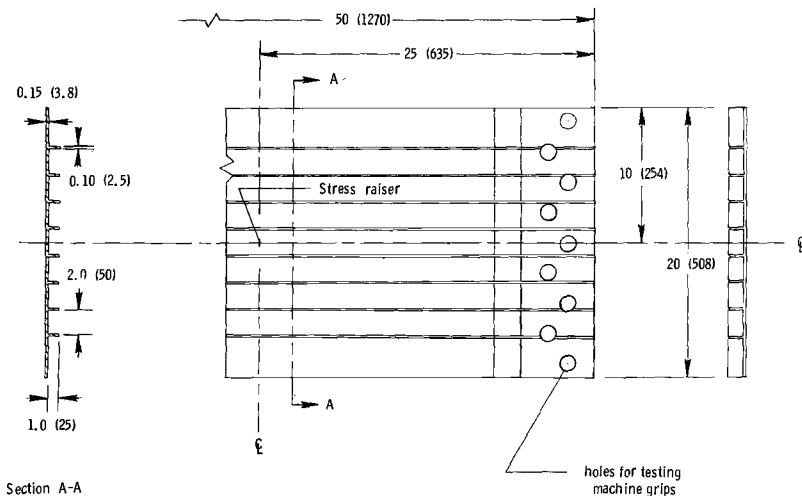
FIG. 2—*Panels with integral stringers. Dimensions are in inches (millimeters).*

TABLE 2—*Average tensile properties of sheet and stringer materials (longitudinal grain direction).*

Material	Thickness in. (mm)	Ultimate Tensile Strength, ksi (MN/m²)	Yield Stress (0.2 percent Offset), ksi (MN/m²)	Young's Modulus of Elasticity, ksi (GN/m²)	Elongation in 2-in. (51-mm) Gage Length, Percent	No. of Tests
2024-T3	0.071 (1.80)	72.7 (501)	54.1 (373)	10 400 (71.7)	18	10
2024-T3	0.090 (2.29)	71.4 (492)	52.9 (365)	10 400 (71.7)	19	21
2024-T3	0.190 (4.83)	69.7 (481)	55.0 (379)	10 600 (73.1)	18	10
2024-T4	0.375 (9.53)	71.5 (493)	60.4 (416)	10 700 (73.8)	17	6
7075-T6[a]	0.156 (3.96)	85.9 (592)	78.1 (538)	10 300 (71.0)	11.5	. . .
AM350-CRT	0.050 (1.27)	230 (1590)	217 (1500)	28 400 (196)	22	6

[a] Extruded material—data taken from Ref 3.

Three unstiffened panels, 20 in. (508 mm) wide by 50 in. (1270 mm) long, also were made from the 7075-T6 extruded sheets. One of these specimens was made from the remnant of each piece of material that had been used in making the integrally stiffened panels in Fig. 2. The stringers were machined from the extruded sheets.

A crack starter notch 0.10 in. (2.54 mm) long by 0.01 in. (0.25 mm) wide was made in the center of all the unstiffened panels. An electrical discharge machining process was used to make the notches.

Test Equipment and Procedure

All of the panels were subjected to axial cyclic loading of constant amplitude. The numbers of cycles required for the fatigue crack to reach various lengths were recorded. Loading was discontinued when the crack had extended across one third to one half the width of the specimen. Readings were made typically at 0.05-in. (1.3-mm) increments of crack length using 10-power microscopes mounted on an adjustable slide assembly with a scale and vernier. The scale and vernier could be read to within 0.001 in. (0.025 mm).

All of the specimens with the exception of the 2024-T3 unstiffened panels were tested in a 400,000-lbf (1780-kN) axial load, fatigue testing machine. Loading is controlled in this machine by a servohydraulic system capable of a wide range of loading frequencies. The 2024-T3 unstiffened panels were tested in a 132,000-lbf (590-kN) axial load, fatigue testing machine. This machine operates subresonantly at 820 cpm (14 Hz) or hydraulically at 40 cpm (0.7 Hz). Loading frequencies for all the tests were in the range 30 to 820 cpm (0.5 to 14 Hz). The lower frequencies were necessary to provide time for the crack length measurements when the crack growth rates were high.

The gross stresses in the sheet and stringers, respectively, were calculated in terms of the applied load P as follows:

$$S = \frac{P}{A + A_{st}E_{st}/E} \quad \dots\dots\dots\dots\dots\dots\dots (2)$$

and

$$S_{st} = SE_{st}/E \dots\dots\dots\dots\dots\dots\dots (3)$$

Equations 2 and 3 were derived by assuming the sheet and stringers were equally strained by the applied load P. For the 2024-T3 aluminum alloy sheet material, the maximum cyclic value of gross stress in the sheet was 15.0 ksi (103 MN/m²). For the panels with steel stringers, the stress in the stringers was nearly three times the stress in the aluminum alloy sheet. The maximum cyclic stress for the stiffened and unstiffened panels made with 7075-T6 aluminum alloy extrusions was 10.0 ksi (68.9 MN/m²). The load ratio R was 0.10 for all tests.

In the tests of the stiffened panels with bolted stringers, one crack tip advanced more rapidly than the other. When the difference in crack length
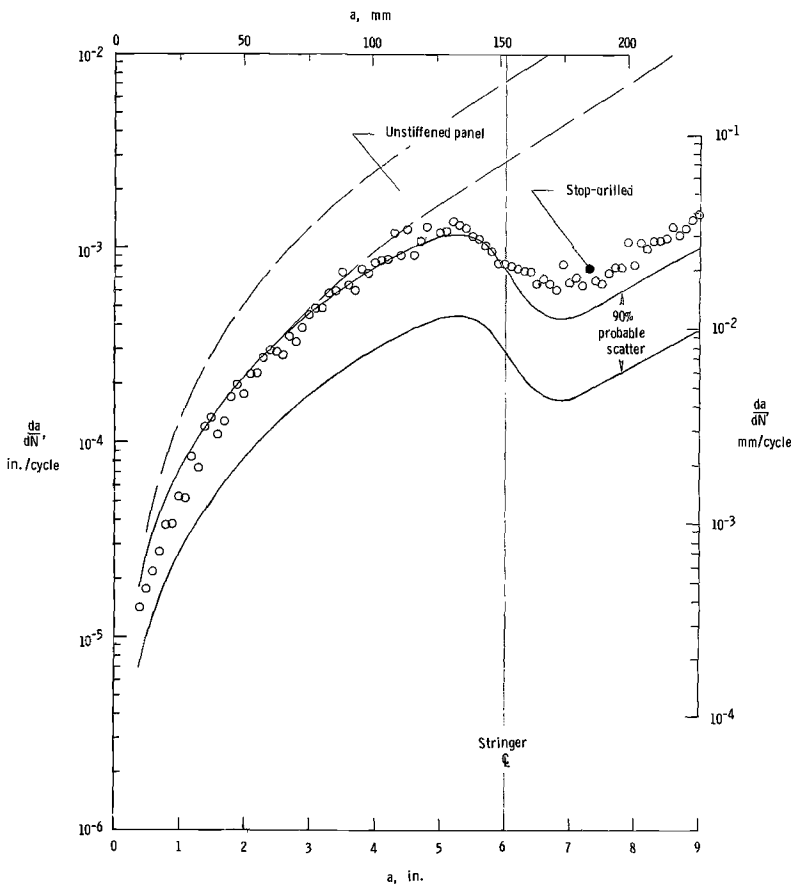
FIG. 3—*Predicted and measured rate of crack growth in panels with bolted stringers.* (a) $\mu = 0.21$, *aluminum alloy stringers spaced at 6 in.* (*152 mm*).

relative to the center line of the panel became more than 0.5 to 2.0 in. (13 to 51 mm), symmetry was restored by one of the following procedures: the laggard crack tip was extended with a jeweler's saw to the same distance from the panel center line as the other crack tip, or the advance crack tip was stop drilled to allow the laggard crack tip to catch up to the advance crack tip.

Axial load, residual static strength tests were conducted on the unstiffened panels following the fatigue crack growth tests. The specimens were loaded to failure at a stress rate of 30 ksi/min (3.4 MN/m²/s) and 100 ksi/min (11.5 MN/m²/s) for the 2024-T3 and 7075-T6 panels, respectively.

The 2024-T3 unstiffened panels were restrained from buckling in the vicinity of the crack by means of two heavy plates, one located on each side of the specimen. The plates were clamped together with a small clearance between
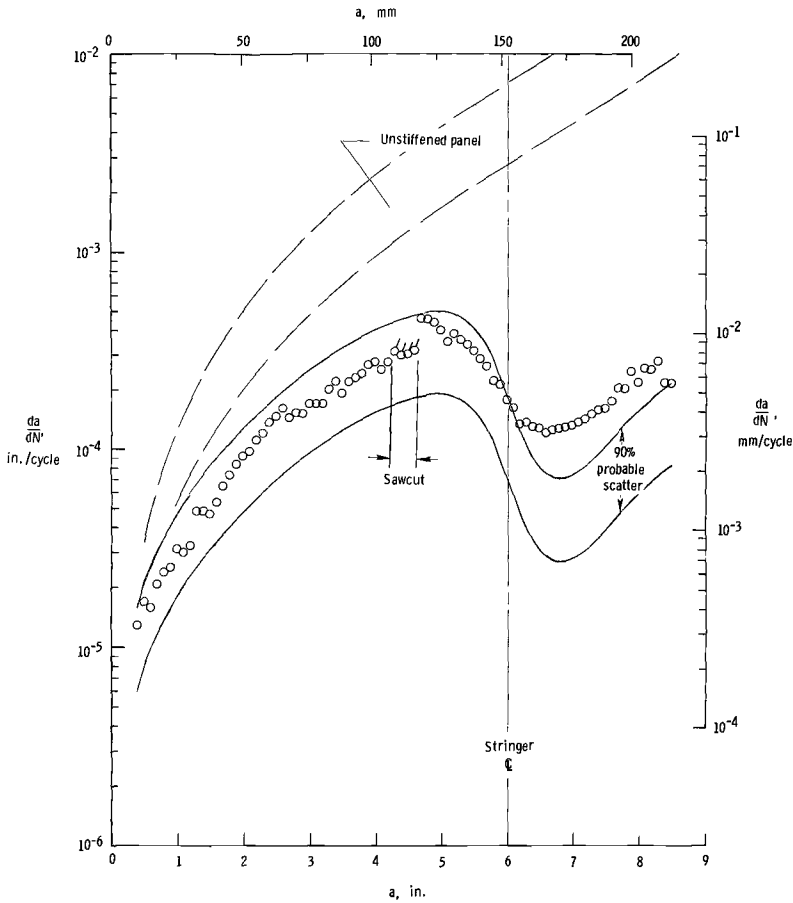
FIG. 3—*Continued.* (b) $\mu = 0.58$, *aluminum alloy stringers spaced at 6 in. (152 mm).*

the plates and the specimen. A slot 1.5 in. (38 mm) wide was made across the width of one plate so that the crack could be observed.

Results and Discussion

The K-rate relationships for the 2024-T3 and 7075-T6 unstiffened panels are given in Appendix I. An analysis of the scatter in the K-rate relationships also is given. The stress intensity factor-crack length relationships for the panels with bolted and integral stringers are given in Appendix II.

Figures 3 and 4 show the measured and predicted crack growth rates plotted against half crack length for the stiffened panels with bolted stringers and with integral stringers, respectively. The measured rates were determined by numerically differentiating the relationship between crack length and load cycles. The derivatives were calculated for each crack length measurement
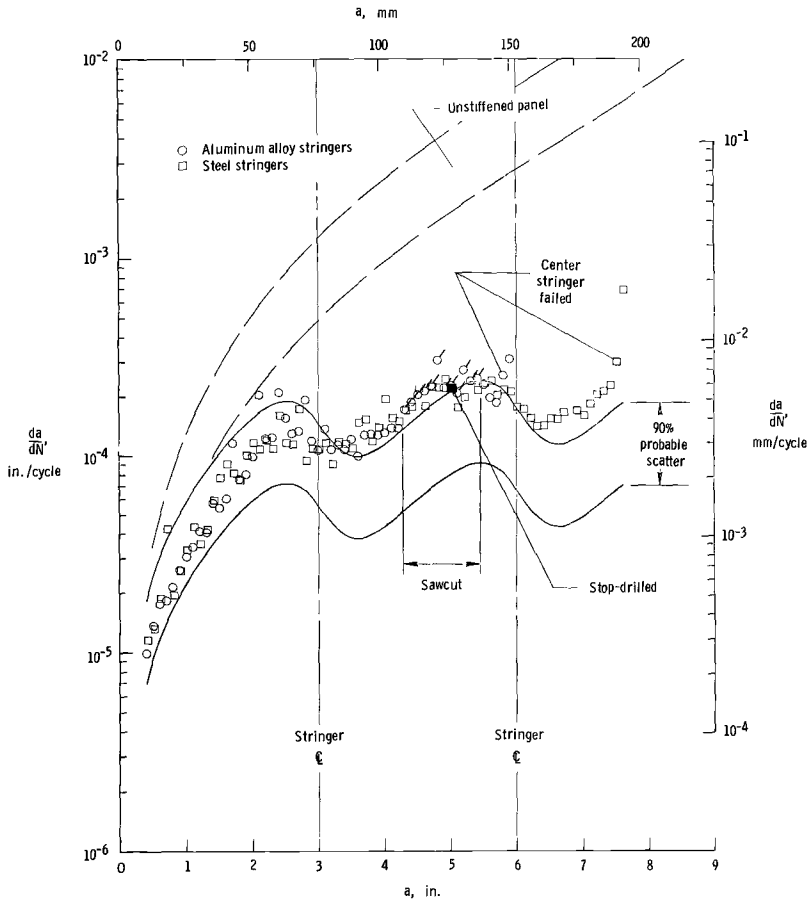
FIG. 3—*Continued.* (c) $\mu = 0.41$, *aluminum alloy and steel stringers spaced at 3 in. (76 mm).*

using Lagrange's interpolation formula of second degree [4]. The plotted values represent the average for both crack tips except where a crack tip was extended with a jeweler's saw or was stop drilled. In those cases the rate for the unaltered crack tip, shown as a ticked or filled symbol, respectively, was plotted in lieu of an average value. The general continuity of the rates measured before and after a saw cut was made indicates that the absence of symmetry had little effect upon the stress intensity factor. The predicted rates are shown in each figure as a band representing a probable scatter. The curves defining this band represent the fifth and ninety-fifth percentiles of the scatter in the K-rate relationship; thus, 90 percent of the rates should be within the band. The predicted rates for an unstiffened panel with the same applied stress also are shown in each figure for comparison. The stress intensity factor for an unstiffened sheet, $K = S\sqrt{\pi a}$, was used in making these calculations.
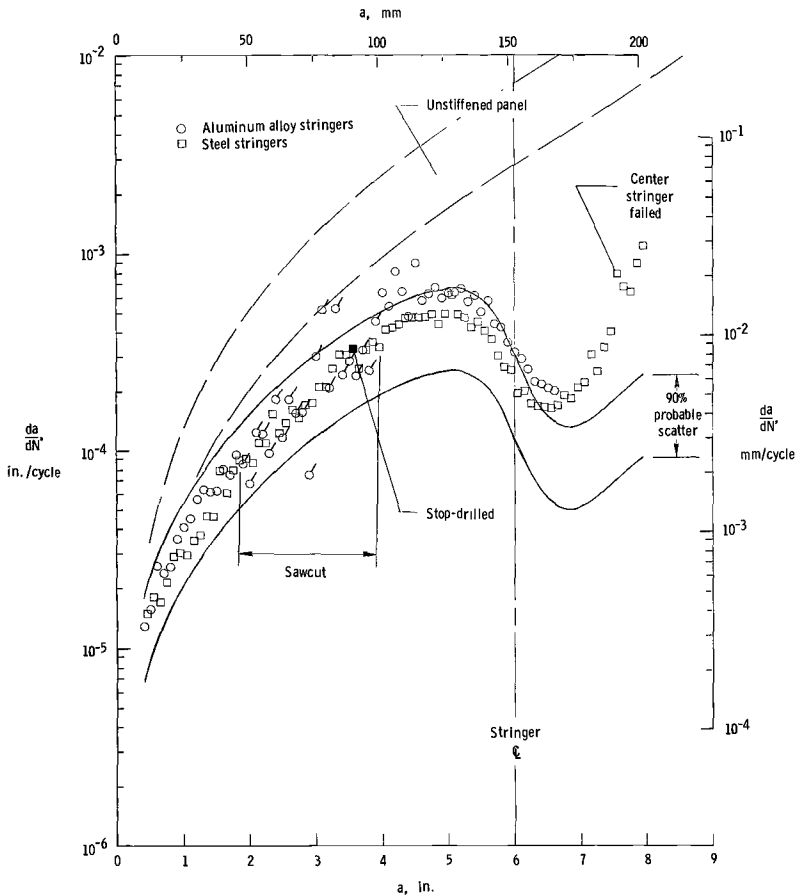
FIG. 3—*Continued.* (d) $\mu = 0.41$, *aluminum alloy and steel stringers spaced at 6 in.* (*152 mm*).

Panels with Bolted Stringers

The measured and predicted crack growth rates in Fig. 3 show that the method correctly predicted the rates for the panels with bolted stringers, except that the measured rates were slightly higher than the predicted rates when the crack tip was beyond the first stringer. Two major factors contribute to these differences. First, the forces on the bolts nearest the crack became very high when the crack advanced beneath a stringer, and the bearing stresses around the holes exceeded the bearing yield strength of the sheet material. Thus, the stringers were not as effective in reducing the crack tip stresses as had been indicated by the calculated value of the stress intensity factor. Second, because the sheet and stringers were not coplanar, the crack in the sheet caused bending stresses to develop in the center of the panel. These bending stresses, which increase with crack length, were not considered in the stress intensity factor calculations. Strain gage measurements revealed
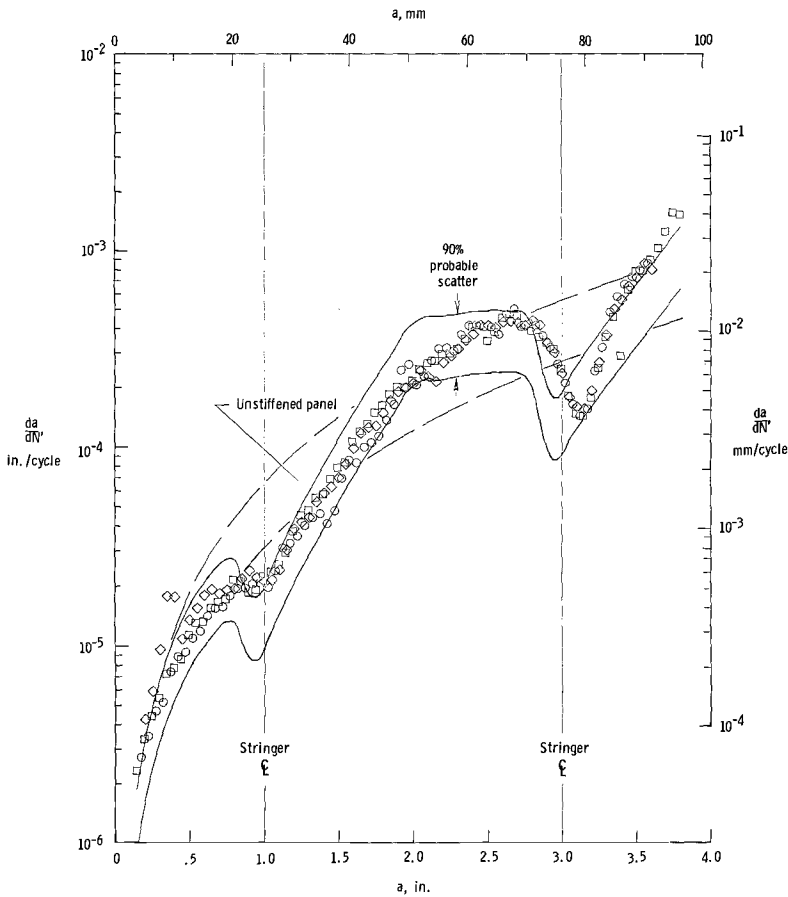
FIG. 4—*Predicted and measured rate of crack growth in panels with integral stringers. Symbols denote three tests.*

that the bending stresses near the crack tips could be as large as one fourth of the axial stresses when the crack was long.

The results in Fig. 3 also show that the stress intensity factor correctly predicted the lower crack growth rates for the panels with stiffer and more closely spaced stringers. Furthermore, the results show that the stress intensity factor correctly predicted equal rates for the equivalent panels with steel and with aluminum alloy stringers. The predicted rates for the panels with bolted stringers, especially those with stiffer and more closely spaced stringers, generally are much lower than the rates for equally stressed unstiffened panels. Thus, the bolted stringers were effective in reducing crack growth rates.

The center stringer failed in both of the panels with stringers spaced at 3 in. (76 mm) and in the panel with steel stringers spaced at 6 in. (152 mm)

(see Figs. 3c and 3d). Fatigue crack growth rates were noticeably higher immediately thereafter indicating the detrimental effect of a broken stringer. The fatigue cracks that caused the failures always initiated in one of the two bolt holes nearest the crack in the center stringer. The calculated stress in the stringer at the center of the panel is higher for the panels with the smaller stringer spacing [2]; thus, fatigue failures should be more likely to occur in the stringers of the panels with 3-in. (76-mm) strap spacing.

Panels with Integral Stringers

The measured and predicted crack growth rates in Fig. 4 show that the method also correctly predicted the rates for the panels with integral stringers except when the crack tip is in the immediate vicinity of a stringer. In these cases, the measured rates are higher than the predicted rates, indicating that the calculated stress intensity factor is too low. The predicted curves for an unstiffened panel are not significantly different from the curves for an equally stressed panel with integral stringers. The integral stringers did not cause any overall reduction in the crack growth rates.

The solid symbols in Fig. 5 show the measured crack growth rates in the stringers of one of the integrally stiffened panels. For comparison, the rate of growth of the crack in the sheet also is shown and is plotted in open symbols. For convenience, both crack lengths were made nondimensional by
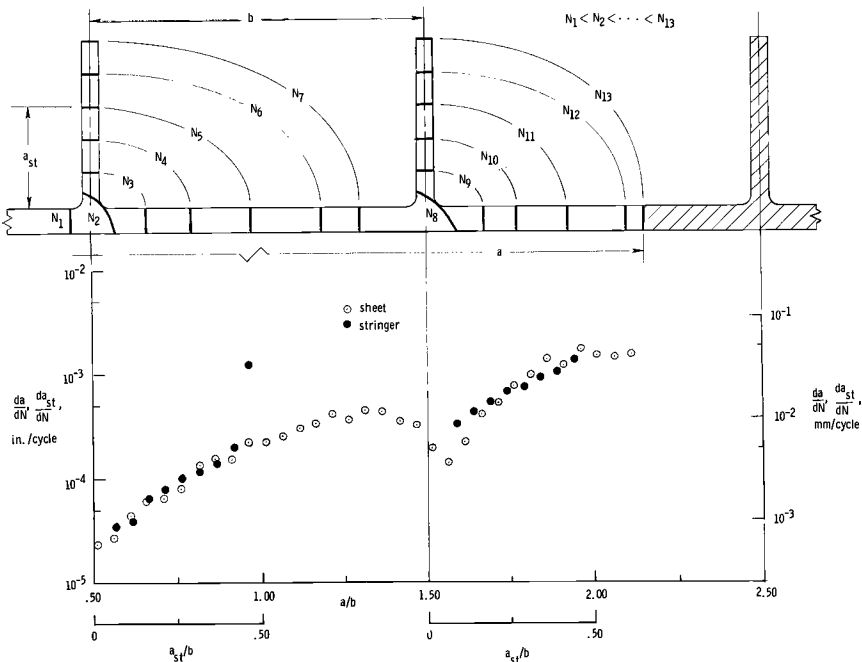
FIG. 5—*Measured rate of crack growth in stringers of integrally stiffened panel.*

dividing by the stringer spacing. The results show that the rates are essentially the same for both crack tips. The lines in the sketch at the top of the figure show the crack front at various cycles of load. The crack tips developed straight fronts normal to the direction of growth shortly after the crack branched at each stringer. Also, the stringers failed when the crack tip in the sheet was approximately 1.5 in. (38 mm) beyond the stringer. This distance is larger than that assumed in estimating the stress intensity factor; however, this discrepancy caused only slight disagreement between the measured and predicted rates.

Summary

The rate of growth of a fatigue crack was measured in fatigue tests of stiffened panels with bolted stringers and with integral stringers. Stringer spacing, stringer stiffness, and stringer material were varied systematically in the panels with bolted stringers. A probable scatterband of crack growth rates was predicted for the stiffened panels on the basis of a K-rate relationship determined from tests of unstiffened sheets and of stress intensity factor calculations for the stiffened panels.

The stress intensity factor calculated by the method in Ref 2 correctly predicted the crack growth rates in the panels with bolted stringers except when the crack was long. In these cases the measured rates were slightly higher than the predicted rates. The calculated stress intensity factor correctly predicted the crack growth rates to be lower in the panels with stiffer and more closely spaced stringers and to be the same in panels with steel and with aluminum alloy stringers of equal stiffness. For longer cracks, the bolted stringers caused a significant reduction in crack growth rates compared to an equally stressed unstiffened panel.

The stress intensity factor calculated for the stiffened panels with integral stringers also correctly predicted the crack growth rates. The stress intensity factor was estimated satisfactorily by assuming the integral stringers to be attached to the sheet with closely spaced rivets and by assuming the crack to branch at each stringer and grow simultaneously through the sheet and stringer at the same rate. Also, as predicted, the integral stringers had an insignificant effect on the crack growth rates compared with an equally stressed unstiffened panel.

APPENDIX I

Relationship Between Stress Intensity Factor and Crack Growth Rate

In Fig. 6 the values of crack growth rate measured in the tests of the unstiffened panels are plotted against the range of the stress intensity factor, ΔK. The values of ΔK were calculated by the following equation:

$$\Delta K = S_{\max} (1 - R)\sqrt{W \tan (\pi a/W)} \dots\dots\dots\dots\dots(4)$$

where $S_{\max}$ is the maximum cyclic stress and W is the width of the unstiffened panel.
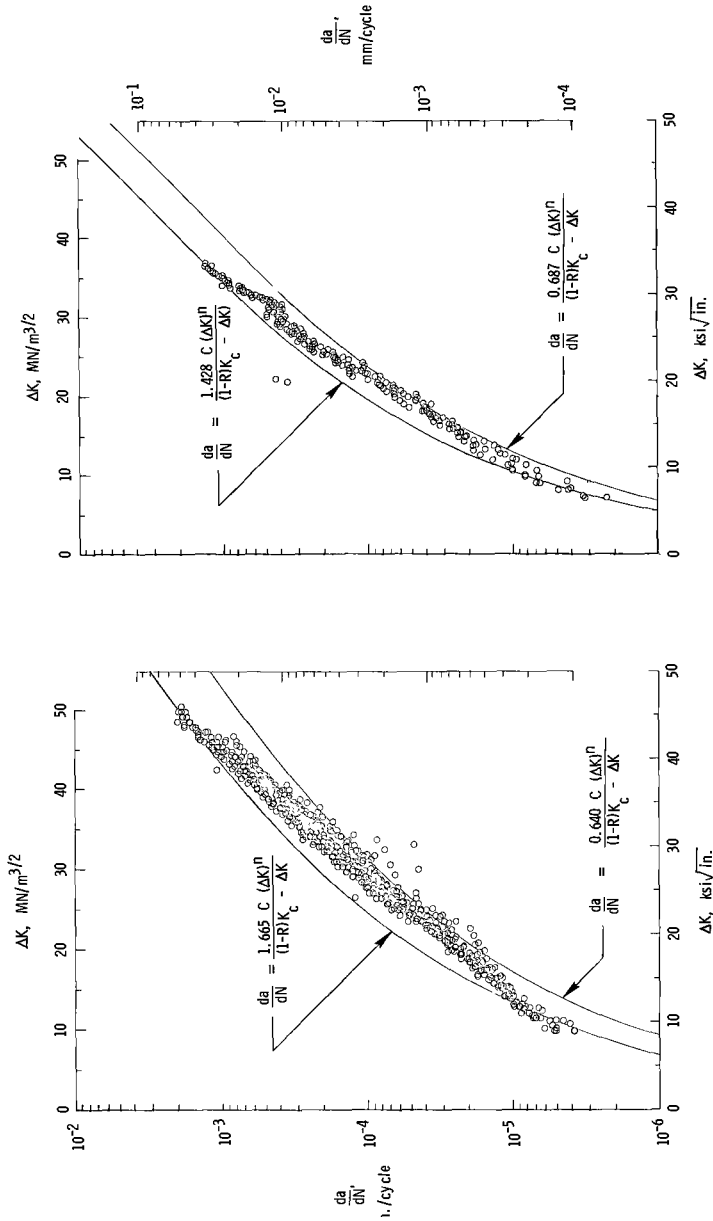
FIG. 6—K-rate measurements in unstiffened panels of (left) 2024-T3 and (right) 7075-T6 aluminum alloy.

The rate of crack growth with respect to cycles of load was calculated by numerically differentiating the crack length-cycles measurements. The differentiation was carried out using Lagrange's interpolation formula of second degree [4].

For convenience, an empirical equation proposed by Forman [5] was used to represent the K-rate relationship mathematically. Hudson [6] has shown that this equation provides an excellent mathematical representation of the K-rate relationship for both 2024-T3 and 7075-T6 aluminum alloys with various values of mean and alternating load. This equation gives the rate of crack growth with respect to cycles of load as

$$\frac{da}{dN} = \frac{C(\Delta K)^n}{(1 - R) K_c - \Delta K} \dots\dots\dots\dots\dots\dots\dots(5)$$

where K_c is the critical value of the stress intensity factor and C and n are constants.

The values of K_c used in Eq 5 were determined from the residual static strength tests of the panels without stiffeners. The values of the constants C and n were determined by a least squares fit of Eq 5 to the K-rate measurements. The values of K_c, C, and n for the two alloys are given in the following table:

Material	K_c, ksi $\sqrt{\text{in.}}$	K_c, MN/m$^{3/2}$	C^a	n^a
2024–T3	92	101	2.165×10^{-15}	3.50
7075–T6	68	75	1.046×10^{-14}	3.40

^{a} These values are for U.S. customary units only.

The error that was minimized in the least squares fit of Eq 5 to the K-rate measurements in Fig. 6 is defined by

$$\ln \epsilon = \ln (da/dN)_m - \ln (da/dN) \dots\dots\dots\dots\dots(6)$$

where $(da/dN)_m$ is the measured crack growth rate, da/dN is the crack growth rate calculated by Eq 5, and $\ln \epsilon$ is the error. Substituting Eq 5 into Eq 6, ϵ can be written as

$$\epsilon = \frac{(da/dN)_m}{\dfrac{C(\Delta K)^n}{(1 - R) K_c - \Delta K}} \dots\dots\dots\dots\dots\dots(7)$$

The cumulative distribution of ϵ for the measurements in Fig. 6 is shown in Fig. 7. The values of ϵ that represent the fifth and ninety-fifth percentiles of ϵ are given in the following table:

Material	ϵ, $F(\epsilon) = 0.05$	ϵ, $F(\epsilon) = 0.95$
2024–T3	0.640	1.665
7075–T6	0.687	1.428

The fifth and ninety-fifth percentiles of the measured rates were obtained by multiplying Eq 5 by the corresponding values of ϵ in the table. The resulting equations are shown in Fig. 6 with the measured rates.
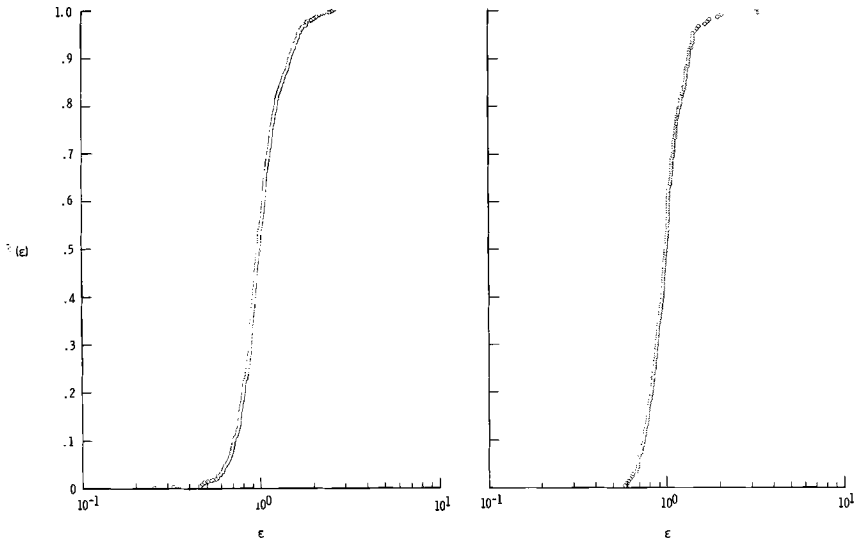
FIG. 7—*Cumulative distribution of ε for K-rate measurements in tests of unstiffened panels of (left) 2024-T3 and (right) 7075-T6 aluminum alloy.*

APPENDIX II

Stress Intensity Factor Calculations for Stiffened Panels

The stress intensity factor for the stiffened panels was calculated by a previously developed method [2] that accounted for riveted stringers of uniform size and spacing. Figure 8 shows the stress intensity factor for each panel with bolted stringers in Table 1 plotted against half crack length. The curves for $\mu = 0.41$ represent a panel with aluminum alloy stringers and a panel with steel stringers. For convenience, the stress intensity factor and the half crack length are made nondimensional by dividing by the stress intensity factor of an unstiffened sheet, $S\sqrt{\pi a}$, and the stringer spacing, b, respectively.

The stress intensity factor for the panels with integral stringers was calculated by assuming that the stringers were attached to the sheet with very closely spaced rivets. As the rivet spacing approaches zero, this situation approaches the case of integral stringers. Figure 9a shows the stress intensity factor plotted against half crack length for a value of rivet spacing of $p/b = 1/15$. Preliminary calculations revealed that smaller values of rivet spacing would not alter the results. The stress intensity factor and the half crack length are made nondimensional by dividing by $S\sqrt{\pi a}$ and b, respectively. Because a fatigue crack advances through an integral stringer as well as through the sheet itself, the calculations were made with the assumption that the stringers intersecting the crack were severed completely by the crack. The large discontinuities in the curve are a result of load transfer from the severed stringers to the sheet in the immediate vicinity of the crack tip. These discontinuities are unrealistic because the stringers are not likely to be severed completely until the crack tip in the sheet has advanced some distance beyond the stringers. The curve was modified in Fig. 9b to approximate the behavior of the stringer as the crack branches and proceeds simultaneously through the sheet and stringer. The crack
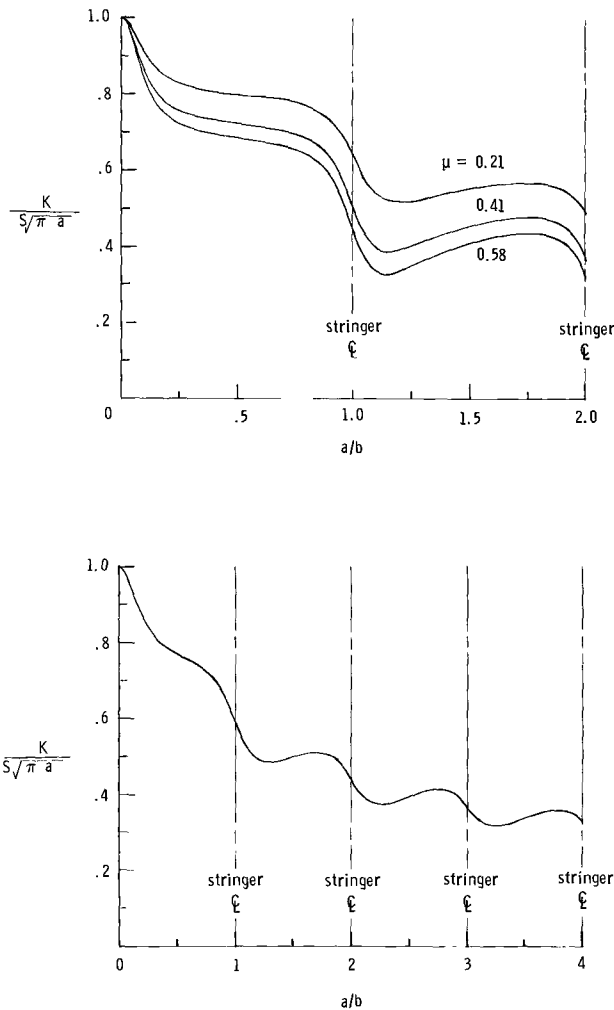
FIG. 8—*Relationship between stress intensity factor and crack length for panels with bolted stringers: top, 6-in. (152-mm) stringer spacing; bottom, 3-in. (76-mm) stringer spacing; $\mu = 0.41$.*

growth rate was assumed to be equal in the sheet and stringer so that the stringer is not severed completely until the crack in the sheet has advanced an additional distance equal to the height of the stringer. Between the edge of the stringer and the point at which the stringer is assumed to be severed completely, $K/S\sqrt{\pi a}$ was assumed to increase linearly with a/b, as shown.

References

[*1*] Figge, I. E. and Newman, J. C., Jr., "Prediction of Fatigue-Crack-Propagation Behavior in Panels with Simulated Rivet Forces," NASA TN D-4702, National Aeronautics and Space Administration, 1968.
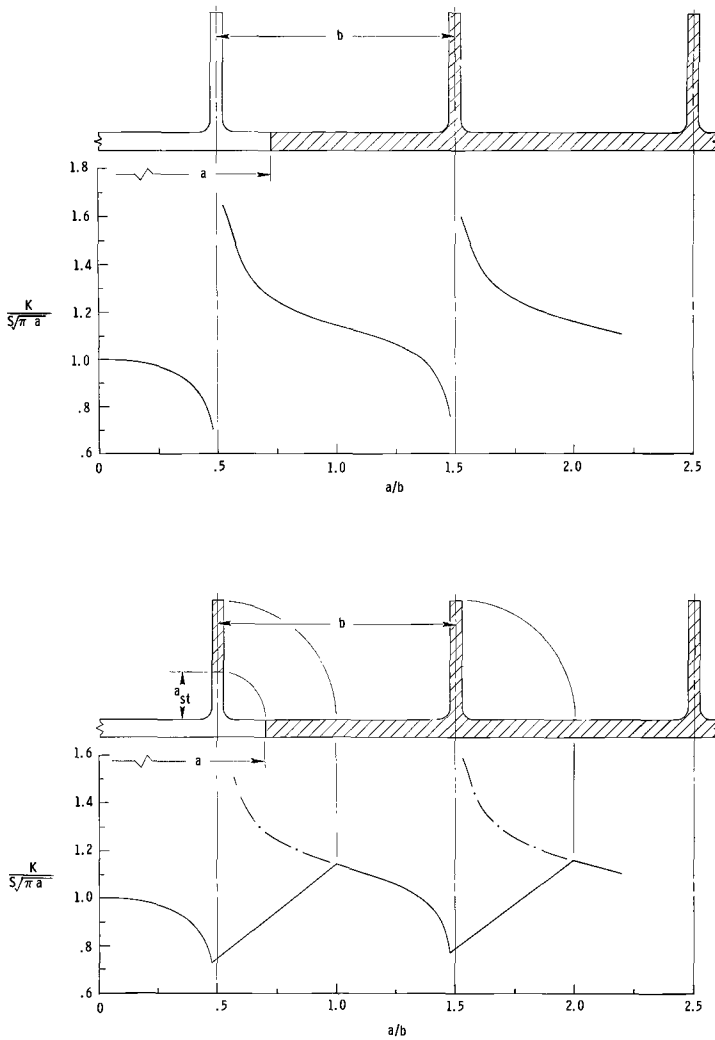
FIG. 9—*Relationship between stress intensity factor and crack length for panels with integral stringers: top, completely severed stringers; bottom, partially severed stringers.*

[2] Poe, C. C., Jr., "The Effect of Riveted and Uniformly Spaced Stringers on the Stress Intensity Factor of a Cracked Sheet," M.S. thesis, Virginia Polytechnic Institute, 1969.

[3] Leybold, H. A., "Residual Static Strength of Aluminum-Alloy Box Beams Containing Fatigue Cracks in the Tension Covers," NASA TN D-796, National Aeronautics and Space Administration, 1961.

[4] Neilson, K. L., *Methods in Numerical Analysis*, second ed., Macmillan Co., 1965, pp. 150–154.

[5] Forman, R. G., Kearny, V. E., and Engle, R. M., *Journal of Basic Engineering, ASME Transactions*, Series D, JBAEA, Vol. 89, No. 3, Sept. 1967, pp. 459–464.

[6] Hudson, C. M., "Effect of Stress Ratio on Fatigue-Crack Growth in 7075-T6 and 2024-T3 Aluminum Alloy Specimens," NASA TN D-5390, National Aeronautics and Space Administration, 1969.

A. F. Liu[1] *and J. C. Ekvall*[1]

Material Toughness and Residual Strength of Damage Tolerant Aircraft Structures

ABSTRACT: Fracture tests were conducted on precracked panels reinforced with various crack stoppers. Motion pictures and continuous graphical records of load and local strains were taken during the tests. The purpose of these tests was to study variables affecting residual strength of reinforced panels. Results show that, for 2024-T3 aluminum skin panels reinforced with riveted or bonded flat straps made of various alloys, the residual strength increases with the product of reinforcement area and reinforcement strength. Reinforcement stiffness, which is of primary importance for other classes of panel configurations, was found not to be a significant variable for the panel configurations tested. A crack opening displacement model is proposed to illustrate the influence of the reinforcements, the skin fracture toughness, and the slow stable tear characteristics on the arrest of a stably propagating crack. The model helps to elucidate the interactions between skin variables and reinforcement variables.

KEY WORDS: aircraft panels, reinforcement (structures), stiffening, fuselages, damage, fracture properties, toughness, residual stress, loads (forces), cyclic loads, strains, fatigue (materials), cracking (fracturing), crack propagation, mechanical properties, adhesive bonding, alloys, aluminum, fracture tests

Nomenclature

A Stiffener cross section area, in.^{2}
A_s Skin cross section area, in.^{2}
b Stiffener spacing, in.
C Correction factor to account for broken stiffener; function of λ and $2p/l$
C_1 Constant
D Rivet diameter, in.
E_s Skin elastic modulus, 10^3 ksi
E_r Stiffener elastic modulus, 10^3 ksi
F_g Applied stress level or fracture stress, ksi
F_{ty} Stiffener material tensile yield strength, ksi

[1] Senior structures engineer and senior design specialist, respectively, Advanced Design and Laboratories, Science and Engineering Branch, Lockheed-California Co., Burbank, Calif. 91503.

F_{tu} Stiffener material tensile ultimate strength, ksi

G Crack extension force ($= K^2/E$ for plane stress), in.·lb/in.^{2}

G_c Fracture toughness ($= K_c^2/E$ for plane stress), in.·lb/in.^{2}

K Stress intensity factor, ksi$\sqrt{\text{in.}}$

K' Stress intensity factor for a reinforced panel, ksi$\sqrt{\text{in.}}$

K_c Critical stress intensity factor for an unreinforced center cracked panel with $l = l_c$, ksi$\sqrt{\text{in.}}$

K_0 Critical stress intensity factor for an unreinforced center cracked panel with $l = l_0$, ksi$\sqrt{\text{in.}}$

k_r Reduction of stress intensity due to the stiffener, ksi$\sqrt{\text{in.}}$

l Crack length, in.

l_1 l plus a plastic region at each end of the crack, in.

l_0 Initial crack length, in.

l_c Critical crack length, in.

M_r Rivet material

n Number of intact stiffeners

N Fatigue cycles

p Rivet spacing, in.

P' Fracture load, 10^3 lb

P_0 Calculated fracture stress times the area of skin and unbroken stiffeners, 10^3 lb

t Thickness of strap or stringer, in.

t_s Thickness of skin, in.

w Width of strap, in.

W Panel width, in.

W' Distance between two intact stiffeners, in.

δ Crack opening displacement ($= G/F_{ty}$), in.

δ_c Critical crack opening displacement ($= G_c/F_{ty}$), in.

λ Stiffening index ($= ltE_s/AE_r$)

The current trend in the areas of design and evaluation of fail-safe aircraft structures is to extend the crack tip stress intensity factor concept to include fail-safe criteria. Crack propagation rate and fracture are controlled by the stress intensity at the crack tip. Fail-safe, or "damage tolerant," design can be achieved by making use of an effective barrier to retard fast propagation of a crack under normal operating conditions (stress levels); reinforcements also increase the residual strength of the cracked structure. These barriers or reinforcements redistribute the stress field in the vicinity of the crack tip; in other words, they provide a region of low stress intensity in the path of the advancing crack front. Research efforts are required to develop analysis methods for designing fail-safe structures having various structural geometries under various loading conditions. Adequate prediction of fracture

strengths for the skin stiffener-type structure relies on a thorough under-standing of

The mechanics of crack growth under monotonically increasing load
The basic residual strength properties of the skin material
Factors which govern the effectiveness of the reinforcements

Fatigue crack propagation and residual strength tests, to determine the role of reinforcement on the mechanics of crack arrest and residual strength of reinforced flat panels, were conducted on flat sheet panels having various combinations of skin materials and stiffeners. The stiffeners were either aluminum stringers or flat straps made of various alloys fastened to the panel by riveting or adhesive bonding.

Basic Considerations

In the development of fracture mechanics, it has been assumed that the residual strength for a structural component is controlled by K, the stress intensity factor at the crack tip. According to this assumption, the structural member will fail when K reaches some critical value K_c. It also has been shown that K and K_c are proportional to the square root of the crack extension force G and the material fracture toughness G_c, respectively [1].[2] Furthermore, K is a function of geometry, crack size, and loading conditions but G_c (K_c) is a material constant. For a flat panel, containing a through the thickness crack, subjected to monotonic loading normal to the crack at infinity,

$$K = F_g \left[\frac{\pi l}{2} \sec \left(\frac{\pi l}{2W} \right) \right]^{1/2} \qquad \dots \dots \dots \dots \dots \dots \dots (1)$$

where

W = the panel width,
F_g = applied stress, and
l = crack length [2].

For example, consider the case of reinforcements attached to a plate as shown in Fig. 1. If the panel is subjected to uniform extension stress F_g, the stress intensity for the skin crack will be reduced by the presence of a stiffener. A portion of the load acting on the skin is transmitted through the fastener and will be carried by the stiffener. Consequently, the general stress intensity factor K for this case will consist of two terms, the term involved with the overall stress acting on the skin, K' (based on uniform stress and crack length only), for the reinforced panel and the term involved with the transmitted load in the reinforcement, k_r, when K reaches K_c,

$$K_c = K' - k_r \dots \dots \dots \dots \dots \dots \dots \dots \dots \dots \dots (2)$$

where the minus sign for the k_r term refers to the reduced crack tip stress

---

[2] Italic numbers in brackets refer to the list of references at the end of this paper.
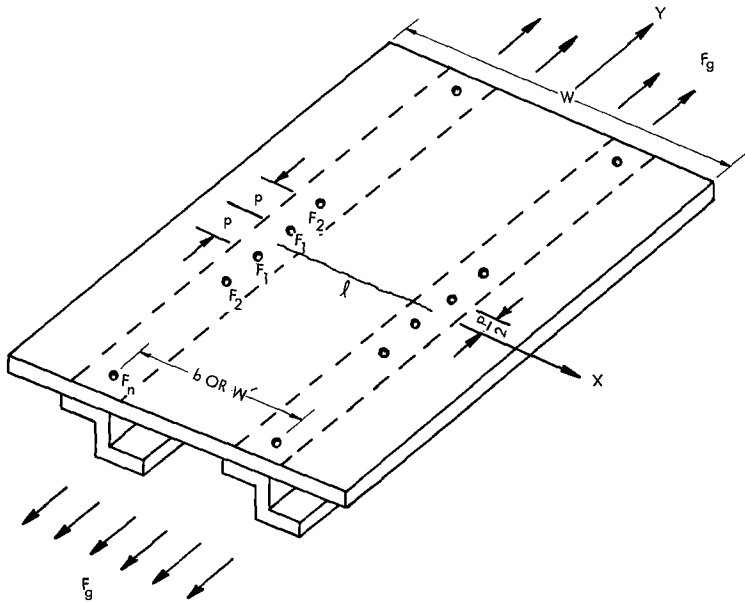
FIG. 1—*Through the thickness cracks in skin stiffened panel.*

intensity due to the effect of the stiffener. In other words, the term k_r quantitatively reflects the efficiency of the reinforcement and may be a function of stiffener material, fastener material, sizing, and spacing.

The Characteristics of Slow, Stable Crack Extension

Consider an unreinforced, center cracked panel. The stress intensity K at the crack tip increases linearly with the value of the normal tensile stress component acting on the panel. As the K level increases, some point will be reached at which the crack will start to increase in length (point A in Fig. 2). As illustrated in Fig. 2a, a crack in a material with high fracture toughness will extend gradually as the load continues to increase, until reaching the critical size at which rapid fracture occurs. However, for a material with low fracture toughness or for cases in which the environment, thickness, and other characteristics of the material are such that it is brittle, the start of slow crack growth will be followed immediately by the onset of rapid fracture (Fig. 2b). Final failure curves (a locus of B points) are shown in Figs. 2a and 2b.

The crack growth behavior for a reinforced panel is extrapolated as the dotted line in Fig. 2a. Notice that the effect of the reinforcement on the residual strength is to increase the critical failure curve for the stiffened panel over the sheet alone. For cases typified by Fig. 2b, or if the crack tip is remote from the reinforcements, the stiffening is not likely to increase the critical load.

Fracture is defined generally to occur at point B in Fig. 2a. Data on aluminum alloys and steels [3, 4] indicate that the critical crack length is approxi-
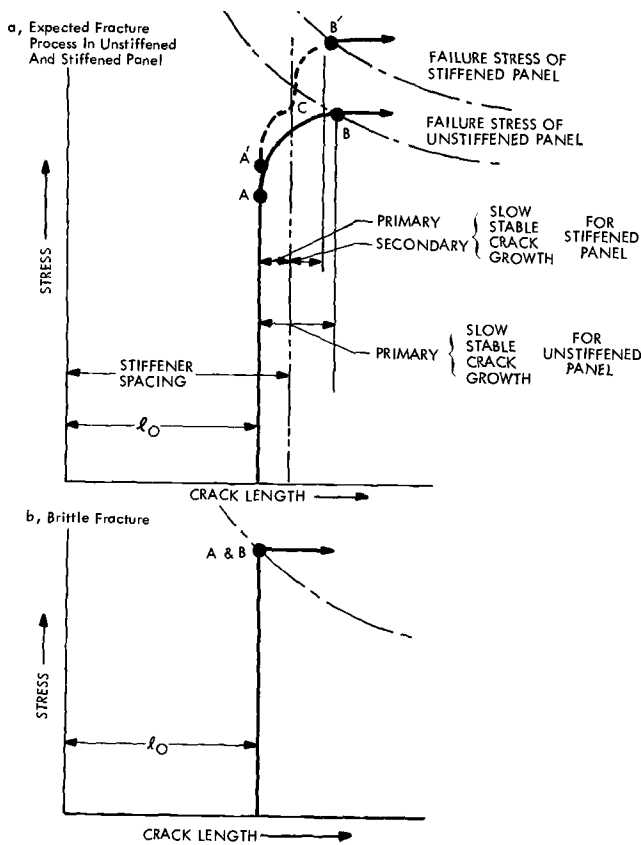
FIG. 2—*Slow crack growth characteristics in a tear test of a cracked panel.*

mately proportional to the initial crack length: $l_c = (1 + C_1) l_0$ where $C_1 \geq 0$ is determined experimentally for the appropriate alloy and thickness. Broek [5] has shown analytically that residual strength for an unstiffened panel can be related directly to either initial or final crack length and maximum load. The amount of slow, stable crack extension, $C_1 l_0$, now can be treated as a material property and will be termed "primary slow crack growth." For the reinforcement to be effective in a stiffened panel, a crack with a length less than W' must grow toward the stiffener by the primary slow crack growth mechanism. If this is the case, the crack which starts growing at A' will be halted at point C in Fig. 2, then extend again and fracture at point B'. The mechanism for this part of crack growth, from C to B', differs from the primary slow crack growth mechanism and is termed the "secondary slow crack growth." Detailed discussions of these mechanisms are given in subsequent sections.

The Concept of Crack Opening Displacement

Tensile stress applied normal to a crack causes the crack to open and produces yielding at the crack tips. It is hypothesized that crack opening measured at some point in the vicinity of the crack tip will reach a critical value when fracture occurs.

For conditions of small scale plastic yielding, the strain energy release rate or crack extension force $G = K^2/E_s$, is equivalent to the product of the crack opening displacement (COD) and the tensile yield strength for the material [6, 7]. Therefore, it is suggested that the critical COD be used as a measure of the fracture toughness of a given material. Figure 3a shows the model used for the COD analysis, which is based on a crack of length *l* in an unreinforced infinite plate. A system of coordinates with its origin at the center of the crack is used with the *x* axis extending along the line of the crack. Under a uniform stress F_g, applied in the *y* direction at infinity, plastic zones are produced at the tip of the crack extending to $x = \pm l_1/2$, resulting in an opening δ at the tip of a real crack.

For a crack reinforced by a stiffener (Fig. 3b), the plastic zone at the crack tip will be suppressed; in other words, the crack opening displacement δ will be smaller compared to an unreinforced crack of the same crack length under the same applied stress level (corresponding to $A'C$ in Fig. 2a). However, the crack in the reinforced panel may continue to grow, and final fracture will occur when δ reaches the critical size δ_c equivalent to that for an unstiffened panel (Fig. 3c, corresponding to $A'CB'$ in Fig. 2a).
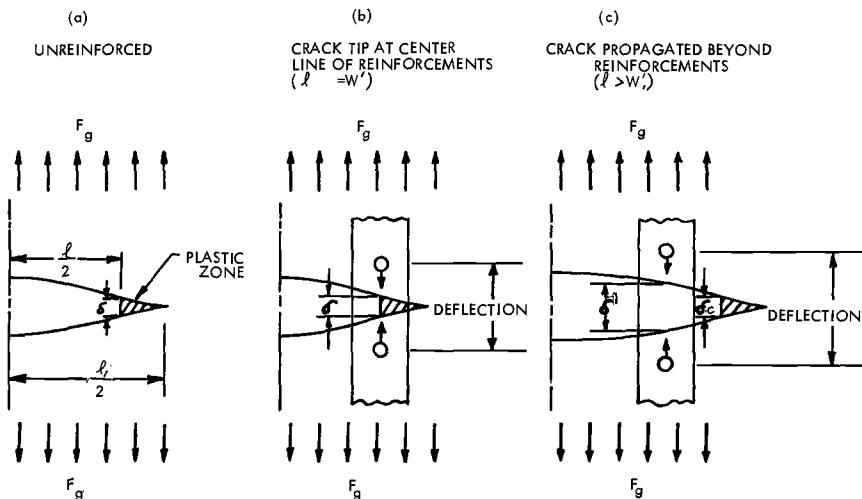
FIG. 3—*Crack opening displacement models for residual strength tests of unreinforced and reinforced panels.*

Definition of Dependent Variable

The aim of any project of applied research and development is to generate meaningful data and to obtain an understanding of the problems involved so that preliminary assumptions can be justified and a workable design procedure developed. Often in order to develop a design procedure, theories are pushed to the very limit of their applicability. In the area of applied fracture mechanics, this is apparently the case for 2024-T3 aluminum thin sheets, which currently are being used in aircraft as fuselage skins. For this material, fracture toughnesses derived from Eq 1 are considerably dependent upon specimen geometry and, in addition, deviate from values predicted by the theory of linear elasticity. Disputes concerning specimen configurations, critical crack length determination, and usage of plastic zone correction factors have continued over a decade. This necessitates some arbitrariness in initial assumptions when dealing with complex structures such as reinforced panels. As will be discussed in subsequent sections, crack opening displacement, crack tip plasticity, and the so-called secondary slow crack extensions are often suppressed by the stiffener, especially when high strength reinforcement materials are used. Therefore, for a reinforced panel, a realistic, practical approach is to assume that the crack length equals the distance between two intact stiffeners. Thus W' should be used as the crack length for calculating K' in Eq 2. In addition, it is difficult to choose as a test variable a particular critical, final crack length in a material with a great deal of slow, stable tear, such as 2024-T3. K_c in Eq 2 will, therefore, be replaced by K_0, the critical stress intensity factor based on l_0, the initial crack length. If the final crack length is simply a constant times the initial crack length, as reported in Refs 3, 4, and 5, this will change the measure of the reinforcement efficiency k_r by a simple, consistent, constant factor.

Equation 2 can be rewritten as

$$k_r = K' - K_0 \dots\dots\dots\dots\dots\dots\dots\dots (3)$$

For a reinforced panel with $l = W'$, consider the load

$$P_0 = K_0 \left\{ A_s + nA\left(\frac{E_r}{E_s}\right) \middle/ \sqrt{\frac{\pi W'}{2} \sec\left(\frac{\pi W'}{2W}\right)} \right\} \dots\dots\dots\dots (4)$$

P_0 is equivalent to the minimum load required to fracture a reinforced panel, where the reinforcements contribute to the load carrying capacity through the additive area only. The machine load P', at fracture of the reinforced panel, is used for calculating K'. Therefore, the difference between the reported fracture load, P', and P_0 is equivalent to the additional load carried by the reinforcements.

Tests

Phase I—Test Panels Having Riveted Flat Straps or Stringers

Residual strength tests were conducted on reinforced panels 48 in. wide and 83 in. long (between grips). The reinforcements were either flat straps of various alloys or aluminum stringers of various configurations, riveted to thin sheets of 2024-T3 aluminum. The strap materials were selected to provide controlled variations in reinforcement modulus at constant strength and in reinforcement strength at constant modulus. The strap materials were 2024-T3 aluminum, 7075-T6 aluminum, AISI 430 steel, 301 full-hard (FH) stainless steel, and 6A1-4V duplex annealed titanium. The strength and modulus values for these materials are listed in Table 1. In addition, two panels of 7178-T6 aluminum reinforced with 7178-T6 aluminum flat straps were included to provide a variation in values of skin fracture toughness. Base line K_0 values were obtained by testing unreinforced panels of the same size (48 in. wide). Tension coupon tests also were conducted to obtain engineering stress-strain curves for all skin and stiffener materials.

The majority of the panels tested were reinforced with seven stiffeners having one stiffener located at the center line of the panel. The remaining stiffeners were placed symmetrically on either side of the center line stiffener. The stiffener spacing was either 6 in. or 7½ in. One panel had nine aluminum stringers with a stringer spacing of 5 in. The panel configurations are shown in Fig. 4a and are listed in Table 1.

Both the center line stiffener and the skin were cut at the panel midlength between two rivets. The end of the saw cut was approximately 1 in. from the inner edge of the adjacent stiffener. The panels were then subjected to tension-tension fatigue cycling at a stress level low in comparison with the yield strength for critical F_g values for the skin. The crack tips were extended approximately to the strap edges, that is, the crack length was approximately equal to (but slightly less than) two stiffener spacings. Strain gages were put on the straps in front of the crack tip (between two rivets, three gages on each strap). In the cases where stringer-type stiffeners were used, strain gages were installed on both the top and the bottom flanges. During static fracture testing, closeup motion pictures (film speed, 128 frames per second) were taken to show the slow crack growth behavior of the panel. Strain gage and load data were recorded on an FM tape unit using 1-in. magnetic tape and a recording speed of 30 in./s. At the completion of the test, the tape was processed by playback to a recorder which produced a continuous time plot for each data channel. The instrumentation used permitted cross-correlation of the data and film strip with reference to either a time basis or to any significant event that occurred during the test run.

TABLE 1—*Test panel configurations.*

| GROUP NO.	PANEL NO.	STIFFENER	b INCH	E_r 10³ KSI	A INCH²	F_{ty} KSI	F_{tu} KSI	p INCH	M_r	D INCH	SKIN	REMARKS
1	X2	NONE (CONTROL SPECIMEN)									.063 X 48 BARE 2024-T3(L)	
	101A	.063 X .85 BARE 2024-T3 STRAP	6.0 INCH	10.5	.0535	49.7	70.5	1.0	2117-T3	5/32	.063 X 48 BARE 2024-T3(L)	7 STRAPS (CENTER ONE BROKEN)
	101B	.063 X .85 BARE 2024-T3 STRAP	6.0 INCH	10.5	.0535	49.7	70.5	1.0	2117-T3	5/32	.063 X 48 BARE 2024-T3(L)	7 STRAPS (CENTER ONE BROKEN)
	103A	.063 X .85 AISI 630 STEEL ANNEALED STRAP	6.0 INCH	27.0	.0535	46.7	67.5	1.0	2117-T3	5/32	.063 X 48 BARE 2024-T3(L)	7 STRAPS (CENTER ONE BROKEN)
	103B	.063 X .85 AISI 630 STEEL ANNEALED STRAP	6.0 INCH	27.0	.0535	46.7	67.5	1.0	2117-T3	5/32	.063 X 48 BARE 2024-T3(L)	7 STRAPS (CENTER ONE BROKEN)
	105A	.063 C .85 STAINLESS STEEL (301 FH) STRAP	6.0 INCH	26.0	.0535	165.0	190.0	1.0	2117-T3	5/32	.063 X 48 BARE 2024-T3(L)	7 STRAPS (CENTER ONE BROKEN)
	107A	.063 X .85 Ti-6A1-4V DUPLEX ANNEALED STRAP	6.0 INCH	17.0	.0535	147.0	153.0	1.0	2117-T3	5/32	.063 X 48 BARE 2024-T3(L)	7 STRAPS (CENTER ONE BROKEN)
2	115A	.063 X .875 2024-T3 STRAP + 2024-T3 STRINGER	7.5 INCH	10.5	.19	50.9 STG 49.7 STRAP	73.4 STG 70.5 STRAP	1.0	2117-T3	5/32	.063 X 48 BARE 2024-T3(L)	7 STIFFENERS (CENTER ONE BROKEN)
	117A	BARE 2024-T3 STRINGER	5.0 INCH	10.5	.066	48.6	71.1	1.0	2117-T3	5/32	.063 X 48 BARE 2024-T3(L)	9 STRINGERS (CENTER ONE BROKEN)
	111A	BARE 2024-T3 STRINGER	6.0 INCH	10.5	.135	50.9	73.4	1.0	2117-T3	5/32	.063 X 48 BARE 2024-T3(L)	7 STRINGERS (CENTER ONE BROKEN)
3	101	NONE (CONTROL SPECIMEN)									.0756 X 48 CLAD 2024-T3(L)	
	103	.08 X 1.25 CLAD 7075-T6 STRAP	7.5 INCH	10.3	.10	69.3	76.5	1.0	2024-T3	3/16	.0756 X 48 CLAD 2024-T3(L)	7 STRAPS (CENTER ONE BROKEN)
	105	.125 X .8 CLAD 7075-T6 STRAP	7.5 INCH	10.3	.10	72.9	78.4	1.0	2117-T3	3/16	.0756 X 48 CLAD 2024-T3(L)	7 STRAPS (CENTER ONE BROKEN)
	107	.10 X 1.0 CLAD 7075-T6 STRAP	7.5 INCH	10.3	.10	69.7	75.1	1.0	MONEL	3/16	.0756 X 48 CLAD 2024-T3(L)	7 STRAPS (CENTER ONE BROKEN)
	109	.08 X 1.25 CLAD 7075-T6 STRAP	7.5 INCH	10.3	.10	69.3	76.5	1.5	MONEL	3/16	.0756 X 48 CLAD 2024-T3(L)	7 STRAPS (CENTER ONE BROKEN)
	115	.08 X 1.25 CLAD 7075-T6 STRAP	7.5 INCH	10.3	.10	69.3	76.5	.75	2117-T3	3/16	.0756 X 48 CLAD 2024-T3(L)	7 STRAPS (CENTER ONE BROKEN)
4	52-101	.0203 X 4.57 7075-T6 STRAP	20 INCH	10.3	.0928	64.1	73.3		BONDED		.071 X 42 CLAD 2024-T3(T)	2 STRAPS, STRAIGHT EDGE; 3 FRAMES (CENTER ONE BROKEN)
	52-125	.0203 X 4.57 7075-T6 STRAP	20 INCH	10.3	.0928	64.1	73.3		BONDED		.071 X 42 CLAD 2024-T3(T)	2 STRAPS, STRAIGHT EDGE
	52-133	.0211 X 4.57 Ti-6A1-4V STRAP	20 INCH	16.0	.0964	132.8	140.0		BONDED		.071 X 42 CLAD 2024-T3(T)	2 STRAPS, STRAIGHT EDGE
5	52-155	.0164 X 3.75 Ti-6A1-4V STRAP	20 INCH	16.0	.0615	141.1	149.2		BONDED		.071 X 42 CLAD 2024-T3(T)	2 STRAPS, SCALLOPED EDGE
	52-167	.0233 X 3.75 Ti-6A1-4V STRAP	20 INCH	16.0	.0874	138.8	144.6		BONDED		.071 X 42 CLAD 2024-T3(T)	2 STRAPS, SCALLOPED EDGE
	52-149	.012 X 3.75 Ti-6A1-6V-25n STRAP	20 INCH	15.0	.045	154.4	166.4		BONDED		.071 X 42 CLAD 2024-T3(T)	2 STRAPS, SCALLOPED EDGE
	52-161	.0192 X 3.75 Ti-8A1-1Mo-1V STRAP	20 INCH	17.5	.072	140.3	149.2		BONDED		.071 X 42 CLAD 2024-T3(T)	2 STRAPS, SCALLOPED EDGE
	52-143	.0151 X 3.75 Ti-13V-11Cr-3A1 STRAP	20 INCH	15.5	.0566	128.2	132.0		BONDED		.071 X 42 CLAD 2024-T3(T)	2 STRAPS, SCALLOPED EDGE
6	109A	.043 X .85 STRAP 7178-T6 BARE	6.0 INCH	10.3	.0535	85.7	92.2	1.0	2117-T3	5/32	.063 X 48 BARE 7178-T6(L)	7 STRAPS (CENTER ONE BROKEN)
	109B	.063 X .85 STRAP 7178-T6 BARE	6.0 INCH	10.3	.0535	85.7	92.2	1.0	2117-T3	5/32	.063 X 48 BARE 7178-T6(L)	7 STRAPS (CENTER ONE BROKEN)
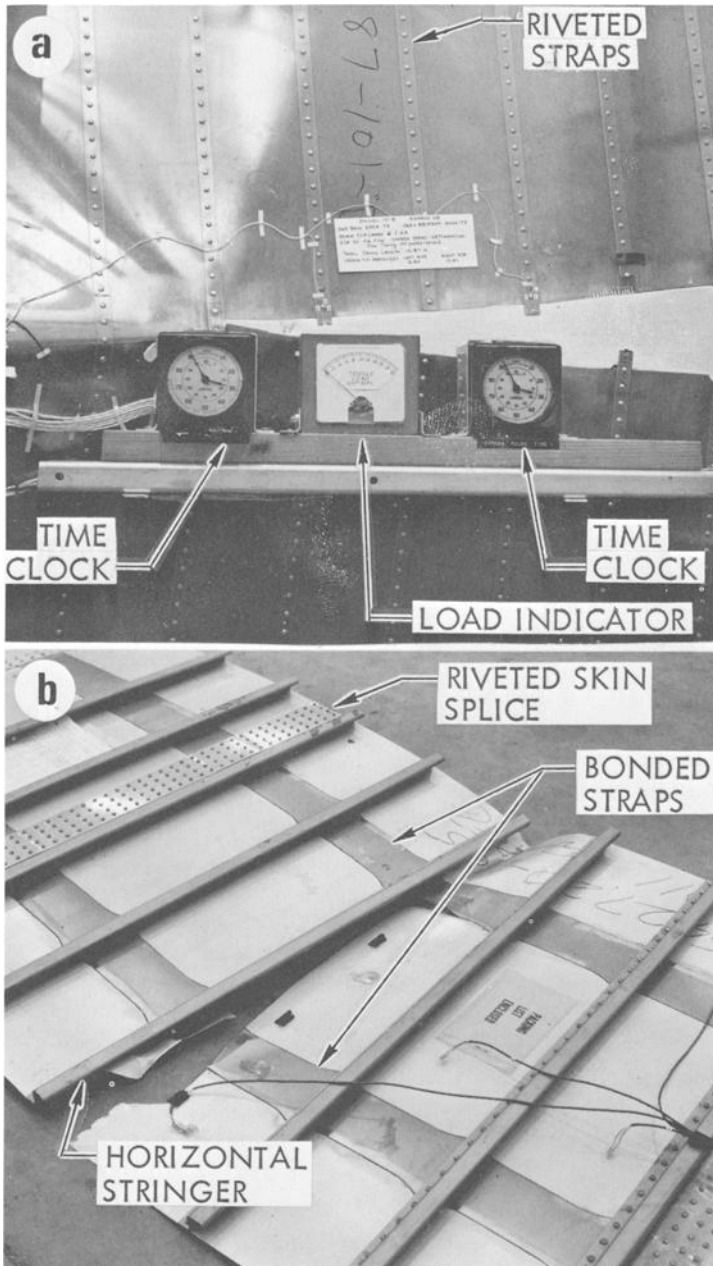
FIG. 4—*Photographs of typical failed fail-safe panels reinforced with* (a) *riveted flat straps and* (b) *adhesive bonded flat straps. Note that the edges of the bonded straps were either scalloped* (*as shown*) *or unscalloped* (*not shown*).

Phase II—Test Panels Having Adhesive Bonded Flat Straps

These panels were 40 by 120 in. (including grips), having two adhesively bonded straps (lengthwise) and several riveted stringers (widthwise). The strap spacing was 20 in. (each 10 in. from the panel center line). The stringer spacing was 8.55 in. (simulating an actual airplane configuration). The skin was 2024-T3 aluminum and the straps were either 7075-T6 aluminum or various kinds of titanium alloys (Table 1). The stringers were 7075-T6 aluminum. A 4-in. saw cut was made in the center of each panel adjacent to a stringer near the panel midlength (Fig. 4b). The crack was allowed to grow by applying constant amplitude repeated loading. The maximum cyclic stress level was 13.2 ksi on the skin, determined by strain gage measurement prior to making the saw cut. The minimum to maximum stress ratio was 0.05. The data recorded during the test included the testing conditions as well as the crack length as a function of the number of loading cycles. The constant amplitude cyclic loading was applied until the skin crack reached the center line of the straps (20-in. crack length). The cracked panels were then loaded in tension to failure. Neither film nor instrumentation records were taken during these tests.

Results and Discussion

Mechanics of Secondary Slow Crack Growth (2024-T3 Aluminum Skin Panels Only)

Load (stress) versus crack length plots for panels reinforced by riveted flat straps were determined by superimposing the load versus time curves reduced from FM tape records onto the crack length versus time curves reduced from the film. Critical crack lengths were determined from these plots in accordance with the slow, stable tear model illustrated in Fig. 2. The photographs in Fig. 5 show the crack lengths corresponding to point B' in Fig. 2a for panels having flat straps of various materials. In all these tests the skins were 2024-T3 aluminum and the initial crack tips were approximately $\frac{1}{4}$ in. from the edge of the straps. Although considerable buckling in the panels is shown in the photographs, it is evident that such buckling, especially in the area near the crack tip, was suppressed by the reinforcements.

Motion pictures show that the skin crack first grew by the primary slow crack growth mechanism up to the rivet line. The amount of secondary slow crack growth (the increment of crack growth under increasing load from the rivet center line to the critical length) is dependent upon the mechanical properties of the strap material used. Figures 5a and 5b show that panels reinforced with 2024-T3 aluminum or AISI 430 steel (F_{ty} = 50 ksi, E_r = 10,500 ksi and F_{ty} = 47 ksi, E_r = 27,000 ksi, respectively) exhibit more slow crack growth than the panels reinforced with duplex annealed Ti-6Al-4V (F_{ty} = 145 ksi, E_r = 17,000 ksi, Fig. 5c) or 301 FH stainless steel (F_{ty} = 165 ksi, E_r = 26,000 ksi, Fig. 5d). The fact that panels having 7075-T6 aluminum

(a) 2024-T3 STRAP
     (PANEL #101B, b = 6")

(b) AISI 430 STEEL STRAP
     (PANEL #103A, b = 6")

(c) TI, 6A1-4V, D.A. STRAP
     (PANEL #107A, b = 6")

(d) 301 FH STAINLESS STEEL STRAP
     (PANEL #105A, b = 6")

(e) 7075-T6 STRAP
     (PANEL #105, b = 7.5")
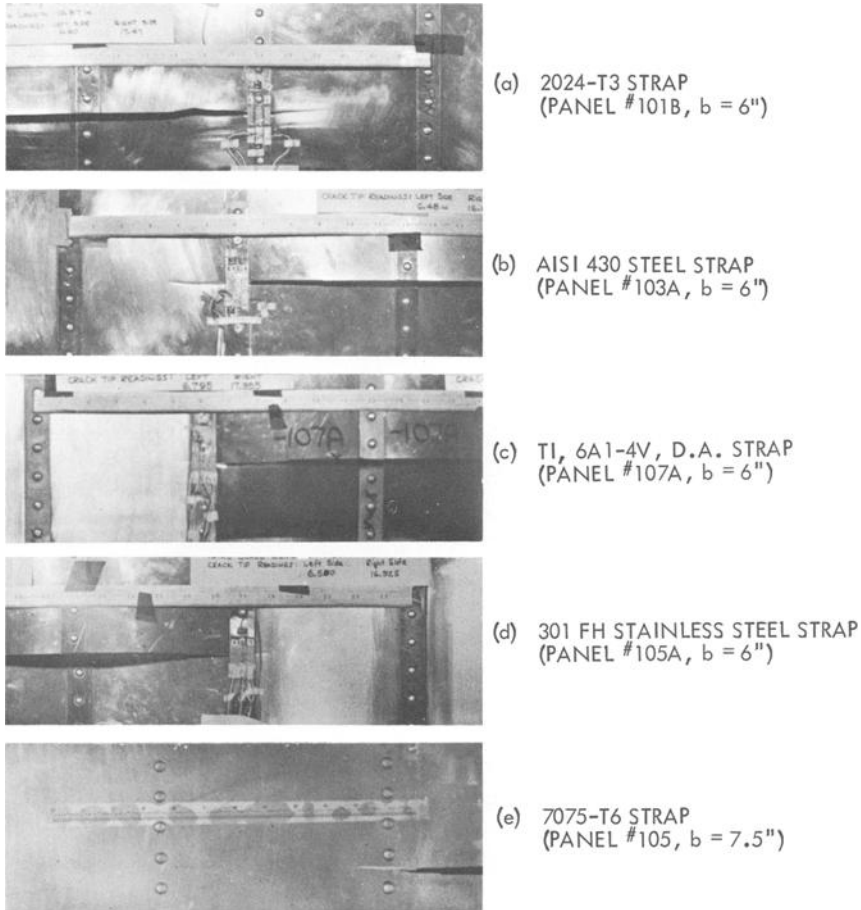
FIG. 5—*Effect of different stiffeners on the secondary slow crack growth behavior of 2024-T3 aluminum flat panels reinforced with riveted flat straps.*

straps (F_{ty} = 71 ksi, E_r = 10,300 ksi, Fig. 5e) also exhibited a negligible amount of secondary slow crack growth indicated that the slow crack growth behavior for the reinforced panels was not determined solely by the strength of the reinforcement.

According to the crack opening displacement (COD) model of Figs. 3b and 3c, the crack will start to grow at a COD below the critical value by the primary slow, stable tear mechanism. Either the reinforcement will stop the crack near the rivet line and deform, picking up load from the skin and allowing further opening of the crack surfaces until the critical COD has been reached, or it will permit the crack to grow beyond the reinforcement. When the skin reaches its critical COD, the stiffener will have stretched more in the second case than in the first case.
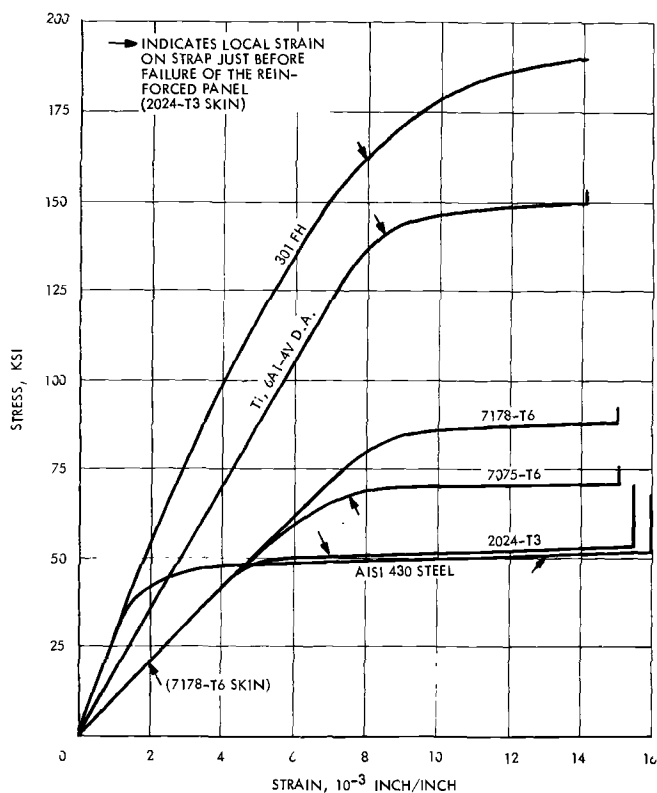
FIG. 6—*Tensile properties of flat strap materials.*

Figure 6 shows the stress-strain curves obtained from tension coupons made from stock of strap material. This figure also shows the local strains on straps just prior to fracture of the panel as determined by strain gage measurements. Such local strains on the strap were approximately equal to or slightly below the yield point for 301 FH stainless steel, duplex annealed Ti-6Al-4V, and 7075-T6 aluminum. In these panels, crack opening was constrained at the rivet line under increasing load until the straps were loaded almost to their yield strength. Then, as soon as the crack started to propagate again, the skin crack simultaneously reached the critical COD without a significant amount of secondary slow crack growth and final failure ensued. These cases could be described in Fig. 2a by making CB' approximately a vertical line.

On the other hand, the AISI 430 steel and 2024-T3 aluminum straps yielded earlier, and the local strap strains just prior to failure were above the yield points (as indicated by Fig. 6). This early yielding occurred before the skin crack had reached its critical COD, and thus large amounts of secondary slow crack growth were permitted in the manner described in Fig. 3c. Note that the local strain on the AISI 430 steel straps was large compared to the

other cases. Observing Fig. 6, the strain corresponding to the 0.2 percent offset yield stress is approximately 0.0035 in./in. For the other straps, the corresponding yield strain is about 0.007 in./in. or greater. Therefore, in the AISI 430 steel strap test, the strap yields much earlier and large, nonlinear deformation of this strap is expected. In general it appears that the sooner the strap yields the greater the tendency for secondary slow crack growth in the skin material to occur.

The Effect of Independent Variables on Residual Strength

2024-T3 Aluminum Skin Panels—First consider the groups of test panels manufactured with straps of the same size and spacing but different material. Note that there was a broken stiffener at the center of all of the panels. The broken stiffener reduces the residual strength of the panel. In other words, if the broken stiffener were not there, P' would have been higher than the value indicated by the test. A correction factor C, from Sanders et al [8, 9], can be adopted to account for the effect of the broken stiffener. C is defined to be a crack tip stress intensity ratio. The numerator is the stress intensity when the broken stiffener is present; the denominator is the stress intensity without a stiffener. Thus the reinforcement efficiency parameter $(P' - P_0)$ is generalized to be $CP' - P_0$, where $C = 1$ if the broken stiffener is absent.

An approximately linear relationship was obtained when the reinforcement efficiency parameter $(CP' - P_0)$ was plotted against the tensile strength for the strap (see Fig. 7). With the effect of modulus considered at infinity (by definition of P_0) and locally (by definition of C), as it relates to the broken strap, the modulus becomes a secondary variable. As shown in Tables 1 and 2 and Figs. 6 and 7, the panels with 2024-T3 aluminum straps or AISI 430 steel straps have similar reinforcement efficiencies. The tensile yield strength and ultimate tensile strength for the aluminum and steel were approximately the same in spite of the fact that the elastic modulus of steel is nearly three times the elastic modulus of aluminum. Likewise, the reinforcement efficiency for panels having stainless steel or titanium straps were similar despite a factor of 1.6 difference in strap elastic modulus. The tensile yield strengths of these strap materials also were similar. Perhaps the most significant observation is that the tensile yield strength and the reinforcement efficiency for 301 FH stainless steel were three times as great as those for AISI 430 steel, although their elastic moduli were almost equal.

A comparison of data for 2024-T3 and AISI 430 straps does show a mild effect of modulus not accounted for by the broken strap correction of Sanders et al. The data indicate that the modulus was more damaging in this multi-strap configuration than in the single-strap configuration analyzed in Refs 8 and 9. As an approximation, however, this effect can be neglected.

The function of the reinforcements of a reinforced cracked panel is to take up as much load as possible from the skin while permitting a minimum of deflection. Higher deflections lead to higher crack opening displacement and

TABLE 2—*Test results.*

GROUP NO.	PANEL NO.	A●F_ty (10³ LBS)	P_o (10³ LBS)	P' (10³ LBS)	C P'-P_o (10³ LBS)	REINFORCEMENT GROSS AREA STRESS ~ KSI LEFT	RIGHT	l_o (INCH)	C	λ
1	X2	-	-	89.0	-	-	-	9.61		
1	101A	2.51	87.2	104.0	18.8	50.5	49.0	10.60	1.02	14.1
1	101B	2.51	87.2	99.2	13.8	50.5	49.0	10.87	1.02	14.1
1	103A	2.50	100.0	101.0	10.0	53.0	48.7	10.20	1.09	5.5
1	103B	2.50	100.0	100.0	9.0	52.0	51.0	10.59	1.09	5.5
1	105A	8.83	99.4	127.25	39.5	161.0	161.0	10.38	1.09	5.7
1	107A	7.76	91.6	123.0	37.5	139.0	139.0	10.56	1.05	8.7
2	115A	9.70	102.7	138.5	49.7	54.0 [△2] 50.1 [△1]	54.0 [△2] 50.4 [△1]	12.71	1.10	4.98
2	117A	3.21	102.8	115.5	19.2	50.7 [△2] 47.8 [△1]	49.5 [△2] 46.5 [△1]	8.92	1.045	10.5
2	111A	6.87	100.0	124.0	35.0	54.0 [△2] 51.5 [△1]	52.0 [△2] 51.5 [△1]	10.42	1.09	5.6
3	101	-	-	79.0	-		-	13.26		
3	103	6.93	85.5	115.5	35.5		64.0	13.51	1.05	9.64
3	105	7.29	85.5	110.0	29.0		66.0	13.23	1.05	9.64
3	107	6.97	85.5	119.7	38.3		68.0	13.29	1.05	9.64
3	109	6.93	85.5	113.6	32.3		67.5	13.25	1.05	9.64
3	115	6.93	85.5	118.5	38.0		69.0	13.26	1.05	9.64
4	52-101	5.95	68.0 [△3]	67.1 [△4]	-			20.19		
4	52-125	5.95	52.3 [△3]	73.8	21.5			15.78 [△6]	1.0	
4	52-133	12.80	54.0 [△3]	97.0	43.0			19.60	1.0	
5	52-155	8.67	52.3 [△3]	76.7	24.4			19.99	1.0	
5	52-167	12.13	53.6 [△3]	82.3	28.7			20.01	1.0	
5	52-149	6.95	51.4 [△3]	71.9	20.5			19.58	1.0	
5	52-161	10.10	52.2 [△3]	55.9 [△4]	-			19.55	-	
5	52-143	7.26	51.1 [△3]	64.1 [△4]	-			19.35	-	
6	109A	4.58	-	30.0	-	20.0	20.0	10.45	-	
6	109B	4.58	-	45.4 [△5]	-			6.0 [△7]	-	

NOTES:
[△1] ON UPPER FLANGE
[△2] ON BOTTOM FLANGE
[△3] EXTRAPOLATED K_o = 108.3 KSI INCH
[△4] STRAP OR STRAPS CRACKED DURING FATIGUE CYCLING
[△5] PANEL FAILED DURING FATIGUE CYCLING
[△6] FATIGUE CYCLING STOPPED AS SOON AS CRACK INITIATED IN STRAP
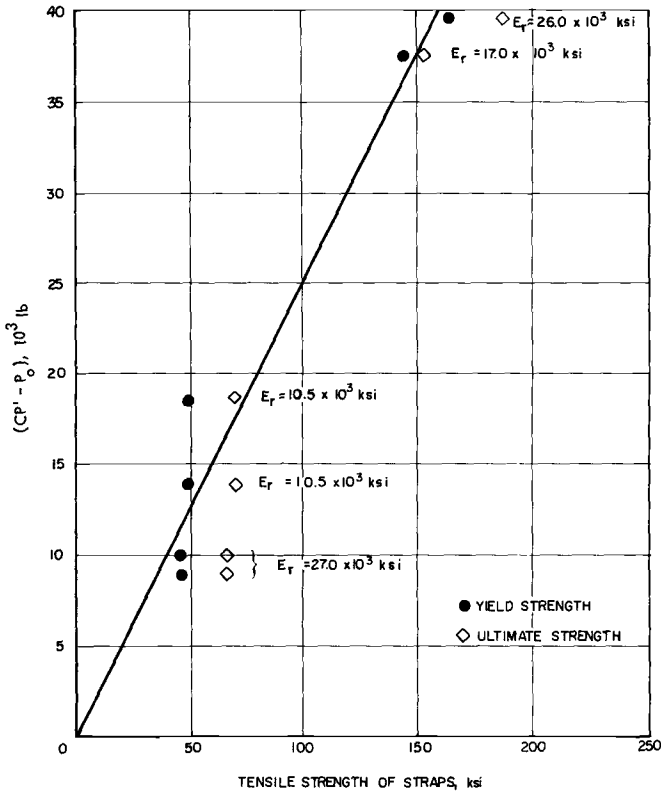[△7] INITIAL SAW CUT

FIG. 7—*Effect of reinforcement strength on load carrying capacity of straps.*

a greater tendency for the crack to propagate. Hence the important variable is the load-deflection relationship of the strap.

If the loads are low, as in the typical fatigue crack growth test, or the skin material has a low δ_c value (7178-T6 aluminum, 7075-T6 aluminum, or thick sections of 2024-T3 aluminum), the reinforcements will remain elastic throughout the test. The elastic variable relating load to deflection is then the elastic stiffness, as shown by analyses [8–10] and experiments [11]. If, however, the δ_c value for the skin is large (as in the cases studied), then rapid propagation of the skin crack will not take place until the strap strain is in the plastic range. That this is exactly what happened in the tests which were conducted is clear from Fig. 6. Once a strap has yielded, its elastic modulus has no effect on the load it carries; rather, the strap load in the plastic range can be approximated by the product of strap area and yield strength. (This is exact for zero strain hardening.) Therefore, this product is a plasticity variable relating load to deflection. The parameter $CP' - P_0$ was replotted in Fig. 8 versus a reinforcement parameter AF_{ty}, where A is the cross-sectional area of the reinforcement and F_{ty} is the 0.2 percent yield strength of the reinforcement.
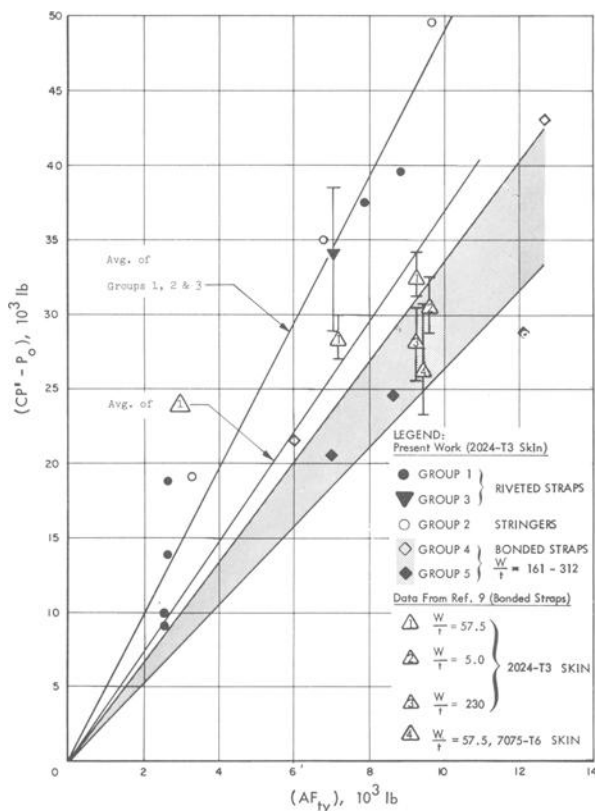
FIG. 8—*Effect of stiffener area and strength on load carrying capacity of stiffeners.*

The second group of test panels included three panels having different stringer sizes and spacings. The stiffeners were 2024-T3 aluminum and the skin material, as in group 1, was also 2024-T3 aluminum. CP' and calculated P_0 values are tabulated in Table 2. Note that strain gage measurements taken at the upper and lower flanges of the stringers in the panels of this group indicated that, prior to failure of the panel, the entire cross section of the stringer was loaded locally to the yield point. $CP' - P_0$ values for panels of group 2 were plotted versus AF_{ty}, and a straight line was drawn through the data points for both groups 1 and 2 as shown in Fig. 8.

The third group consisted of five reinforced panels and a control specimen (unreinforced). The panels had clad 2024-T3 aluminum skins and clad 7075-T6 aluminum straps ($W' = 2b = 15$ in.). The width and the thickness of the straps varied but the cross-sectional area of the straps was kept constant. The rivet material and the rivet spacing also were varied (see Table 1). $CP' - P_0$ values for these panels agree with the trend line previously constructed in Fig. 8. The variations in the residual strength for these panels

are attributable to the effects of rivet material, rivet spacing, and the cross-sectional geometry of the straps. An evaluation of these second-order effects is being conducted [*12*].

Some previously published Lockheed data [*4*] are tabulated in Table 3. The Ref *4* data show a generally lower reinforcement efficiency when compared to the present data (Fig. 9). Apparently this was because most of these tests had an initial crack length that was short compared to the stiffener spacing. In some cases maximum load was reached before the crack had propagated into the region influenced by the strap.

The fourth and the fifth groups are test panels having clad 2024-T3 aluminum skins and adhesive bonded flat straps. Again, good correlations were obtained for the calculated parameters (see Fig. 8). K_0 values extrapolated from these tests were used to eliminate effects, if any, attributed to the horizontal stringer. Data drawn from Ref *13* also are plotted in Fig. 8 for comparison. Details about the tests are listed in Table 3. It is shown that for test panels having strap width to strap thickness ratios either extremely low ($w/t = 5$) or extremely high ($w/t = 230$, the same as for the panels of groups
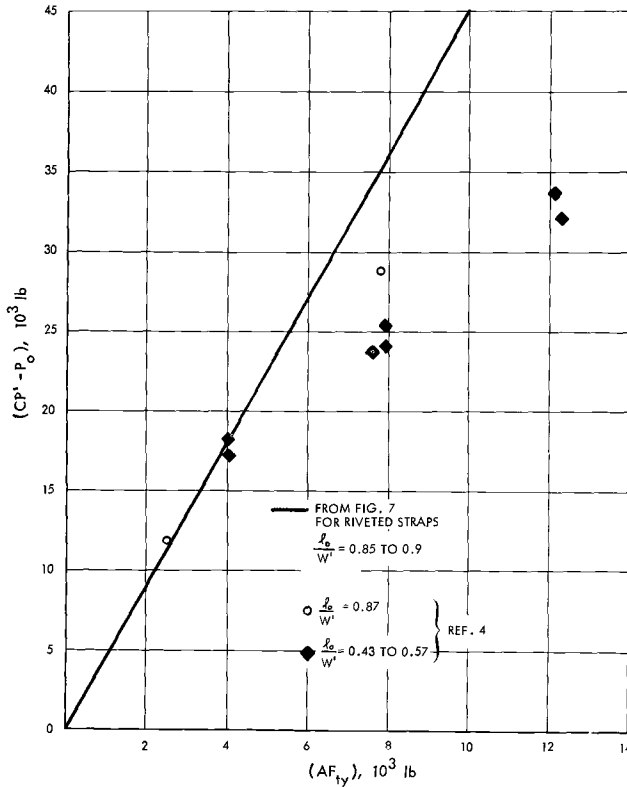

FIG. 9—*Relation between additional load carrying capacity of reinforced 2024-T3 aluminum panels and strap* AF_{ty} *for various* l_0/W' *ratios.*

TABLE 3—*Data from the literature.*

DATA SOURCE	SKIN	w × t	STRAP	w¹ INCH	ℓ_o INCH	P¹ (10³ LBS)	CP¹ - P₀ (10³ LBS)	PANEL NO.	REMARKS
REF 4	.04 X 35 CLAD 2024-T3 (L)	1.18 X .033	CLAD 7075-T6 △2	6	5.11	64.3	11.8 △6	7	△1 △3
REF 4	.04 X 35 CLAD 2024-T3 (L)	1.19 X .100	CLAD 7075-T6 △2	6	5.20	93.5	28.8 △6	8	△1 △3
REF 4	.04 X 35 CLAD 2024-T3 (L)	1.19 X .051	CLAD 7075-T6 △2	9	5.10	54.9	17.2 △6	2	△1 △4
REF 4	.04 X 35 CLAD 2024-T3 (L)	1.19 X .102	CLAD 7075-T6 △2	9	5.10	68.6	24.3 △6	1	△1 △4
REF 4	.04 X 35 CLAD 2024-T3 (L)	1.19 X .156	CLAD 7075-T6 △2	9	5.01	84.0	33.6 △6	5	△1 △4
REF 4	.04 X 35 CLAD 2024-T3 (L)	1.19 X .051	CLAD 7075-T6 △2	12	5.10	49.7	18.3 △6	4	△1 △4
REF 4	.04 X 35 CLAD 2024-T3 (L)	1.19 X .102	CLAD 7075-T6 △2	12	5.11	61.7	25.2 △6	3	△1 △4
REF 4	.04 X 35 CLAD 2024-T3 (L)	1.20 X .157	CLAD 7075-T6 △2	12	5.03	70.9	31.1 △6	6	△1 △4
REF 4	.04 X 35 CLAD 2024-T3 (L)	1.19 X .100	CLAD 7075-T6 △2	12	5.15	57.1	**23.9** △6	11	△1 △5
REF 9	.04 X 36 CLAD 2024-T3 (L)	.58 X .25	CLAD 7075-T6 △2	18	17.72	64.10	32.5		△7 △8 △9 △10
REF 9	.04 X 36 CLAD 2024-T3 (L)	.58 X .25	CLAD 7075-T6 △2	18	17.70	60.23	28.5		△7 △8 △10
REF 9	.04 X 36 CLAD 2024-T3 (L)	.90 X .16	CLAD 7075-T6 △2	18	17.03	60.47	28.8		△7 △8 △10
REF 9	.04 X 36 CLAD 2024-T3 (L)	2.0 X .072	CLAD 7075-T6 △2	18	16.12	61.17	29.5		△7 △8 △10
REF 9	.04 X 36 CLAD 2024-T3 (L)	2.88 X .05	CLAD 7075-T6 △2	18	15.39	63.33	31.6		△7 △8 △10
REF 9	.04 X 36 CLAD 2024-T3 (L)	2.88 X .05	CLAD 7075-T6 △2	18	15.31	65.92	34.2		△7 △8 △10
REF 9	.04 X 36 CLAD 2024-T3 (L)	4.0 X .036	CLAD 7075-T6 △2	18	14.15	64.85	33.2		△7 △8 △10
REF 9	.04 X 36 CLAD 2024-T3 (L)	5.76 X .025	CLAD 7075-T6 △2	18	12.55	57.42	25.7		△7 △8 △10
REF 9	.04 X 36 CLAD 2024-T3 (L)	5.76 X .025	CLAD 7075-T6 △2	18	12.47	62.11	30.4		△7 △8 △10
REF 9	.04 X 36 CLAD 7075-T6 (L)	2.88 X .05	CLAD 7075-T6 △2	18	15.92	49.77	23.4		△7 △8 △10
REF 9	.04 X 36 CLAD 7075-T6 (L)	2.88 X .05	CLAD 2024-T3 △1	18	15.45	58.33	30.9		△7 △8 △9
REF 9	.04 X 36 CLAD 2024-T3 (L)	2.88 X .05	CLAD 2024-T3 △1	18	15.48	58.59	26.9		△7 △8 △9
REF 9	.04 X 36 CLAD 2024-T3 (L)	2.88 X .05	CLAD 2024-T3 △1	18	15.34	60.00	28.3		△7 △8 △9
REF 9	.04 X 36 BARE 2024-T3 (L)	2.88 X .05	BARE 2024-T3 △1	18	15.15	62.00	30.3		△7 △8 △9
REF 9	.04 X 36 CLAD 2024-T3 (L)	-	NONE	-	18.01	24.51	-		△7
REF 9	.04 X 36 CLAD 7075-T6 (L)	-	NONE	-	18.01	19.59	-		△7
REF 9	.04 X 36 CLAD 2024-T3 (L)	-	NONE	-	17.91	24.10	-		△7
REF 9	.04 X 36 CLAD 7075-T6 (L)	-	NONE	-	18.12	21.12	-		△7

NOTES:
△1 Mr = 2024-T3, D = 3/16, ρ = 1.0 INCH
△2 ESTIMATED F_{ty} = 65 KSI
△3 SIX STRAPS
△4 FOUR STRAPS
△5 FIVE STRAPS (CENTER ONE BROKEN)
△6 ESTIMATED K_o = 91 KIS/INCH

△7 BUCKLING RESTRAINED
△8 TWO STRAPS PLUS 1/2 STRAP ON PANEL EDGES
△9 BONDED STRAPS, 0.03 INCH THICK ADHESIVE
△10 BONDED STRAPS, 0.005 INCH THICK ADHESIVE
△11 ESTIMATED F_{ty} = 50 KSI

4 and 5), the residual strength data agree well with the data of groups 4 and 5. Figure 8 shows some scatter in reinforcement efficiency between the data of groups 4 and 5. Since these two groups of test panels were not fabricated at the same time, it is likely that the bonding systems were not the same. Bonding variables can affect the residual strength of a reinforced panel. For example, Smith [13] claimed that the scatter in his data could be attributed to the variation in the adhesive thicknesses.

   7178-T6 Aluminum Skin Panels—Two panels of 7178-T6 aluminum skin reinforced with 7178-T6 aluminum flat straps (F_{ty} = 85.7 ksi, A = 0.0535 in.^{2}) were tested. One of the panels (109B) failed during fatigue precracking with an initial 6-in.-long saw cut under a maximum cyclic stress of 13.6 ksi at R = 0.35. The critical K level for this panel was calculated to be 42.0 ksi$\sqrt{\text{in.}}$, which is a typical K_0 value for 7178-T6 aluminum [14]. The k_r term for this panel was zero because the crack tips were far from the stiffener at the time of panel failure. Panel 109A was precracked under a lower cyclic stress level of F_{max} = 7.05 ksi at R = 0.5, and the fatigue crack was grown close to the edge of the adjacent straps. A residual strength of 9.0 ksi was obtained during the static test. The critical K value was calculated to be 40.3 ksi$\sqrt{\text{in.}}$, which again is equivalent to the typical K_0 value for skin material. In other words, the k_r term was equal to zero, and no stiffening effect was achieved in this case.

   Figure 10 shows load versus time and crack length versus time curves obtained from the motion pictures for test panel 109A. No slow crack growth was observed. At the failure load each end of the crack grew rapidly from its initial location. One of the ends was arrested at the rivet hole right in front
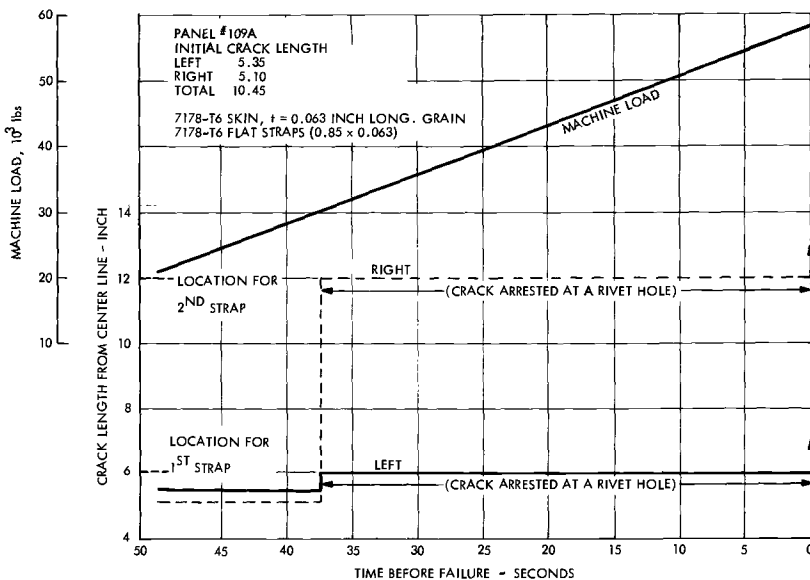

FIG. 10—*Crack resistance behavior of reinforced 7178-T6 aluminum flat panel.*

of the initial crack, while the other propagated through the nearest (first) intact strap and then was arrested by a rivet hole in the second strap.

Elastic analysis [9] shows that in order to accomplish significant load transfer, the crack tip has to be in line with or slightly beyond the rivet line. Strain gage measurements indicated that the strains on the straps were 0.002 in./in., whereas the strain for yielding of 7178-T6 aluminum straps was 0.01 in./in. (see Fig. 6). The inadequate load transfer and the resulting low failure load were attributed primarily to the low critical COD value and lack of primary slow, stable tear capability in the 7878-T6 aluminum skin. The failure mode for this case was the same as that illustrated in Figs. 2b and 3a.

Two experimental studies of 7075-T6 aluminum panels, with 7075-T6 aluminum reinforcements, can be cited from the literature. Results of Sorenson [15] for panels with riveted stringers show no improvement in residual strength compared to that of an unreinforced panel. However, the initial crack length in his tests was small compared to the stringer spacing ($l_0/W' \leq$ 0.2). As a result, catastrophic failure occurred while the crack tip was remote from the stringer, and the stringer could not be effective. In contrast, the data of Smith et al [13] on bonded flat straps indicate some improvement in residual strength. Still, however, the strap efficiency is low compared to the trend in Fig. 8 established by the test results for panels with 2024-T3 aluminum skin. This is due to the fact that the critical COD for 2024-T3 aluminum is higher than that for the 7075-T6 aluminum. In other words, for 7075-T6 aluminum skin reinforced with 7075-T6 straps, the panel probably failed prior to yielding of the strap and the strength of the strap was not utilized fully.

Fatigue Crack Propagation

An essential advantage in designing damage tolerant aircraft with fail-safe straps is that local high stresses at the crack tip will be transferred partially into the strap and carried by the strap. In other words, the crack tip stress intensity will be reduced by the strap in a way similar to that described by Eq 2. Therefore, since the rate of crack propagation is dependent on stress intensity, the rate is retarded. If a sufficient number of data are on hand, an analysis procedure can be developed to estimate the number of cycles required for a crack (with a known crack length) to propagate across one or several stiffeners. Inspection intervals and repair procedures also can be established.

Fatigue crack propagation tests conducted on test panels having adhesive bonded flat straps (groups 4 and 5) showed that fail-safe straps provide an effective means for reducing the rate of crack extension under constant amplitude fatigue cycling. In all the cases (see Fig. 11), fatigue cracks initially propagate at an increasing rate with increasing crack length (K level increases). As soon as the crack has grown close to the edge of the strap, the rate of crack growth reduces, since the crack tip stress intensity is reduced by the presence of the strap. However a nonuniform stress distribution is introduced into the
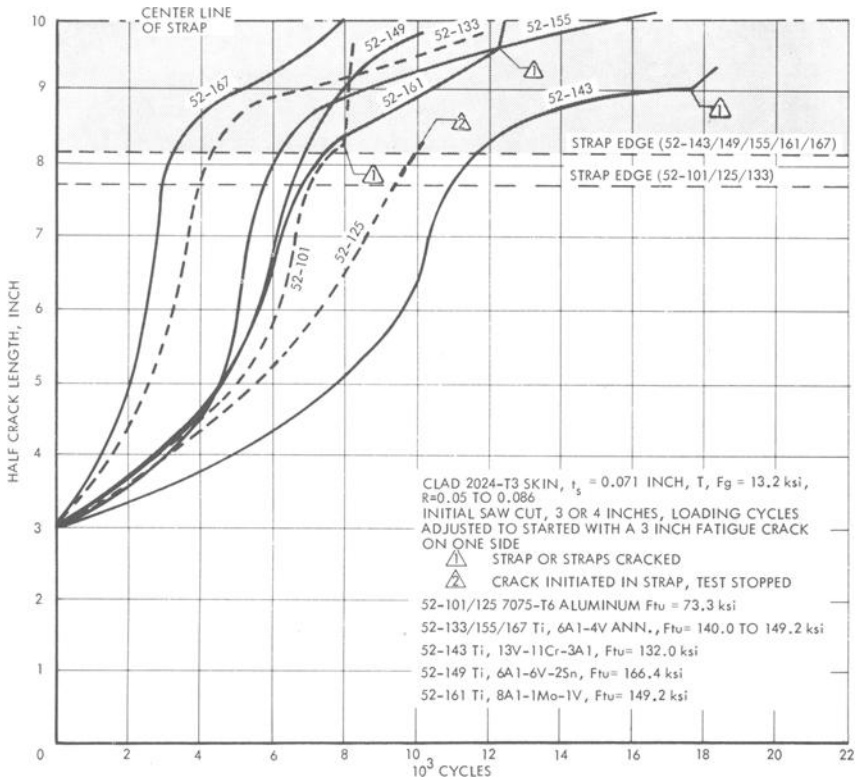
FIG. 11—*Fatigue crack propagation behavior of reinforced flat panels.*

strap with a peak at the edge nearest the end of the crack. The high stresses associated with that peak travel across the width of the strap as the crack continues to propagate. The life of the strap is then determined by the low cycle fatigue properties of the strap material. Figure 11 shows test results for panels having five different strap materials. Note that only one side of the crack growth history is shown for each test. Also, load cycles for each test were adjusted to start with a 6-in. fatigue crack so that scatter due to initation of the fatigue crack from an elox slot could be eliminated. The ability of the strap to withstand the effects of low cycle fatigue can be evaluated by starting to count load cycles with the crack at the edge of the strap. 7075-T6 aluminum straps were cracked within 800 to 1000 cycles (two tests). Titanium straps, Ti-8Al-1Mo-1V and Ti-13V-11Cr-3Al, survived for 4750 and 6000 cycles, respectively. Three tests on panels containing Ti-6Al-4V flat straps and one test on Ti-6Al-6V-Sn flat straps showed that the straps remained intact throughout the tests. It is worthwhile to note that as soon as cracks initiated to a visible size in the strap, the growth rate of the skin crack markedly increased. Also, for the panels containing a partially cracked strap (or straps), no improvement in residual strength was noted.

Summary

The fundamental aspects of crack growth and arrest have been studied and interpreted by making use of a modified crack opening displacement model. It has been shown that slow, stable crack growth is a function of skin fracture toughness and the mechanical properties of the reinforcement material. The skin material fracture toughness is related to a critical value of crack opening displacement, and this relates (although indirectly) to a value of local strain in the strap. If this strain is in the elastic range of the reinforcement, the reinforcement elastic stiffness will be the primary variable; if in the plastic range, then the strength and area product will be the primary variable.

The fatigue crack propagation and residual strength data presented serve to aid in the design of fail-safe aircraft structures and in the prediction of residual strength.

References

[1] Irwin, G. R. in *Proceedings*, Ninth International Congress of Applied Mechanics, University of Brussels, Sept. 1957, pp. 245–251.

[2] Fedderson, C. E., discussion in *Plane Strain Crack Toughness Testing of High-Strength Metallic Materials, ASTM STP 410*, American Society for Testing and Materials, 1967, p. 77.

[3] Newman, J. C., Jr., "Fracture of Cracked Plates Under Plane Stress," presented at the National Symposium on Fracture Mechanics, Bethlehem, Pa., June 1967.

[4] Crichlow, W. J. in *Full-Scale Fatigue Testing of Aircraft Structures*, Pergamon Press, New York, 1960, pp. 149–209.

[5] Broek, D., "The Residual Strength of Light Alloy Sheets Containing Fatigue Cracks," presented at the Fifth Congress of the International Council of the Aeronautical Sciences, London, Sept. 1966.

[6] Wells, A. A., *British Welding Journal*, MCBWA, Vol. 12, Jan. 1965, pp. 2–3.

[7] Burdekin, F. M. and Stone, D. E. W., *Journal of Strain Analysis*, JSTAB, Vol. 1, 1966, pp. 145–153.

[8] Greif, R. and Sanders, J. L., Jr., *Journal of Applied Mechanics, ASME Transactions*, Series E, JAMCA, Vol. 32, March 1965, pp. 59–66.

[9] Bloom, J. M. and Sanders, J. L., Jr., *Journal of Applied Mechanics, ASME Transactions*, Series E, JAMCA, Vol. 33, Sept. 1966, pp. 561–570.

[10] Poe, C. C., "The Effect of Riveted and Uniformly Spaced Stringer on the Stress Intensity Factor of a Cracked Sheet," M.S. thesis, Virginia Polytechnique Institute, April 1969.

[11] Poe, C. C. in *Damage Tolerance in Aircraft Structures, ASTM STP 486*, American Society for Testing and Materials, 1971, pp. 79–97.

[12] Liu, A. F., "Residual Strength of Flat Panels Reinforced with Riveted Flat Straps," Report No. LR 22819, Lockheed-California Co., Burbank, Jan. 1970.

[13] Smith, S. H., Porter, T. R., and Engstrom, W. L., "Fatigue Crack Propagation Behavior and Residual Strength of Bonded Strap Reinforced, Lamellated and Sandwich Panels," presented at the Air Force Conference on Fatigue and Fracture of Aircraft Structures and Materials, Miami Beach, Fla., Dec. 1969.

[*14*] Liu, A. F., "Statistical Variation in Fracture Toughness Data of Airframe Materials," presented at the Air Force Conference on Fatigue and Fracture of Aircraft Structures and Materials, Miami Beach, Fla., Dec. 1969.
[*15*] Sorensen, A., "Some Design Considerations for Tear-Resistant Airplane Structures," presented at the 24th Annual Meeting, Institute of the Aeronautical Sciences, 23–26 Jan. 1956.

T. R. Brussat[1]

An Approach to Predicting the Growth to Failure of Fatigue Cracks Subjected to Arbitrary Uniaxial Cyclic Loading

ABSTRACT: A general approach to prediction is discussed which would treat crack growth as a continuous stochastic process. Each different crack description and length would be a state in this process, with residual strength failure constituting the terminal state.

The specific theory necessary for crack growth prediction is discussed. The effective stress intensity variable developed by Walker for crack growth under tension-tension cycling is extended to compression-tension cycling. The use of this variable with constant amplitude data for prediction of crack growth under spectrum loading is described. A means of calculating the conditional probability of residual strength failure (given the predicted crack growth history) is outlined.

The prediction method is tested on a controlled set of laboratory data from large center cracked 7075-T76 aluminum panels. Constant amplitude data are used to predict crack growth under a randomized flight-by-flight load spectrum typical of a location on an aircraft wing. Agreement is found to be good despite evidence of mechanism differences between the constant amplitude and variable amplitude crack growth processes.

KEY WORDS: failure, fatigue (materials), cracking (fracturing), crack propagation, toughness, cyclic loads, cyclic variations, stresses, residual stress, mathematical prediction, stochastic processes, frequency distribution, probability, aircraft, aircraft panels, structural members, aluminum, evaluation

Nomenclature

a Half crack length, in.

α Geometry correction factor for stress intensity which accounts for method of load application, crack shape, and geometry of the structural component. For a finite-width panel, $\alpha = \sqrt{\sec(\pi a/w)}$ approximately

$\dfrac{d(2a)}{dN}$ Crack growth rate, inches per cycle or inches per flight

[1] Stress engineer, Fatigue and Fracture Mechanics, Science and Engineering, Lockheed-California Co., Burbank, Calif. 91503.

$D(j)$ A measure of relative deviation of the crack growth rate curve for the jth specimen in a data set from the mean rate curve for the data set

K Stress intensity $= \alpha S\sqrt{\pi a}$, ksi$\sqrt{\text{in.}}$

$K_{\max}$ = maximum stress intensity $= \alpha S_{\max}\sqrt{\pi a}$

$\bar{K}$ = effective stress intensity for crack growth $= \alpha \bar{S}\sqrt{\pi a}$

K_c = critical stress intensity (plane stress fracture toughness) of the material. Residual strength failure occurs if $K_{\max} > K_c$

m Empirical constant for a particular material and possibly environment

R Stress range ratio, the minimum stress in a fatigue loading cycle divided by the maximum stress

R_c = critical range ratio for a material. It is claimed that compressive stresses below the stress $R_c S_{\max}$ do not effect crack growth rate significantly

S Stress, ksi

$S_{\max}$ = maximum stress in a cycle

$\bar{S}$ = effecitve stress for fatigue crack growth

P Probability

$P_{\text{tough}}(k)$ = probability that the material fracture toughness is less than k

$P_{\text{peak}}(k,n)$ = probability distribution for the largest $K_{\max}$ to occur in the nth time interval

$P_{\text{fail}}(T|i)$ = conditional probability of failure during the first T time periods, given the ith possible crack growth history

w Panel width, in.

There are several techniques for maximizing the structural integrity of a mechanical or structural system that is to be subjected to repeated loading in service. The rate of crack initiation can be minimized by careful design and quality control. When despite such care cracks still initiate, the survival time of the cracked component will be long if slow crack growth rate and high fracture toughness were criteria in the design and choice of material. Then with proper scheduling of structural inspection the cracks will be detected and repaired before the probability of component failure becomes too high. Finally, redundant structure (fail-safe design) can be utilized so that component failure does not imply system failure.

Given an existing system, control of the inspection schedule is the primary remaining means to enhance system reliability. The choice of the interval between consecutive inspections is dictated by the effectiveness of the inspection procedure, the frequency of crack initiation, the rate of crack propagation, and the acceptable level of probability of component failure.

A method of predicting the rate of crack propagation and probability of component failure is presented. First, this method is outlined, essentially independent of specific fatigue and fracture theory, models, or assumptions, as a general prediction strategy. Then, the fatigue and fracture theory presently available for use in making such predictions is discussed. Finally, this theory is assimilated into the prediction method and tried against actual spectrum crack growth data generated on simple laboratory specimens.

The Strategy for Prediction

To obtain a valid crack growth prediction, proper consideration must be given to all major aspects of the problem. The initial crack must be described, and the anticipated load history must be defined in terms of how that history can cause that existing crack to propagate to the point of residual strength failure.

Immediately after an inspection the size, number, and configuration of existing cracks will be partially random. The randomness arises from the variability in the phenomena of microscopic crack initiation and early growth, as well as the variability in the effectiveness of the structural inspection. To account for variability, a frequency distribution should be estimated for flaw shape, size, and location. The frequency distribution of crack size immediately after an inspection is obtained by subtracting the frequency distribution of crack sizes discovered and repaired from the anticipated frequency distribution for all existing cracks in the component.

The number of existing cracks will vary from one component to the next because of consistent differences in load severity between components. More and earlier cracks will result from the imposition of consistently higher loads. The crack growth, too, will change significantly with consistent variations in severity level between loading histories. There is a probability distribution on this severity level which arises both from natural stochastic variability between service experiences and from unavoidable inaccuracies in load estimation and measurement. This probability distribution should be taken into account in predicting crack growth.

Even fixing the severity level of the load history an additional source of randomness remains, because the order of occurrence of loading events in service is, in general, a partially random function of time. (Here a "loading event" can be defined to consist alternatively of one load cycle or a sequence of consecutive load cycles.) The response to a loading event can be either some increment of crack growth or failure of the structural component; this response is a random variable.

Thus, crack growth is viewed as a step-by-step random walk through time, from some random initial state to a single terminal state; that is, crack growth is a stochastic process. Each state of this process, including the initial state, is determined by the crack length and whatever other measured quantities may be preferred. Since the crack length is a continuous variable, the state space of the process is continuous; however, it can be considered

approximately to be discrete, consisting of a large number of temporary states and one terminal state, failure of the component.

In a discrete stochastic process the probability of passing from some state i to another state j in a specified unit of time is termed the "transition probability" and can be denoted by $P(j|i)$. For crack growth the specified unit of time can be one loading event. $P(j|i)$ will then depend upon both the likelihood that each possible loading event will occur and the conditional probability that transition from state i to state j would result from that occurrence. In particular, $P(j|i)$ is the sum over all possible loading events of the products of these two probabilities. And if $P_n(i)$ is the probability that the process is in the ith state before the nth loading event, the probability that it will be in the jth state after this loading event is

$$P_{n+1}(j) = \sum_i P_n(i) P(j|i) \dots\dots\dots\dots\dots\dots(1)$$

The method of calculating transition probability applies, of course, to the transition into the terminal state by a residual strength failure of the component. (Here the term "residual strength" is defined as a random variable equal in magnitude to the minimum severity required of the present loading event in order to fail the component.) Therefore, if state j is the terminal state, then Eq 1 gives the probability that failure will occur during the first n loading events. If n is the length of the inspection interval, then this is the probability that the structural component will fail prior to next inspection; its complement $[1 - P_{n+1}(j)]$ is the survival probability.

As previously mentioned, different levels of load history severity are possible, and with each severity level a slightly different frequency distribution on initial crack size exists. It is simplest to deal with each load severity level as a separate stochastic process and weight the results by the likelihood of that particular level. The sum of the failure probabilities so calculated gives the total probability of component failure prior to the next inspection.

From the above discussion it is evident that the calculation of failure probability of a structural component, done rigorously, will require a tremendous number of known quantities and relationships and a great deal of calculation. Even in the somewhat distant future, drastic simplifying assumptions will have to be made. The objective must be to choose these assumptions carefully to maximize the usefulness of the results. One set of such assumptions permits the development of a workable version of the prediction method based on presently used fatigue crack growth models. These assumptions and models are discussed in the following section.

Some Theories and Models for Fatigue Crack Growth Prediction

Models for Constant Amplitude Fatigue Crack Propagation

Real loading conditions can deviate dramatically from the idealized constant amplitude fatigue cycling condition; however, the simplicity of the constant amplitude condition permits easy study of first-order relationships

between load levels and crack growth responses. Such studies provide a natural foundation of understanding upon which a general theory can be built.

For constant amplitude tests at the same (positive) stress ratio R (the ratio of minimum to maximum stress) the stress intensity factor has been used widely to account simultaneously for the variables of stress and crack length. Stress intensity can be defined by

$$K = \alpha S \sqrt{\pi a} \dots\dots\dots\dots\dots\dots\dots(2)$$

where S is gross area stress, a is half crack length, and α is a function of the crack length, component geometry, and method of load application. As an example, the value of α for a flat panel of width w and load applied at its (distant) ends is given approximately by

$$\alpha = [\sec(\pi a/w)]^{1/2} \dots\dots\dots\dots\dots\dots(3)$$

which approaches unity for a panel of infinite width.

More recently, useful methods have been developed to account for various values of R in correlating constant amplitude tension-tension crack growth data [1, 2].[2] In Ref 1 Walker introduced the effective stress $\bar{S}$ defined by

$$\bar{S} = S_{max} (1 - R)^m \dots\dots\dots\dots\dots\dots(4)$$

in which S_{max} is the maximum gross area stress and m is an empirical constant that depends upon the material and possibly the environment. Crack growth rate in a given material and environment under arbitrary constant amplitude tension-tension cycling can be plotted as a function of the single variable $\bar{K}$, the effective stress intensity, defined simply by replacing S in Eq 2 by $\bar{S}$:

$$\bar{K} = \alpha \bar{S} \sqrt{\pi a} \dots\dots\dots\dots\dots\dots\dots(5)$$

Since general uniaxial loading can include compressive loads, it was desired to obtain a crack growth model for compression-tension fatigue cycling. (No crack growth is assumed to result from compression-compression cycling.) For crack growth under the compression-tension condition, past practice has been to ignore the compressive portion for analysis. It can be demonstrated that to neglect the effects of compressive stressing leads to nonconservative estimates of crack growth rate.

Compression-tension data from 20 center cracked specimens of 7075-T6 are presented by Hudson [3], along with data from five additional specimens tested at a minimum stress of zero. These data were reviewed statistically to test the hypothesis that compressive stressing accelerates the crack growth rate against the null hypothesis that there is no difference in rate between compression-tension cycling and zero-to-tension cycling.

---

[2] Italic numbers in brackets refer to the list of references at the end of this paper.

The first step was to select the data to be analyzed. Since stress intensity methods were to be used in the comparison, two specimens tested at a maximum stress of 50 ksi were not considered because the plastic zone size based on S_{max} was judged to be too large compared to the crack length. (The requirement chosen for this selection was that S_{max} could not exceed 60 percent of the tensile yield strength.)

Crack growth rates for each of the remaining 23 specimens were calculated as functions of K_{max}, the maximum stress intensity obtained from Eq 2 by replacing S with S_{max},

$$K_{max} = \alpha S_{max} \sqrt{\pi a} \dots\dots\dots\dots\dots\dots\dots\dots(6)$$

A mean rate curve was obtained as the locus of points defined by taking the geometric mean crack growth rate over all the specimens at fixed K_{max} values. The truth of the null hypothesis would require randomness in the scatter of actual data points about this mean rate curve. Rejection of the null hypothesis would be warranted if the zero-to-tension specimens showed consistently slower cracking rates than indicated by the mean rate curve.

A measure of relative deviation from the mean rate curve was obtained for each specimen, from the arbitrarily defined quantity

$$D(j) = \left[\sum_{i=1}^{DP(j)} \frac{\bar{K}_{max}(i,j)}{K_{max}(i,j)} \right] \frac{1}{DP(j)} - 1 \dots\dots\dots\dots\dots(7)$$

Here $DP(j)$ is the number of data points for the jth specimen, where the pair $[K_{max}(i,j), \frac{d(2a)}{dN}(i,j)]$ constitutes the ith such data point. The term $\bar{K}_{max}(i,j)$ is the value of K_{max} obtained from the mean crack growth rate curve which corresponds to the crack growth rate $\frac{d(2a)}{dN}(i,j)$ for the ith data point of the jth specimen. Thus, the specimens with the most negative values of relative deviation $D(j)$ have the slowest crack growth rate relative to the mean rate curve.

The specimens were arranged in order of increasing magnitude of $D(j)$, and the rank sum test was applied to measure any tendency of the zero-to-tension specimens to assume low values of this statistic. The ranks of these four specimens were 1, 5, 6, and 7. There exists a probability P_r (null) of only 0.008 that the summed ranks of these four specimens would not exceed 19 if the null hypothesis were true. From this it was concluded that compressive stressing has a detrimental effect on crack growth in these center cracked 7075-T6 aluminum panels subjected to compression-tension cycling.

This same statistical test was repeated for other compression-tension data from the literature. Consistently low values of P_r (null) in Table 1 tend to confirm that the compressive stressing in compression-tension cycling increases the resulting crack growth rates. In these cases also, some specimens

TABLE 1—*Effect of compression stresses in compression-tension cycling.*

Material	Number of Specimens		P_r(null)	Decision	Reference
	$R = 0$	$R < 0$			
2024-T3 aluminum....	4	5	0.008	Reject null hypoth- esis	*3*
2024-T3 aluminum....	4	4	0.014	Reject null hypoth- esis	*5, 6*
7075-T6 aluminum....	4	19	0.008	Reject null hypoth- esis	*3*
7075-T6 aluminum....	6	3	0.452	Cannot reject null hypothesis	*5, 6*
Ph-15-7Mo stainless steel	5	7	0.0013	Reject null hypoth- esis	*4*

with high maximum stresses (and, therefore, excessive plastic zone sizes for valid use of fracture mechanics analysis) were deleted from consideration prior to the calculation.

Having shown the consistent effect of compressive stressing, a quantitative evaluation of this effect was sought using the same 23 specimens of 7075-T6 aluminum [*3*]. A geometric mean curve for the zero-to-tension specimens only was obtained and compared with the data points from the compression-tension specimens in terms of the same relative deviation variable $D(j)$.

It should be noted that a plot of the variable K_{max} $[1 + D(j)]$ versus $\frac{d(2a)}{dN}$ for each compression-tension specimen will coincide approximately with the mean rate curve from the zero-to-tension tests. Hence, the quantity $1 + D(j)$ can be thought of as a correction factor on K_{max} arising from nonzero values of R, in the manner of the $(1 - R)^m$ factor for tension-tension cycling of Eq 4.

The value of $D(j)$ was observed to be reasonably constant for all compression-tension specimens, so a critical range ratio R_c was defined in terms of an average $D(j)$ by

$$(1 - R_c)^m = 1 + D_{avg} \dots \dots \dots \dots \dots \dots (8)$$

where m, the empirical constant in Eq 4, is known to be 0.5 for 7075-T6 aluminum in ambient air [*1*], and D_{avg} is the average value of $D(j)$ obtained from those specimens for which $R < R_c$. For these specimens, $D_{avg} = 0.06$ was calculated; thus, it was concluded that $R_c = -0.12$ for 7075-T6 aluminum.

Then the definition of effective stress $\bar{S}$ can be extended to include the entire range of constant amplitude fatigue cycling:

$$
\left.
\begin{aligned}
\bar{S} &= S_{max} (1 - R)^m && \text{if} && R > R_c \text{ and } S_{max} > 0 \\
\bar{S} &= S_{max} (1 - R_c)^m && \text{if} && R \leq R_c \text{ and } S_{max} > 0 \\
\bar{S} &= 0 && \text{if} && S_{max} \leq 0
\end{aligned}
\right\} \ldots\ldots\ldots(9)
$$

and for a given material and environment the crack growth rate can be expressed as a single function of effective stress intensity $\bar{K}$ defined by Eq 5.

Of course, the variable $\bar{K}$ as defined by Eqs 5 and 9 is still not "complete," since only uniaxial stresses are accounted for, whereas, in general, service loads on a structural member are multiaxial. A crack usually has aligned itself normal to the direction of most severe tensile stress cycling by the time it approaches observable size. Thereafter, its propagation rate can be expected to depend primarily upon the magnitude of these principal uniaxial stresses. It is reasonable, therefore, to consider only the cyclic tensile and compressive stresses in the direction of most severe loading when defining the loading history affecting fatigue crack growth.

A Palmgren-Miner Type Approach to Crack Propagation Prediction

A variable correlating uniaxial, constant amplitude fatigue crack growth behavior has been obtained in anticipation of its being useful for predicting crack growth under variable amplitude loading conditions. The Palmgren-Miner linear cumulative damage rule has been used widely with constant amplitude fatigue data, despite inaccuracies, for the prediction of fatigue crack nucleation times under variable amplitude loading conditions. An analogous approach for predicting the growth rate of fatigue cracks can be devised, which is superior in some ways to the traditional version for crack initiation.

The two basic assumptions of the rule as it has been applied to fatigue crack nucleation are

(a) Fatigue damage accumulates as a linear function of cyclic load occurrences.

(b) The rate of increase of fatigue damage per cycle for a cyclic load of a given magnitude is independent of the nature of previous loads.

These assumptions lead to the well known result that the partial damage due to the ith stress level in a spectrum is $n(i)/N(i)$, where $n(i)$ is the number of occurrences of the ith stress level and $N(i)$ is the constant amplitude fatigue life (to crack initiation) for the ith stress level. In a flight-by-flight load history of aircraft structure, for example, if $n(i)$ is the number of cycles at level i per flight, then the damage per flight (or rate of damage) is the sum taken over all stress levels of the ratios $n(i)/N(i)$.

In a Palmgren-Miner type of approach to fatigue crack growth prediction it is not necessary to assume that damage is linear. Instead, assumptions (a) and (b) can be restated:

(A) The observed crack size can be used as a measure of damage.

(B) The rate of growth of fatigue cracks per cycle for a cyclic stress intensity of a given magnitude is independent of the nature of previous stress intensity values.

These assumptions lead to the result that the partial damage (measured as an increment of crack length) due to the ith stress intensity level in a spectrum is

$$\left[\frac{d(2a)}{dN}(i) \times n(i)\right]$$

where

$n(i)$ = the number of occurrences of the ith stress intensity level and

$\dfrac{d(2a)}{dN}(i)$ = the constant amplitude fatigue crack growth rate for the ith stress intensity level.

Again, in the example of a flight-by-flight load history for aircraft structure, if $n(i)$ is the cycles at level i per flight, then the damage (crack growth) per flight, or rate of damage (crack growth rate), is the sum, taken over all L stress intensity levels, of the product $\dfrac{d(2a)}{dN}(i) \times n(i)$; that is,

$$\Delta(2a) \text{ per flight } = \sum_{i=1}^{L} \left[\frac{d(2a)}{dN}(i) \times n(i)\right] \dots\dots\dots\dots(10)$$

The observed crack length is used both as a measure of damage and in the stress intensity expression as a magnification factor on the severity of each stress level in a spectrum. In this respect, assumption (A) represents a significant improvement over the assumption of linear damage accumulation that is necessary in applying the traditional Palmgren-Miner rule to fatigue crack initiation prediction.

Assumption (B), of course, is only correct to the first approximation; generally speaking, the crack growth response to some applied load will depend upon the history of stress and plastic strain in the crack tip vicinity. These, in turn, are determined by the present and "recent" values of stress intensity, provided the zone of plasticity in the vicinity of the crack tip remains small compared with the crack length. Because the crack growth process readily lends itself to observation, it is likely that first-order stress history effects eventually will be evaluated experimentally. (Effects of overloads on crack growth rates already have been a subject of study [7–10].) When assumption (B) is modified to include such history effects, substantial improvements can be expected in the accuracy of crack growth predictions.

For crack growth in actual structure the Palmgren-Miner type approach would be applied in a stochastic manner, as described earlier. For controlled crack growth experiments, however, the sources of variability in material, initial crack size, applied stress, and atmospheric environment are minimized; therefore, in the following, the approach is used deterministically. A load spectrum at a single severity level is used in place of a probability distribution of possible load history severities. The expected value of loads occurring during a specified time interval replaces the random sequence of loads. A deterministic crack growth rate response rule (represented by a single curve of $\bar{K}$ versus rate) is used to estimate the expected value of the response to each cycle of load. The error in this response rule is not considered statistically but, in effect, is assumed to be zero. The result is a single predicted crack growth history instead of a probability distribution on possible histories.

Upon obtaining this prediction of crack length versus time a stochastic approach can be used to calculate the probability of residual strength failure of the structural component. The result of this calculation is actually the conditional probability of failure, conditional upon the occurrence of this crack history.

The hope is that this single crack history will be sufficiently representative of all possibilities that the conditional probability of failure is approximately equal to the actual probability of failure; however, it is anticipated that errors in applying the crack growth model to spectrum data will be in a consistent direction so that this single crack history will not be a true average. Furthermore, even with exact theory (zero mean error) the numerical value of probability of failure will be influenced most dramatically by the unlikely worst cases that are not considered in this mean value approach. This points up a statistical "fact of life," that the best estimate of a combination is not necessarily the same as the combination of best estimates.

Better estimates of failure probability could be obtained by assuming (or calculating) several representative crack growth histories, each with its probability of occurrence. This possibility is left open in the discussion of the probability of failure calculation given in the Appendix.

An Application: Prediction of Spectrum Test Data

A set of tests was conducted to determine whether the theory of the previous section could lead to useful predictions of crack growth. Both constant amplitude and random amplitude tests were conducted on center cracked panels of 7075-T76 aluminum, 6 ft by 2 ft by $\frac{3}{16}$ in. An environment of 100 percent humidity was applied to the neighborhood of the crack by means of a constant, fine spray of distilled water. Loads were parallel to the rolling direction.

The load was imposed by a 150,000-lb-capacity, horizontal, hydraulic fatigue machine. The test fixture used was designed to accommodate tension-compression cycling. This design included clamped connections instead of pinned connections to prevent hammering in the transition between tension

and compression, and 1-in. steel plates a few thousandths of an inch above and below the specimen to limit buckling during compression. A 1⅜-in. gap between the plate ends permitted access to the crack for the observer and the water spray as shown in Fig. 1.

Four tension-tension specimens were tested, three at $R = 0$ and different maximum stresses and one at $R = 0.6$. The test data are given in Table 2 and the rate curves plotted in Fig. 2 against effective stress intensity $\bar{K}$, where the exponent m from Eq 4 was 0.60 for this material and environment. This m value was obtained from previous test data [11] and substantiated by this data. From these four individual specimens an average rate curve for tension-tension cycling was obtained.

Since metallurgically 7075-T76 aluminum is nothing more than an over-aged 7075-T6, strong similarities between the two materials are anticipated. Therefore, it was reasonable to hypothesize that Eq 9 with $R_c = -0.12$ could be used for 7075-T76 aluminum. Compression-tension crack growth data for this material were generated in the test fixture just described covering the range $-3.0 < R < -0.6$, and no significant deviation from this hypothesized behavior was observed.

In this same test fixture eight crack growth tests were conducted using four variations of a loading spectrum typical of the most severe uniaxial cyclic loads anticipated for a point on the lower surface of a typical airplane wing. The load content of these four spectra is listed in Table 3. A complete and a truncated version are given for each of two loading spectra. The main difference between these spectra is that the magnitudes of all loads in spectrum II are approximately 70 percent of the magnitudes of corresponding loads in spectrum I.
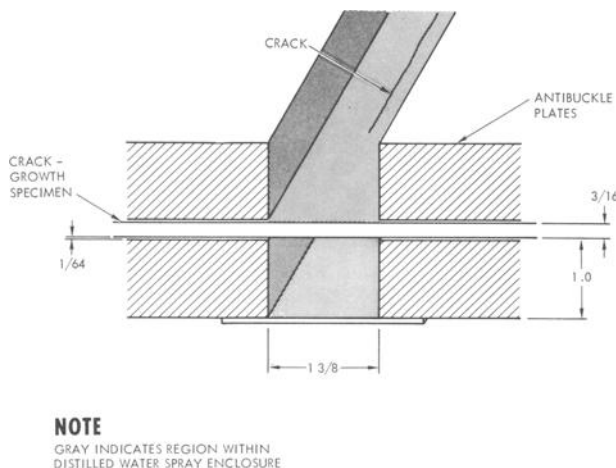

NOTE
GRAY INDICATES REGION WITHIN
DISTILLED WATER SPRAY ENCLOSURE

FIG. 1—*Details of crack vicinity on crack growth tests.*

TABLE 2—*Tension-tension data for 7075-T76 aluminum in 100 percent humidity.*

Specimen No.	S_{max}, ksi	S_{min}, ksi	R	Number of Cycles Required for Crack to Propagate to a Full Length, $2a$, of										
				0.60 in.	0.85 in.	1.2 in.	1.7 in.	2.4 in.	3.3 in.	4.6 in.	6.2 in.	8.2 in.	10.5 in.	12.8 in.
41......	16.02	0	0	...	...	7 790	9 900	11 163	12 357	13 210	13 762	14 045	...	...
42......	10.30	0	0	8 860	19 266	25 900	32 759	38 127	42 283	45 768	48 342	50 204	51 234	51 706
44......	6.32	0	0	31 367	82 435	118 390	146 540	165 000	181 400	195 160	205 000	213 640	219 400	222 748
43......	10.15	6.09	0.6	79 950	156 600	201 580	239 500	271 200	295 700	315 448	329 872	340 568	347 450	350 642

TABLE 3—*Randomized flight-by-flight spectra used in spectrum tests.*

	Stresses, ksi				Cycles per Flight	
	Spectrum II		Spectrum I			
Comments	S_{max}	S	S_{max}	S	Complete Spectrum	Truncated Spectrum
GAG cycles......	17.10	18.30	24.47	26.19	0.0020	0.00200
	16.41	17.57	23.51	25.17	0.0020	0.00200
	15.66	16.76	22.39	23.97	0.0040	0.00400
	14.98	16.04	21.42	22.93	0.0095	0.01000
	14.21	15.21	20.33	21.76	0.0300	0.02900
	13.41	14.35	19.24	20.60	0.0725	0.07425
	12.62	13.51	18.14	19.42	0.1735	0.18075
	11.81	12.64	17.05	18.25	0.3760	0.38450
	11.07	11.85	16.08	17.21	0.2280	0.22800
	10.14	10.85	14.97	16.03	0.1025	0.08325
	9.23	9.88	13.83	14.80	0	0.00225
Flight cycles.....	14.98	14.92	21.42	20.90	0.0005	0.
	14.21	13.60	20.33	18.97	0	0.00100
	13.41	12.20	19.24	16.98	0.0075	0.00575
	12.62	10.78	18.14	14.92	0.0465	0.03925
	11.81	9.33	17.05	12.90	0.3240	0.31550
	11.07	7.98	16.08	10.99	0.7720	0.77200
	10.14	6.27	14.97	8.69	4.8975	1.91675
	9.23	4.72	13.83	6.12	12.9520	2.94975
Ground cycles....	2.62	2.80	4.53	4.85	0.002	0.002
	1.97	2.11	3.58	3.83	0.002	0.002
	1.55	1.66	2.99	3.20	0.004	0.004
	0.73	0.78	1.78	1.91	0.012	0.012
	0.10	0.11	0.88	0.94	0.040	0.040
	−0.53	0	−0.04	0	0.080	0.080
	−1.16	0	−0.97	0	0.240	0.240
	−1.67	0	−1.74	0	0.720	0.720
	−2.29	0	−2.64	0	1.600	1.600
	−2.82	0	−3.38	0	3.000	1.600
	−3.45	0	−3.99	0	5.000	1.600
	−4.05	0	−5.22	0	6.300	2.100

The truncated spectrum resulted from deleting most of the lowest stress level cycles, with a simultaneous reduction in the number of cycles per flight. This truncation was designed so that the average per flight frequency of higher stresses was preserved.

Two replications were made of each of these four test conditions. Each replication consisted of a different random order of cyclic occurrences but the same total load content over the 1000 or 2000-flight loading tape. The loads were applied in a flight-by-flight sequence, each flight consisting of a fixed number of ground loadings at an approximately constant compressive mean stress, a fixed number of flight loadings at an approximately constant
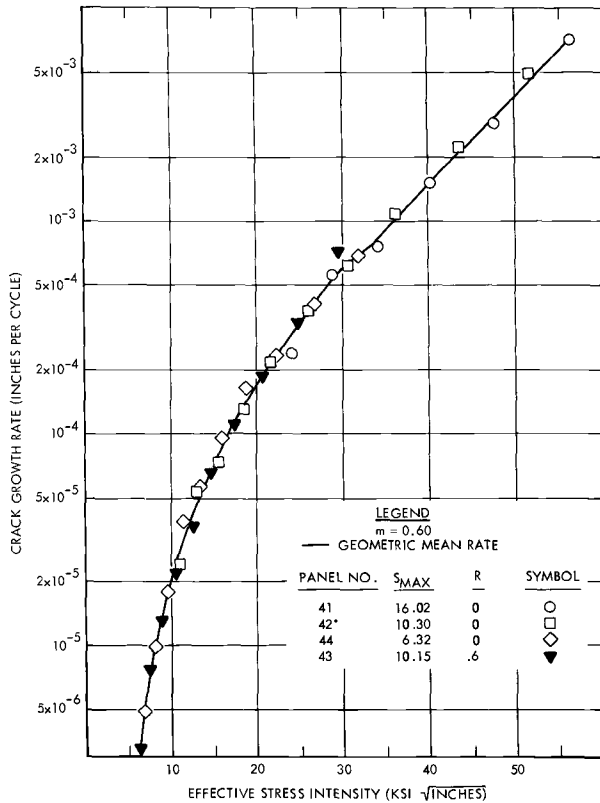
FIG. 2—*Crack growth for 7075-T76 aluminum in water spray environment.*

tensile mean stress, and one peak-to-peak ground-to-air-to-ground (GAG) cycle. Sample flight traces are shown in Fig. 3 for both the complete and truncated versions of the spectra.

The effective stress S given in Table 3 has been calculated for each stress level by using Eq 9 with $m = 0.6$ and $R_c = -0.12$.

Using the spectra from Table 3, the mean constant amplitude rate curve from Fig. 2, a specimen width of 24 in., and Eqs 9 and 10, Miner's rule type predictions of crack growth rate per flight were calculated for each of the four test conditions. These calculated spectrum crack growth rate plots are shown as solid lines in Fig. 4. The dotted lines show the average experimental crack growth rates for the two specimens tested at each spectrum condition.

A prediction of crack length versus number of flights was obtained for each case by numerical integration of the calculated rate curves using essentially a trapezoidal rule approach. The predicted histories are compared to actual data from individual specimens in Fig. 5.
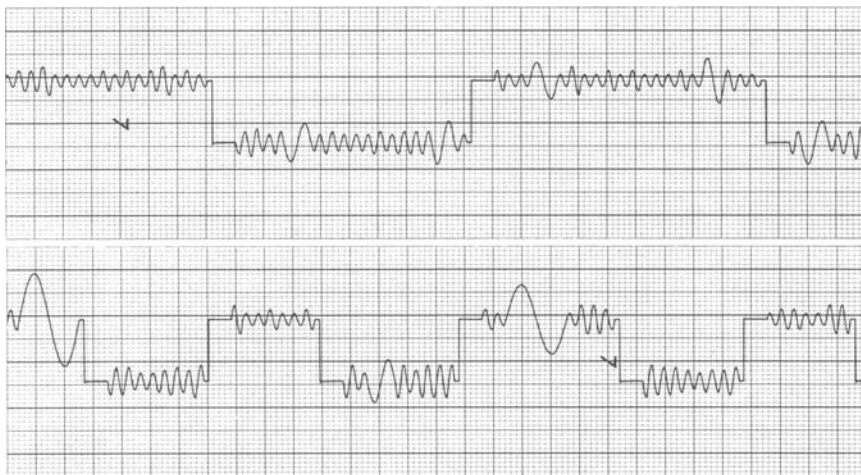
FIG. 3—*Loading traces from applied load histories from Table 3: top, complete spectrum; bottom, truncated spectrum.*
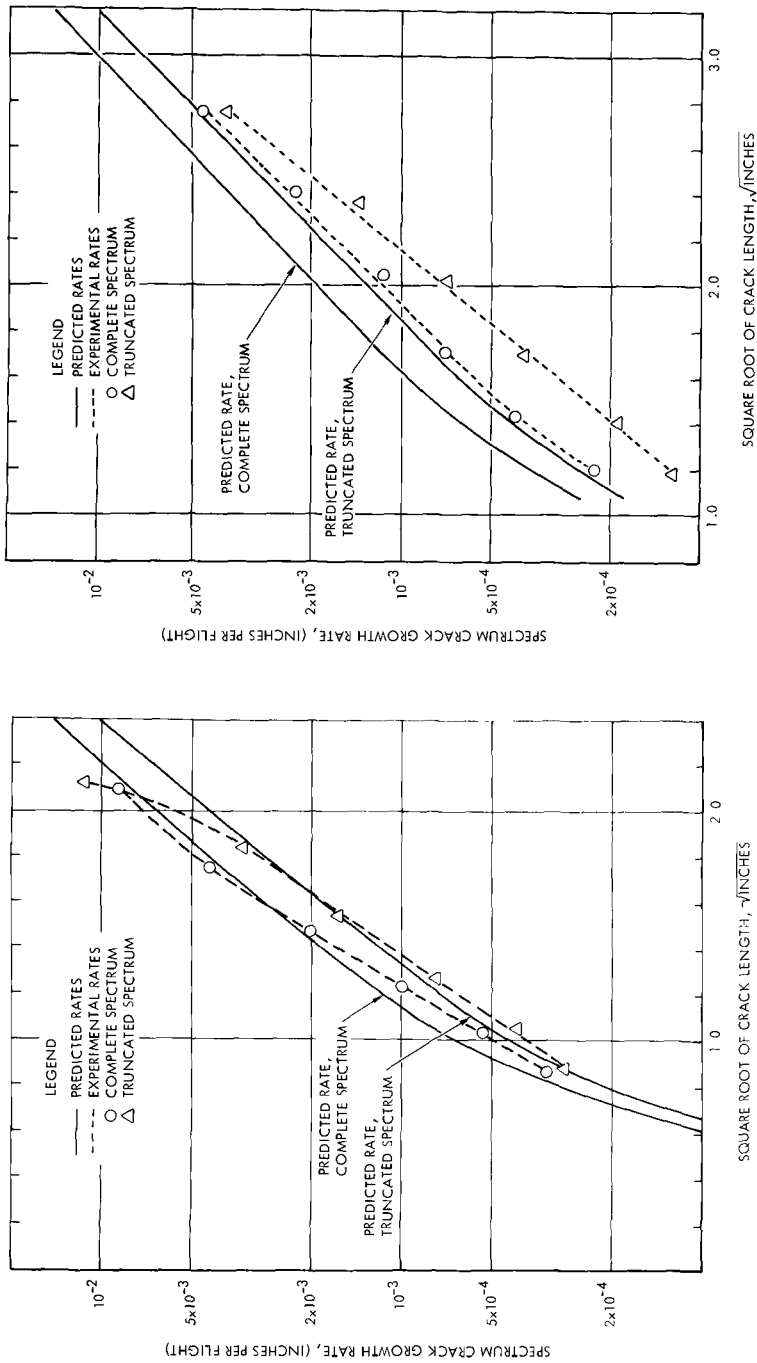
Discussion of the Results

Comparison between predicted and experimental crack growth rates from Fig. 4 ranged from close agreement to conservatism in predicted rate by a factor or two. As a natural result, the crack growth histories were predicted within similar limits of accuracy, as shown in Fig. 5.

There would appear to be two alternative explanations possible for the close agreement between experimental and predicted crack growth rates and histories observed for these eight tests. Either stress history effects on crack growth rate were small in this case or they were significant but cancelled each other out.

To obtain evidence toward deciding which explanation might be more accurate, a comparison was made between the fracture surfaces of specimens taken from constant amplitude tests (both tension-tension and compression-tension) and spectrum tests. Figure 6 is from a specimen that had been spectrum tested. The alternating dark and light areas on the crack surface probably indicate alternating periods of slow growth followed by *jumps* in growth. On the face of the same specimen are diagonal bands of plastic deformation which undoubtedly occurred during each occasional high load in the spectrum. This same sort of evidence is presented and discussed by von Euw [7]. No evidence of these kinds of behavior was present on any of the constant amplitude specimens studied.

Researchers [7–10, 12] have identified at least two common types of stress history effect. A jump in crack growth such as was evident on the fracture surface usually occurs with the application of a high-stress cycle following several lower stress cycles. A period of crack deceleration (slower growth than would occur in a constant amplitude test at the same stress intensity level)
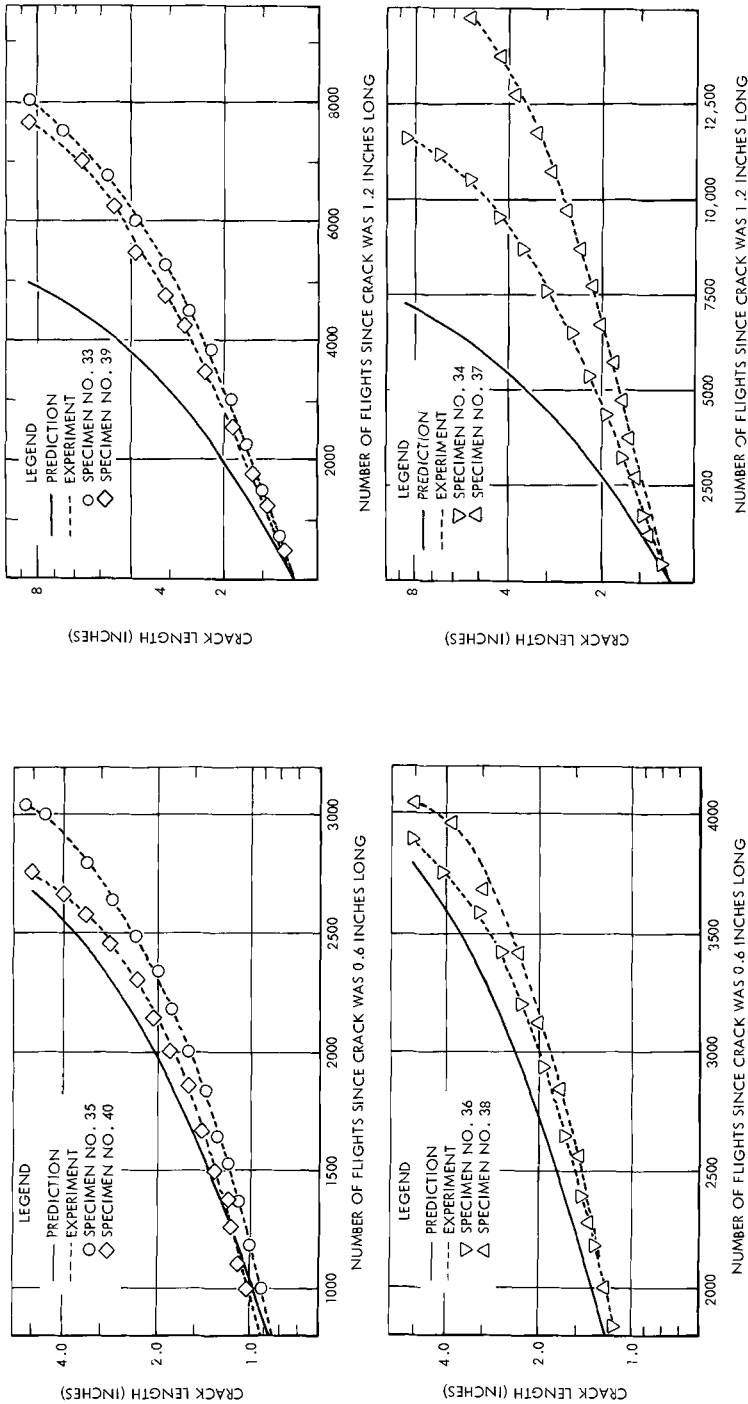
FIG. 4—*Agreement between predicted and experimental crack growth rates for (left) spectrum I, high-stress level, and (right) spectrum II, low-stress level.*

FIG. 5—*Agreement between experimental and predicted crack growth histories: left, spectrum I (top) complete and (bottom) truncated version; right, spectrum II (top) complete and (bottom) truncated version.*
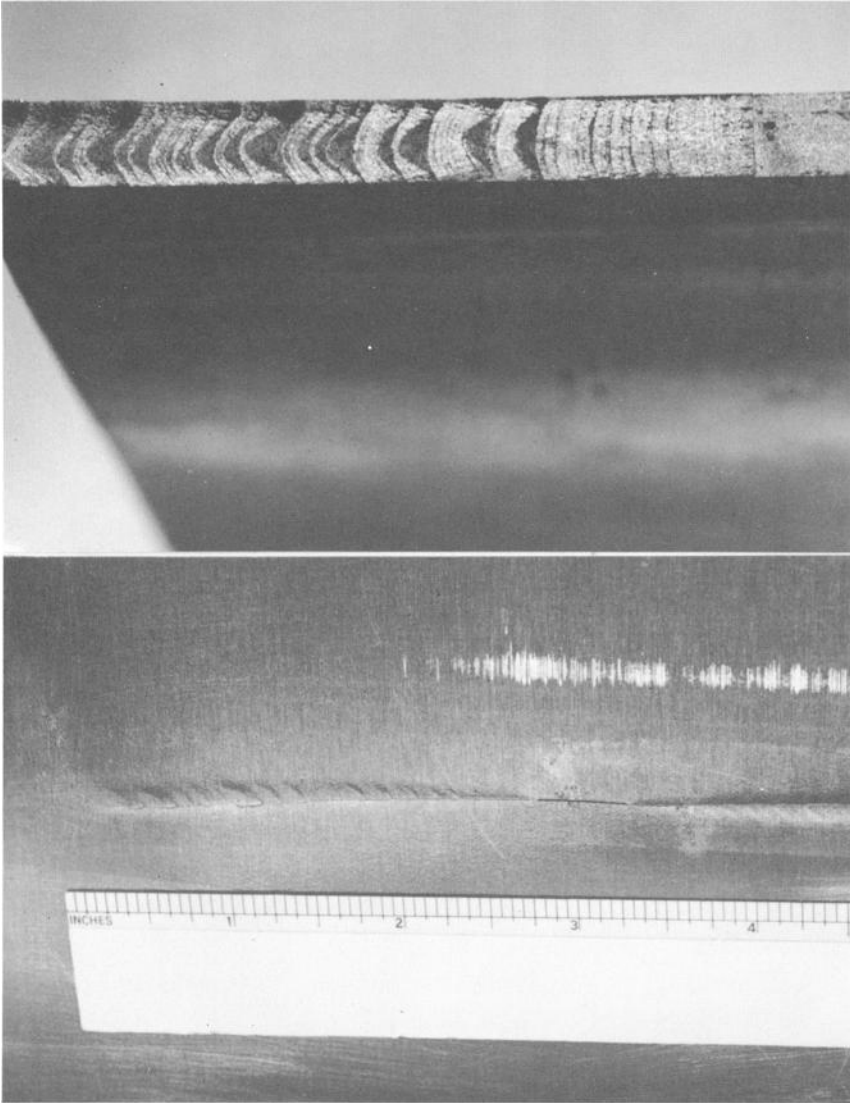
FIG. 6—*Fracture appearance of specimen 35 after variable amplitude fatigue cycling: top, alternating dark and light bands on crack surface; bottom, evidence of extreme local yielding on specimen face.*

or in some cases crack arrest then follows the transition from high- to low-stress cycles. For the present test conditions, these two compensating effects approximately cancelled each other out, and the constant amplitude based prediction was found to be accurate. Similar results are reported for Rayleigh random loading tests on 7079-T6 aluminum [13]; crack growth rates agreed

with constant amplitude based predictions despite evidence of jumps in growth on the fracture surface.

Clearly, however, it would be dangerous to assume that the load interaction effects always cancel. For other classes of spectrum loading or other materials these effects may produce greater deviations between predicted and actual crack growth rates than were observed here. Under certain conditions a factor of three or four difference between predicted and actual rate has been observed [14, 15]. The quantitative prediction of load interaction effects deserves a great deal of study.

Conclusions

Proper scheduling of structural inspections can be made if the probability of failure is known for each structural component as a function of time.

Crack growth is a stochastic process and must be treated as such (at least approximately) to obtain better estimates of failure probability.

Spectrum crack growth rates predicted by use of a Palmgren-Miner type approach with constant amplitude data were accurate within a factor of two. Strong evidence of load interaction effects indicates, however, that this accuracy may not be achieved generally. Efforts should be continued to evaluate first-order load interaction effects for inclusion in the crack growth prediction procedure.

The compression stresses during constant amplitude compression-tension cycling of center cracked specimens tend to increase the crack growth rates. It is hypothesized that for a given material a critical range ratio R_c can be defined such that range ratios less than R_c are assumed to be equal to R_c for purposes of crack growth rate calculation. Then, whatever crack growth rate law is used for tension-tension cycling can be used for compression-tension cycling as well. For 7075 aluminum R_c was calculated to be equal to -0.12.

Acknowledgments

I wish to thank test engineer W. J. Craig for his successful efforts in co-ordinating the test program.

APPENDIX

Probability of Component Failure

By present fracture mechanics theory a residual strength failure of a component containing a crack occurs when the imposed maximum stress intensity exceeds the material fracture toughness. The fracture toughness of any material can be treated as a random variable of approximately log-normal probability distribution [16]. This observation provides the foundation for a means of calculating probability of component failure: it is assumed that the fracture toughness value is random but for a particular component remains fixed regardless of the crack tip location or

prior load history. The mean and standard deviation on log of fracture toughness for a given material and thickness define its cumulative probability distribution $P_{tough}(k)$, which is the probability that the fracture toughness is less than the random variable k.

The crack growth process is divided into a finite number of time intervals, chosen to satisfy two criteria:

1. The probability $P_{peak}(k,n)$ that the maximum stress intensity during the nth time interval is in the range k to $k + dk$ must be known for all n and all k.
2. Each time interval must be sufficiently small that the crack length remains essentially constant throughout the interval for purposes of calculating stress intensity.

Then for the ith possible crack growth history the conditional probability of failure prior to the $T + 1$ such time interval is

$$P_{fail}(T|i) = \int_k^\infty P_{tough}(k)[P_A(k,T) P_B(k,T) dk]. \ldots \ldots \ldots \ldots (11)$$

where

$$P_A(k,T) = 1 - \prod_{n=1}^{T} [1 - P_{peak}(k,n)]. \ldots \ldots \ldots \ldots \ldots (12)$$

is the probability that stress intensity $k \leq K_{max} \leq k + dk$ happens during the first T time periods and

$$P_B(k,T) = \prod_{n=1}^{T} \left[1 - \int_k^\infty P_{peak}(j,n) \, dj \right]. \ldots \ldots \ldots \ldots (13)$$

is the probability that k is not exceeded during these T time periods. Such excess, according to the assumption of a fixed value of residual strength for the structural component, would either fail the component itself or indicate that the fracture toughness was greater than k.

In general, Eq 11 must be integrated numerically by considering the loading spectrum to be "stepped," consisting of a finite number of stress levels (or, if crack length is specified, the same finite number of K_{max} values). If this number of levels is L, and they are numbered consecutively from highest K_{max} to lowest K_{max}, then Eqs 11 through 13 can be approximated as

$$P_{fail}(T|i) \doteq \sum_{g=1}^{L} \left[P_{tough}(k_g) \left\{ 1 - \prod_{n=1}^{T} [1 - P_{peak}(k_g,n)] \right\} \right.$$

$$\left. \times \prod_{n=1}^{T} \left(1 - \sum_{j=1}^{g-1} P_{peak}(k_j,n) \right) \right] \ldots (14)$$

The conditional probabilities for all possible crack histories can then be utilized in calculating the total risk for an inspection interval of time T,

$$P(T) \doteq \sum_{i=1}^{I} P_{fail}(T|i) P_H(i). \ldots \ldots \ldots \ldots \ldots (15)$$

where I is the total number of alternative crack growth histories considered and $P_H(i)$ is the probability of occurrence of the ith such history.

For each stress history used in the spectrum tests of this paper, Eq 14 was applied to calculate probability of failure. For this calculation it was necessary only to evaluate $P_{tough}(k)$ and $P_{peak}(k_g,n)$, the cumulative probability function for fracture toughness and the probability of occurrence of the gth stress intensity level during the nth time interval.

The mean fracture toughness of 7075-T76 aluminum 3/16 in. thick is 79 ksi$\sqrt{in.}$ [17]. It was judged that the value of standard deviation on log of K_c to the base 10 should be 0.06, the value for 7075-T6 aluminum [16]. This fully defined $P_{tough}(k)$.

To apply Eq 14 the time history is divided into a finite number of time intrevals and $P_{peak}(k,n)$ applies to the nth such interval. If the interval length is chosen to be one flight, then $P_{peak}(k,n)$ becomes the probability that the largest K_{max} for the nth flight exceeds random variable k. This probability can be obtained directly from Table 3. The largest K_{max} for any flight is the one caused by the peak-to-peak GAG cycle. Let S_{max_g} be the maximum stress for the gth possible GAG cycle listed in the first set in Table 3. Assuming the nth flight occurs when the crack length is $2a$,

$$k_g = S_{max_g}[\pi a \sec(\pi a/w)]^{1/2} \dots\dots\dots\dots\dots\dots\dots(16)$$

Its probability $P_{peak}(k_g,n)$ of occurrence during the nth flight is given in the Cycles per Flight column of Table 3. (As required, the total cycles per flight over all GAG cycles in Table 3 is one, indicating certainty that exactly one of these cycles will occur each flight.)

Equation 14 can now be applied to calculate failure probability for any time T. In this calculation it is necessary only to consider the few highest stress levels and the time just prior to time T to obtain convergence to the algebraically correct answer. T was chosen to be the time necessary to attain the crack length at which each spectrum test was stopped, as predicted from constant amplitude data.

The calculated probability of failure results are given in Table 4. Because all tests were stopped prior to failure, no experimental check on the calculated failure probabilities could be obtained, except that the nonfailure of these specimens is consistent with the low failure probabilities calculated.

TABLE 4—*Calculated probability of failure for specimens tested.*

Spectrum Description	Final Crack Length, in.	Final Probability of Failure
Spectrum I: complete.........	5.10	0.058
Spectrum I: truncated.........	5.10	0.073
Spectrum II: complete........	8.5	0.041
Spectrum II: truncated........	8.55	0.050

References

[1] Walker, E. K. in *Effects of Environment and Complex Load History on Fatigue Life*, *ASTM STP 462*, American Society for Testing and Materials, Jan. 1970, pp. 1–14.
[2] Forman, R. G., Kearney, V. E., and Engle, R. M., "Numerical Analysis of Crack Propagation in Cyclic-Loaded Structures," ASME Paper No. 66-WA/Met-4, American Society of Mechanical Engineers, Aug. 1966.
[3] Hudson, C. M., "Effects of Stress Ratio on Fatigue Crack Growth in 7075-T6 and 2024-T3 Aluminum Alloy Specimens," NASA Report TN D-5390, National Aeronautics and Space Administration, Aug. 1969.
[4] Hudson, C. M., "Fatigue Crack Propagation and Residual Static Strength of 15PH-7Mo (TH 1050) Stainless Steel," NASA Report TN D-3151, National Aeronautics and Space Administration, Dec. 1965.

[5] McEvily, A. J. and Illg, W., "The Rate of Fatigue-Crack Propagation in Two Alumi-num Alloys," NACA Technical Note TN 4394, National Advisory Committee for Aeronautics, Sept. 1958.

[6] McEvily, A. J. and Illg, W., "The Rate of Fatigue-Crack Propagation for Two Alumi-num Alloys Under Completely Reversed Loading," NASA Technical Note TN D-52, National Aeronautics and Space Administration, Oct. 1959.

[7] von Euw, E. F. J., "Effect of Single-Peak Overloading on Fatigue-Crack Propagation," Masters thesis, Lehigh University, 1968.

[8] Hudson, C. M. and Raju, K. N., "Investigation of Fatigue-Crack Growth Under Simple Variable-Amplitude Loading," NASA Technical Note TN D-5702, National Aeronautics and Space Administration, March 1970.

[9] Schijve, J., Jacobs, F. A., and Tromp, P. J., "Crack Propagation in 2024-T3 Alclad Under Flight-Simulation Loading. Effect of Truncating High Gust Loads," NLR TR 69050U, National Aerospace Laboratory, Amsterdam, June 1969.

[10] McMillan, J. C. and Pelloux, R. M., *Engineering Fracture Mechanics*, EFMEA, Vol. 2, No. 1, July 1970, pp. 81–84.

[11] Walker, E. K., "A Study of the Effect of Crack Propagation in 7075-T76 Aluminum Alloy for Dry Air and Corrosive Environments," Report No. LR 23124, Lockheed-California Co., Dec. 1969.

[12] McMillan, J. C. and Pelloux, R. M. N. in *Fatigue Crack Propagation, ASTM STP 415*, American Society for Testing and Materials, 1967, pp. 505–535.

[13] Swanson, S. R., Cicci, F., and Hoppe, W. in *Fatigue Crack Propagation, ASTM STP 415*, American Society for Testing and Materials, 1967, pp. 310–362.

[14] Schijve, J. and Broek, D., *Aircraft Engineering*, AIENA, Nov. 1962, pp. 314–316.

[15] Schijve, J. and DeRijk, P., "The Crack Propagation in Two Aluminum Alloys in an Indoor and Outdoor Environment Under Random and Programmed Load Sequences," NLR-TR M.2156, National Aerospace Laboratory, Amsterdam, Nov. 1965.

[16] Liu, A. F., "Statistical Variation in Fracture Toughness Data of Airframe Materials," presented at Air Force Conference of Fatigue and Fracture of Aircraft Structures and Materials, Miami Beach, Fla., Dec. 1969.

[17] Liu, A. F., "Fail-Safe Allowables, L-1011 Materials," Report No. LR 22652, Lockheed-California Co., Jan. 1970.

W. D. Graziano[1] and G. E. Fitch, Jr.[1]

Initiation and Growth of Fatigue Cracks in and Residual Strength of the F-100 Wing

ABSTRACT: Full scale fatigue tests were conducted on the F-100 wing. Service connected fatigue failure data were collected and compared with test results. Test lives to initiate fatigue cracks are compared with predicted lives using Miner's rule of linear cumulative damage and by a method accounting for plasticity at the crack origin. Calculated failure stresses using the principles of fracture mechanics are compared with laboratory test failure data. Crack growth data measured during testing are compared with values predicted from the relation dl/dN versus ΔK, the range in the stress intensity factor. Modifications to the wing structure are described, and the resulting fatigue life improvement is presented.

KEY WORDS: military aircraft, airframes, wings, failure, fatigue (materials), cracking (fracturing), crack propagation, cyclic loads, fracture strength, residual strength, aluminum, fatigue tests

Full scale fatigue tests of the F-100 airframe, conducted as a part of a comprehensive structural integrity program for the U.S. Air Force, Sacramento Air Material Area (SMAMA), McClellan AFB, Calif., offered a unique opportunity for the study of the growth of fatigue cracks and their effect on the strength of actual aircraft structures. The principles of fracture mechanics, virtually unknown to the aircraft industry at the time the F-100 was designed, are now a valuable tool necessary to describe the behavior of structures damaged by the initiation of fatigue cracks. In fact, if extensions of the theory [1][2] are accepted in their entirety, the entire useful life of the structure from fabrication to final failure can be described adequately only by the use of fracture mechanics. It is the intent of this paper to show the correlation between the theoretical strengths and crack growth rates at three service locations and the laboratory fatigue cracks in the F-100 wing structure.

---

[1] Supervisor, Structures, and member of technical staff, respectively, North American Rockwell/LAD, Los Angeles International Airport, Los Angeles, Calif. 90009.

[2] Italic numbers in brackets refer to the list of references at the end of this paper.

Experimental Program

Description of F-100 Wing

The wing outer panel (WOP) of the F-100 is of multispar plate construction in the inboard section and of integrally stiffened multirib construction over the outboard one third of the span. The upper and lower skins, Fig. 1, are sculptured from 7075-T651 bare aluminum plate. The maximum thickness of the lower skin is 1.50 in. at the wing root, and the minimum thickness is 0.070 in. in pocket areas near the tip. The wing center section (WCS) is a simple box structure, Fig. 2, with upper and lower covers consisting of two skins, each separated by spacer bars. The skins are tapered from 0.40 in. at the rear beam to 0.25 in. at the front beam and are made from 7075-T6 aluminum rolled plate. The outer panels and center section are spliced inboard of the heavy root rib by a step tapered double shear joint with three rows of bolts.

Description of Fatigue Tests

During the structural integrity program, five different wing assemblies were fatigue tested to a realistic flight-by-flight loading spectrum. The test setup, shown in Fig. 3, incorporated a servo-closed loop system controlled by MTS Systems Corp. Data Trak and Servac control units. Maneuver-gust load cycles were applied at various, randomly sequenced magnitudes, including down bending from infrequent negative load factors.

Main landing gear load cycles representing landing, taxi, and ground handling conditions were applied, together with 1-g down bending loads to complete the ground-air-ground nature of the loading spectrum. The spectrum used was derived from a fatigue load statistical survey conducted during the first calendar year of the program and utilizing 122 instrumented aircraft throughout the fleet. The initial test goals were 11,000 h for the unmodified structure. Those areas which failed to survive the 11,000-h test or were shown deficient by fatigue analysis were then considered for design modification.
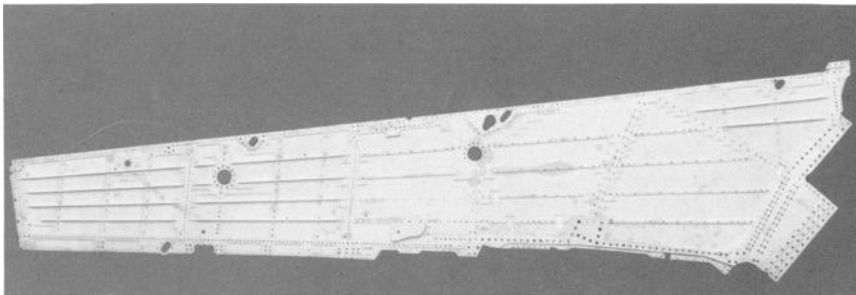

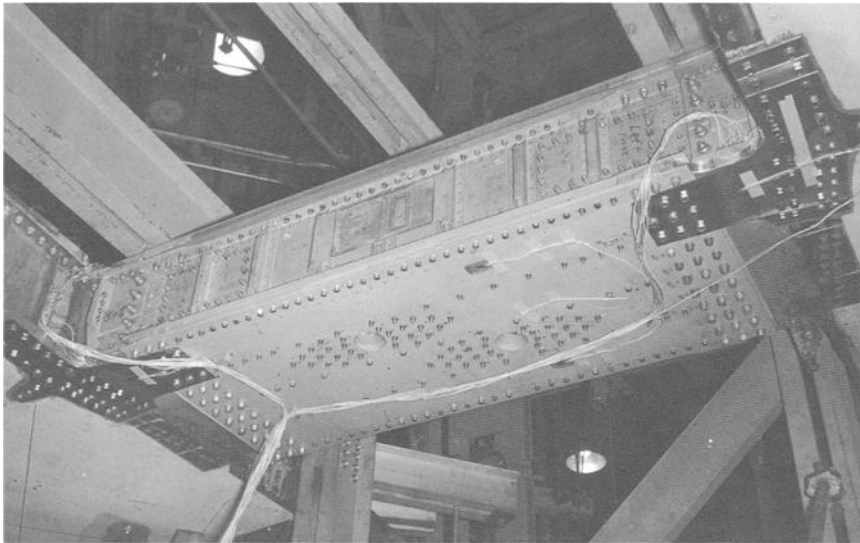FIG. 1—*F-100 wing outer panel milled skin.*

FIG. 2—*Wing center section assembly.*

Fatigue Failures

Three important failures which had the most impact on the modification program will be discussed in this paper. Of the three shown in Fig. 4, only the wing root fillet failure had been experienced in the fleet prior to the laboratory failures. A summary of pertinent fatigue data of the three cracks is shown in Table 1. Note that test lives exceed service life in all cases. This is due to the fact that the test life includes the prior service history of the specimen, 2800 h. When prior service history was subtracted from the total test time, or when virgin specimens were tested, there was good agreement between test life and the early fleet failures, indicating a conservative loading spectrum. Predicted lives were calculated by Miner's rule and are typically, for a fighter spectrum, conservative. For the wing root fillet crack, a plasticity correction was applied in a manner developed by C. R. Smith [2] and the agreement with the test results is much better.

Lower Skin 51 percent Spar Bolt Hole—The first, full scale wing fatigue test specimen failed in 4674 h total, test plus service hours. The failure was complete full chord across the wing structural box. The fracture surface is shown in Fig. 5, with the initiating fatigue crack emanating from a bolt hole at the 51 percent spar. This spar is located approximately 6.5 in. forward of the rear spar. The fracture shows intermittent slow and rapid growth areas typical of spectrum loading prior to attainment of the critical lengths approximately 0.37 in. from the edge of the bolt hole.

Wing Root Skin Fillet—Cracking had occurred in service on Thunderbird demonstration aircraft prior to the laboratory test failure shown in Fig. 6.

TABLE 1—*Summary of fatigue failures.*

Wing Assembly	Maximum Spectrum Stress Level, psi	Geometric Stress Concentration, K_t	Predicted Life, h	Test Life,[a] h	Average Service Life, h
WOP lower skin 15 percent spar bolt hole...........	34 300[b]	2.5	1 120	4 500 (1 failure)	2 140 (2 failures)
WOP lower skin 51 percent spar bolt hole with strap.....	18 400	2.5	27 000	7 500	No failures
WOP lower skin wing root fillet, Thunderbird crack..	23 000	4.7	4 460	5 508	2 530 (7 failures)
WCS lower cover outer skin bolt hole..	39 000	2.5	2 600	6 192	2 890 (1 failure)

[a] Includes 2800 h of service life.
[b] Spectrum reduced from value shown in Table 2 subsequent to failure.
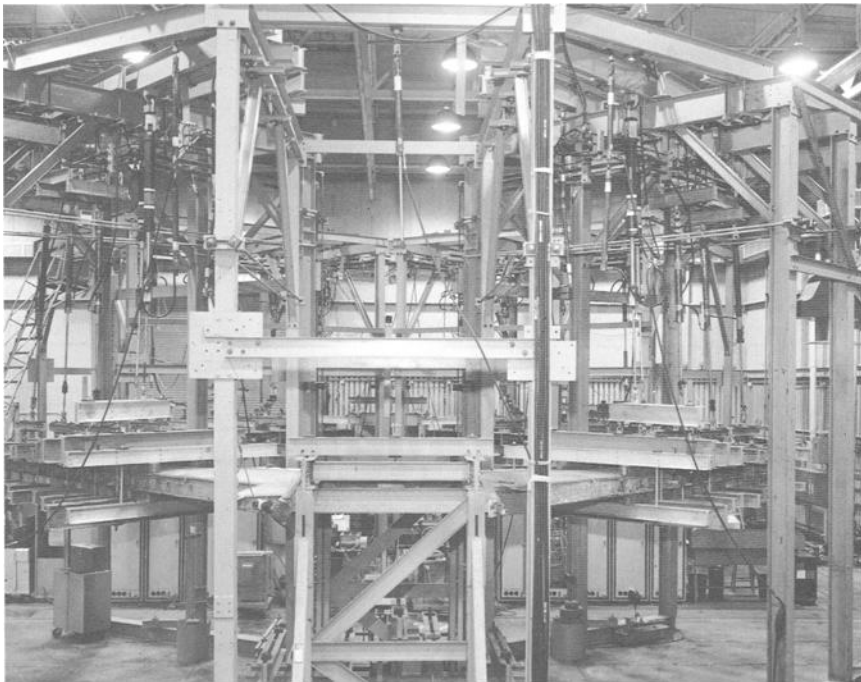
FIG. 3—*Wing fatigue test setup.*
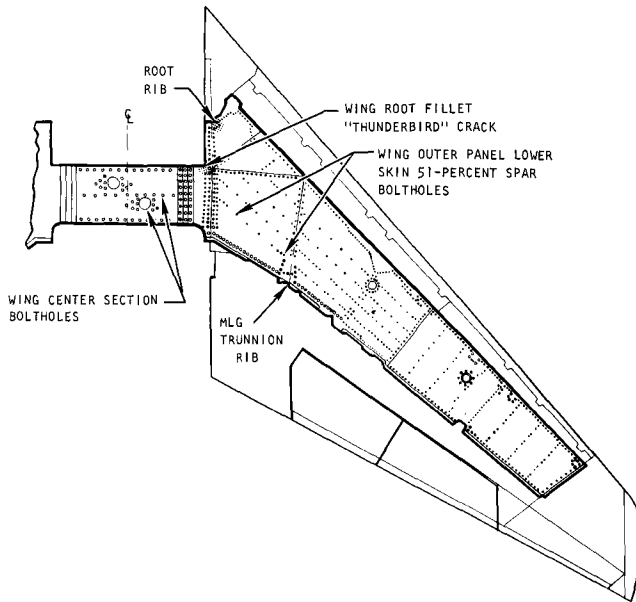
FIG. 4—*Location of fatigue cracks in F-100 wing structure.*

The crack shown is in the lower skin. Both the upper, compression, skin and the lower, tension, skin have been subject to fatigue cracking in this area—with the upper skin cracking most frequently. Neither upper nor lower cracks have caused complete failure. The lower skin fillet crack becomes critical at a minute size and propagates rapidly to the first bolt hole at least and as far as the crack shown in the figure.

The alternate load path provided by the heavy flange of the root rib is considered to be the reason why cracks have stopped short of full chord failure.

Wing Center Section Bolt Hole—The third failure, shown in Fig. 7, was full chord in the outer skin of the wing center section; however, the inner skin did not fail. This could have been due to load dumping features of the loading system, which were activated by the failure rather than inherent damage tolerance of the double skin design. Subsequent to the laboratory failure, a fleet failure did occur in the wing center section, and both skins of the lower cover ruptured causing loss of the wing.

Fracture Strength Analysis

The methods described by Paris [3] and Tiffany [4] were used to predict the stresses at failure in the three crack locations. The wing outer panel lower skin bolt hole crack was analyzed as a through crack from one side of the bolt hole. The critical stress intensity factor is

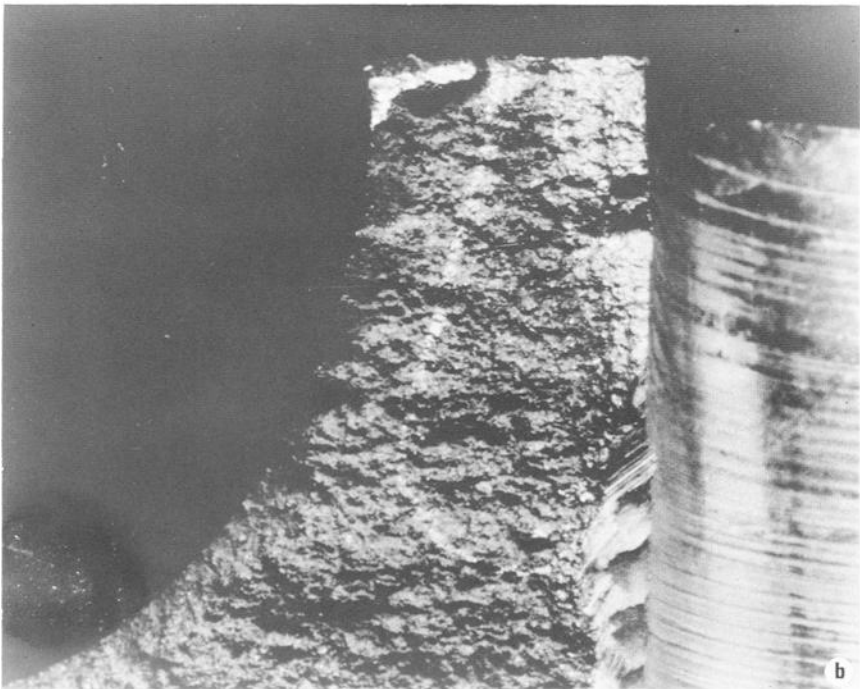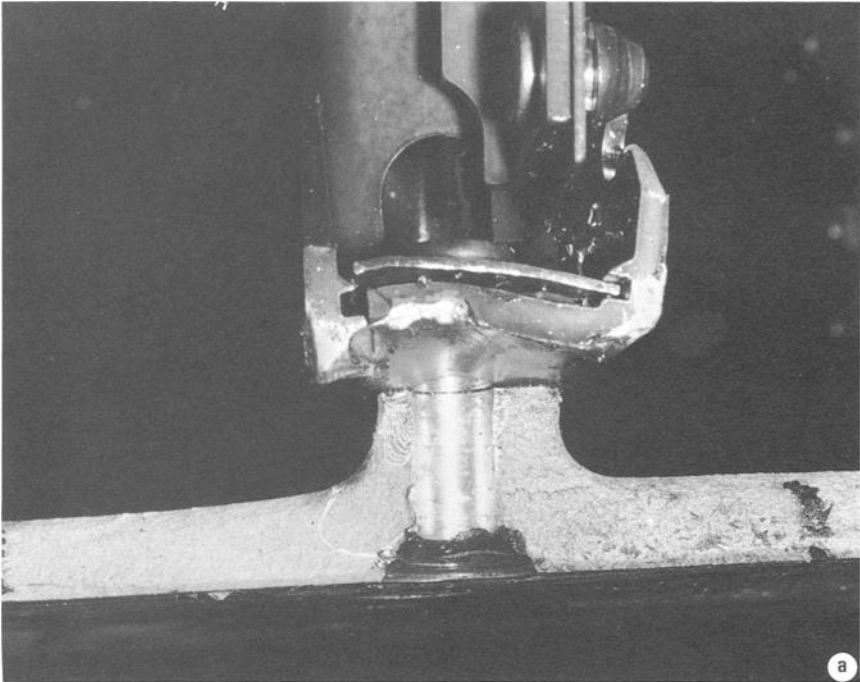$$K_{\mathrm{I}c} = \sigma_g \sqrt{L_c \pi}\ F(L/r)$$

FIG. 5—*Lower skin wing outer panel fatigue cracks 51 percent spar bolt hole:* (a) *laboratory failure, 4674 h;* (b) *service failure, 2140 h.*
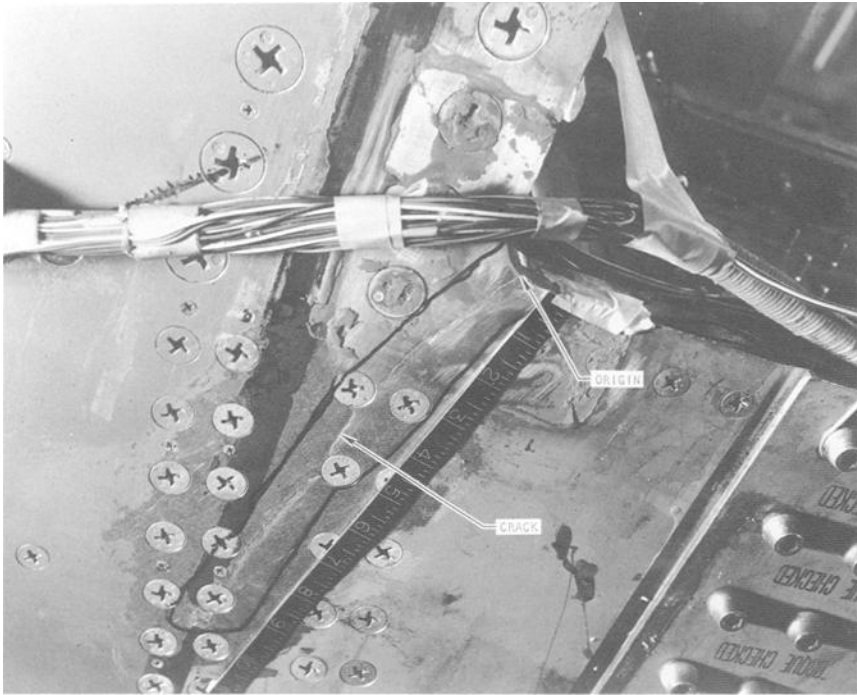
FIG. 6—*F-100 lower skin wing root fillet crack (Thunderbird crack).*

where

σ_g = gross stress,
K_{Ic} = the plane strain critical stress intensity factor,
L_c = crack length = 0.37 in.,
$F(L/r)$ = stress concentration due to bolt hole, and
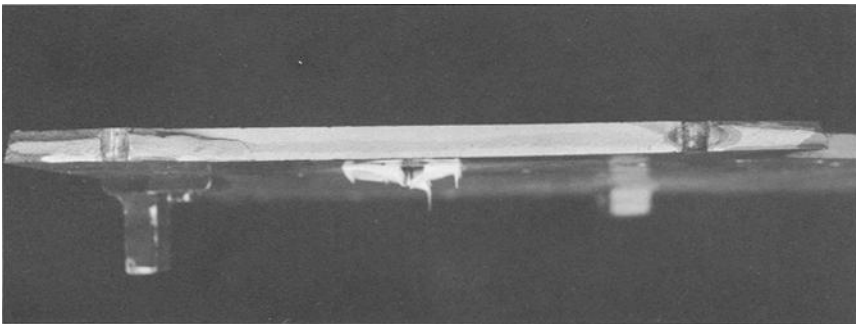r = radius (bolt hole) = 0.156 in.

FIG. 7—*F-100 wing center section lower skin crack.*

The WOP root fillet crack was analyzed as an edge crack in an infinitely wide sheet,

$$K_{Ic} = 1.12\sqrt{\pi a_c}\,\sigma_g$$

where a_c, the total crack length measured from the edge of the plate, $= 0.25$ in.

The wing center section crack was analyzed as a through crack with the stress field influenced by the presence of a bolt hole,

$$K_c = \sigma_g\sqrt{L\pi}\,F(L/r)$$

where K_c is the critical mixed mode stress intensity factor from Fig. 8 for 0.30-in. thickness.

The wing center section crack was analyzed also as a completely enclosed elliptical crack:

$$K_{Ic} = (1.1)\sqrt{\pi}\,\sigma_g\sqrt{a_{cr}/Q_{cr}}$$

where

    $a =$ short semiaxis of ellipse $= 0.16$ in.,
    $c =$ long semiaxis of ellipse $= 0.45$ in., and
    $Q = \phi^2 - (0.212)\,(\sigma_g/\sigma_{ys})^2$,

where

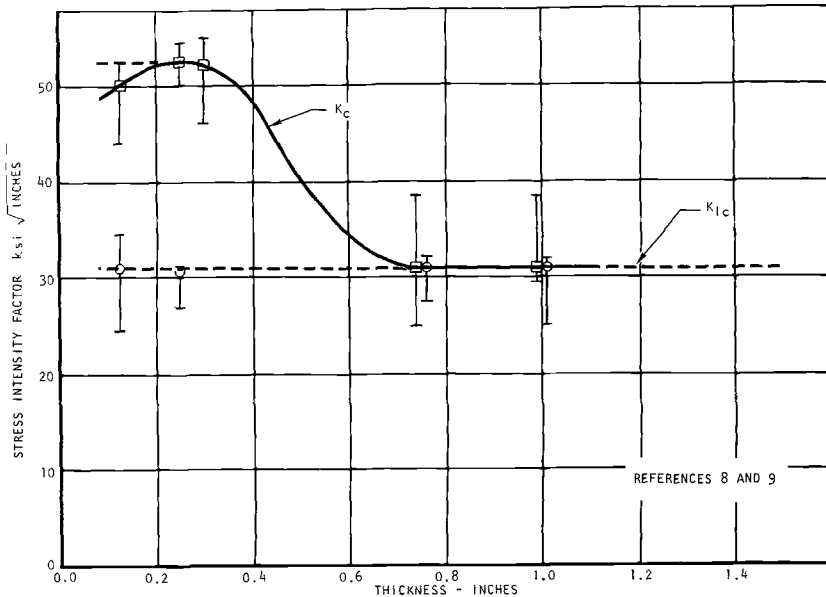$$\phi = \int_0^{\pi/2} [\sin^2\phi + (a/c)^2\cos^2\phi]^{1/2}d\phi$$

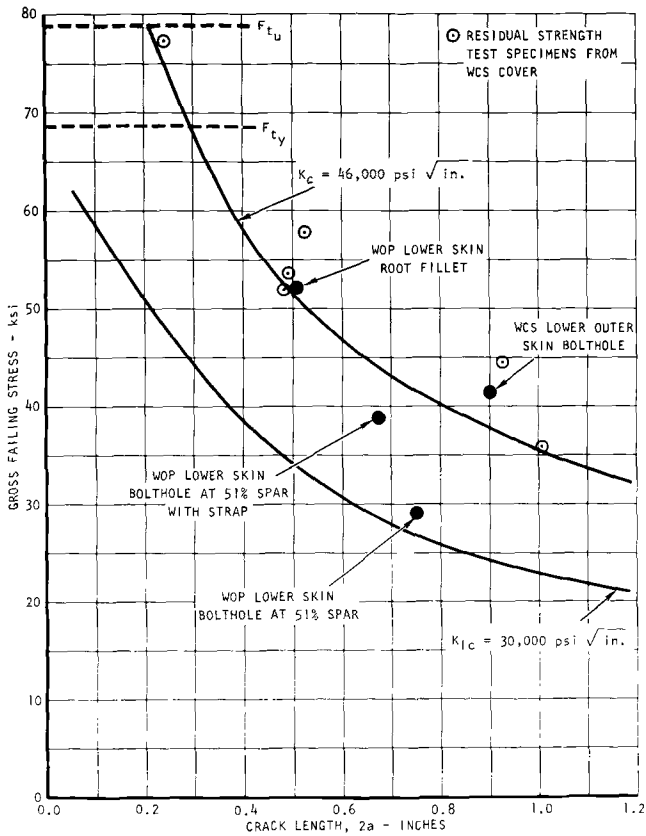FIG. 8—*Stress intensity versus thickness, 7075-T6 aluminum.*

FIG. 9—*Residual strength test data comparison.*

The geometry of all the cracks and the results of the calculations are summarized in Table 2. The critical stress intensity factors for 7075-T6 aluminum are shown in Fig. 8. If the mixed mode K_c value had been used for the outer panel 51 percent spar bolt hole, better agreement with applied stresses would have been obtained.

Shown in the table is the crack length at this bolt hole with a reinforcement strap installed. The strap lowered the stress levels in the skin so that the critical crack length was longer. The effect of the strap, which did not fracture in the test, was accounted for by a correction factor calculated by the method of Bloom [5]. The correction factor was small, 0.93, because of the short crack length compared to spar spacing and, also, the geometry of the strap and fastener spacing.

The stress level in the fillet area for comparison to flawed strength was calculated by means of a fine-grid triangular element energy program, which was used to analyze the fillet area to study the effect of fillet radius enlargement on fatigue life. Because of the small critical size of a natural fatigue crack, the predicted flaw strength shown in Table 2 refers to a 0.25-in. crack,

artificially induced for a residual strength test which will be discussed later in the paper.

The bolt hole in the wing center section at which the crack initiated is adjacent to a larger, 3.0-in.-diameter hole. The local stress level shown in the table accounts for the stress concentration factor imposed by the larger hole at the location of the bolt hole.

The predicted strengths and test failures are compared also on a chart of crack length versus gross stress in Fig. 9.

Crack Growth 51 percent Spar Bolt Holes

Subsequent to the complete wing failure in the lower wing skin at the 51 percent spar bolt hole, visual observations with a binocular microscope were made of crack growth in similar bolt holes on fatigue test panels. The crack growth was predicted in the manner suggested by Paris [1]. For this purpose, dl/dn data for 7075-T6 aluminum taken from Ref 6 are shown in Fig. 10. Both the upper and lower bounds of the scatter of the dl/dn were
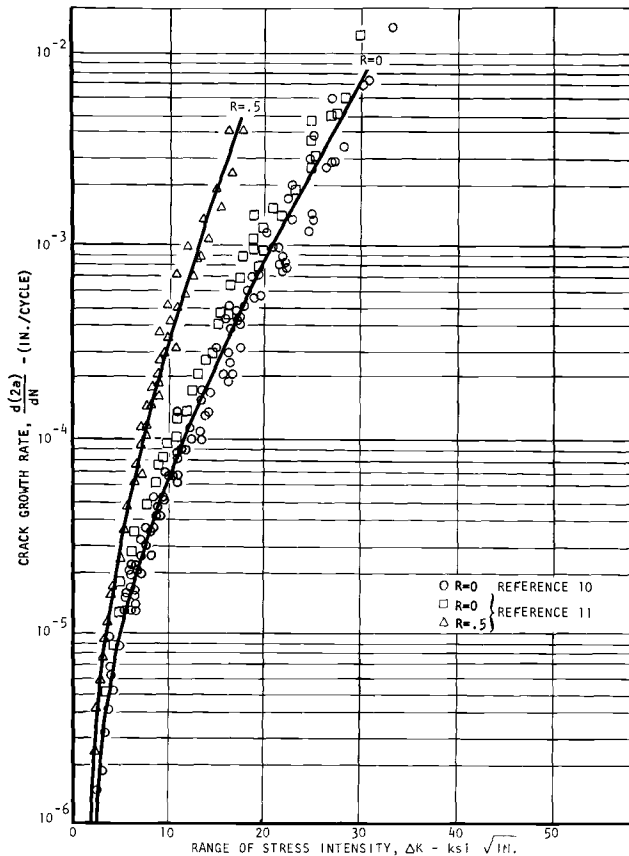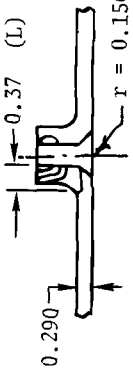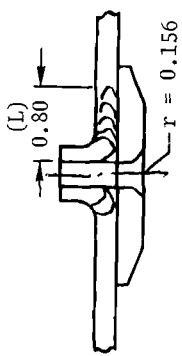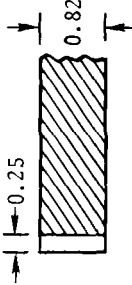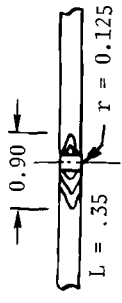

FIG. 10—Crack growth rate versus range of stress intensity.

TABLE 2—Summary of residual strength calculations.

Location	Analytical Stress, psi	Strain Gage Stress, psi	Crack Size, in.	Theoretical Failure Stress, psi	
				Through Crack	Alternate Method
WOP lower skin bolt hole at 51 percent spar..........	39 000	34 600		28 000	...
With strap..........	19 200	29 000		18 600	Correction for stringer $\beta = 0.93$ 20 000
WOP lower skin root fillet......	52 200	Not available		30 300	...
WCS lower outer skin gross.......... with fuel hole K_t..........	28 900 41 400	26 900 Not available		27 200 38 900	Elliptical crack 29 400 42 000

CRACK GROWTH IN 51-PERCENT SPAR BOLTHOLE

FOURTH BOLTHOLE OUTBOARD OF ROOT RIB ON 51-PERCENT
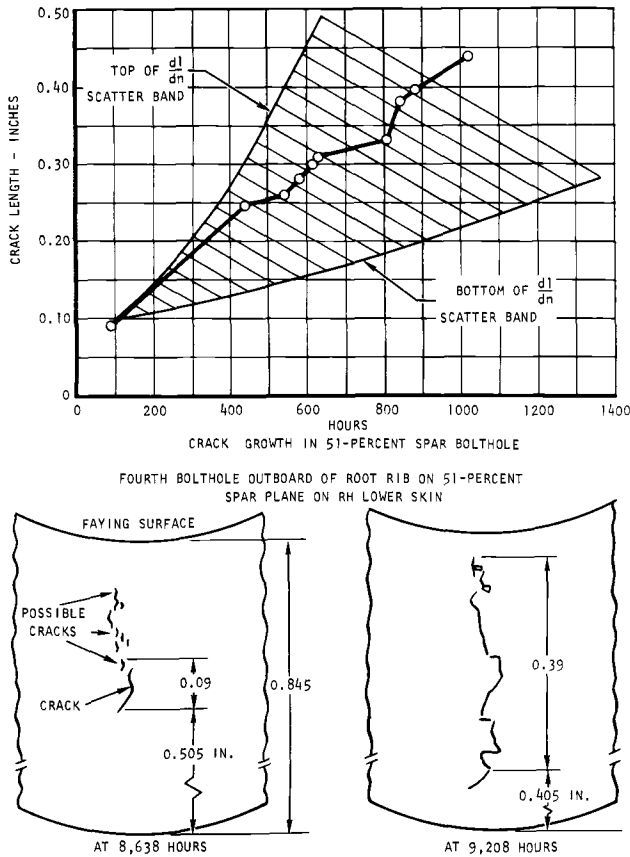SPAR PLANE ON RH LOWER SKIN

FIG. 11—*Growth of crack in 51 percent spar bolt hole.*

used, and the results are shown in Fig. 11. The growth measured by optical means falls within the scatter of the predicted growth curves. Figure 12 shows the actual crack sectioned after the test. The total crack length in this case was made up of many smaller semielliptical cracks joining to form the final sectioned shape.

Residual Strength Test Root Skin Fillet Crack

A simulated crack was imposed on the skin fillet at the wing root by means of a saw cut, Fig. 13*a*. The intent was to grow a natural crack from the ¼-in. saw cut prior to the residual static strength test. Before attaining the load level selected for cycling, the crack became unstable and grew rapidly to the first bolt hole, as shown in Fig. 13*b*. Later analysis, as summarized in Table 2, indicated that this should have been expected because of the high stress level in the fillet area. The residual strength test was continued, and the wing sustained 130 percent of limit load before the crack ran rapidly to the bolt hole,
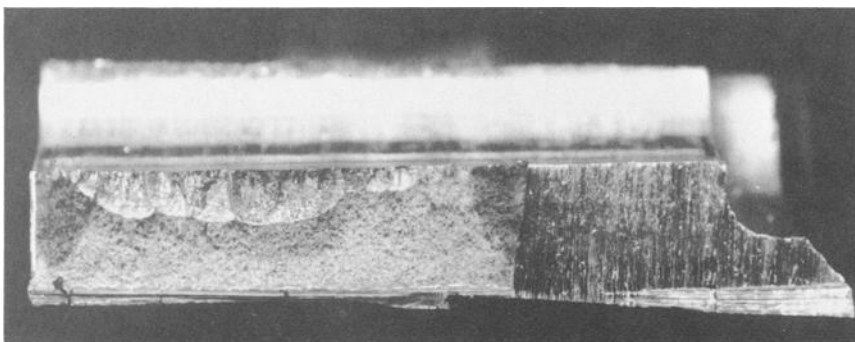
FIG. 12—*Crack progression in lower skin wing outer panel 51 percent spar bolt hole.*

as shown in Fig. 13c. This test demonstrated the damage tolerance of the design configuration caused by the presence of the massive root rib in this location. The same specimen sustained ultimate load, 150 percent of limit, with a doubler reinforcement in the fillet area.

Wing Center Section Crack Propagation Tests

Following the full scale laboratory test failure and a similar service failure, an inspection teardown program was initiated to determine the crack condition of fleet aircraft. Over 80 wing center section lower covers from aircraft with 2500 to 4000 service hours were shipped to the Los Angeles Division of North American Rockwell to receive a thorough inspection of the bolt holes for cracks. Cracks less than through-the-thickness were found in all panels. The number of cracks found in each panel was correlated with service hours as shown in Fig. 14.

Over 30 test specimens, 4 in. wide, were cut from the inspection panels, as shown in Fig. 15. The first series of tests indicated that the partly through service cracks would not propagate rapidly. In fact, these specimens exhibited spectrum fatigue lives well within the scatter of virgin test specimens. To obtain crack growth data representing the worst case, through cracks were induced in subsequent test specimens by means of a saw cut and constant load level cycling. Then the specimens were subjected to a realistic load spectrum identical to that used for the full scale wing fatigue tests. The specimen data are shown in Table 3. Three different spectra were used in these tests:

(1) the unrestricted, statistically based spectrum representing a 7.33-*g* load factor,

(2) a 6-*g* load factor spectrum representing fleet operations restricted to maneuver load factor of 6 *g*, and

(3) a 4-*g* load factor spectrum representing fleet operations restricted to 4-*g* maneuver load factor.

TABLE 3—Crack growth specimen data.

| Specimen No.	Material Properties 7075-T6 Bare Plate			Constant Load Cycles to Initiate Crack			Spectrum, g	Spectrum Test		
	F_{tw}, ksi	F_{ty}, ksi	Elongation, %	Gross Stress, ksi	Cycles, N	Crack Length, in.		Load Block Size, h	Hours To Fail	Final Crack Size, in.
1........	82.1	74.3	11.5	15.0	11 000	0.33	6	50	1250	1.25
2........	83.5	77.8	12.0	15.0	50 000	0.34	6	50	950	1.45
3........	84.4	77.3	11.5	15.0	44 500	0.40	6	50	450	1.65
4........	83.8	75.1	9.0	15.5	4 000	0.27	4	20	1260	1.35
5........	79.7	73.2	13.5	15.5	7 000	0.35	4	20	1160	1.39
6........	86.6	79.7	9.0	15.5	8 500	0.31	4	20	900	1.36
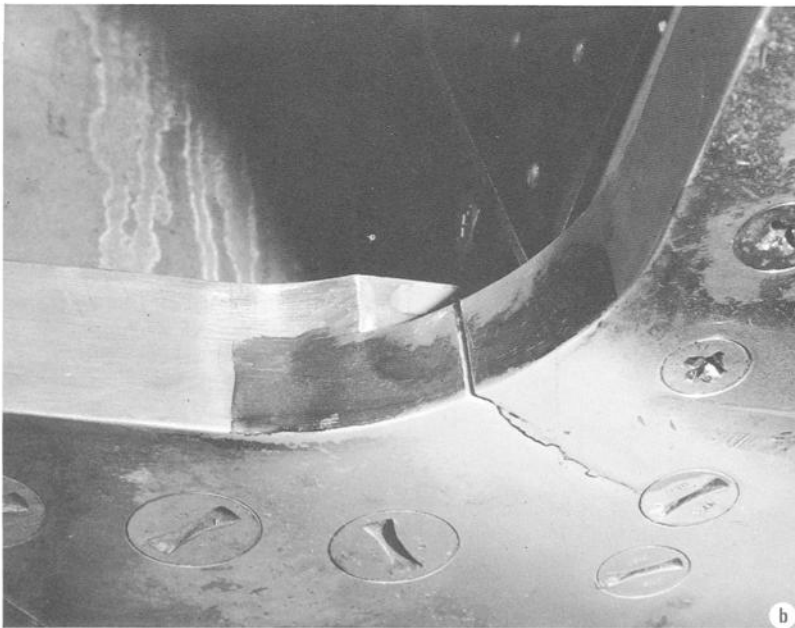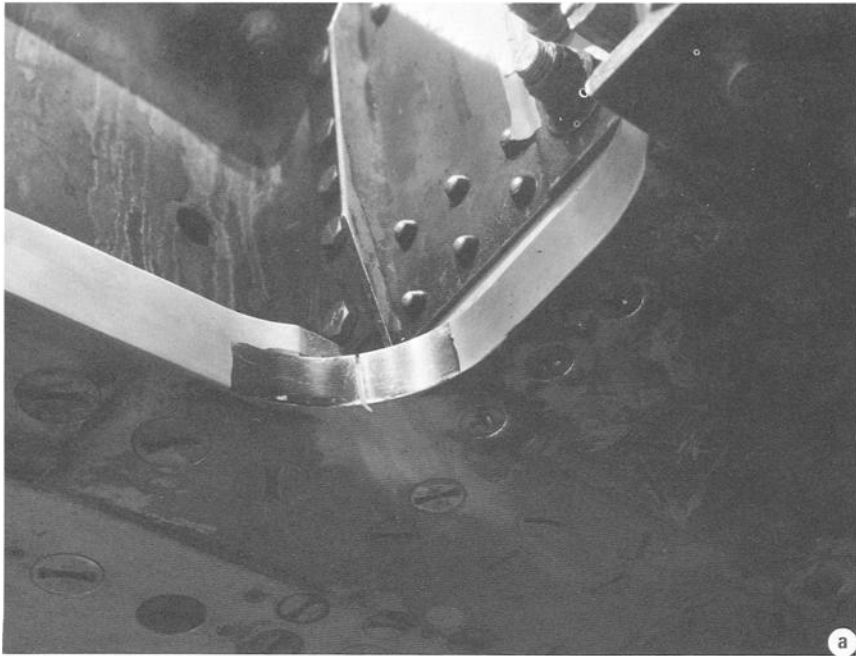
FIG. 13—*Wing root fillet residual strength test crack progression:* (a) *saw cut;* (b) *crack at 58 percent limit load.*
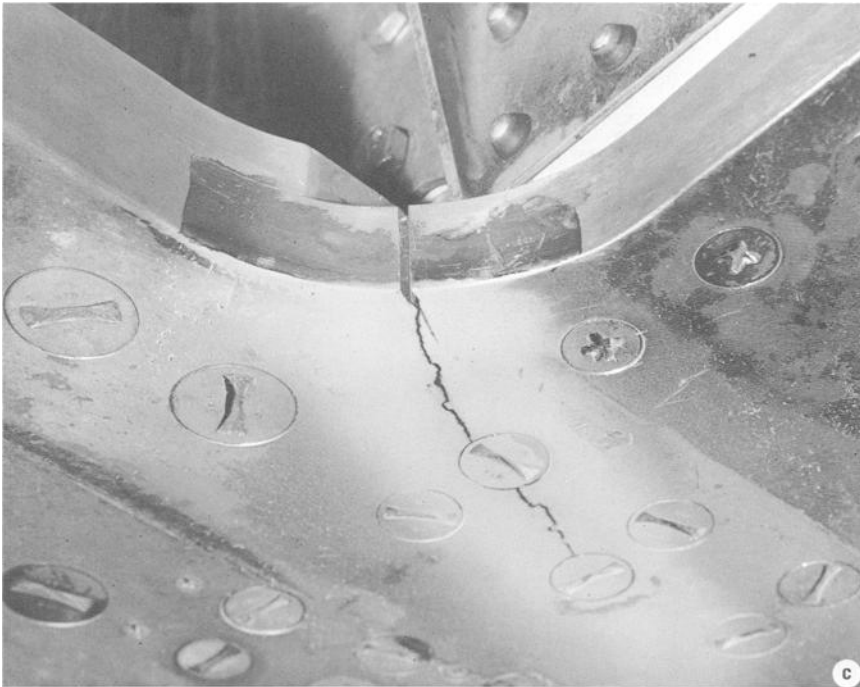
FIG. 13—*Continued:* (c) *crack at 130 percent limit load.*

The results of these tests are shown in Fig. 16, compared to predicted growth curves. The unrestricted spectrum grew cracks so rapidly that growth data could not be obtained. The predicted curves were calculated in the manner suggested by Paris [*1*] using cyclic growth rate data for 7075-T6 aluminum shown in Fig. 10. In all cases—unrestricted, 6-*g*, and 4-*g* spectra— the predicted crack growth rate was greater than the actual growth rate. A computer program based on Forman's equation for fitting crack growth data [*7*] was used to calculate growth rates also. The computer program results were more conservative than hand calculations because a more severe growth rate curve was used with the program.

The results of these tests were used, conservatively, to (1) establish flight limitations on maneuver load factor in the fleet and (2) establish a safe time period, in service hours, to modify all fleet aircraft with redesigned wing center section lower covers. A 4-*g* flight restriction was issued to the fleet, and all aircraft were modified with new wing center lower covers prior to attainment of 450 service hours subsequent to the teardown inspection program.

Wing Modifications

As a result of the full scale fatigue tests and fatigue analysis, modifications were designed and tested to improve the fatigue life.
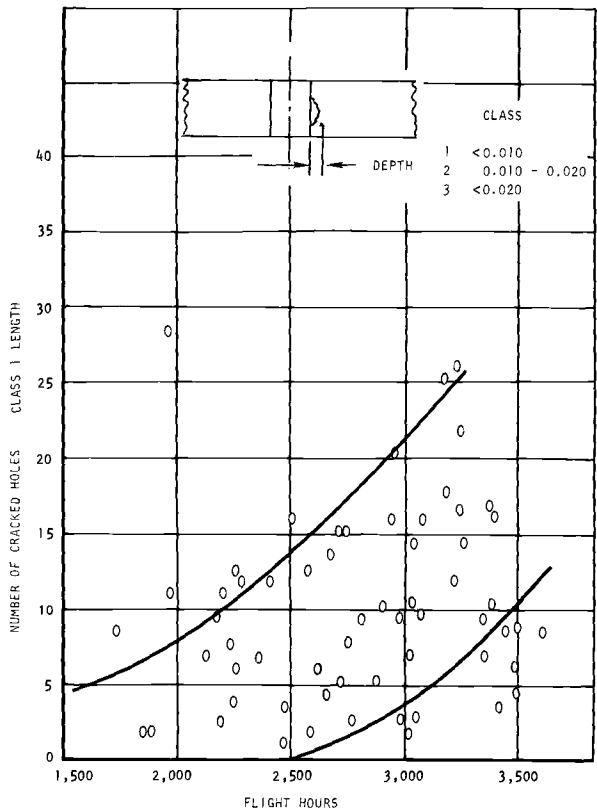
FIG. 14—*Correlation of number of cracked holes with flight hours.*
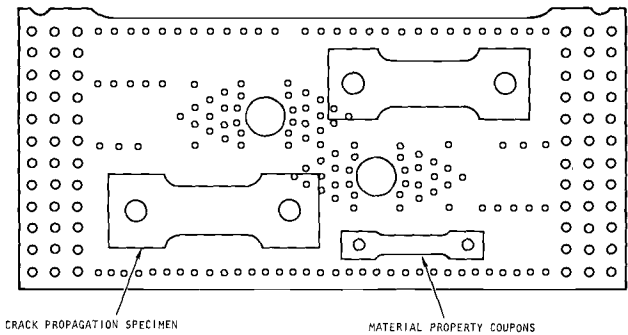
FIG. 15—*Crack propagation specimens from wing center section panels.*

Figure 17 shows an external strap added to the wing outer panel lower skin along the 51 percent spar plane. The purpose of the strap was to delay crack initiation in the skin bolt holes and to provide residual static strength capacity after crack initiation. As shown by the fracture surface in the figure, the strap did increase the crack length requisite to cause failure by lowering

the local stress intensity. The critical crack length was increased; however, the strap was incapable of preventing full chord failure at the maximum spectrum load level. Also, the crack was much less detectable with the presence of the strap.

Because of this test and fatigue cracking in other bolt holes in the lower skin, the strap which had been installed throughout the fleet was determined
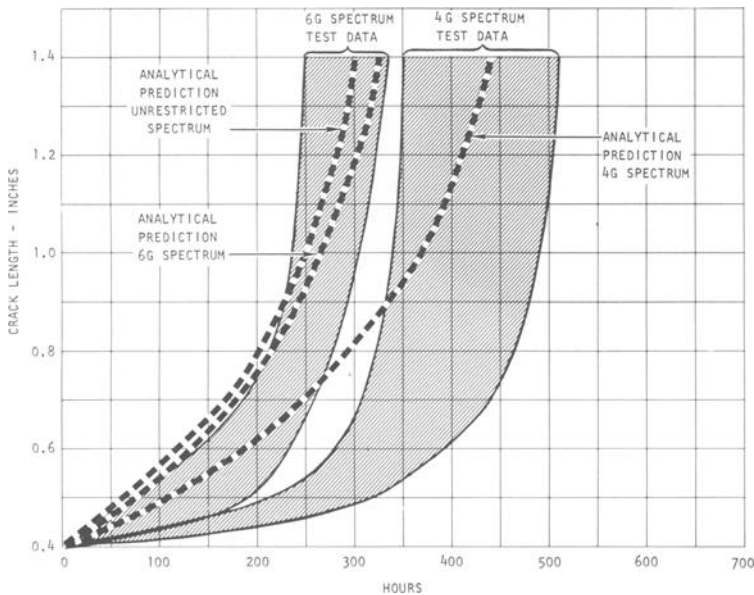

FIG. 16—*Wing center section crack growth curves.*

FIG. 17—*Fatigue crack in lower skin wing outer panel 51 percent spar bolt hole with strap.*
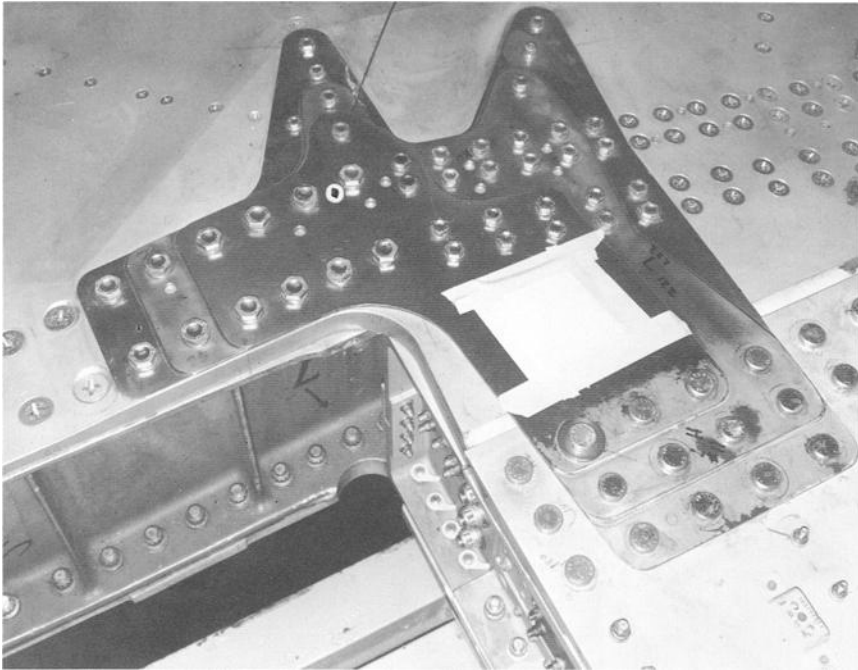
FIG. 18—*Reinforcing doubler lower skin wing outer panel wing root fillet.*

to be incapable of attaining planned service life goals. A decision was reached to install new lower skins on the wing outer panels throughout the fleet.

In the wing root fillet area, tests of enlarged fillet radii and aluminum doublers proved inadequate to extend the service life even with skin replacement. A laminated steel doubler, Fig. 18, was designed to reinfore this area.

The wing center section lower cover was replaced with skins which were approximately twice the thickness of the original skins. The splice from the wing center section to the wing outer panel was redesigned to incorporate interference-fit Taperlok fasteners.

A full scale fatigue test article incorporating all of these modifications has been tested to 17,200 h without catastrophic failure. Figure 19 shows a crack found in a bolt hole at 11,000 h in the modified lower skin just outboard of the wing root fillet. As a result of this fatigue crack, an element test program has been initiated to investigate cold working of the bolt holes to improve the fatigue life. Modified wings presently are being fabricated and installed throughout the fleet.

General Conclusions

The program, as described, illustrates the use of the fracture mechanics approach to analyzing full scale test results. The validity of the use of fracture mechanics to make important decisions involving flight safety of a fleet of aircraft is substantiated to some degree by the fact that at no time was it

FIG. 19—*Wing outer panel lower skin fatigue crack in bolt hole to diagonal spar.*

necessary to ground the F-100 fleet and no loss of aircraft was sustained during modification periods.

Acknowledgments

References

[1] Paris, P. C., Gomez, M. P., and Anderson, W. E., "A Rational Analytic Theory of Fatigue," unpublished report, Boeing Company.

[2] Smith, C. R., "A Method for Estimating the Fatigue Life of 7075-T6 Aluminum Allow Aircraft Structures," NAEC ASL-1096, Naval Air Engineering Center, Dec. 1965.

[3] Paris, P. C. and Sih, G. C. in *Symposium on Fracture Toughness Testing and Its Applications, ASTM STP 381*, American Society for Testing and Materials, 1964, pp. 30–81.

[4] Tiffany, C. F. and Masters, J. N. in *Symposium on Fracture Toughness Testing and Its Applications, ASTM STP 381*, American Society for Testing and Materials, 1964, pp. 249–277.

[5] Wilhem, D. P., "Fracture Mechanics Guidelines for Aircraft Structural Applications," AFFDL TR 69-111, Air Force Flight Dynamics Laboratory, Feb. 1970.

[6] Hudson, C. M., "Effect of Stress Ratio on Fatigue Crack Growth in 7075-T6 and 2024-T3 Aluminum Alloy Specimens," NASA TND-5390, National Aeronautics and Space Administration, Aug. 1969.

[7] Forman, R. G. and Hudson, J. P., "Digital Computer Program for the Analysis of Crack Propagation in Cyclic Loaded Structures," AFFDL TR67-5, Air Force Flight Dynamics Laboratory, April 1967.

[8] "Fatigue Fracture Propagation Rate Study in F-100 Aircraft Wing Center Section Skins," Report NA-68-406, Los Angeles Division of North American Rockwell, June 1968.

[9] Kaufman, J. G., Nordmark, G. E., and Lifka, B. W., "Fracture Toughness, Fatigue, and Corrosion Characteristics of 7075-T651, 7075-T7351, and 7079-T651 Aluminum Alloys," AFML-TR-65-170, Air Force Materials Laboratory, May 1965.

[10] Hudson, C. M. and Hardrath, H. F., "Effects of Changing Stress Amplitude on the Rate of Fatigue-Crack Propagation in Two Aluminum Alloys," NASA TN D-960, National Aeronautics and Space Administration, Sept. 1961.

[11] Hudson, C. M., "Effect of Stress Ratio on Fatigue-Crack Growth in 7075-T6 and 2024-T3 Aluminum Alloy Specimens," NASA TN D-5390, National Aeronautics and Space Administration, Aug. 1969.

T. Swift[1]

Development of the Fail-safe Design Features of the DC-10

ABSTRACT: The degree of damage tolerance used in the design of the DC-10 fuselage pressure shell is discussed with reasons for its selection. Analysis methods are presented for the prediction of the residual strength of damaged, stiffened panels, based on the matrix force solution of an idealized structure combined with fracture mechanics equations. The results of 20 different configurations are included. A description of the development test program to verify the analytical techniques and to substantiate the fail-safe strength of the fuselage shell is given together with the results for many of the tests.

KEY WORDS: airplanes, damage, tolerance (mechanics), aircraft panels, fuselages, reinforcement (structures), stiffening, cracking (fracturing), fatigue (materials), failure, fracture strength, axial stress, loads (forces), residual stresses, tests

With the introduction of wide-bodied jet transport such as the McDonnell Douglas DC-10, fail-safe design has become increasingly important, particularly in the pressurized fuselage shell. The radial loading due to pressure has increased dramatically since the introduction of the first pressure shell design. This paper presents some of the steps taken during the development phases to ensure a fail-safe fuselage design.

The DC-10 aircraft is designed for a life of 120,000 hours which, based on a scatter factor of 2, represents 60,000 crack-free hours or 20 years of service at 3000 flight hours per year [1].[2]

A more realistic review of damage tolerance was required in which areas where fatigue damage is more likely to occur were considered. Analysis methods which included the capability to vary the degree of damage were developed to determine the residual strength of damaged, stiffened structure. A self-propagating crack can be arrested in a region of low stress ahead of the crack tip by providing adequate circumferential and longitudinal stiffening. The crack tip stress is reduced as the load is redistributed into the

---

[1] Senior engineer scientist, Douglas Aircraft Co., McDonnell Douglas Corp., Long Beach, Calif. 90801.

[2] Italic numbers in brackets refer to the list of references at the end of this paper.

164

stiffeners. Various configurations were studied to produce an optimum structure, consistent with economy in manufacturing, which not only would provide fail-safe capability but also would improve the service life of the fuselage shell.

A comprehensive test program was initiated to verify the analytical method and to study various configurations and materials. Flat and curved panels were tested under unixial and biaxial loading, respectively. It was shown that, while flat panel testing is in many ways adequate from a qualitative viewpoint, certain secondary effects are present while others are neglected which should be accounted for in the determination of allowable stresses.

Damage Tolerance

The degree of damage to be tolerated in a pressurized fuselage shell, without catastrophic failure, is not specified completely in any of the requirements of the regulating agencies. The FAA requires that the structure shall be capable of sustaining damage amounting to a single principal structural element when subjected to the loading for the fail-safe conditions listed in section 25.571, part 25 of the Federal Aviation Regulations. However, owing to the large size of fuselage skin panels (approximately 400 by 80 in. for the DC-10), the single critical element normally is interpreted to mean one skin panel between any two longitudinal or circumferential stiffening members. This one-bay panel damage has been adopted by many designers in the past. To be realistic, however, one should consider how structural damage is initiated. Past experience has shown that the majority of damage incurred in service is due to fatigue, although isolated incidents such as engine cowls becoming detached, thrown engine parts, and small arms fire have been known to cause varying degrees of skin damage and should not be overlooked.

It was noted previously that the DC-10 is designed to be crack free for 60,000 hours (including scatter factors), which represents about 20 years of service; however, imperfections in manufacturing such as badly driven rivets which do not fill holes properly, the preloading of parts due to mismatch, and scratches received in service can reduce fatigue life, and thus the possibility of fatigue cracks occurring cannot be ignored.

Longitudinal Skin Cracks

Cabin pressurization is the main source of loading causing longitudinal skin cracks. Figure 1 shows that radial loading due to internal pressure on the DC-10 is $3\frac{1}{2}$ times as great as that for the DC-6, which was the first pressurized aircraft designed at Douglas. Testing on basic pressurized fuselage shell structure has indicated that longitudinal skin cracks are more likely to start in two critical locations, as follows:

1. Along the line of attachments which attach the outer fingers of a longitudinal splice member to the skin, as shown in Fig. 2: The radial tension stress due to pressure varies across a longitudinal skin bay and reaches a
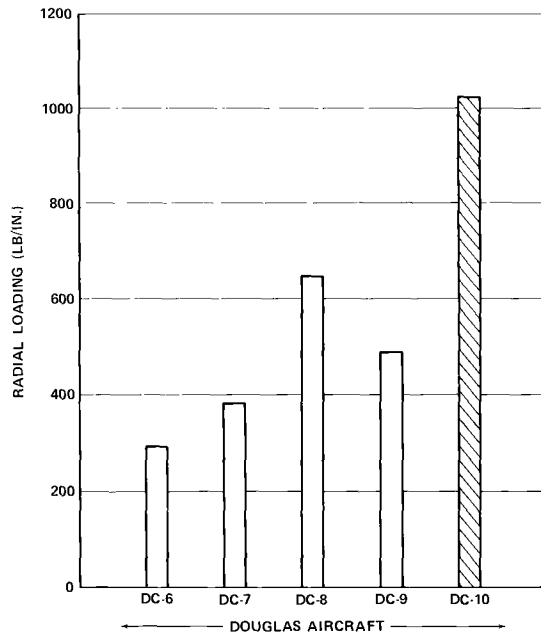
FIG. 1—*Fuselage shell radial loading due to nominal cabin pressure.*

maximum value midway between frames. Transfer of load from the skin into the finger doubler causes a high attachment bearing stress which, when combined with the radial tension stress, may cause a fatigue crack in a longitudinal direction. A large number of configurations for the longitudinal splice shown in Fig. 2 were fatigue tested. The configurations were changed until all failures occurred as shown in Fig. 2, where they can be detected by visual inspection methods. Fatigue cracks hidden by splice plates could propagate a considerable distance before detection.

2. At the first attachment of a frame shear clip to skin joint, as indicated in Fig. 3: The stress σ_c in the region of the shear clip cutout is higher than the midbay stress due to the discontinuity of the clip. In addition, the skin may be carrying tension stress due to frame bending. The high local stress, combined with the bearing stress in the first attachment hole as the shear clip picks up load, can cause a fatigue crack in the skin. The skin crack shown in Fig. 3a is just as likely to propagate into both adjacent bays as into one bay.

Transverse Skin Cracks

Testing under combined pressure and axial loads has indicated that transverse or circumferential skin cracks occur in two locations, as follows:

1. At the attachment of the skin to frame shear clip midway between longerons, as shown in Fig. 4: Local bending of the skin due to pressure, combined with axial stress due to fuselage bending, can cause skin cracks in a circumferential direction.

2. In the longeron flanges where they attach to the frame, as shown in Fig. 4: Bending due to transfer of some of the pressure loading into the frame increases the axial tension stress in the longeron flanges locally, causing fatigue cracks. After failure of the longerons, the skin stress increases locally (see Fig. 12) causing fatigue cracks in the skin which propagate into the two adjacent skin bays.

In view of the above facts, it is evident that damage extending to two skin bays should be considered. Materials and stress levels normally are chosen so that cyclic crack growth rates are low and a propagating crack will be noticed within a reasonable inspection period and before reaching a critical length; nonetheless, hairline cracks are extremely difficult to find under zero-load conditions and can easily escape detection. The design should, therefore, include the capability to arrest a crack after a fast fracture has occurred. The damage tolerance selected for the DC-10 fuselage shell was, therefore,

Two-bay longitudinal crack with the center frame intact
Two-bay circumferential crack with a center longeron failed

Configuration Candidates

The basic shell configuration selection is the result of many trade studies conducted to satisfy a number of requirements such as shell general instability, frame flexibility and strength, as well as fatigue and fail-safe strength. The results of these studies indicated that the frame spacing should be 20 in. and longeron spacing should vary from 8 in. at the top of the shell to 6.5 in. at the
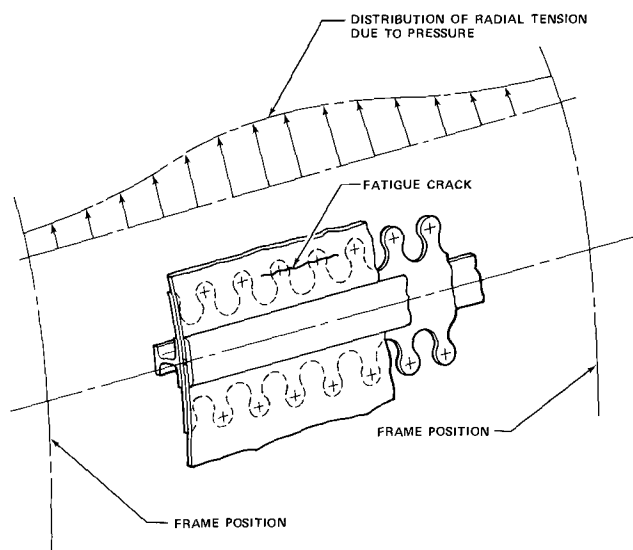

FIG. 2—*Horizontal splice, fatigue crack location.*

(a) MINIMUM FRAME SECTION
(ANGLE SHEAR CLIP)

(b) EXTENDED SHEAR CLIP   (c) TEE SHEAR CLIP

(d) HAT LONGERON   (e) TEE LONGERON
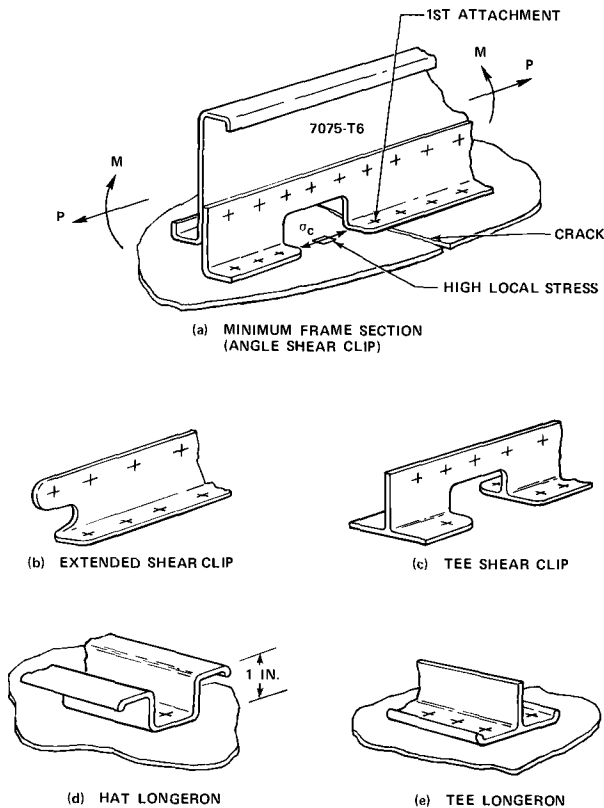
FIG. 3—*Frame and longeron configurations.*

bottom. The minimum bending stiffness of the frame section was set from general instability requirements. The outer and inner radii of the frame cross section were set by airplane performance and inside cabin dimension requirements, respectively. Although these basic dimensions were set for the minimum shell, several means were available to satisfy the fail-safe requirements to the damage tolerance specified. These were the selection of (a) skin thickness, (b) skin material, (c) whether or not to use crack stoppers, and (d) longeron geometric shape.

Skin Thickness

The skin thickness selection for the minimum gage portion of the fuselage is particularly important for an aircraft such as the DC-10. The surface area of the shell is approximately 8700 ft² with 84 percent of this minimum gage; one gage variation can thus represent a weight change of approximately 950 lb.

The most predominant loading condition for the minimum gage portion of the shell is due to pressurization. The fuselage is subjected to one full pressure cycle virtually every flight and, therefore, fatigue plays a vital part

in the selection of the minimum gage. Hoop tension stresses should be kept to reasonably low limits to prevent failures in horizontal splices and in longeron-to-skin rivet lines. It should also be noted that local bending stresses due to pressure, in areas such as those illustrated in Fig. 4, increase in inverse proportion to the skin thickness squared. Longitudinal crack propagation is decreased with decreasing hoop tension stress due to increasing skin thickness. Residual strength is increased to a lesser degree as will be illustrated later.

Skin Material

The skin material choice is perhaps the most important factor affecting the residual strength of a damaged fuselage shell. An independent research and development (IRAD) program on residual strength of stiffened flat wide panels [2] had resulted in the following values of plane stress fracture toughness K_c for four candidate materials: 52,700 to 63,500 psi$\sqrt{in.}$ for 7075-T6, 70,000 psi$\sqrt{in.}$ for 2014-T6, 90,000 psi$\sqrt{in.}$ for 7075-T73, and as high as 158,000 psi$\sqrt{in.}$ for 2024-T3. From a static strength standpoint, the ideal choice would be 7075-T6. In the past, 2014-T6 had been used successfully; but, in view of the increased radial loading (Fig. 1) and the tendency to work to higher stress levels [1], it was considered that a material with a higher fracture toughness would be more desirable. 7075-T73 and 2024-T3 were therefore considered as candidates.

Crack Stopper Straps

The use of crack stopper straps is an effective means of increasing the residual strength of damaged panels. An unstable fast fracture can be confined to a local area by providing an area of low stress ahead of the crack tip. The crack tip stress is reduced as a large part of the redistributed load is transferred into the strap. A region of low stress also can be provided, to a lesser degree, by a frame connected to the skin by shear clips as indicated in
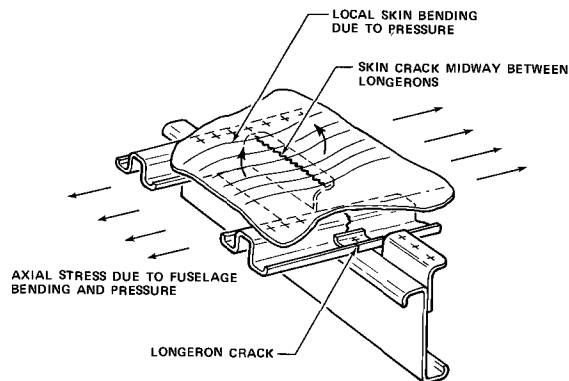

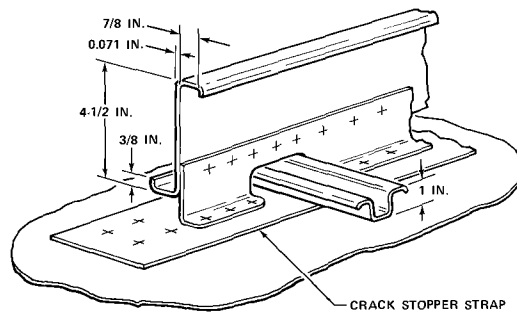FIG. 4—*Crack locations, fuselage shell.*

FIG. 5—*Frame crack stopper configuration.*

Fig. 3. The latter configuration would be desirable from a cost standpoint if the required residual strength could be attained.

When crack stopper straps are required, it has been Douglas policy to install them at a frame location, as illustrated by Fig. 5, for several good reasons. Without crack stopper straps, the skin stress level in the vicinity of the frames between shear clips (Fig. 3) has been determined both from flat panel and curved panel pressure tests to be up to 18 percent higher than the midbay hoop stress. With crack stopper straps to provide continuity across the gap, the stress level in this critical area is reduced to 15 percent below the midbay stress, thus reducing the possibility of a fatigue crack starting. In addition, the crack stopper strap can be used as bending material to increase the frame stiffness and static strength. Tests have shown that after cutting a 3-in.-long slot in the skin over a titanium crack stopper strap almost 14,000 cycles are required at 15,500-psi gross stress with a stress ratio $R = 0.05$ to fail the strap. During this number of cycles, crack propagation was negligible until the crack stopper had failed. Prior to failure of the crack stopper, the increase in frame stress due to the crack was negligible, thus reducing the possibility of frame fatigue failure. With the strap at any other location, the possibility of starting a crack in the skin is increased, and, once a crack started, propagation would be much faster and the possibility of failing the frame in fatigue would be increased.

There is one advantage in placing the crack stopper midway between frames for cracks which start at frames: the crack would be confined to 20 in. in length; however, with this configuration the crack is more likely to start. If a midbay crack stopper is installed by riveting, a crack is just as likely to start at a rivet hole and propagate both ways. Tests have shown that before a crack propagates very far, the crack stopper would fail in fatigue due to the high load transfer into the strap. In highly loaded areas the adjacent frames (without crack stoppers) would be incapable of arresting the crack. The outer crack stoppers would therefore be required to arrest a 40-in. crack without the help of a backup frame. The possibility of starting a crack at a midbay crack stopper would be reduced if the strap were bonded to the skin without

additional rivets. This configuration was considered for the DC-10 and abandoned for several reasons. The candidate material for crack stoppers was titanium and bonding of this material to aluminum was not considered as reliable as riveting. The bonding could easily become delaminated in service, especially under repeated shear loading of the skin panels and possible wrinkling due to tension field action. The longerons, passing over the bonded-on strap, would still require riveting through the strap. The bonding is subjected to delamination locally where the holes are drilled and the subsequent riveting operation is completed. Delaminations have been experienced where bonding is combined with riveting due to differences in the shear stiffness of the bonding material and the rivets. In addition, moisture seeping into the rivet holes and subsequently into the bonded surface has been known to cause delamination through corrosion.

Minimum weight structure with maximum reliability, consistent with the damage tolerance selected, was required. It also should be remembered that fatigue cracks, if they occur in service, usually form after many years of service. Techniques used to prevent rapid fracture should therefore be designed to perform other functions, for maximum economy, and yet be ready to stop a fast fracture without having deteriorated during service.

Another reason for abandonment of the bonding process, and possibly the most significant, is the distortion of the aluminum skin caused by thermal effects due to the difference in the coefficient of expansion of the titanium and the aluminum. A small test panel was fabricated as shown in Fig. 6 and a strap of 0.025-in.-thick titanium bonded to it and cured at a temperature of 250 F (121 C). On cooling to room temperature, the panel curved to approximately 70 in. in radius with the strap on the convex side. The panel was rolled to the correct radius with the strap on the concave side. The resulting
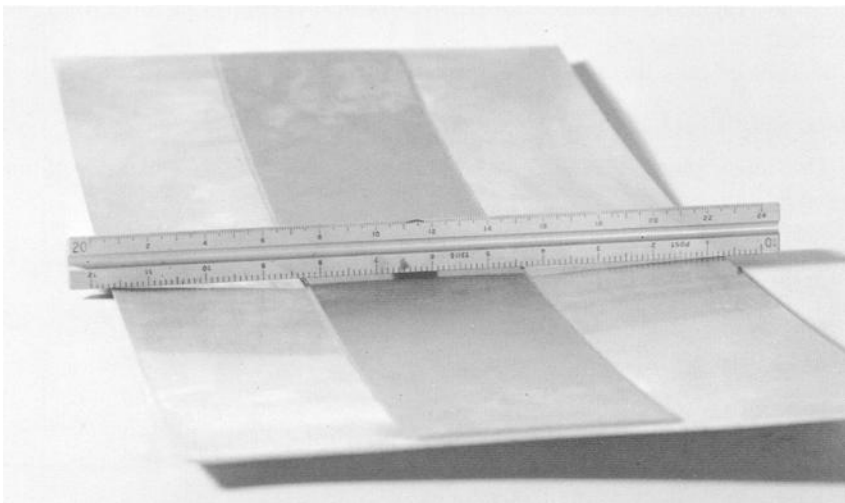

FIG. 6—*Test panel distortion due to bonding process.*

anticlastic curvature due to residual stresses is illustrated in Fig. 6. It was thought that this effect would be more severe on large panels, especially with longerons and frames assembled to the panels; the resulting quilted appearance of the shell would almost certainly be unacceptable to the customer.

Longeron Geometric Shape

Hat-section longerons such as those illustrated in Fig. 3d have been used on all previous Douglas aircraft. However, analysis indicated that for the damage tolerance selected for circumferential cracks, T-section longerons riveted to the skin with two rows of rivets would give higher allowable stresses. The hat-section longerons were desirable from a cost standpoint because of the cost of the extra row of rivets required in the T-section longerons. Both T- and hat-section longerons were therefore chosen as candidates. Analysis and test programs were introduced to study the configurations.

Analysis

Analysis of the candidate configurations for the damage tolerance selected was highly desirable prior to starting the development test program. In early work at Douglas [3, 4, 5] parametric lumped parameter analysis had been performed on 60-in.-wide panels with a single stiffening element containing a one-bay crack. Although this analysis proved to be extremely helpful in preliminary design work, further refinements were required to answer some of the questions listed below for panels containing two-bay cracks.

How effective was the frame member working in conjunction with a crack stopper strap?

How did the stress vary across the frame?

What effect did a broken longeron have on the crack tip stress for a circumferential crack and how did the stress vary across the outer longeron cross section?

In view of this, the analysis described herein was initiated.

Analysis of Cracked Unstiffened Panels

The most generally accepted equation for the fracture strength of unstiffened thin panels containing a central crack is

$$\sigma_R = \frac{K_c}{C\sqrt{W \tan \dfrac{\pi a_c}{W}}} \quad\dots\dots\dots\dots\dots\dots\dots(1)$$

where

σ_R = gross stress at failure,
K_c = plane stress fracture toughness, psi$\sqrt{\text{in.}}$,
C = width correction factor [7] $1.0 + 0.3\ (2a/W)^2$,
a_c = half crack length at fast fracture, and
W = panel width.

For large panel widths, Eq 1 can be simplified as follows:

$$\sqrt{W \tan \frac{\pi a_c}{W}} = \left[\pi a_c + \frac{W}{3}\left(\frac{\pi a_c}{W}\right)^3 + \frac{2W}{15}\left(\frac{\pi a_c}{W}\right)^5 + \cdots \right]^{1/2}$$

For large values of W then

$$\sqrt{W \tan \left(\frac{\pi a_c}{W}\right)} \rightarrow \sqrt{\pi a_c}$$

therefore Eq 1 reduces to

$$\sigma_R = \frac{K_c}{\sqrt{\pi a_c}} \dots\dots\dots\dots\dots\dots\dots\dots\dots\dots\dots(2)$$

Analysis of Cracked Stiffened Panels

The effects of stiffeners on the fracture strength of stiffened panels can be determined by a lumped parameter analysis of a structure representing the panel. The analysis is based on the matrix force method of structural analysis [8, 9] and uses the Fortran matrix abstraction technique (FORMAT) [10] to solve the matric operations. Figures 7 and 8 show the idealized structure representing the stiffened panels for one- and two-bay longitudinal cracks, respectively. Figure 9 shows the idealized model for the two-bay circumferential crack. As illustrated, the panels are divided into a series of discrete bars and shear panels, the bars carry axial load and the panels carry shear load. The panels have the same thickness as the plate, and the bar areas are determined from the dimensions shown in Fig. 8 as follows:

$$A_y = t(z_1 + z_2)/2 \quad \text{and} \quad A_z = t(y_1 + y_2)/2$$

Loads are applied to the tops of the panels, and reactions are provided at the bottoms. The propagating crack is simulated by successive disconnection of the reactions in the skin at the horizontal center line of the panel by an element modification procedure which is part of the computer program. The crack tip stress is defined by the stress in the last bar adjacent to the simulated crack as shown in Fig. 7. The stiffening elements are represented by additional lumped bars connected to the main panel by a series of continuous shear panels.

A typical frame cross section with crack stopper strap is idealized by lumping areas as shown in Fig. 10. As the crack propagates in the skin, the frame outer cap picks up load through the shear clip-to-frame attachment row. The area of the outer cap, A_0, is therefore calculated so that its center of gravity (cg) lies on this attachment row. Frames without crack stoppers (see Fig. 3) are idealized by three lumped bars. The thickness of the idealized shear panels connecting the crack stopper and frame members to the skin is extremely important and is calculated to include the rivet stiffnesses.
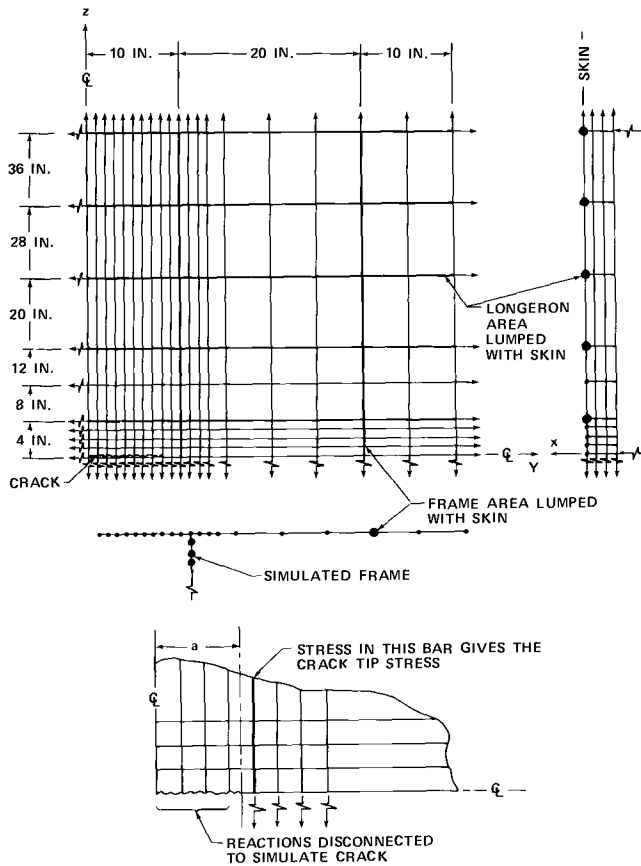
FIG. 7—*Idealization for one-bay longitudinal crack.*

Rivet shear deflection in aluminum alloy sheet is expressed as

$$\delta = \frac{Pf}{E_a d}. \dots\dots\dots\dots\dots\dots\dots\dots\dots\dots\dots(3)$$

where

δ = deflection,
P = applied load,
E_a = modulus of aluminum, and
d = rivet diameter.

and, for aluminum alloy rivets,

$$f = 5.0 + 0.8\left(\frac{d}{t_1} + \frac{d}{t_2}\right)\dots\dots\dots\dots\dots\dots(4)$$

where t_1 and t_2 are the thicknesses of the joined sheets.

For the shear clip to crack stopper and skin to crack stopper rivets,

$$f = 5.0 + 0.8\left(\frac{d}{t_1} + \frac{d}{t_2}\frac{E_a}{E_{cs}}\right) \dots\dots\dots\dots\dots(5)$$

where E_{cs} = modulus of crack stopper material.

These equations have been substantiated by test (see Fig. 26). The thickness of the idealized shear panels connecting the crack stopper to the skin is calculated as follows:

$$\text{Rivet deflection } \delta_r = \frac{Pf}{nE_a d}$$

where n = number of rivets between longerons.

$$\text{Idealized shear panel deflection } \delta_{csp} = \frac{Ph_{csp}}{Lt_{csp}G_a}$$

where L = distance between longerons and G_a = shear modulus of aluminum. However, $\delta_r = \delta_{csp}$, and equating deflections and solving for t_{csp},

$$t_{csp} = \frac{h_{csp}nE_a d}{LG_a f} \dots\dots\dots\dots\dots\dots\dots\dots(6)$$

The shear clip is idealized in a similar manner including both rows of rivets and the sheet metal clip.
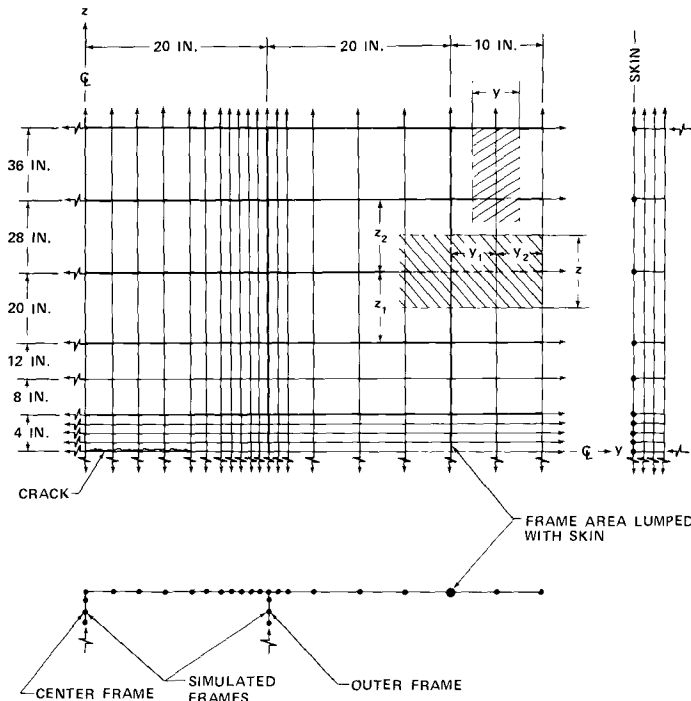

FIG. 8—*Idealization for two-bay longitudinal crack.*

For longitudinal bars located at longeron positions, the longeron area is included with the skin area in the plane of the sheet. Longerons in panels containing circumferential cracks are idealized into two lumped bars connected to the skin by a continuous shear panel. The thickness of the panel is determined using an equation similar to Eq 6.

The effect of stiffeners on the crack tip stress is determined by analyzing both unstiffened and stiffened panels having the same grid size and taking ratios between the crack tip stresses. The crack tip stress ratio, which is a function of crack length, is expressed as

$$R_{ct} = \frac{\sigma_{yct} \text{ in unstiffened panel}}{\sigma_{yct} \text{ in stiffened panel}}$$

where σ_{yct} is the stress in the y direction at the crack tip. Since Eqs 1 and 2 are directly related to the plate net stress in the region of the crack tip, they can be rewritten to include the effects of stiffening.

The presence of secondary effects [11] such as crack buckling makes the determination of K_c as a material parameter extremely difficult. K_c is, therefore, replaced by K_c^* which includes secondary effects; thus Eqs 1 and 2 become, for finite width panels,

$$\sigma_R = \frac{K_c^* R_{ct}}{C\sqrt{W \tan \dfrac{\pi a_c}{W}}} \quad\dots\dots\dots\dots\dots\dots\dots\dots(7)$$

and for infinite panels,

$$\sigma_R = \frac{K_c^* R_{ct}}{\sqrt{\pi a_c}} \quad\dots\dots\dots\dots\dots\dots\dots\dots\dots(8)$$

K_c^* determined from tests on stiffened panels of one configuration can be used to determine the fracture strength of a fuselage shell of another configuration by using Eq 8, provided R_{ct} versus crack length has been determined. The use of R_{ct}, determined from analysis of a finite panel, can be justified for use in Eq 8 for an infinite plate if the panel is wide enough. A comparison of the net section stress for the panel of Fig. 7 to Westergaard's equation for the net section stress of an infinitely wide plate is shown in Fig. 11.

Analysis Results

Table 1 lists some of the more important analysis cases considered. Cases 1 to 9 and 10 to 12 are for two-bay and one-bay longitudinal cracks, respectively, where the frame members and circumferential crack stopper straps cause a reduction in crack tip stress. Cases 13 to 20 are for two-bay circumferential cracks with a broken central longeron, where the outer longerons cause a reduction in the crack tip stress. For all of the cases listed in Table 1,

FIG. 9—*Idealization for two-bay circumferential crack.*

FIG. 10—*Frame idealization with crack stopper.*
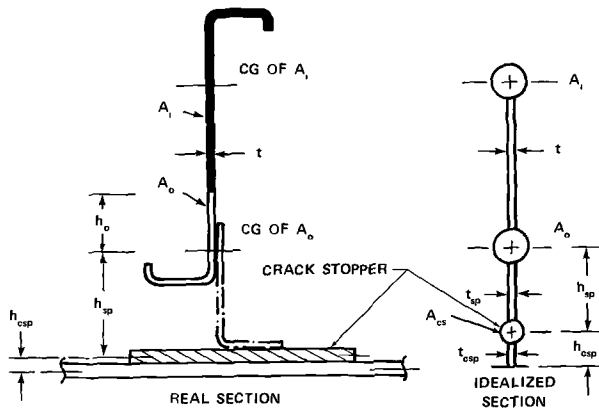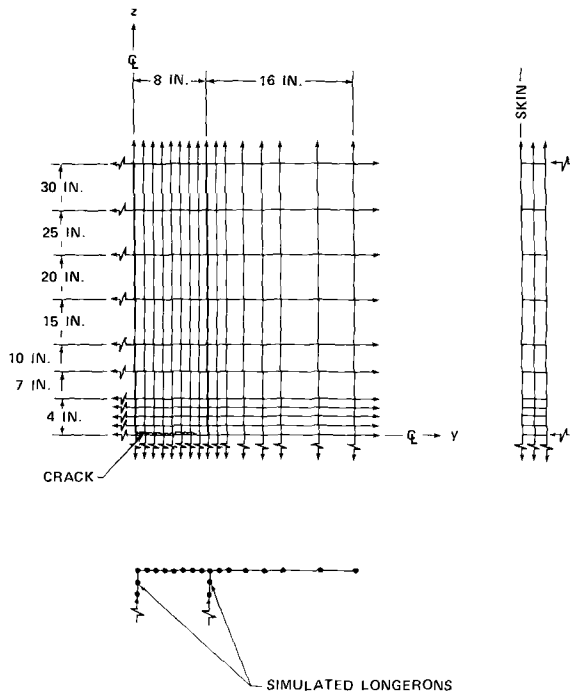
a uniform stress level was applied to the upper boundary of the panels (shown in Figs. 7, 8, and 9) to both skin and stiffening elements. The results of the analysis cases considered are listed in Tables 2, 3, and 4. The frame cross sections for cases 1 to 12 and the hat sections for cases 13 to 18 are similar to those shown in Fig. 5. The stress ratio terms are defined below.

σ Gross stress applied to the upper boundary of the panel, psi

σ_{ccs} Center crack stopper stress, psi

σ_{ocs} Outer crack stopper stress, psi

σ_{occf} Outer cap stress in the center frame, psi

σ_{iccf} Inner cap stress in the center frame, psi

σ_{ocof} Outer cap stress in the outer frame, psi

σ_{icof} Inner cap stress in the outer frame, psi

σ_{of} Longeron outer fiber stress, psi

σ_{if} Longeron inner fiber stress, psi

All of the stresses shown are lumped stresses in the idealized members. The stress distributions in the sheet after a longeron is broken and prior to skin cracking are shown in Fig. 12 for conditions 15 and 17 of Table 1.

Skin Fracture Criterion

The significance of Eqs 7 and 8 is illustrated in Fig. 13 and represents the residual strength of a panel, based on skin criteria. The lower curve (dotted) represents an unstiffened panel and the upper two curves are for stiffened panels with longitudinal cracks plotted for cases 1 and 4 of Table 1. The change in slope of the curves for stiffened panels as the crack tip approaches the stiffener spacing is due to a reduction in crack tip stress as the stiffener picks up load. The maximum reduction in crack tip stress occurs in the region of the stiffeners, as can be seen by the increase in R_{ct} values listed in Table 2.

If the panel contains a fatigue crack of half length a_A, and a gross stress of σ_{RA} is applied, then fast fracture will occur at A and the crack will be arrested at B. If, on the other hand, a gross stress of σ_{RC} is applied with half crack length equal to a_C, then fast fracture will occur at C and the crack will not be arrested. The residual strength of the panel is represented as σ_{RD} and any fracture at stress level higher than σ_{RD} will not be arrested and would represent an explosive failure in a pressurized shell. The value of the crack stoppers for case 4 can be seen by their influence on the residual strength when compared to case 1 for the panel without crack stoppers. The frame, connected to the skin by a flexible shear clip, is not as effective in picking up load as a crack stopper strap connected directly to the skin with three rows of rivets.

Stiffener Strength Criteria

In considering the gross residual strength of a stiffened panel, one must consider both skin fracture criteria and stiffener strength. Tables 2, 3, and 4

TABLE 1—*Description of analysis cases.*

Case No.	Case Description	Crack Type
1	Frames without crack stoppers; 0.071 skin; center frame intact	
2	Frames without crack stoppers; 0.080 skin; center frame intact	
3	Frame with crack stopper; 0.071 skin; crack stopper 3 by 0.025-in. titanium with three rows of 3/16 rivets; center crack stopper intact	
4	Same as case 3 with center crack stopper failed	
5	Same as case 3 with both center crack stopper and center frame failed	Two-bay longitudinal crack
6	Frame with crack stopper; 0.071 skin; crack stopper 2.8 by 0.025-in. titanium with two rows of 3/16 rivets; center crack stopper failed	
7	Frame with crack stopper; 0.071 skin; crack stopper 2 by 0.02-in. titanium with two rows of 3/16 rivets; center crack stopper failed	
8[a]	Frame with crack stopper; 0.063 skin; crack stopper 3.25 by 0.016-in. titanium with two rows of 3/16 rivets; center crack stopper failed	
9	Same as case 8 with center frame failed	
10	Frames without crack stoppers; 0.071 skin	One-bay longitudinal crack
11	Frames without crack stoppers; 0.08 skin	
12	Frames with crack stopper; 0.071 skin; crack stopper 3 in. by 0.025-in. titanium with three rows of 3/16 rivets	
13	Rolled hat-section longeron; net area 0.205 in.^{2}; 0.063 skin; one row of 3/16 rivets at $1\frac{1}{4}$ pitch	
14	Same as case 13 with 0.071 skin	
15	Extruded hat-section longeron; net area 0.3029 in.^{2}; 0.071 skin; one row of 3/16 rivets at $1\frac{1}{4}$ pitch	Two-bay circumferential crack with central longeron
16	Same as case 15 with 0.080 skin	
17	Extruded hat-section longeron; net area 0.5121 in.^{2}; 0.071 skin; one row of 3/16 rivets at $1\frac{1}{4}$ pitch	
18	Same as 17 with one row of 3/16 steel attachments at $1\frac{1}{4}$ pitch	
19	Extruded T-section longeron; net area 0.2895 in.^{2}; two rows of 3/16 rivets at $1\frac{1}{4}$ pitch	
20	Extruded T-section longeron; net area 0.4865 in.^{2}; two rows of 3/16 rivets at $1\frac{1}{4}$ pitch	

[a] Case 8 frame thickness is 0.063 in. with dimensions as shown in Fig. 5.

list stiffener stresses as a function of crack length. To maintain the skin fracture strength illustrated by Fig. 13, the stiffeners must remain intact. In cases where the stiffener may be critical, yielding of the stiffener will take place prior to failure, resulting in an effective increase in the crack tip stress and a decrease in R_{ct}. Stiffener failure and skin fracture then occur simultaneously, but the failure is precipitated by stiffener criteria.

To obtain a balanced design, both skin and stiffener criteria must be considered, an example of which is illustrated in Fig. 14. The curves represent gross residual strength for a flat panel, stiffened by frames and crack stoppers and subjected to a uniform gross stress at the boundary. Curves are shown

TABLE 2—Stress ratios for two-bay longitudinal cracked panels.

Case		Half Crack Length, a, in.									
		4.5	7.5	10.5	12.75	15.5	17.5	18.5	19.5	20.5	21.5
R_{ct}	1	1.100	1.160	1.220	1.270	1.350	1.435	1.500	1.615	1.750	1.810
	2	1.088	1.128	1.182	1.227	1.376	1.435	1.480	1.550	1.704	1.721
	3	1.260	1.317	1.392	1.446	1.540	1.651	1.758	2.171	2.908	2.786
	4	1.054	1.123	1.197	1.248	1.339	1.448	1.551	1.931	2.616	2.535
	5	0.777	0.824	0.867	0.896	0.954	1.033	1.112	1.402	1.940	1.923
	6	1.054	1.122	1.195	1.245	1.336	1.442	1.541	1.866	2.437	2.415
	7	1.075	...	1.207	1.255	1.341	1.438	1.523	1.785	2.268	2.266
	8	1.043	1.104	1.175	1.233	1.338	1.444	1.538	1.833	2.316	2.298
	9	0.769	...	0.851	...	0.952	1.027	1.099	1.324	1.701	1.724
σ_{ccs}/σ	3	5.622	7.448	9.149	10.09	11.45	12.42	12.86	13.24	13.40	13.50
σ_{ocs}/σ	3	1.727	1.777	1.874	1.976	2.243	2.698	3.185	4.266	6.364	7.354
	4	1.750	1.825	1.955	2.087	2.417	2.960	3.529	4.772	7.141	8.249
	5	1.858	1.994	2.229	2.451	2.994	3.844	4.695	6.499	9.804	11.33
	6	1.749	1.824	1.953	2.084	2.408	2.934	3.461	4.549	6.690	7.767
	7	1.745	...	1.943	2.073	2.408	2.985	3.621	5.103	8.640	10.44
	8	1.743	1.811	1.938	2.069	2.402	2.944	3.489	4.607	6.942	8.159
	9	1.841	...	2.190	...	2.955	3.802	4.625	6.259	9.549	11.252
σ_{occt}/σ	1	1.643	2.104	2.576	2.851	3.261	3.566	3.710	3.845	3.956	4.050
	2	1.720	2.246	2.804	3.139	3.613	3.979	4.153	4.318	4.460	4.577
	3	1.251	1.447	1.658	1.782	1.965	2.099	2.160	2.213	2.235	2.251
	4	1.765	2.235	2.713	2.988	3.394	3.689	3.824	3.939	3.987	4.020
	6	1.760	2.224	2.696	2.969	3.372	3.665	3.800	3.916	3.972	4.011
	7	1.702	...	2.628	2.899	3.301	3.597	3.734	3.856	3.921	3.968
	8	1.672	2.113	2.574	2.884	3.245	3.538	3.674	3.792	3.855	3.899

σ_{icof}/σ . . .	1	0.966	1.019	1.117	1.192	1.317	1.420	1.471	1.519	1.561	1.596
	2	0.933	0.976	1.069	1.143	1.262	1.361	1.411	1.460	1.503	1.539
	3	1.024	1.092	1.189	1.256	1.364	1.449	1.489	1.524	1.539	1.550
	4	1.000	1.076	1.191	1.271	1.400	1.501	1.549	1.591	1.609	1.622
	6	1.001	1.078	1.193	1.273	1.403	1.505	1.553	1.596	1.617	1.632
	7	0.996	⋯	1.183	1.263	1.393	1.497	1.547	1.592	1.617	1.635
	8	0.981	1.041	1.136	1.206	1.322	1.414	1.459	1.499	1.521	1.537
σ_{ocof}/σ . . .	1	1.022	1.057	1.119	1.176	1.304	1.470	1.596	1.781	2.082	2.325
	2	1.015	1.048	1.108	1.168	1.294	1.463	1.596	1.797	2.139	2.402
	3	1.013	1.036	1.077	1.118	1.208	1.321	1.402	1.505	1.579	1.634
	4	1.024	1.058	1.115	1.167	1.281	1.419	1.516	1.636	1.722	1.784
	5	1.073	1.136	1.239	1.329	1.523	1.750	1.904	2.091	2.217	2.306
	6	1.023	1.057	1.114	1.165	1.277	1.412	1.506	1.623	1.716	1.784
	7	1.022	⋯	1.113	1.166	1.282	1.427	1.531	1.666	1.790	1.882
	8	1.021	1.054	1.109	1.161	1.259	1.407	1.499	1.614	1.713	1.788
	9	1.069	⋯	1.228	⋯	1.509	1.731	1.879	2.059	2.206	2.316
σ_{icof}/σ . . .	1	1.031	1.079	1.152	1.210	1.311	1.393	1.427	1.447	1.434	1.429
	2	1.025	1.070	1.144	1.204	1.308	1.396	1.434	1.457	1.437	1.430
	3	1.017	1.047	1.095	1.135	1.208	1.271	1.302	1.325	1.327	1.331
	4	1.032	1.077	1.144	1.197	1.292	1.374	1.413	1.443	1.447	1.453
	5	1.101	1.184	1.309	1.406	1.581	1.734	1.807	1.865	1.878	1.891
	6	1.032	1.076	1.114	1.196	1.291	1.374	1.413	1.445	1.453	1.461
	7	1.030	⋯	1.142	1.195	1.292	1.376	1.416	1.448	1.454	1.462
	8	1.029	1.070	1.134	1.184	1.275	1.352	1.389	1.419	1.425	1.433
	9	1.096	⋯	1.292	⋯	1.552	1.697	1.768	1.826	1.844	1.862

TABLE 3—Stress ratios for one-bay longitudinal cracked panels.

	Case	Half Crack Length, a, in.										
		1.5	3.5	4.5	5.5	6.5	7.5	8.5	9.5	10.5	11.5	12.5
R_{ct}......	10	1.004	1.016	1.025	1.038	1.056	1.081	1.119	1.192	1.287	1.353	...
	11	1.040	1.045	1.048	1.054	1.065	1.083	1.111	1.169	1.259	1.323	...
	12	1.005	1.019	1.030	1.047	1.070	1.106	1.172	1.442	1.945	2.017	...
σ_{ocs}/σ....	12	1.720	1.806	1.882	1.991	2.153	2.405	2.852	3.840	5.749	6.713	7.418
σ_{oeof}/σ....	10	1.009	1.046	1.076	1.118	1.174	1.249	1.353	1.509	1.765	1.989	2.183
	11	1.008	1.045	1.074	1.117	1.174	1.253	1.364	1.533	1.819	2.066	2.281
	12	1.008	1.040	1.067	1.103	1.149	1.210	1.289	1.389	1.462	1.518	1.571
σ_{ieof}/σ....	10	1.008	1.040	1.064	1.093	1.125	1.159	1.191	1.214	1.209	1.210	1.217
	11	1.008	1.040	1.065	1.095	1.130	1.167	1.203	1.228	1.217	1.217	1.224
	12	1.007	1.036	1.058	1.085	1.116	1.150	1.184	1.213	1.218	1.225	1.235

TABLE 4—Stress ratios for two-bay circumferential cracked panels with broken central longeron.

|					Half Crack Length, a, in.						
Case	1.5	2.5	3.5	4.5	5.5	6.5	7.5	8.5	9.5	11.0	13.0
R_{ct}											
13	0.818	0.853	0.881	0.907	0.937	0.980	1.101	1.327	1.394	...	...
14	0.843	0.867	0.892	0.916	0.943	0.983	1.092	1.298	1.362	...	...
15	0.778	0.820	0.852	0.883	0.918	0.970	1.107	1.353	1.428	...	...
16	0.798	0.836	0.865	0.894	0.926	0.972	1.092	1.306	1.378	...	...
17	0.683	0.736	0.779	0.822	0.871	0.942	1.124	1.428	1.520	...	...
18	0.681	0.713	0.782	0.827	0.880	0.966	1.370	2.062	1.966	...	...
19	0.763	0.813	0.851	0.886	0.926	0.988	1.201	1.593	1.646	...	...
20	0.662	0.727	0.778	0.826	0.881	0.967	1.241	1.704	1.766	...	...
$\sigma_{ol}/\sigma_{\cdot}$											
13	1.066	1.107	1.172	1.270	1.425	1.694	2.247	3.504	4.304	5.436	6.451
14	1.063	1.104	1.168	1.268	1.425	1.699	2.269	3.606	4.475	5.741	6.848
15	1.074	1.114	1.176	1.269	1.414	1.660	2.153	3.212	3.875	4.805	5.606
16	1.069	1.109	1.170	1.263	1.408	1.653	2.143	3.230	3.937	4.958	5.830
17	1.094	1.132	1.189	1.271	1.394	1.591	1.955	2.637	3.043	3.601	4.052
18	1.109	1.152	1.216	1.311	1.462	1.740	2.423	3.441	3.867	4.449	4.932
19	1.077	1.121	1.186	1.280	1.420	1.649	2.089	2.864	3.290	3.890	4.412
20	1.100	1.143	1.202	1.284	1.398	1.568	1.855	2.273	2.496	2.810	3.080
$\sigma_{it}/\sigma_{\cdot}$											
13	1.074	1.107	1.154	1.214	1.287	1.373	1.465	1.518	1.573	1.619	1.837
14	1.070	1.103	1.149	1.209	1.284	1.372	1.466	1.520	1.579	1.705	1.863
15	1.088	1.120	1.165	1.223	1.292	1.372	1.455	1.497	1.542	1.639	1.759
16	1.082	1.114	1.159	1.217	1.287	1.369	1.454	1.501	1.551	1.659	1.793
17	1.119	1.151	1.193	1.246	1.306	1.372	1.432	1.444	1.465	1.517	1.588
18	1.124	1.158	1.203	1.257	1.320	1.384	1.422	1.377	1.371	1.387	1.427
19	1.080	1.113	1.158	1.210	1.267	1.317	1.318	1.180	1.123	1.079	1.081
20	1.108	1.141	1.180	1.221	1.257	1.268	1.201	0.982	0.881	0.772	0.715
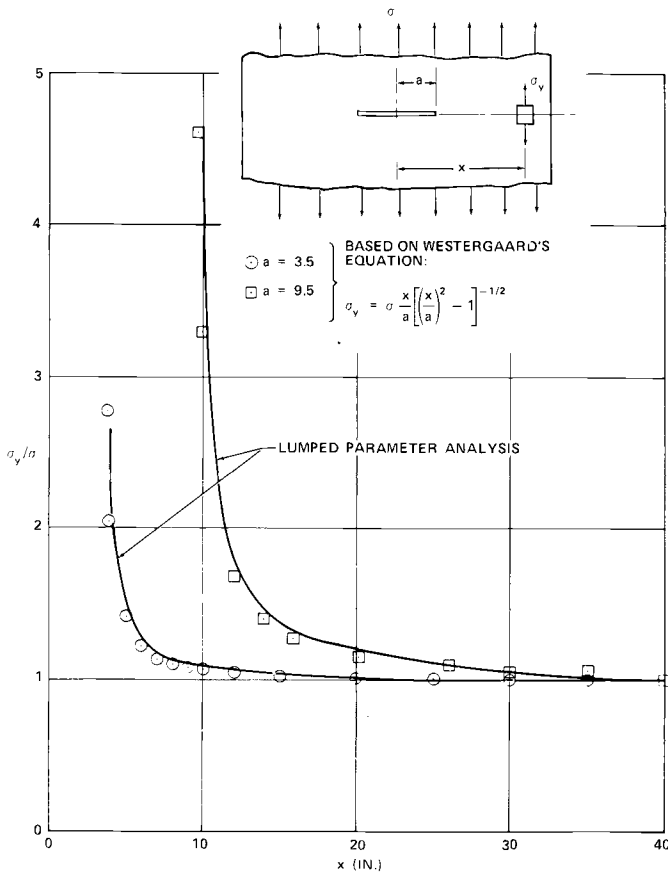
FIG. 11—*Comparison of lumped parameter analysis with Westergaard's equation for infinitely wide plate.*

for both skin fracture and center crack stopper criteria for case 3 of Table 1 where the center crack stopper is intact and for case 4 where the center crack stopper is broken. The skin material is assumed to be 7075-T73 with $K_c^* =$ 90,000 psi $\sqrt{\text{in.}}$ [1]. The crack stopper and frame are assumed to be titanium 8-1-1 and 7075-T6, respectively, with ultimate tensile strengths of 149,000 and 75,000 psi. If the damage tolerance criteria selected require that the center crack stopper should not fail, then for a half crack length of 20 in. the gross strength would be limited to 11,000 psi from curve *A* of Fig. 14; however, the residual strength based on skin criteria is 31,500 psi from curve *B*, resulting in an unbalanced design. If, however, the center crack stopper is allowed to break, leaving the frame intact, the strength based on skin criteria would be reduced to 30,000 psi from curve *D*. The residual strength of the panel would be 19,000 psi for a half crack length of 20 in. based on center frame criteria. This is a case where increasing the damage tolerance would
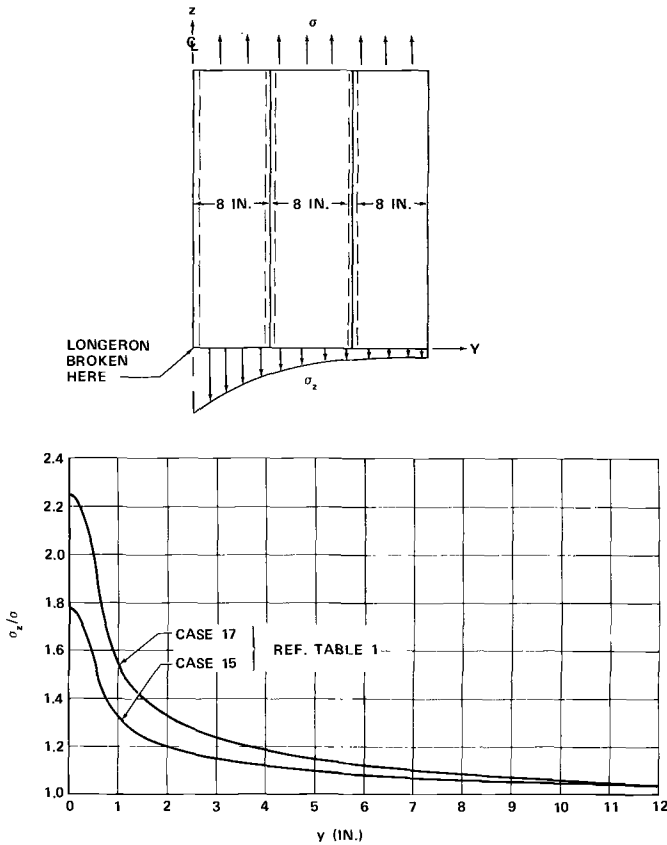
FIG. 12—*Axial skin stress in the vicinity of a broken longeron.*

reduce the weight, since the area of the crack stoppers would have to be more than doubled to maintain their continuity at a gross stress of 19,000 psi. The rivets attaching the crack stopper to the skin become highly loaded as the crack extends. Figure 15 shows outer crack stopper total rivet load as a function of crack length for cases 3, 4, and 6 of Table 1. Only the first and second rows are shown. For case 3, the rivets attaching the center crack stopper to the skin are extremely highly loaded analytically: for $a = 21.5$, P_r/σ is 0.348.

Test Program

Extensive fatigue and fail-safe testing had been completed during the development of the DC-8 and DC-9 aircraft. The general philosophy during the DC-8 testing was to subject a panel or shell structure to pressure loading which would simulate a principal stress in the skin. Rotary saws were then
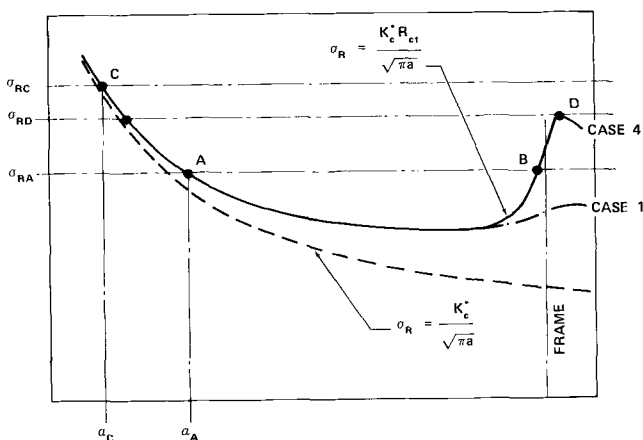
FIG. 13—*Comparison of gross residual strength curves for unstiffened and stiffened panels, cases 1 and 4 of Table 1.*
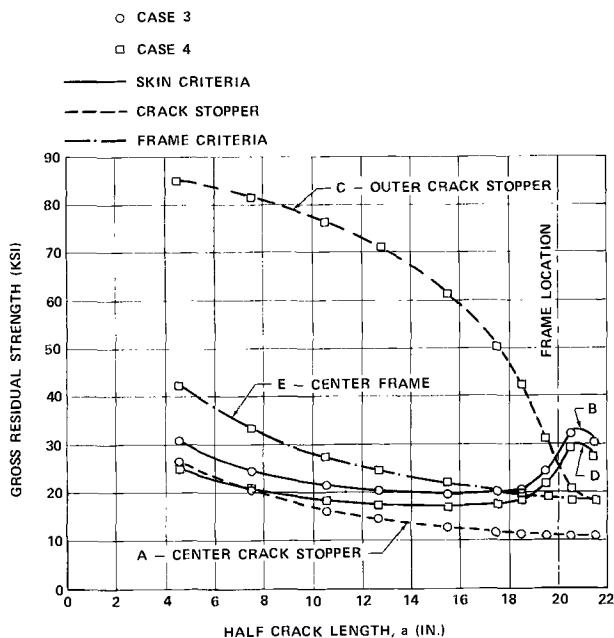
FIG. 14—*Gross residual strength for a typical flat panel with two-bay longitudinal crack.*

inserted into the skin and advanced until rapid fracture occurred. This method is excellent for determining the crack arresting capability of the crack barriers, but little information on fracture toughness is gained that can be used in future designs.

The methods changed during the DC-9 testing, where saw cuts were made in the skin and cyclic pressure applied so that the saw cuts were converted to fatigue cracks prior to fast fracture. Fracture toughness can be determined from this type of testing if the crack length at fast fracture is known. All of these early data were extremely useful during the development of the DC-10 fail-safe capability; nevertheless, in order to produce the most efficient design, further development testing was required. Figure 16 illustrates some of the fail-safe development test specimens completed to date.

Curved Panels

Figure 16a shows a large curved panel of 118.5-in. radius which is stiffened by eight frames and eleven longerons. Axial loading is applied by a series of whiffletrees attached to the ends of the panel. Pressure loading is applied to the underside of the panel by lowering a vacuum chamber onto the panel and evacuating the chamber. Both axial load and pressure loading can be cycled or applied statically. Transverse and longitudinal saw cuts can be made in the
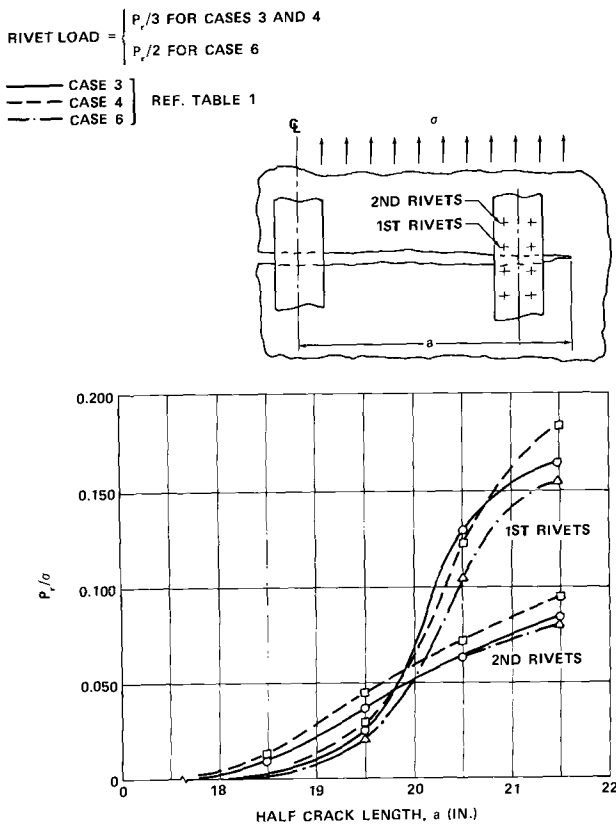
FIG. 15—*Rivet shear load, outer crack stopper to skin rivets.*
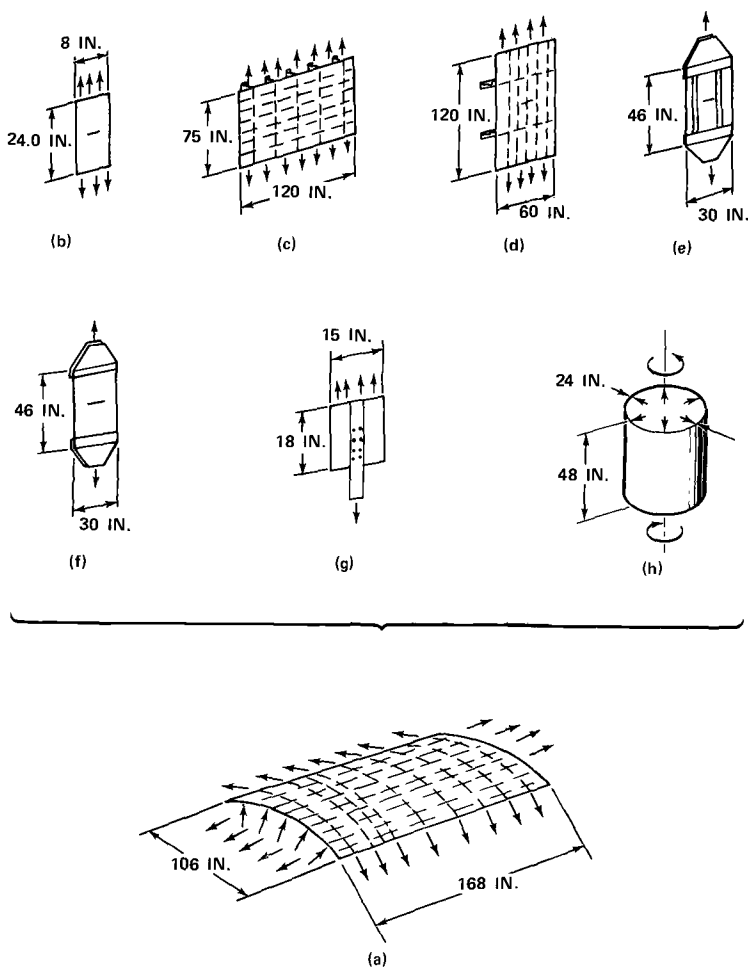
FIG. 16—*Fuselage fatigue and fail-safe development tests.*

skin and propagated into fatigue cracks prior to applying static loading to determine the effects of fast fracture and arrest.

The vacuum test machine was initiated during the DC-10 development and considerable effort was required to perfect its operation. The main innovations in this machine are the capability to apply axial load and the ability to observe the inner side of the panel during pressure loading. One circumferential and six longitudinal crack tests have been performed on two panels to date. Panel 15 was made from 0.080-in. 7075-T73 clad sheet, with a frame configuration as shown in Fig. 3a with a net area of 0.5042 in.[2]. Longerons were extruded hat as seen in Fig. 3d with a gross area of 0.312 in.[2]. Panel 16 was made from 0.063-in. 2024-T3 clad sheet with frame configuration as shown in Fig. 5 but of 0.063-in. thickness and 0.425-in.[2] net area. Crack

stoppers were 3.25 by 0.016-in. titanium 8-1-1 and longerons were rolled hat section with a gross area of 0.214 in.². During the development of the vacuum test machine shown in Fig. 17, all of the specimen types *b* to *g* of Fig. 16 were tested to give early data to be incorporated into the larger curved panels. A view of the upper side of curved panel 16 is shown in Fig. 18.

Figure 16*b* shows narrow specimens for material screening. Crack propagation and residual strength tests were performed on these specimens, but the fracture toughness data obtained are not representative of wide panels such as fuselage panels. This is illustrated by Liu [13] who shows the increase in plane stress fracture toughness K_c with increasing panel width. This effect is particularly noticeable in 2024-T3 sheet.

Flat Panels with Longitudinal Cracks

Figure 16*c* shows flat panels stiffened by longerons and frames. Fourteen tests were performed on six panels of this type. Frames on each of the panels were 7075-T6 with cross sections as shown in Fig. 3. Longerons were all 7075-T6 extruded hat section with a gross area of 0.312 in.². A description of the panel is given in Table 5. Three-inch-wide titanium crack stoppers 0.025 in. thick were incorporated into panels 5 and 6 with three rows of rivets. Cracks were propagated under uniaxial cyclic loading from saw cuts in the skin to simulate one-and two-bay longitudinal cracks. Static loading was applied at predetermined crack lengths to fast fracture the skin. Cracks were normal to the frames and crack stoppers provided the crack barriers.
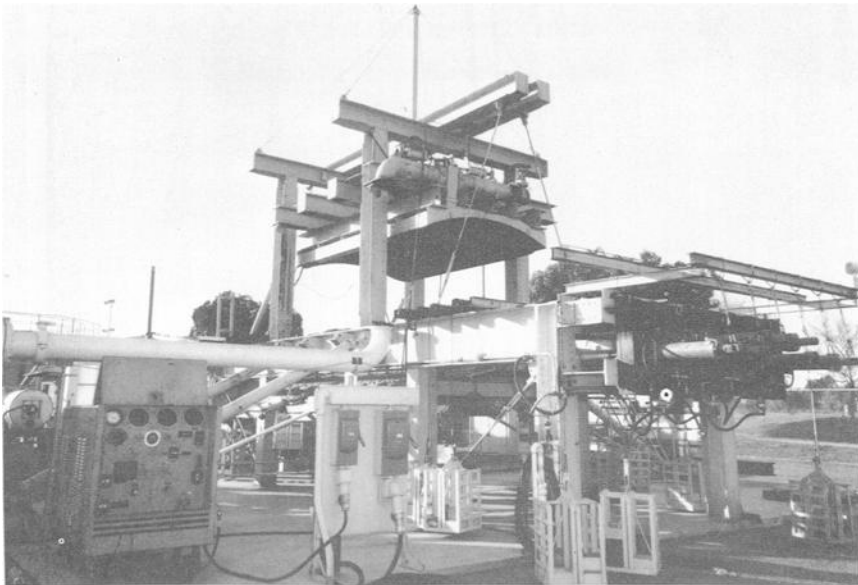

FIG. 17—*Vacuum test rig for testing curved panels under combined pressure and axial loading.*

FIG. 18—*Upper side of curved test panel 16.*

TABLE 5—*120-in.-wide flat panel configuration for longitudinal cracks (frame spacing 20.0 in., skin thickness 0.071 in.).*

Panel No.	Skin Material	Longeron Spacing, in.	Crack Stopper	Shear Clip Type[a]
1	7075-T73	6.5	None	(a)
2	7075-T73	8.0	None	(b)
3	7075-T73	6.5	None	(c)
4	7075-T73	8.0	None	(a)
5	7075-T73	8.0	3 by 0.025-in. titanium 8-1-1	(a)
6	2024-T3	8.0	3 by 0.025-in. titanium 8-1-1	(a)

[a] Refer to Fig. 3.

Flat Panels with Circumferential Cracks

Figure 16d shows flat panels stiffened by longerons and frames. Eighteen tests were performed on nine panels of this type. The configurations of eight of these panels, listed from 7 to 14, are shown in Table 6. Longerons were saw cut, and cracks propagated into two adjacent bays under uniaxial cyclic loading to simulate a two-bay circumferential crack with a broken central

TABLE 6—*60-in.-wide flat panel configuration for circumferential cracks (longeron spacing 8.0 in., skin thickness 0.071 in.).*

Panel No.	Skin Material	Longeron Type[a]	Longeron Net Area, in.²	Longeron to Skin Attachments
7.............	7075-T73	Hat (d)	0.3029	NAS 1097 DD6
8.............	7075-T73	Hat (d)	0.5121	NAS 1097 DD6
9.............	7075-T73	T (e)	0.2895	RV 5176-6 7075-T73
10.............	7075-T73	T (e)	0.4865	NAS 1097 DD6
11.............	2024-T3	Hat (d)	0.3029	NAS 1097 DD6
12.............	2024-T3	Hat (d)	0.5121	NAS 1097 DD6
13.............	2024-T3	T (e)	0.2895	RV 5170-6 7075-T73
14.............	2024-T3	T (e)	0.4865	RV-5170-6 7075-T73

[a] Refer to Fig. 3.

longeron. At predetermined crack lengths, static loads were applied to fast fracture the skin. Cracks were normal to the longeron so that the longerons acted as crack barriers.

Figure 16e shows flat panels stiffened by crack stopper straps. Six panels of this type were tested, made from 0.071-in. 2024-T3 sheet with straps of various widths and thicknesses spaced 10 in. apart. The results of the two large flat panels with crack stoppers had indicated that perhaps two rivet rows were adequate, but, in view of the high rivet loads predicted by the analysis (Fig. 15), tests were needed to determine if the required load could be transferred without rivet failure. Nine-inch-long saw cuts were made in the skin with ⅛-in.-diameter holes drilled at the ends of the saw cut to delay any tendency to fast fracture the skin. Rivet edge distances were also varied, since the large flat panels had indicated the crack stoppers to be loaded more highly on the side from which the crack was approaching. Increasing edge distance would reduce the tendency to overload one side of the strap. Static loads were applied to failure in all of the tests. Loads input to the straps was measured by strain gages. Antibuckling guides were used on these tests.

Figure 16f shows 30-in.-wide unstiffened panels loaded uniaxially. During the early testing on the DC-8 where saw cuts were used, fracture toughness had been determined for 2024-T3 where the fracture had been initiated by a saw cut. Predictions were that for this material no difference would exist between fracture from a saw cut and fracture from a fatigue crack [14]. Two panels were tested for residual strength, one with a saw cut 9 in. long and the other with the same length of fatigue crack.

Figure 16g shows one of five small panels which had been cut from the fractured panels shown in Fig. 16e. The purpose of these panels was to determine the crack stopper to skin rivet shear load. Analysis had shown that the first rivets in the vicinity of the crack were highly loaded, and the possibility existed that these rivets could yield and redistribute load to the rivets away from the crack. Strain gages were installed between rivets and the load applied to the strap to failure. These panels were intended to simulate the case where the crack had propagated beyond the crack stopper.

Figure 16h shows one of 16 small, unstiffened cylinders 24 in. in diameter and 48 in. long made from 0.032 2024-T3 sheet. The purpose of these tests was to assess qualitatively the effects of shear and axial compression combined with pressure. The setup for testing the cylinders is illustrated in Fig. 19. An internal pressure source was provided by water and compressed air. Torque loading, applied to the top of the cylinders, was provided by two servo-controlled hydraulic jacks. The system was capable of applying cyclic or static pressure and torque loading simultaneously. Both torque and pressure loading were monitored and recorded using oscillograph instrumentation. Axial constraint was provided on some of the cylinders by using long steel bolts to hold the two end flanges together. Relief to the axial tensile stress due to pressure or the application of axial compressive stress was provided. Rosette strain gages located on the cylinders were monitored continuously by oscillograph recorders. Longitudinal fatigue cracks, initiated from saw cuts, were propagated to predetermined lengths by cyclic pressure loading. The test procedure subsequent to this operation is listed in Table 7.

TABLE 7—*Test procedure for 24-in.-diameter unstiffened cylinder test.*

| Cylinder Number	Test Procedure
1	Cycle pressure loading until failure.
2	Increase pressure in increments to failure.
3	
4	
5	Increase torque and pressure in increments to failure, torque:pressure ratio = 7750 in.³
6	
7	
8	Increase pressure to stabilize the cylinder. Tighten down the tie bolts to provide axial constraint. Increase pressure to failure.
9	
10	
11	
12	Hold pressure constant. Cyclic torque applied from zero to a torque:pressure ratio of 7750 in.³ until failure.
13	
14	
15	Increase pressure to stabilize the cylinder. Increase torque to a constant value. Cycle the pressure between 6.5 psi and 13.85 psi for cylinder 15 and between 9.0 psi and 21 psi for cylinder 16.
16	
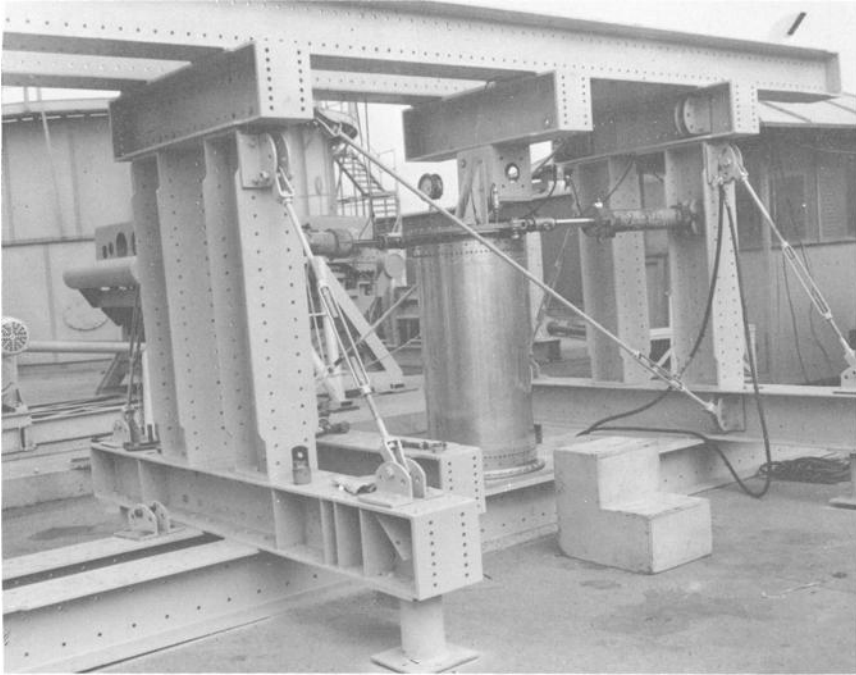
FIG. 19—*Test fixture for 24-in.-diameter cylinders.*

Test Results

Flat Panels with Longitudinal Cracks

The results of tests on the 120-in.-wide flat panels are shown in Table 8. Symbols not yet defined and used in the tables are

a_{aC} Half crack length at crack arrest from calculation
a_{FC} Half crack length at failure from calculation
σ_{RC} Gross stress at failure from calculation

Test values are the same with the subscript T replacing the subscript C. Fracture toughness $K_c{}^*$, listed for panels 1 and 2 tests 1 and 2, panel 3 test 1, and the first part of test 2 on panel 6, is the maximum value applied without fast fracture at the most critical crack length. For the two-bay tests on panels 2 and 5, the frame, central to the crack, was reinforced locally so that frame failure would not interfere with the skin critical criteria. Analysis had indicated (see Table 2) that the frame could fail prior to the skin and this was substantiated very accurately by the strain gages on panel 4. Analyses were performed to account for the reinforcing so that accurate R_{ct} values shown in Table 8 were available to determine $K_c{}^*$. Final failure of panels 1, 2, 3, 4, and 6 was due to skin fast fracture during static loading. In all cases where cracks had terminated in rivet holes, cyclic loading was applied to restart a fatigue

TABLE 8—*Test results for 120-in.-wide flat panels with longitudinal crack (panels 1 to 5, 0.071-in. 7075-T73 material; panel 6, 0.071-in. 2024-T3 material; all cracks parallel to grain).*

Panel No.	Test No.	Gross Stress, psi	Half Critical Crack Length, in.	R_{ct}	C	K_c*	Calculated				Test		Test/Calculated		
							a_{aC}, in.	a_{FC}, in.	σ_{RC} at Failure	a_{aT}, in.	a_{FT}, in.	σ_{RT} at Failure	a_{aT}/a_{aC}, in.	a_{FT}/a_{FC}, in.	σ_{RT}/σ_{RC}, in.
1............	1[a]	19 410	8.90	1.145	1.006	> 91 000	...	...	...	...	...	...	...	...	...
	2[a]	19 410	8.90	1.145	1.006	> 91 000	...	...	...	...	...	...	...	...	...
2............	1[a]	22 000	8.90	1.145	1.006	>103 137	...	...	...	...	...	...	...	...	...
	2[a]	20 888	8.90	1.145	1.006	> 97 929	...	...	...	...	...	...	...	...	...
	3[b]	17 300	16.60	1.430	1.023	92 000	18.30	21.50	19 000	19.63	21.48	18.476	1.072	0.999	0.972
3............	1[a]	19 410	8.90	1.145	1.006	> 91 000	...	...	...	...	...	...	...	...	...
	2[b]	19 124	12.05	1.250	1.012	96 200	20.08	21.0	19 700	20.08	20.46	19.744	1.0	0.974	1.002
4............	2[b]	17 000	17.50	1.435	1.0255	93 400	18.63	21.50	19 000	19.63	20.97	18 100	1.054	0.975	0.953
5............	2[b]	20 138	10.285	1.710	1.0085	95 700	19.0	20.40	24 994	19.00	20.40	25 118	1.0	1.0	1.004
6............	2[b]	19 000	16.325	0.98	1.0222	>145 500	...	...	...	...	...	...	...	...	...
	2[b]	20 000	21.875	1.26	1.040	145 500	...	...	...	...	21 875	20 000	...	...	...

[a] One-bay crack.
[b] Two-bay crack.

FIG. 20—*Arrest of two-bay longitudinal crack after fast fracture, test 2, panel 3.*

crack. Final failure of panel 5 was due to outer crack stopper failure. Test 2 was performed on panel 6 with the center frame completely saw cut, and final failure occurred with center frame, center crack stopper, and one outer crack stopper failed. Figure 20 shows the crack arrestment after fast fracture on panel 3. The fail-safe value of the separate shear clip frame configuration is illustrated by the crack in the clip leaving the main frame intact. If the frames had been designed such that the clip were part of the main frame member, the crack would have propagated through the frame.

Flat Panels with Circumferential Cracks

The results of tests on the 60-in.-wide panels are shown in Tables 9 and 10. K_c^* values listed for panels 7 to 10 and for test 2 of panel 11 are determined at fast fracture from a two-bay crack with saw cut central longeron. The other K_c^* values listed are the maximum values applied without fast fracture at the most critical crack length. During test 2 of panels 11, 13, and 14, the maximum value of residual strength required for the aircraft had been applied without failure. In order to obtain data for a higher degree of damage, two longerons were saw cut so that failure occurred with three bays of skin and

TABLE 9—*Test results for 60-in.-wide flat panels with circumferential crack (0.071-in. 7075-T73 skin material; cracks transverse to grain).*

Panel No.	Test No.	Gross Stress, psi	Half Critical Crack Length, in.	R_{ct}	C	K_c^*	Calculated a_{aC}, in.	a_{FC}, in.	σ_{RC} at Failure	Test a_{aT}, in.	a_{FT}, in.	σ_{RT} at Failure	Test/Calculated a_{aT}/a_{aC}, in.	a_{FT}/a_{FC}, in.	σ_{RT}/σ_{RC}, in.
7	1	25 160	4.040	0.870	1.0054	104 358	8.100	...	...	8.095	...	...	0.999	...	...
	2	26 540	4.123	0.875	1.0057	110 627	8.100	9.000	30 100	7.688	8.155	31 200	0.949	0.906	1.036
8	1	23 060	3.275	0.770	1.0036	97 330	7.750	...	...	7.675	...	...	0.990	...	...
	2	23 100	3.625	0.780	1.0044	100 942	7.600	8.900	28 700	7.600	8.350	29 600	1.000	0.938	1.031
9	1	23 100	3.500	0.850	1.0128	91 760	7.700	...	...	7.375	...	...	0.958	...	...
	2	28 600	2.440	0.810	1.0020	98 213	8.250	9.000	29 600	7.600	9.140	29 600	0.921	1.015	1.000
10	1	24 000	1.860	0.685	1.0012	84 973	7.900	...	...	7.265	...	...	0.921	...	...
	2	24 800	1.605	0.670	1.0009	83 318	8.200	8.810	27 500	7.560	8.810	27 800a	0.921	1.000	1.010

a Fast fracture to next longeron. Final failure at a gross stress of 36,052 psi with a total crack length of 32.67 in. and one broken longeron.

TABLE 10—Test results for 60-in.-wide flat panels with circumferential cracks (0.071-in. 2024-T3 skin material; cracks transverse to grain).

Panel No.	Test No.	Gross Stress, psi	Half Critical Crack Length, in.	R_{ct}	C	K_c*	Comments
11....	1	34 000	6.500	0.97	1.0141	>164 284	Final failure at gross stress of 27,921 psi with crack length of 25.69 in. equally spaced about two saw cut longerons
	2	40 000	6.205	0.95	1.0128	192 432	
12....	1	29 800	6.200	0.92	1.0128	>147 869	Final failure at gross stress of 40,855 psi with total crack length of 20.3 in. and one central saw cut longeron
	2	34 000	6.200	0.92	1.0128	>168 631	
13....	1	39 800	5.825	0.94	1.0113	>186 079	Final failure at gross stress of 30,966 psi with total crack length of 23.0 in. equally spaced about two saw cut longerons
	2	40 000	6.020	0.95	1.0121	>188 250	
14....	1	34 000	6.100	0.92	1.0124	>166 034	Final failure at gross stress of 34,293 psi with total crack length of 22.66 in. equally spaced about two saw cut longerons
	2	40 000	6.100	0.92	1.0124	>195 393	
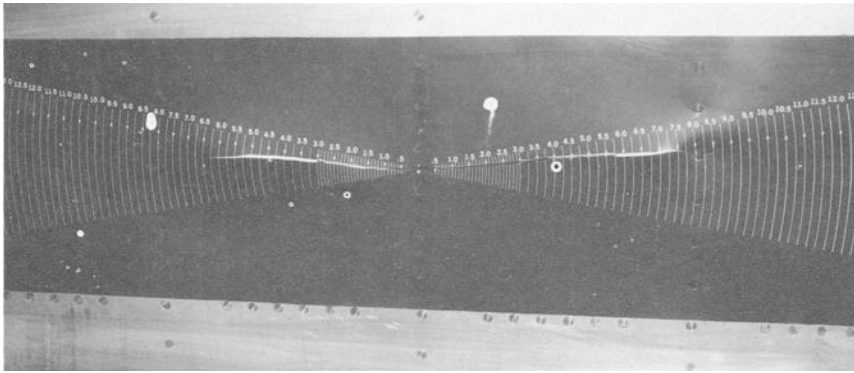
FIG. 21—*Arrest of crack after fast fracture at gross stress of 39,931 psi, panel 11, test 2.*

two cut longerons. The results of these tests are shown in Table 10. Figure 21 shows the crack arrestment during test 2 of panel 11; Fig. 22 shows the panel after final failure from a three-bay crack with two cut longerons.

Curved Panels

The test results for curved panels 15 and 16 are listed in Table 11. Four tests were completed on panel 15. Saw cuts were made in the skin in a longitudinal direction, 1 in. away from a longeron in all cases. Cracks were propagated to predetermined lengths under cyclic loading and static load was applied to cause fast fracture. The skin stresses are functions of both pressure P and axial load per inch of length N_x due to Poisson's ratio effects of the biaxially loaded skin. The equations governing the stresses are determined using the methods of Flugge [15]. Tests 1 and 3 were performed with pressure load only while axial load was present in the case of tests 2 and 4. Fast fracture of the cracks occurred for all tests on panel 15 and in each case the cracks
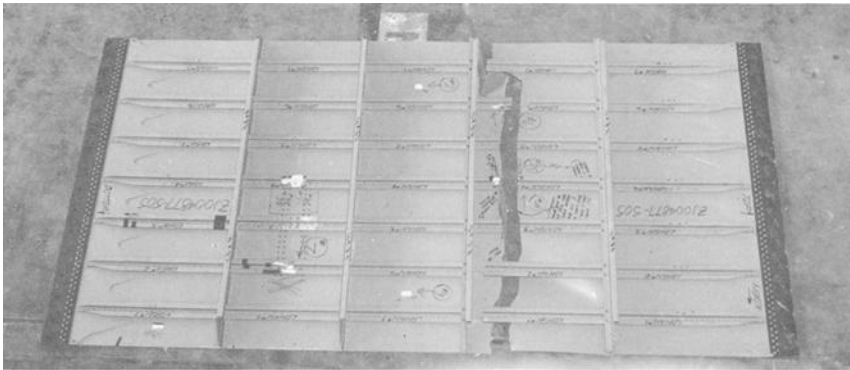
FIG. 22—*Failure of panel 11 at gross stress of 27,920 psi from three-bay crack with two cut longerons.*

TABLE 11—*Test results for longitudinal crack tests on curved panels (panel 15 0.080-in. 7075-T73, panel 16 0.063-in. 2024-T3).*

Panel No.	Test No.	P,[a] psi	σ_h,[b] psi	σ_x,[c] psi	a_c,[d] in.	R_{ct}	C	K^*, psi$\sqrt{\text{in.}}$	Calculated σ_{RC},[e] psi	a_{aC}, in.	a_{aT}, in.	$\dfrac{a_{aT}}{a_{aC}}$	Analysis Case[f]
15....	1[g]	12.8	14 912	0	7.235	1.076	1.0023	66 460	14 750	10.60	10.06	0.95	11
	2[b]	13.36	15 622	2 500	8.050	1.095	1.0028	72 000	16 000	10.06	10.06	1.0	11
	3[h]	10.80	12 600	0	12.10	1.210	1.0064	65 114	13 300	19.60	19.88	1.014	2
	4[h]	11.55	15 380	28 495	12.825	1.230	1.0072	80 573	16 500	19.50	19.88	1.019	2
16....	1[i]	12.1[k]	16 700	0	13.148	1.240	1.0075	>88 090	...	...	...	...	8
	2[j]	11.8[l]	16 300	0	2.150	1.724	1.0200	>81 544	...	...	...	...	9

[a] Pressure at fast fracture, attempts at fast fracture and failure.
[b] σ_h = hoop stress normal to crack = $1165P + 0.597N_z$ for panel 15 and $1383P + 0.9714N_z$ for panel 16.
[c] σ_x = axial stress parallel to crack = $8.4N_z + 121P$ for panel 15.
[d] Crack length at fast fracture, attempts at fast fracture or failure.
[e] σ_{RC} = gross calculated hoop stress at failure.
[f] Reference Table 1.

[g] One-bay crack.
[h] Two-bay crack with center frame intact.
[i] Two-bay crack with center frame intact and center crack stopper cut.
[j] Two-bay crack with both center frame and crack stopper cut.
[k] Maximum pressure applied without fast fracture.
[l] Failure occurred due to outer crack stopper failure.

were arrested at the frames. It can be seen that the value of K_c^* is increased effectively by 8 percent when an axial stress of 2500 psi is present and 23 percent with an axial stress of 28,495 psi. Axial compressive stress parallel to the crack, which normally causes buckling, is minimized by axial tensile stress and would be cancelled out entirely in the case of test 4. Figure 23 shows the crack arrested between rivets after test 1 of panel 15.

The crack stopper was saw cut completely and a cut was made in the skin in a longitudinal direction on panel 16. Cyclic loading was applied to propagate the crack and several attempts were made at various crack lengths to cause fast fracture. The value of K_c^* listed in Table 11 for test 1 on panel 16 is the maximum stress intensity applied without fast fracture at the most critical crack length. The center frame was cut completely for test 2 and the skin crack extended to 43 in. in length. Failure occurred at 11.8-psi pressure as a result of outer crack stopper failure. Just prior to failure, the stress intensity in the skin was as listed for K_c^* during test 2. Analysis case 9 of Table 2 predicts a crack stopper stress of 183,000 psi with total crack length of 43 in. and gross stress of 16,300 psi. Typical values of F_{tu} from coupon tests go as high as 167,000 psi for titanium 8-1-1 so that the analysis was 10 percent conservative.

A two-bay circumferential crack test with a broken central longeron was conducted on panel 16. The equations governing the skin and longeron axial stresses, accounting for Poisson's ratio effects [15], are

$$\sigma_{x\text{skin}} = 11.25 \ N_x + 126.8P$$

$$\sigma_{x\text{long}} = 11.88 \ N_x - 298.6P$$
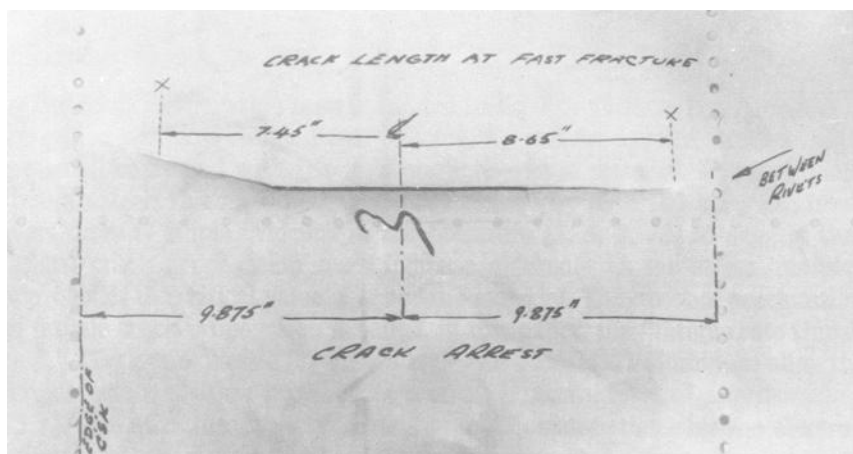
FIG. 23—*View of panel 15 showing arrest of one-bay crack.*
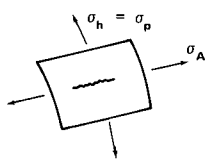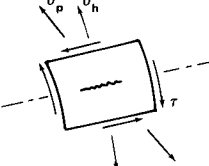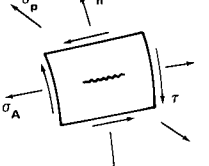
FIG. 24—*Principal stress equations for cases* A, B, *and* C.

Several attempts were made at total crack lengths up to 16.0 in. to cause fast fracture with an axial load $N_x = 2420$ lb/in. and a pressure $P = 9.1$ psi. Skin stress was 28,380 psi and longeron stress 23,600 psi. The maximum value of $K_c{}^*$, determined without fast fracture, was $> 131,700$ psi$\sqrt{\text{in.}}$ During this test it was not intended to fail the panel but merely to show a static capability to carry an axial skin stress of 28,380 psi with a broken longeron and two bays of skin cracked.

Unstiffened Cylinders

The prime purpose of this series of tests was to investigate the effects of shear combined with pressure on the residual strength of a cracked cylinder. The intention was to determine if the gross principal stress at failure, calculated from condition C of Fig. 24, could be compared to the gross allowable stress obtained from condition A. As the presence of the biaxial tension stress σ_A improves the gross strength by cancelling some of the compression stress parallel to the crack edge, it would be more reasonable to determine the principal stress from condition B, neglecting the axial stress σ_A. The terms appearing in Fig. 24 are defined as follows:

σ_h Hoop stress, psi
σ_A Axial stress, psi
τ Shear stress, psi
σ_p Principal stress, psi

The results of the tests are shown in Table 12 and plotted in Fig. 25. It can be seen by comparing the results of the first six cylinders in Table 7 that the presence of shear reduces the gross residual strength. Comparing principal stress at failure of cylinders with applied shear to the allowables for cylinders without shear is conservative; however, the calculation of principal stress, neglecting axial stress (as in case *B* of Fig. 24), gives a closer approximation to condition *A* than the calculation of principal stress from condition *C*.

Rivet Shear Deflection Test Results

In order to verify the rivet deflection (Eqs 3 and 5) for titanium and aluminum, several small tests were performed on lap splice specimens. Each specimen consisted of a strip of 6Al-4V single annealed titanium which was riveted to a strip of 0.071-in. 2024-T3 clad sheet using RV-5197-6 countersunk rivets. The specimens were placed back to back as shown in Fig. 26 to eliminate local bending. Three thicknesses of titanium were used, 0.016, 0.020, and 0.025 in. The extension, under tensile loading, was measured over a 2-in. gage length using an extensometer. Extension of the sheet was calculated and subtracted from the overall deflection so that actual rivet deflection would be obtained. The stiffness P/δ, where P is the applied load and δ is shear deflection of the rivet (obtained from the elastic portion of the resulting load deflection curve), is compared in Fig. 26 to the value calculated from Eqs 3 and 5.
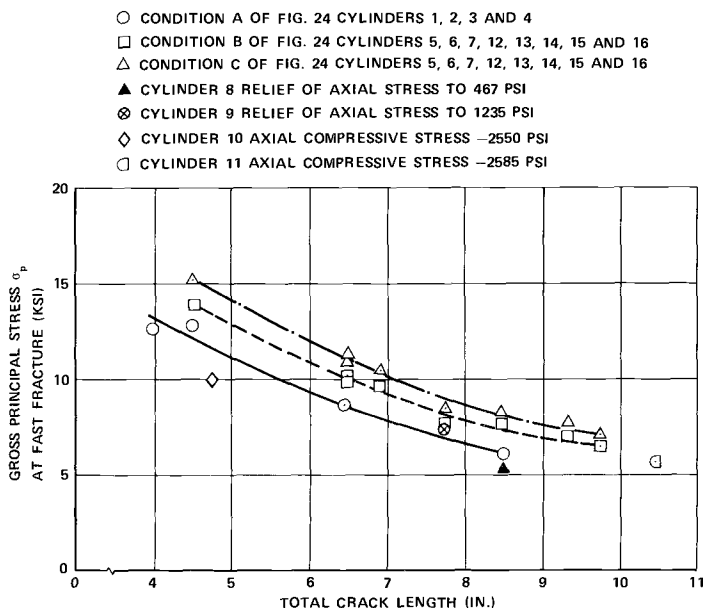
FIG. 25—*Test results for 24-in.-diameter cylinder.*

TABLE 12—Test results for 24-in.-diameter cylinders.

Cylinder Number	Crack Length at Failure, in.	Loads at Failure		Stresses at Failure			Maximum Principal Stress at Failure		Condition
		Pressure, psi	Torque, in.·lb	Hoop Stress, psi	Shear Stress, psi	Axial Stress, psi	Case B $\sigma_A = 0$,[a] psi	Case C Including σ_A,[a] psi	
1	4.00	34.0	0	12 750	0	6 275	12 750	12 750	P
2	4.50	34.3	0	12 880	0	6 440	12 880	12 880	P
3	6.44	23.0	0	8 630	0	4 315	8 630	8 630	P
4	8.50	16.1	0	6 030	0	3 015	6 030	6 030	P
5	4.50	27.3	209 250	10 250	7240	5 125	13 995	15 368	$P + T$
6	6.88	19.0	147 250	7 125	5085	3 563	9 772	10 732	$P + T$
7	8.44	15.0	116 250	5 625	4020	2 813	7 719	8 478	$P + T$
8	8.50	14.5	0	5 440	0	467	5 440	5 440	$P + C$
9	7.70	20.0	0	7 500	0	1 235	7 500	7 500	$P + C$
10	4.75	27.0	0	10 130	0	−2 550	10 130	10 130	$P + C$
11	10.50	15.0	0	5 630	0	−2 585	5 630	5 630	$P + C$
12	9.75	13.0	93 000	4 875	3210	2 435	6 468	7 089	$P + T_c$
13	7.75	15.0	117 400	5 625	4060	2 813	7 752	8 516	$P + T_c$
14	6.50	20.0	159 650	7 500	5520	3 750	10 423	11 455	$P + T_c$
15	9.313	13.85	105 090	5 190	3630	2 595	7 057	7 748	$P_c + T$
16	6.47	20.9	133 145	7 840	4600	3 920	9 964	10 880	$P_c + T$

NOTE—Condition definition:

P = static pressure only
$P + T$ = static pressure + static torque
$P + C$ = static pressure + compression
$P + T_c$ = static pressure + cyclic torque
$P_c + T$ = cyclic pressure + static torque

[a] Reference Fig. 24.
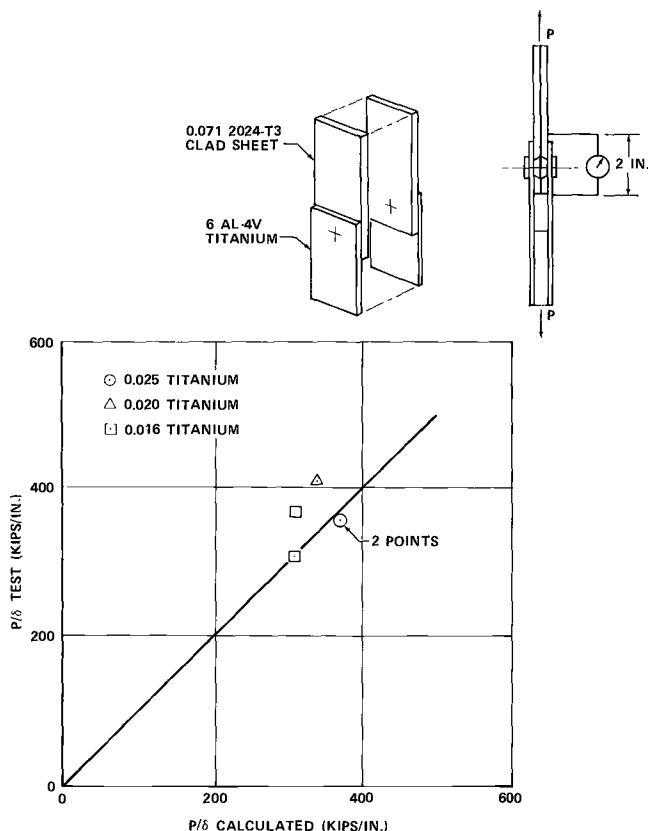
FIG. 26—*Rivet shear deflection test result correlation.*

Stiffened Panels, 30 in. Wide

The test results for these panels are shown in Table 13. In all cases, the straps failed without failure of the rivets. The maximum load to be transferred to a strap in the DC-10 configuration is 4370 lb for a 42.0-in.-long crack. It can be seen from Table 13 that the value of P_c in all cases is higher than this number so that strap failure will always precede rivet failure, even with two rivet rows.

Unstiffened Panels, 30 in. Wide

Two unstiffened panels made from 0.071-in. 2024-T3 clad sheet were tested (see Fig. 27). A 9-in.-long central crack was propagated in the first panel and static load applied. Slow crack growth took place and final failure occurred at a gross stress of 24,600 psi with the crack 11.0 in. long. The second panel contained a 9-in.-long saw cut. Static load was applied and slow growth again took place to 11.0 in. before failure at the same gross stress of 24,600 psi. Antibuckling guides, set 1.0 in. apart, were used in both cases. K_c as determined for the final crack length from Eq 1 was 114,000 psi$\sqrt{\text{in.}}$

TABLE 13—*Test results for 30-in-wide panels (0.071-in. 2024-T3 clad sheet titanium strap 6Al-4V).*
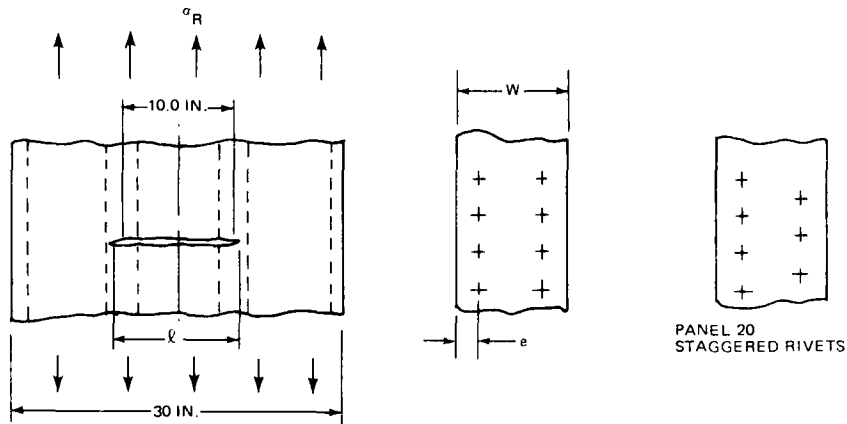
Panel No.	W	t	e, in.	P_F, lb	l_F, in.	P_c	σ_R
17........	2.813	0.025	11/16	89 000	11.45	5880	34 503
18........	2.813	0.025	7/16	87 000	9.80	5725	33 727
19........	3.438	0.020	7/8	94 000	10.50	5700	36 942
20........	3.438	0.020	7/8	89 000	9.60	5380	34 977
21........	4.188	0.016	1 1/16	89 000	10.60	5500	34 745
22^a........	3.625	0.016	29/32	96 000	9.90	3060	36 185

NOTE—P_F = load at failure
l_F = crack length at failure
P_c = load transferred to crack stopper due to crack
σ_R = gross stress at failure

^{a} AM 350 stainless steel strap.

Rivet Shear Load Test

Figure 28 gives the results of tests performed on the small panels shown in Fig. 16g to determine the crack stopper to skin rivet shear load. A lumped parameter analysis, to determine the rivet shear load, was performed on one of the panels with a 0.020-in. strap. This analysis is used for a comparison with the results for the three thicknesses of strap. It is not expected that the strap thickness variation, in the ranges considered, will affect the calculated elastic load distribution to a high degree. The panel was divided into bars and shear panels similar to those shown in Fig. 7. The rivet loads were determined from strain gage readings on the strap. The ordinate of Figs. 28a to 28c is shown as shear flow in pounds per inch and, since the rivets are spaced 1 in. apart, this load would, therefore, be rivet load. The shear flow shown is applied to two rivets. Figure 28a shows a comparison between test and elastic analysis for a 0.025-in. strap. It can be seen that the first rivets yield at a load between 3000 and 5000 lb and more load is carried by the remaining rivets. Yielding
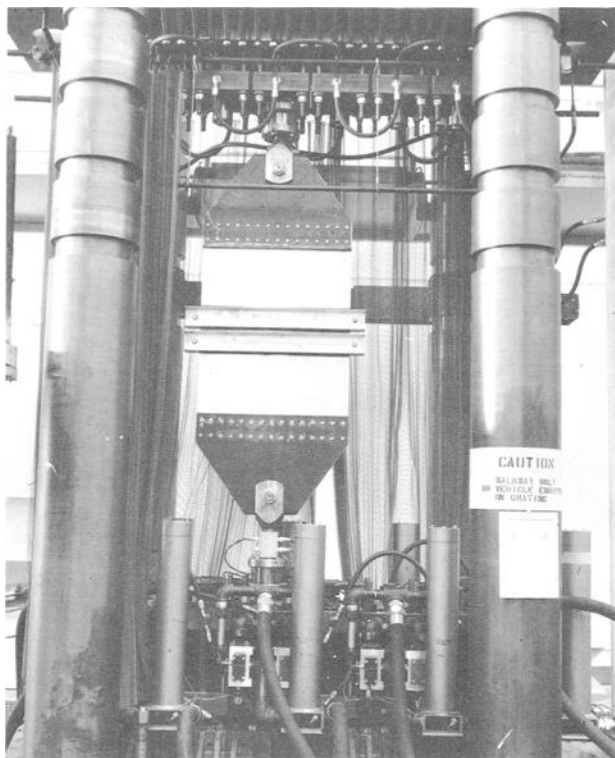
FIG. 27—*Test setup for 30-in.-wide panels.*

occurred early for both the 0.020 and 0.016-in. straps as shown in Figs. 28*b* and 28*c*. Figure 28*d* shows applied load versus shear load in the first rivets for tests on two panels with 0.025-in. straps. The maximum load transferred from the skin to crack stopper for DC-10 loading with a crack 42 in. long is 4370 lb. This is determined from case 6 of Table 1 with a cabin pressure of 9.2 psi and a skin stress 80 percent of PR/t hoop stress, where R is 118.5 in. It can be seen from Fig. 28*d* that little or no loss in first rivet load is experienced at this applied load. However, due to early yielding of the first rivets in the 0.020 and 0.016-in. straps shown in Figs. 28*b* and 28*c*, a loss in the crack tip stress ratio R_{ct} could be expected if 0.020 or 0.016-in.-thick straps were used.

Correlation

Skin Criteria

Space limitations prevent illustrations such as Fig. 13 for every test. Figure 29 shows the results of test 2 on panel 3. The shape of the curve is determined by analysis of case 1 of Table 1 and the height by K_c* at fast fracture. The

curve is plotted from Eq 7. Correlation is shown with the analysis at crack arrest and final failure where the data points fall on the curve. For other tests where fast fracture, arrest, and failure occurred, the correlation is shown in the tables of test results by comparing calculated crack arrest lengths and failure stresses with those obtained from test.

Frame Criteria

An example of frame stress correlation is shown in Fig. 30 for panels 5 and 6. The other cap stresses are extremely close to the analysis but the inner cap stresses are lower. This kind of correlation is typical of all the tests performed. The outer, more critical cap stresses were always extremely close to the analysis results.

Longeron Criteria

Longeron bending stresses were not predicted accurately on any of the tests on flat panels 7 to 14. Secondary effects due to center longeron bending influenced the test results. Figure 31 shows that at some distance from the crack the longeron load P is acting at the centroid of the section. This load is reacted to eventually by the skin ahead of the crack and is thus transferred a distance e, which causes the longeron to bend inwards. The induced bending in the center longeron for a uniaxial loading case causes the outer longerons to be loaded as shown in Fig. 31b. The resultant bending in the outer longerons tends to cancel out the bending caused by transfer of load from the cracked skin as indicated in Table 4. The load input to the longeron, however, is accurately predicted by the analysis for the flat panels as illustrated by Fig. 32 for panels 8 and 12. If the panel section shown in Fig. 31b were a section of a pressurized shell, then the inward bending of the center longeron would be relieved by the cabin pressure and the loading W, causing relief to the outer longeron bending, would not be present. This is illustrated by Fig. 33, which shows outer longeron stress correlation for the circumferential crack test on panel 16. It can be seen that the analysis accurately predicts the longeron stress for the pressurized panel; also, that testing flat panels to determine fail-safe allowable stresses for curved panels under pressure for this condition should be treated with caution, particularly if the residual strength is determined by stiffener criteria. The relief due to longeron bending will produce allowable stresses higher than would be obtained from a curved panel test.

Final Configuration Selection

The test results of the 24-in.-diameter cylinders, although qualitative due to their comparatively diminutive size, do at least indicate that shear stresses reduce the residual strength in the presence of fatigue cracks. Figure 25 indicates that principal stresses determined from condition B of Fig. 24 are slightly conservative when compared to the allowables determined from condition A. It was decided to account for shear by comparing the results for
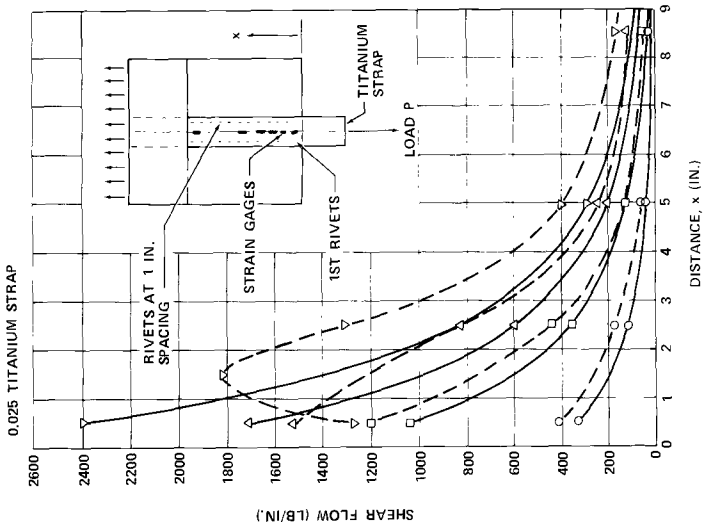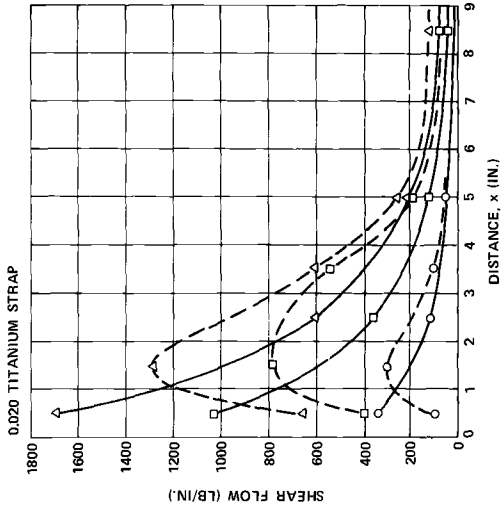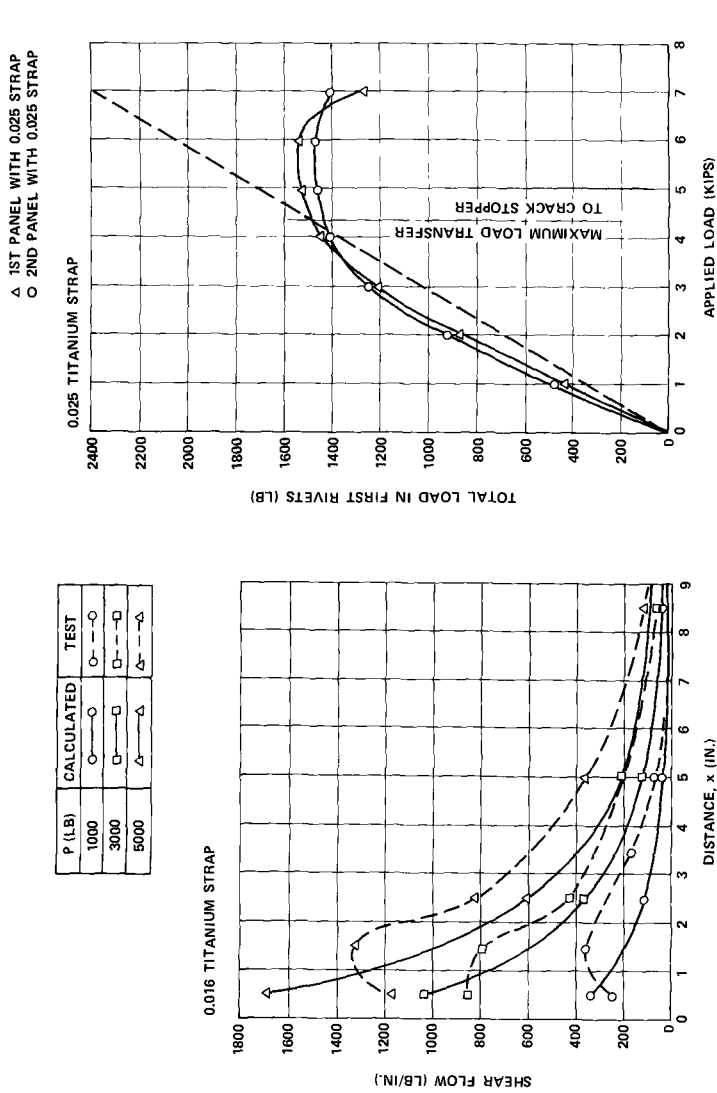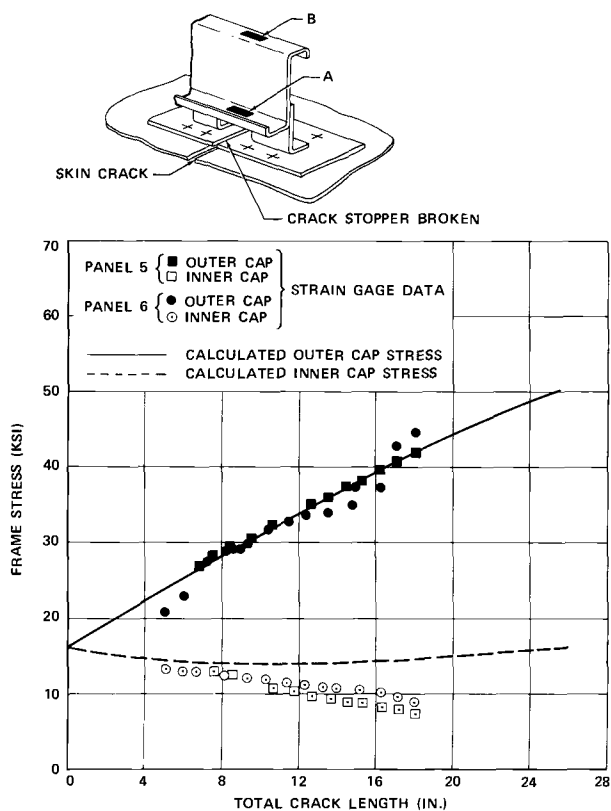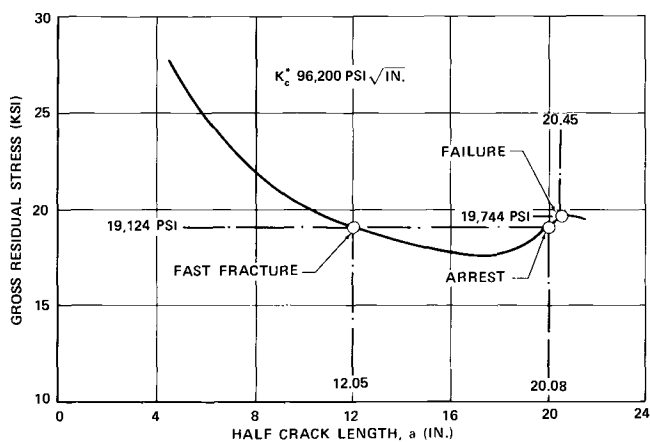
FIG. 28—*Rivet shear load—analysis, test correlation: (a) 0.025, (b) 0.020, (c) 0.016, and (d) 0.025-in. titanium strap.*

FIG. 29—*Gross residual strength curve, test 2, panel 3.*

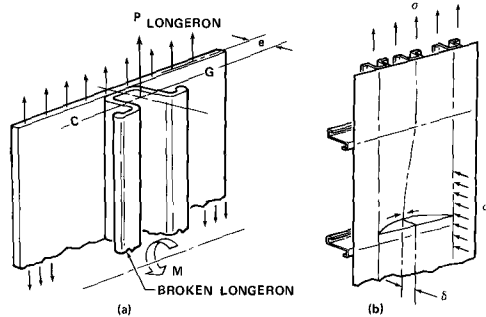FIG. 30—*Center frame stress correlation two-bay crack test, panels 5 and 6, test 2; gross stress, 16,400 psi.*

FIG. 31—*Center longeron bending.*

panels symmetrically loaded to a principal stress determined from condition *B* of Fig. 24 which neglects axial stress. The effects of axial tension increase the allowable stress, as seen from the results of tests 2 and 4 of panel 15 listed in Table 11.

Longitudinal Cracks

The highest limit design principal stress in the minimum gage portion of the shell is approximately 19,000 psi from hoop stress and shear. It was desirable to show that the structure was fail-safe for limit values to satisfy foreign requirements. The gross residual strength from flat panels 2, 3, and 4 without crack stoppers and with 7075-T73 skin range from 18,100 to 19,744 psi as listed in Table 8. The various shear clips on these panels shown in Table 5
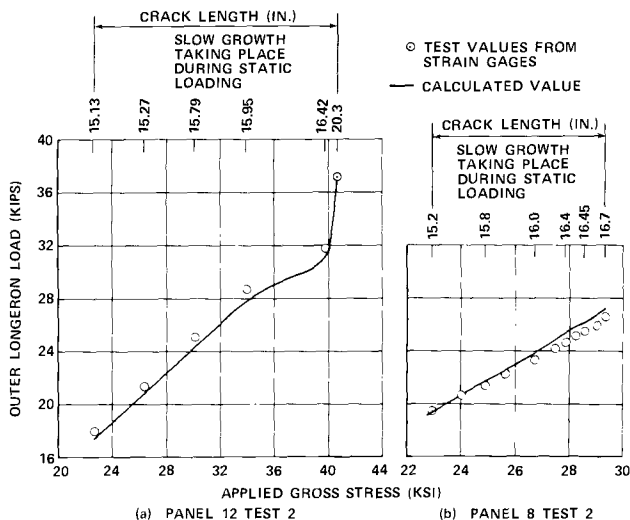
FIG. 32—*Outer longeron load, flat panel with circumferential crack.*
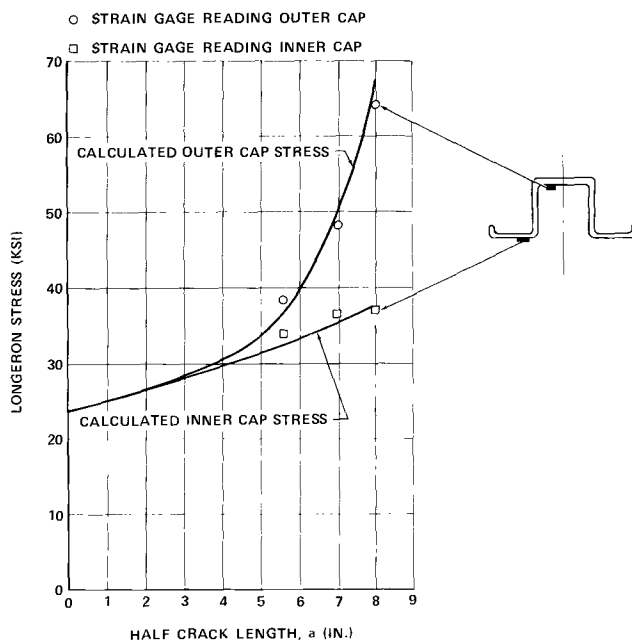
FIG. 33—*Outer longeron stress correlation circumferential crack test, panel 16.*

and illustrated in Fig. 3 do not vary the strength significantly. The results of tests on curved panel 15 indicate a 30 percent loss in strength due to bulging from pressure. This is indicated by $K_c{}^*$ values from flat panels listed in Table 8, compared to those for curved panel 15 for tests without axial load listed in Table 11. It can be seen that 7075-T73 skin on panels without crack stoppers would, at best, only produce an allowable gross stress of 13,800 psi. With 2024-T3 skin without crack stoppers, using R_{ct} for $a = 21.5$ of 1.81 (from case 1 of Table 2) and a $K_c{}^*$ of 88,090 psi$\sqrt{\text{in.}}$ (from Table 11), the gross allowable stress is just a little over 19,000 psi. In view of this, it was decided to use both 2024-T3 skin, 0.071 in. thick, and crack stopper straps for the minimum gage portions of the shell. Test 2 on panel 5 listed in Table 8 had indicated that a gross stress of 25,118 psi could be applied without failure of the crack stopper to skin rivets. It was decided, therefore, to use only two rows of rivets, since the load transfer into the crack stopper would only be based on a gross stress from hoop tension in the region of 12,000 psi. Tests on 30-in.-wide panels listed in Table 13 had indicated that the required load could be transferred to the crack stopper with two rows of rivets. Reducing the crack stopper thickness from 0.025 in. was considered, but tests on panels shown in Fig. 16g, with results plotted on Figs. 28a to 28c, indicated that the first rivets yield early on all thicknesses other than 0.025 in. Figure

28*d* shows that adequate load can be transferred before rivet yield. The gross residual strength of this configuration is approximately 26,000 psi using R_{ct} from case 6 of Table 2. Titanium was chosen for crack stopper material because of its high strength to weight ratio and resistance to fatigue, which ensures skin cracking before crack stopper cracking.

Circumferential Cracks

2024-T3 material had been chosen for the longitudinal crack case. This choice was substantiated by tests on 2024-T3 panels 11 to 14 of Table 10 compared to 7075-T73 panels 7 to 10 of Table 9. K_c^* values are shown to be almost double those of 7075-T73. Comparing allowables for the same longeron, for example, panel 8, using 7075-T73, failed at 29,600 psi (Table 9). Panel 12 with a similar longeron but with 2024-T3 skin failed at 40,855 psi. Hat-section longerons, in conjunction with 2024-T3, were therefore chosen for the circumferential crack condition. This configuration gives more than adequate fail-safe capability for the selected damage tolerance.

References

[*1*] Stone, M., "Structural Reliability Through Detail Design and Development Testing," Air Force Conference on Fatigue and Fracture of Aircraft Structures and Materials, Miami, Fla., 15–18 Dec. 1969.

[2] Wang, D. Y., "An Investigation on Fatigue Crack Propagation and Fail-safe Design of Stiffened Large Aluminum Alloy Panels with Various Crack Stoppers," Proceedings, 10th ASME/AIAA Structures, Structural Dynamics and Materials Conference, New Orleans, La., April 1969.

[*3*] "Crack Propagation Prediction and Crack Stopper Techniques for Stiffened and Unstiffened Flat Sheet in a Supersonic Environment," ASD-TDR-63-773, Douglas Aircraft Co., Inc., Long Beach, Calif., Sept. 1963.

[4] Hunt, R. T., "Residual Strength and Crack Propagation in Stiffened Panels," Douglas Report LB 31837, Douglas Aircraft Co., Inc., Long Beach, Calif., Nov. 1964.

[*5*] Eide, G. R., "Fail-safe Design of Stiffened Panels," Douglas Report LB 32056, Douglas Aircraft Co., Inc., Long Beach, Calif., Dec. 1964.

[*6*] Irwin, G. R., *Journal of Applied Mechanics*, JAMCA, Vol. 24, Sept. 1957, p. 361.

[7] Allen, F. C., "Stress Analysis of Centrally Cracked Plates," presented to ASTM Committee E-24, March 1969.

[*8*] Denke, P. H., "A General Digital Computer Analysis of Statically Indeterminate Structures," Douglas Paper 834, Douglas Aircraft Co., Inc., Long Beach, Calif., Sept. 1959.

[*9*] Denke, P. H., "A Computerized Static and Dynamic Structural Analysis System; Part III. Engineering Aspects and Mathematical Formulation of the Problem," Douglas Paper 3123, presented to the SAE International Automotive Congress and Exposition, Jan. 1965.

[*10*] Picard, J. and Morris, R. C., "Format 11—Second Version of Fortran Matrix Abstraction Technique," AFFDL-TR-66-207, Vols. I and III, Douglas Aircraft Co., Inc., Long Beach, Calif., Dec. 1966.

[*11*] Swift, T. and Wang, D. Y., "Damage Tolerant Design-Analysis Methods and Test Verification of Fuselage Structure," presented to Air Force Conference on Fatigue and Fracture of Aircraft Structures and Materials, Miami, Fla., 15–18 Dec. 1969.

[*12*] Westergaard, H. M., *Journal of Applied Mechanics*, JAMCA, Vol. 6, No. 1, June 1939, p. A49.

[*13*] Liu, A. F., "Statistical Variation in Fracture Toughness Data of Airframe Materials," presented to Air Force Conference on Fatigue and Fracture of Aircraft Structures and Materials, Miami, Fla., 15–18 Dec. 1969.
[*14*] Broek, D., "The Residual Strength of Aluminum Alloy Sheet Specimens Containing Fatigue Cracks or Saw Cuts," C.C.L. Class G 311: G 331, Report NLR-TR M.2143, National Lucht—En Ruimtevaartlaboratorium, National Aero Space Laboratory, NRL Amsterdam.
[*15*] Flugge, W., "Stress Problems in Pressurized Cabins," NACA T.N. 2612, Stanford University, Feb. 1952.

J. E. Jensen[1]

The Ballistic Damage Characteristics and Damage Tolerance of Wing Structural Elements

ABSTRACT: The damage and residual strength of 7075-T6 aluminum panels exposed to caliber 0.50 AP M2 gunfire was found to vary with projectile velocity, impact angle, and target thickness. Maximum damage occurred at low velocities and high impact angles. The strength of thin panels agreed closely with fracture theory because of their predominant cracklike flaws; conversely, the strength of thick panels was close to the material ultimate tensile strength because of the blunt flaw shapes. Damage and residual strength prediction models were developed from the test data for monolithic panels. Alternate design concepts consisting of laminated, planked, and spar cap stiffened panels were investigated. The laminated panels exhibited extensive petaling and star-type cracking and low residual strength. Planked and spar cap stiffened panels provided damage alleviation and crack arrestment with high preload stresses.

KEY WORDS: military aircraft, wings, aircraft panels, stiffening, reinforcement (structures), small arms ammunition, damage, cracking (fracturing), crack propagation, tensile properties, residual strength, aluminum, evaluation

Contemporary military aircraft have been designed for maximum performance with particular attention given to range, altitude, and speed. Structural concepts and materials which provide minimum weight are used with little consideration for damage tolerance. The war in Southeast Asia has placed survivability and damage tolerance high on the list of characteristics to be considered and traded-off in aircraft design.

This paper presents the results of investigations [1][2] into the ballistic damage characteristics and the ballistic damage tolerance of monolithic aluminum panels used for tension skins in multispar wing boxes. Also investigated were benefits and penalties associated with alternate design concepts which included planked wing skins, laminated wing skins, and heavy spar caps. These alternate design concepts were expected to provide improved ballistic damage tolerance, crack arrestment, and damage alleviation.

[1] Design specialist, Convair Division, General Dynamics, San Diego, Calif. 92112.
[2] Italic numbers in brackets refer to the list of references at the end of this paper.

Ballistic Test Program

A ballistic test program was conducted to establish gunfire damage patterns, to measure the residual strength of damaged panels, and to determine the comparative benefits or problems which may result from the use of the alternate design concepts.

Test Categories

For each thickness of specimen, a survey was made to determine the projectile velocity which produced the greatest damage (V_{mld}) at some obliquity (usually 0 deg). This velocity generally was used to produce damage for residual strength testing of monolithic and laminated specimens. Damage data resulting from the surveys also were applicable to damage model development.

The effect of obliquity angle (θ, measured from a plane normal to the target) on damage also was investigated. This included identification of the angles for maximum damage at velocities equal to V_{mld} and 2250 ft/s. The upper velocity limit for this study was 2250 ft/s, chosen because it represents the velocity of a standard service round at 500 yd range. The worst combinations of V and θ were used to produce damage for residual strength testing of planked and simulated spar cap specimens.
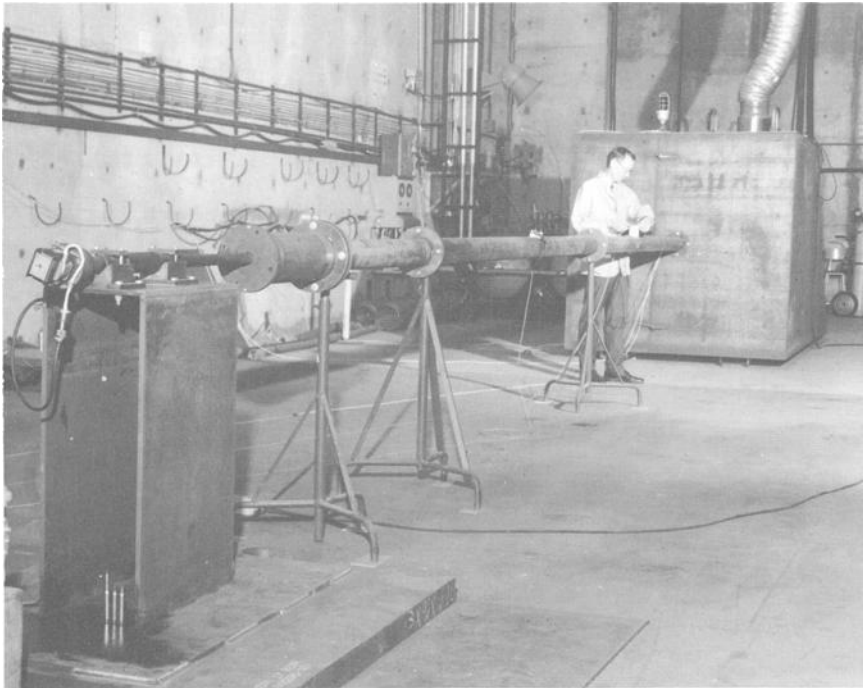
FIG. 1—*Ballistic test facility*
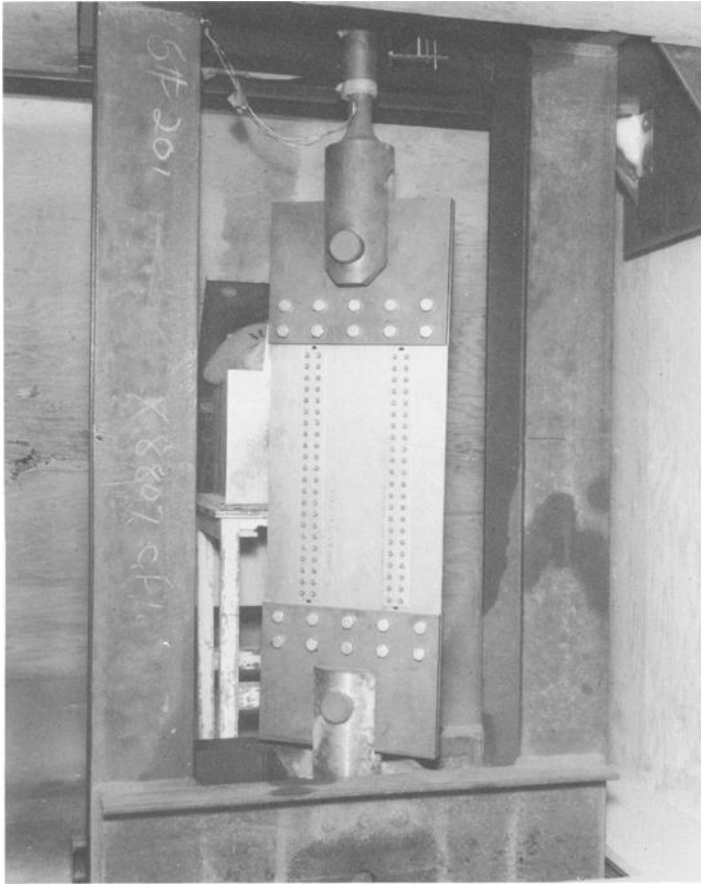
FIG. 2—*Target box and load fixture.*

Test Facility Description

All testing was accomplished in Convair's indoor ballistic test range. The range illustrated in Fig. 1 consists of a remotely fired, custom-made gun, a muzzle blast suppressor, a 35-ft enclosed flight path tube, and a target box containing a 400,000-lb tension fixture.

The fixture shown in Fig. 2 positioned the test specimens at the desired angle to the projectile flight path through rotation of the grips about the longitudinal specimen axis. Tensile load to preload or fail the test specimen was provided by a hydraulic cylinder mounted in the tension fixture outside the target box. Projectile velocities were measured using "make" strips to trigger electronic microsecond counters. Three stations were used to start and stop two counters, providing overlapping of 10-ft and 3-ft velocity timing segments. Rifled gun barrels were used in all tests to provide stable projectiles.

For subsonic projectile velocities, barrels with partial depth rifling were used to lower minimum muzzle velocities.

Test Projectile Description

All test projectiles were caliber 0.50 AP M2[3] obtained from disassembled military rounds. For projectile velocities ranging from service muzzle velocity (~2900 ft/s) to near sonic velocity (~1100 ft/s), standard cartridge cases were loaded with appropriate amounts of Type 5010 gunpowder. Excess volume was filled with coarse corn meal separated from the powder by a thin sheet rubber disk. For velocities below 1100 ft/s, a faster burning powder (Type 4831) was loaded into 0.300 H & H[4] cases. The 0.300 H & H case and the caliber 0.50 projectile were then fitted into a caliber 0.50 chamber adapter.

Test Specimen Description

Test specimens were of four basic types: monolithic, laminated, planked, and simulated spar cap. All were fabricated from 7075-T6 bare sheet or plate and were nominally 16 by 32 in., with the grain direction parallel to the long side. Average material tensile properties based on tension coupon tests and estimated transition mode fracture toughness data (K_c) are presented in Table 1.

TABLE 1—*Test specimen tensile properties and estimated fracture toughness.*

Specimen Thickness, in.	Average $F_{ty},$[a] ksi	Average $F_{tu},$ ksi	Estimated $K_c,$ ksi$\sqrt{in.}$
1/8	78.9	84.4	63
3/16	79.8	83.2	62
1/4	79.0	84.0	59
3/8	...	88.3	43
1/2	75.1	81.5	34
3/4	81.0	87.5	30

[a] Tensile yield strength.

Tests were conducted on monolithic specimens in thicknesses of ⅛, ³⁄₁₆, ¼, ⅜, ½, ¾, and 1 in. Surfaces were all as rolled. Laminated specimens were fabricated from ⅛-in. laminates bonded with FM 123-5 structural adhesive. Tests were conducted on ¼-in. (2-ply), ½-in. (4-ply), and ¾-in. (6-ply) laminated specimens.

Planked construction was simulated by slotting and splicing monolithic panels (see Fig. 2) to provide an 8-in. center plank bounded by two 4-in. half planks. Tests were conducted on ¼, ½, and ¾-in.-thick planked specimens.

[3] U.S. caliber 0.50 armor piercing Type M2 service round.
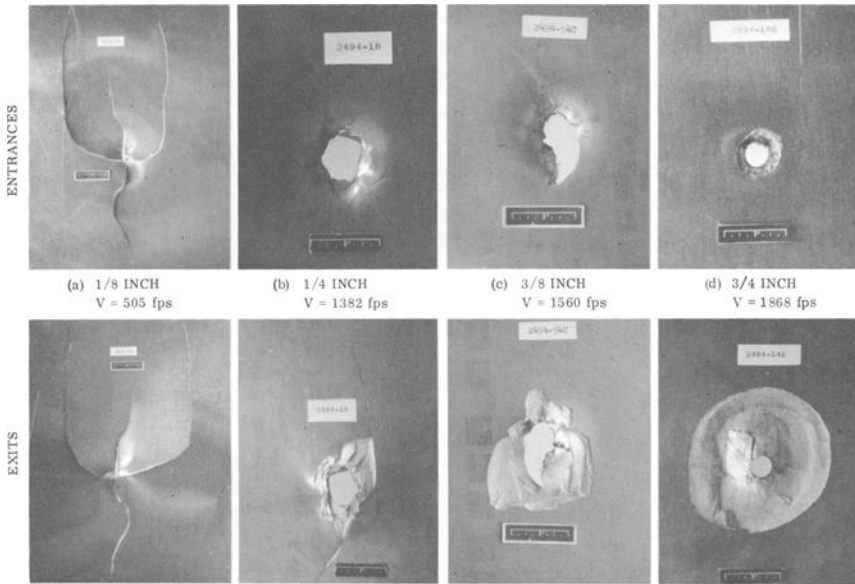[4] Cartridge style for 0.300 H & H magnum rifle.

FIG. 3—*Ballistic test results (monolithic panels, normal hits,* $V = V_{mld}$*).*

Two $\frac{1}{4}$-in. monolithic specimens with spar cap stiffening were tested. Spar caps at 8-in. spacing with areas equal to 50 percent of the skin area were used.

Ballistic Test Results

The ballistic test results for the monolithic test specimens showed that damage varied considerably with target thickness, projectile velocity, and angle of impact.

Figure 3 presents a panoramic view of ballistic damage from normal hits in monolithic panels. The maximum damage from a normal hit occurred at velocities slightly above the velocity required for plate penetration (ballistic limit). Figure 4 shows the velocities for maximum damage (V_{mld}) versus plate thickness from the tests. Higher velocities produced less severe damage, with service round velocities producing clean, round holes. The damage consisted of a mixture of radial cracking and spall, with cracking predominant in thin gages and spalling predominant in thick gages. It was found that tensile preload had no effect on damage unless catastrophic failure occurred.

Figure 5 presents a panoramic view of ballistic damage from oblique hits at constant projectile velocity in monolithic panels. The angle for maximum lateral damage (θ_{mld}) is presented in Fig. 6 and varies from high angles of obliquity in thin gages to nearly normal angles in thick gages.

The laminated, planked, and spar cap stiffened specimens were tested to evaluate the design concept rather than to provide data for damage and strength models. The evaluation was accomplished by comparison with monolithic specimens tested under similar conditions.
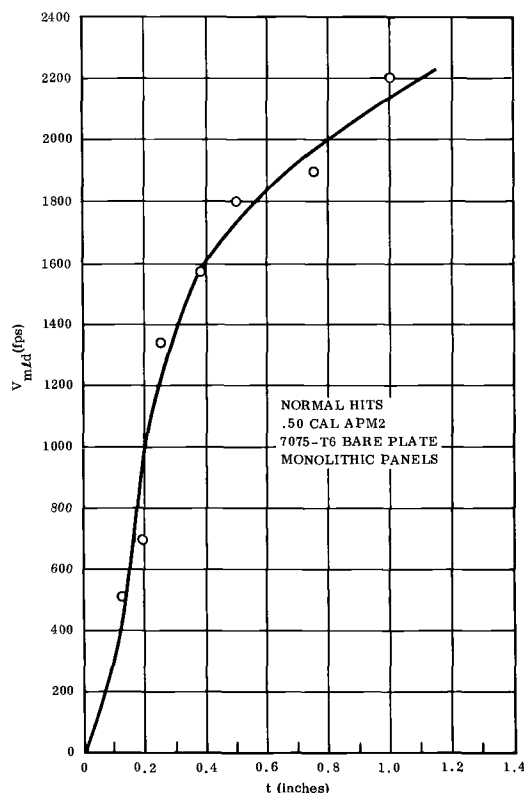
FIG. 4—Velocity for maximum lateral damage versus plate thickness.

The damage observed in the laminated specimens was greater than the damage in the monolithic specimens in all cases. Figure 7 shows that the nature of the damage also was different.

Delamination allowed each layer to "petal," causing the thicker panels to behave like the thinner solid thicknesses. Compared to the monolithic panels, the increased damage and associated cracking resulted in the lower residual strength shown in Fig. 8.

The planked specimens were impacted while under 30-ksi preload at the projectile velocities and angles determined critical for equivalent monolithic thicknesses. Damage patterns obtained were similar to those observed in the equivalent monolithic specimens, with the exception that the ¼-in. planked panels did not fail catastrophically as had the ¼-in. monolithic panels at 30-ksi preload. Lateral cracks extending from the damage were arrested at the plank splices and the load was held by the remaining plank elements.

Each of the spar cap stiffened specimens were preloaded to 30 ksi and impacted at the projectile velocity and angle which produced catastrophic

(a) 1/8 INCH
$\theta = 80°$

(b) 1/4 INCH
$\theta = 75°$

(c) 3/8 INCH
$\theta = 65°$

(d) 3/4 INCH
$\theta = 35°$
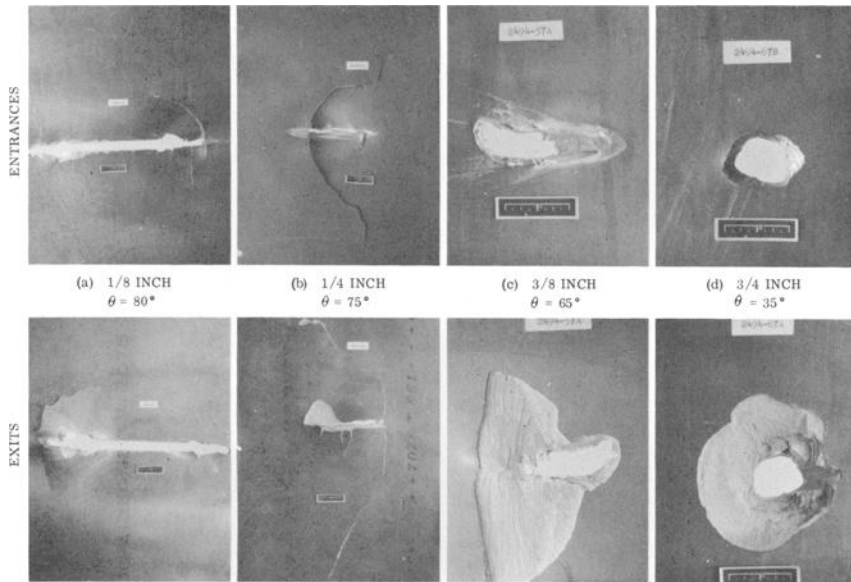
FIG. 5—*Ballistic test results (monolithic panels, angle hits, V = 2250 ft/s).*
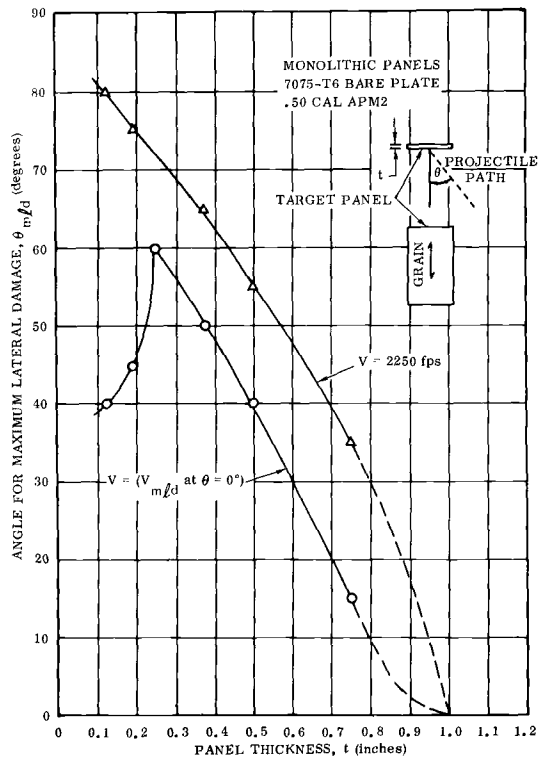
FIG. 6—*Angle for maximum lateral damage versus panel thickness.*
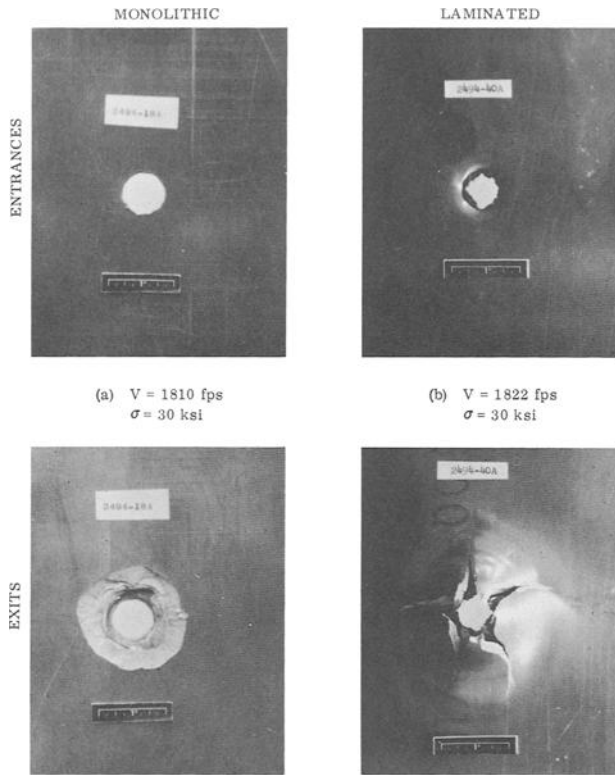
FIG. 7—*Comparison of ballistic damage in laminated and monolithic panels* (t = ½ *in., normal hits*).

failure in the ¼-in. monolithic specimens. Although these specimens did not have splices to arrest running cracks, as did the planked specimens, the heavy caps reduced the lateral cracking and prevented catastrophic failure.

Figure 9 compares the capabilities of the monolithic, laminated, planked, and spar cap stiffened design concepts and illustrates the crack arresting feature offered by plank splices and stiffeners.

Damage Model Development

The objective of developing a damage model was to provide a method for predicting the amount of damage incurred by a skin panel due to projectile impact. The model can be used to determine damage for calculation of residual strength and repair considerations.

In a general form, a damage model would predict damage as a function of target and threat parameters, where target parameters include such quantities as material, thickness, configuration, and preload and threat parameters include type of projectile, velocity, and angle of impact. For the damage

model developed, the parameters were limited to 7075-T6 monolithic panels and caliber 0.50 AP M2 armor piercing projectiles, and projectile flight paths were limited to a plane perpendicular to the panel grain direction. Noting from the test results that preload had no significant effect on damage, the variables were reduced to skin thickness, projectile velocity, and angle of impact.

In order to establish a valid damage model, it was necessary to decide what forms of damage would be significant. For residual strength considerations, lateral damage (perpendicular to the direction of principle stress) was considered to be the significant damage characteristic. Since lateral damage was different at the front and rear faces of the test panels, it was decided to use an average of the two, designating this as "effective lateral damage" L_e.

For repair considerations, maximum extent of damage, D, regardless of orientation was chosen to be the information desired. For versatility, it was desirable to have the damage model predict damage for both normal and oblique hits. It was found that damage from oblique hits normalized by the cosine of the angle gave results consistent with damage from normal hits at the same velocity. The normalized effective lateral damage multiplied by the cosine of the angle of obliquity gave the lateral damage for an oblique hit.

It also was found that within certain bounds high-velocity oblique hits caused more lateral damage than identical shots at a reduced velocity. For this reason, curves for two velocities are shown in the damage model. The two velocities represent the upper and lower limits on projectile velocity
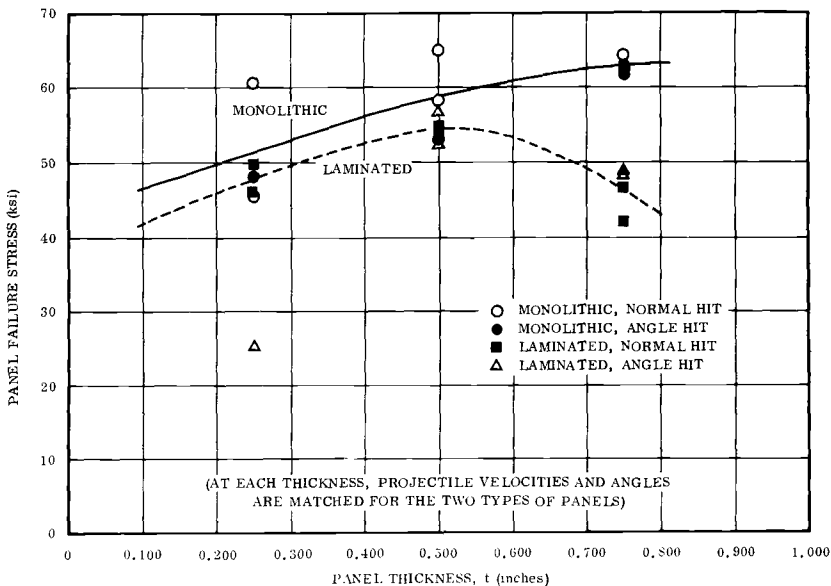

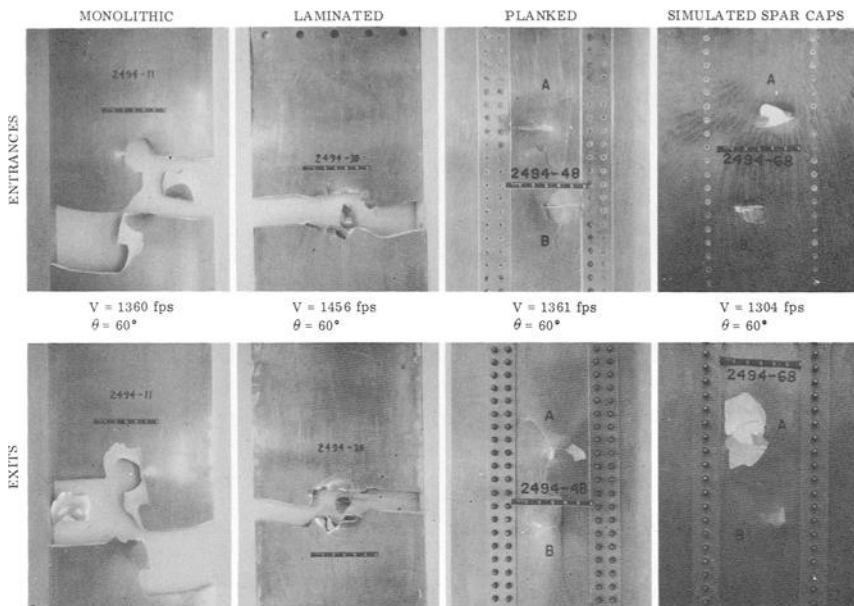FIG. 8—*Monolithic and laminated panel failing stress versus panel thickness.*

FIG. 9—*Comparison of crack arresting features (¼-in. panels, angle hits, 30-ksi preload).*

which reasonably could be expected to be encountered and to cause damage. The lower velocity is the velocity for maximum lateral damage (V_{mld}) from a normal hit. A velocity of 2250 ft/s (the velocity of a service round at a range of 500 yd) was chosen as the upper limit.

Figure 10 presents normalized effective lateral damage data, with a curve drawn through the maximum points. Owing to the sparseness of data, the curves probably are inaccurate for gages less than ¼ in. Reference 2 reports a reduction in damage as the thickness falls below a value of one third of the projectile diameter. For this reason the curves were drawn with a peak at $t = 0.50/3 = 0.166$ in. and damage diminishing to approximately the projectile diameter at foil gages.

Figure 11 presents the damage model developed and predicts the worst damage likely to occur in a flat, monolithic plate. The curves presented were obtained by dividing the normalized curves similar to Fig. 10 by the cosine of the angle for maximum lateral damage presented in Fig. 6.

Residual Strength Model

The purpose of developing a residual strength model was to provide a means for determining the critical tension failing stress of a skin panel damaged by small-caliber projectiles. The residual strength model developed is limited to the target and projectile types and the range of variables encom-

passed by the tests. In order to maintain a degree of confidence in the model, only those test data which provided sufficient points to define a particular characteristic were used. As a result, the model is limited to flat, monolithic 7075-T6 aluminum panels impacted by caliber 0.50 AP M2 projectiles and loaded parallel to the material longitudinal grain direction.

Residual Strength Model Development

The residual strength model was developed from the Griffith-Irwin fracture theory [3], which provides a method for calculating the residual strength of structural elements containing cracks. For true cracks structures can be analyzed using the material property called fracture toughness, K_c, represented by the lower curve in Fig. 12.

Ballistic damage does not necessarily contain true cracks. As discussed previously ballistic damage consists of cracks in thin sheet, with a transition to blunt flaws in thick plate.

It was assumed that the fracture theory relations could be used for predicting strength of ballistically damaged panels provided that the apparent material toughness K_c' is used and that the apparent material toughness is derived from ballistic test specimens using the same relationships.
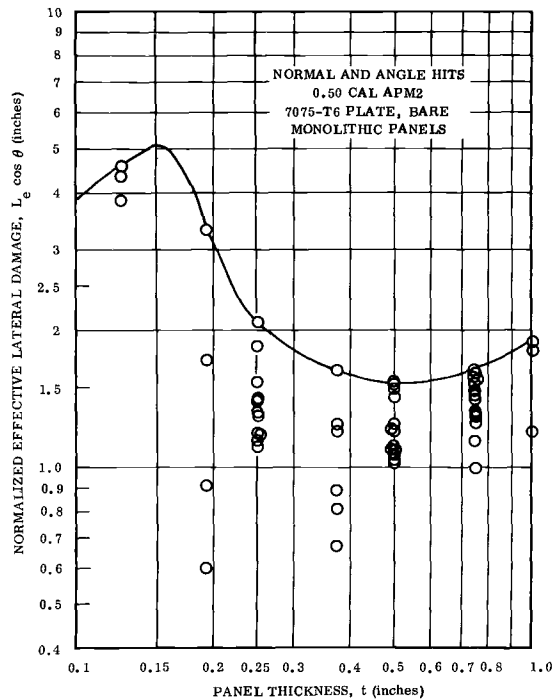
FIG. 10—*Normalized effective lateral damage versus panel thickness* (V = V_{mld} at θ = 0 deg).
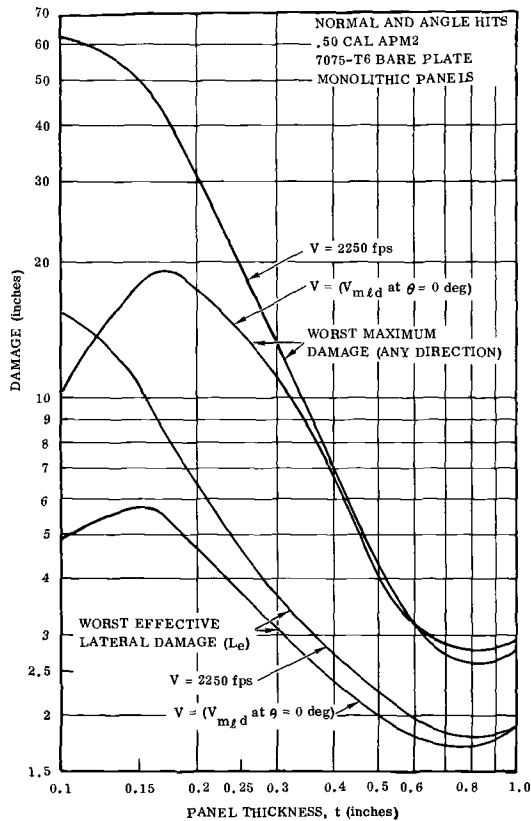
FIG. 11—*Damage model.*

The residual strength model was developed as follows:

1. From fracture theory [3] for a plate of finite width,

$$K_c = \sigma\sqrt{\pi a}\ \sqrt{(w/\pi a)\ \tan{(\pi a/w)}} \dots\dots\dots\dots\dots\dots(1)$$

where

σ = stress,
K_c = stress intensity factor,
w = plate width, and
a = half crack length.

2. The apparent toughness K_c' was then derived from the residual strength of the ballistically damaged panels using Eq 1.

$$K_c' = \sigma\sqrt{w\ \tan{(\pi L_e/2w)}} \dots\dots\dots\dots\dots\dots\dots(2)$$

where $L_e/2 = a$. Figure 12 presents a curve of apparent toughness drawn through the test points.

3. Developing the damage model for panels of large width by using Eq 1 without the tangent correction and the apparent toughness from Fig. 12, an expression for critical stress σ_{CR} as a ratio of the material ultimate tensile strength F_{tu} was derived:

$$\frac{\sigma_{CR}}{F_{tu}} = \frac{(K_c'/F_{tu})}{\sqrt{\pi L_e/2}} \dots\dots\dots\dots\dots\dots\dots\dots\dots(3)$$

4. For each test point the value σ_{CR}/F_{tu} was calculated using Eq 3 and plotted versus the damage-thickness parameter (L_e/t^N). The exponent N was varied until the data plotted in a band, as shown in Fig. 13. Fitting a curve and equation to the test points results in the expression

$$\frac{\sigma_{CR}}{F_{tu}} = \frac{0.920}{(L_e/t^{0.4})^{1/2}} \dots\dots\dots\dots\dots\dots\dots\dots(4)$$

which is the semiempirical solution to the strength of ballistically damaged 7075-T6 panels and is termed the "residual strength model."

Comparisons of conventional fracture theory (using K_c) to the residual strength model and the test points are presented in Fig. 14 for each panel gage. The fracture theory curves were calculated for an ordinary through crack; however, the same curve is obtained using Bowie's solution (Fig. 34
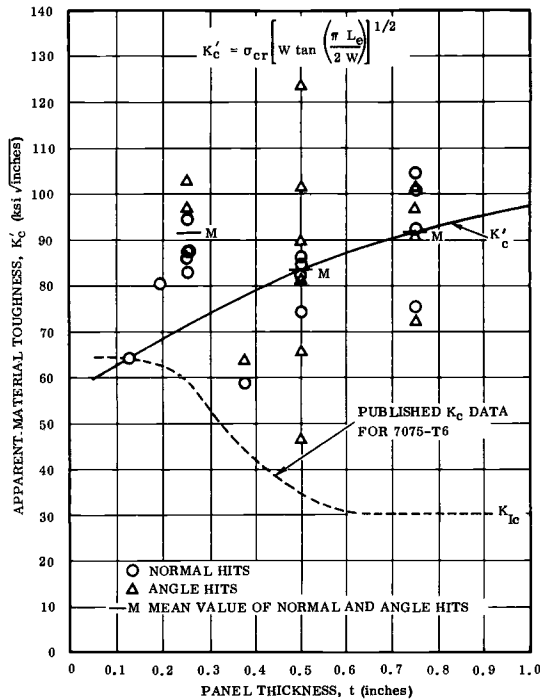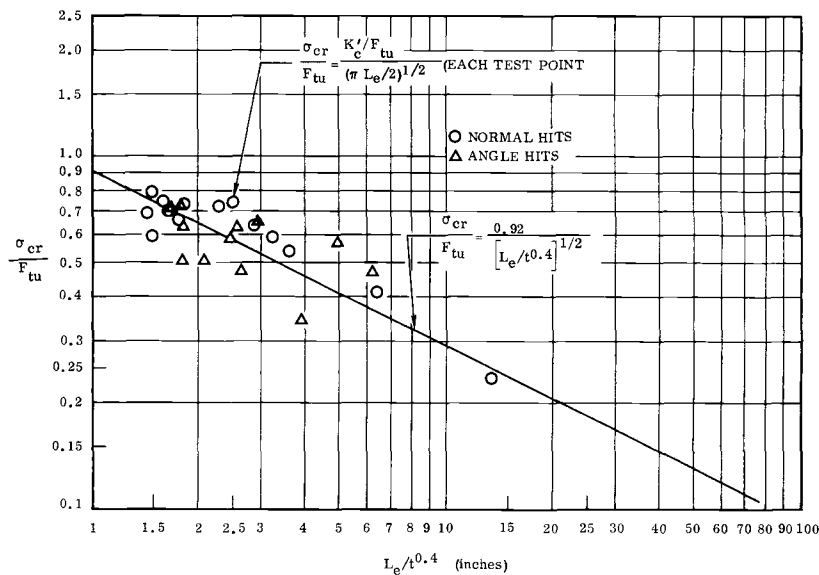

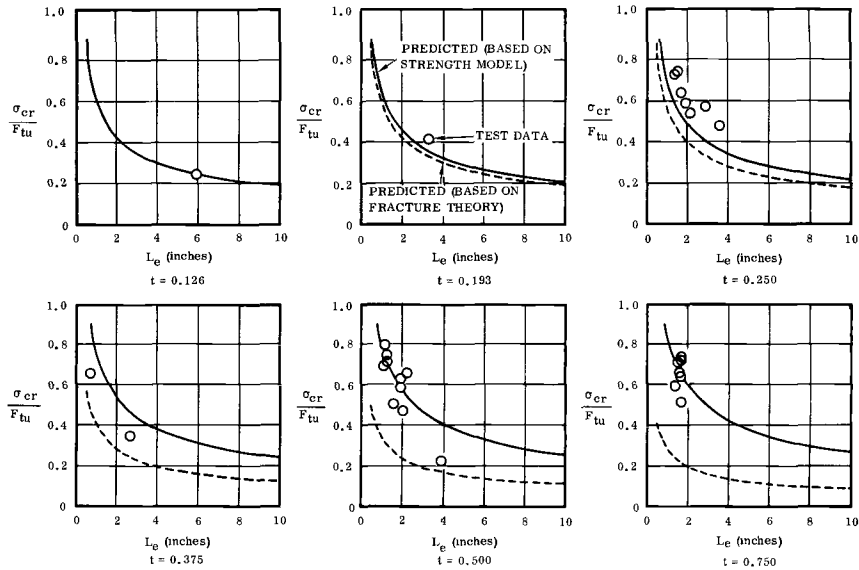FIG. 12—*Apparent material toughness.*

FIG. 13—*Residual strength model.*

FIG. 14—*Comparison of residual strength model, fracture theory, and test data.*

of Ref *3*) for the stress intensity factor of two radial cracks emanating from a central ½-in. circular hole because of the large ratio of crack length to hole radius. The residual strength model and fracture theory agree exactly in the ⅛-in. gage where the damage consisted of radial cracks. As the panel gage increased, the damage model gave progressively higher strength predictions, which can be attributed to the transition from cracklike to blunt flaw shapes.

General Conclusions

From the data presented it can be concluded that ballistic damage is sensitive to several target and threat parameters, particularly thickness, velocity, and angle of obliquity. In addition, the damage in monolithic panels varies from predominantly cracks in thin gages to blunt holes in thick gages, which has a significant effect on the residual strength of the damaged panels.

It appears feasible to develop ballistic damage and residual strength prediction models for specific targets and threats. Models of this type would be useful for evaluating the damage tolerance of new structural designs.

Of the three alternate design concepts investigated, the planked and heavy spar cap stiffened concepts offer advantages in that they prevented catastrophic structural failure by arresting the running crack at splices and stiffening elements. Weight penalties of approximately 2 percent for the planked design and 5 to 7 percent for the heavy spar cap design are associated with these advantages. Owing to the nature of the ballistic impact and the flaws generated, the laminated concept provided no advantage over the monolithic skin concept even though the individual thinner laminates had higher plane stress toughness.

References

[1] Jensen, J., Thorndyke, P., and Campbell, M., "Aircraft Wing Structural Concepts with Improved Ballistic Damage Tolerance," Report No. GDC-DDG69-002, Vols. I and II, General Dynamics/Convair, San Diego, Calif., Oct. 1969.

[2] Lundeberg, J. F. and Bristow, R. J., "Gunfire Damage to Airframe Structures," AIAA Paper No. 66-783, AIAA Military Aircraft Systems Meeeting, Dallas, Texas, Oct. 1966.

[3] Paris, P. C. and Sih, C. M., *Fracture Toughness Testing and Its Applications*, *ASTM STP 381*, American Society for Testing and Materials, 1964, pp. 30–81.

Wolf Elber[1]

The Significance of Fatigue Crack Closure

ABSTRACT: Experiments on 2024-T3 aluminum alloy sheet are described which confirm the occurrence of fatigue crack closure under cyclic tensile loading. The results show that a fatigue crack can be closed at the crack tip for up to half of the loading amplitude, leaving this portion of the cycle ineffective in propagating the crack. An expression for the crack propagation rate in terms of effective stress amplitude is proposed. This expression is fitted to existing constant amplitude crack propagation data for 2024-T3 aluminum alloy. The parameters evaluated provide a better fit to the data than other empirical expressions available. Analysis of qualitative experiments on variable amplitude loading shows that the crack closure phenomenon could account for acceleration and retardation effects in crack propagation.

KEY WORDS: aircraft, cracking (fracturing), crack propagation, fatigue (materials), fatigue tests, closure, fracture properties, loads (forces), cyclic loads, stresses, plastic deformation, aluminum alloys, correlation

Nomenclature

a	Distance from the center of a sheet to the crack tip
da/dN	Crack propagation rate
K_{max}	Maximum applied stress intensity
l	Crack length
R	Stress ratio, S_{min}/S_{max}, in a cycle
S	Applied stress
S_{max}	Maximum applied stress in a cycle
S_{min}	Minimum applied stress in a cycle
S_{op}	Stress level at which the crack is just fully open
U	Effective stress intensity range ratio
ΔK	Stress intensity range in a cycle
ΔK_{eff}	Effective stress intensity range
δ	Gage displacement
δ_{fc}	Crack opening displacement of a fatigue crack
δ_0	Residual displacement

[1] Resident research associate, National Academy of Sciences, NASA Langley Research Center, National Aeronautics and Space Administration, Hampton, Va. 23365.

δ_{sc} Crack opening displacement of a saw cut crack

ϵ_{0y} Residual tensile strain perpendicular to a crack

NOTE—All stresses are gross section stresses.

Recent work [1, 2][2] has shown that fatigue cracks in sheets of aluminum alloy close before all tensile load is removed. Significant compressive stresses are transmitted across the crack at zero load. In previous work, usually the assumption has been made implicitly that a crack is closed under compressive loads and open under tensile loads. This assumption is based on the behavior of a saw cut crack of zero width. However, a fatigue crack differs from a saw cut crack primarily because during crack propagation a zone of residual tensile deformation is left in the wake of the moving crack tip. These deformations effectively decrease the amount of crack opening displacement from that of the saw cut crack. On unloading, this can cause crack closure above zero load. The determination of the crack closure stress must, therefore, be a necessary step in the stress analysis of a cracked structure.

The threefold purpose of the work described here was to show that the loads at which a crack closes can be determined by continuously monitoring the crack opening displacement in the vicinity of the crack tip, to develop an equation for the rate of crack propagation based on crack closure for constant amplitude loading, and to demonstrate the applicability of this concept to variable amplitude loading. In order to achieve these results, constant and variable amplitude loading tests were carried out on sheets of 2024-T3 aluminum alloy. An empirical relation was obtained for the crack opening stress level and this relation was used as a basis for a crack propagation equation. The empirical parameters for this equation were obtained by carrying out a statistical correlation to experimental data from the literature, and the fit of this equation to the data was compared to those of the equations of Forman [3] and Erdogan [4]. From the results of variable amplitude tests, comparisons were made between the trends of the crack propagation rates and the trends of the predictions based on the crack closure phenomenon.

The Crack Closure Phenomenon

Concepts

The application of the fracture mechanics concept to fatigue crack propagation is based on the assumption that a fatigue crack can be represented by a zero-width saw cut. An analysis of elastoplastic behavior at the tip of such an ideal crack was preformed by Rice [5]. The results showed that under cyclic tensile loading the crack would be fully open above zero load. Previous experimental work [1, 2] has shown, however, that a fatigue crack produced under zero-to-tension loading closes during unloading and that large, residual compressive stresses exist normal to the fracture surfaces at zero load.

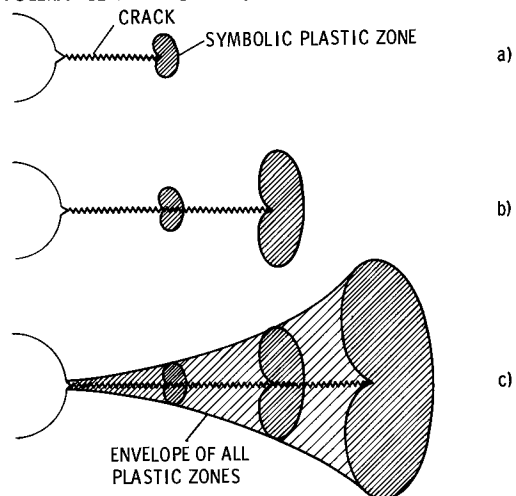[2] Italic numbers in brackets refer to the list of references at the end of this paper.

FIG. 1—*Development of a plastic zone envelope around a fatigue crack.*

The load at which the crack closes is therefore tensile rather than zero or compressive. As the crack cannot propagate while it is closed at the crack tip, a knowledge of the crack opening load is essential to refine the prediction of the crack propagation rate.

The difference between the behavior of a fatigue crack and that of the ideal zero-width cut can be explained by the existence of a zone of material behind the crack tip having residual tensile strains. In Fig. 1 a fatigue crack produced under constant amplitude loading is shown at three crack lengths. Figure 1a shows the crack tip, surrounded by a plastic zone as it is represented normally. Figure 1b shows the crack at a greater crack length surrounded by a larger plastic zone, because the stress intensity is higher. The plastic zone of Fig. 1a has been retained to show that the material had been subjected previously to plastic deformations. Figure 1c represents the crack surrounded by the envelope of all zones which during crack growth had been subjected to plastic deformations. During a single cycle of crack growth, residual tensile deformations are left in the material behind the moving crack front, as only elastic recovery occurs after separation of the surfaces. Just behind the crack tip, these deformations are about the same as the plastic deformation at the crack tip.

In Fig. 2 a comparison is made between a saw cut crack and a fatigue crack to show the significance of these residual tensile deformations. At an arbitrary section Y-Y behind the crack tip, the residual strains ϵ_{0y} existing inside the envelope of all previous plastic zones are shown.

The residual deformation δ_0 of the fatigue specimen at section Y-Y can be obtained from the equation

$$\delta_0 = \int \epsilon_{0y} dy$$

At the same section the saw cut crack has no residual strains. The crack opening displacement δ_{fc} of the fatigue crack at section Y-Y is therefore less than δ_{sc} by an amount δ_0.

On unloading, the crack opening displacements of both cracks will decrease at the same rate. Because of the smaller maximum value of δ_{sc}, the fatigue crack will close, $\delta_{fc} = 0$, before δ_{sc} will reach zero.

Experimental Work

Specimens—Sheets of 2024-T3 aluminum alloy were tested under tensile cyclic loads. The specimens were 5 mm thick and 130 mm wide. Cracks were initiated from jeweler's saw cuts in a 30-mm-diameter central hole. The details of the specimen are shown in Fig. 3. The mechanical properties of the material tested are listed in Ref 6.

Equipment—A displacement pickup (Fig. 4) was developed with a gage length of 1.5 mm between contact points. This gage was mounted on the surface of the specimen straddling the crack. The electrical signal from a foil strain gage bridge in the pickup was displayed on a cathode ray oscilloscope screen. A photo attachment was used to record the trace during load cycling. Depending on the type of experiment carried out, the gage was mounted at the crack tip for the duration of several cycles, or was mounted ahead of the crack tip to record deformations as the crack grew through the gage line. The latter method must be used if residual deformations are required.

A 0.3-MN-capacity fatigue machine with a horizontal test bed was used for all tests.
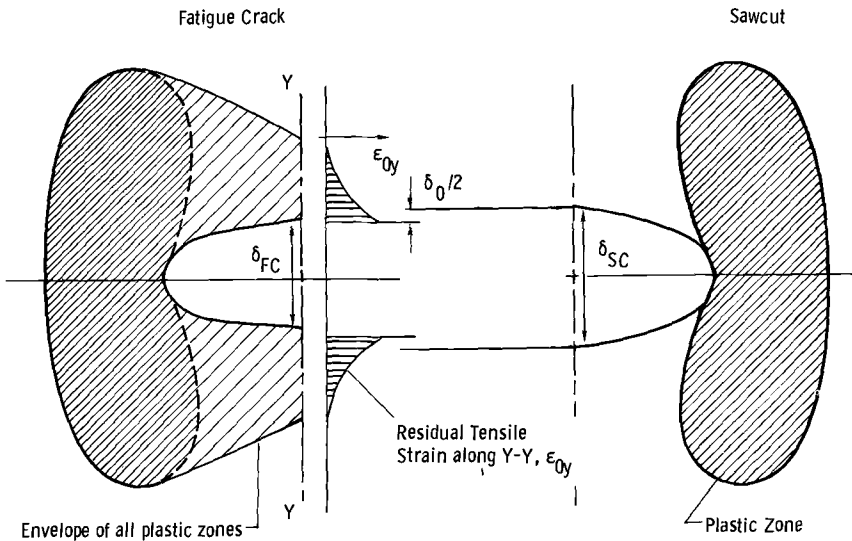

FIG. 2—*Comparison of deformations near the crack tip for a fatigue crack and a saw cut crack.*
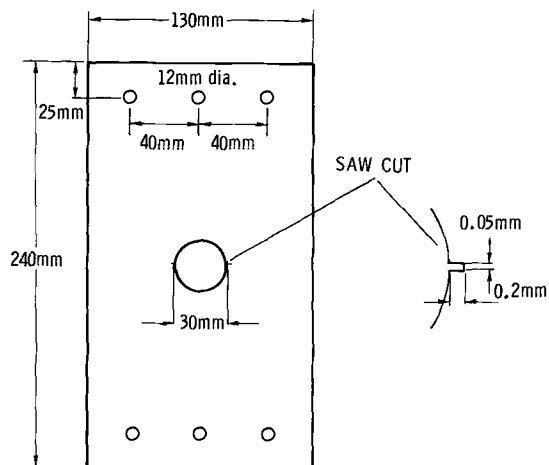
FIG. 3—*Crack propagation specimen.*

Loading Conditions—Constant amplitude tests at 1 Hz were performed to obtain the basic characteristics of the relationship between applied load and crack opening displacement. These tests were performed with a stress ratio $R = 0$ and a maximum applied stress of 150 MN/m².
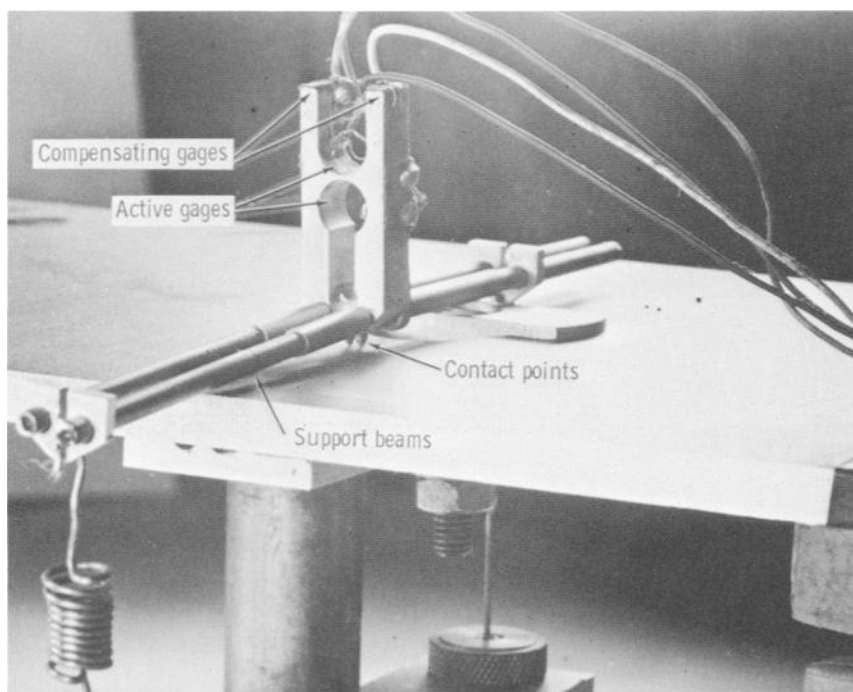

FIG. 4—*Crack opening displacement gage.*

Results—Determination of Crack Opening Stress

Figure 5a shows the crack configuration and gage location for a typical test. Figure 5b shows the relation between the applied stress and the displacement measured by the gage. The main characteristic of this relationship is its nonlinearity. Nonlinear behavior of the structure can have only two causes, material nonlinearity (plasticity) and a change of configuration. In a particular situation, the cause of the nonlinear behavior can be identified by analyzing the curvature of the stress displacement relation. Between points A and B the relation is linear and the measured stiffness $dS/d\delta$ is equal to the stiffness of the uncracked sheet. The stress displacement plot for the uncracked sheet is shown for comparison. Between points C and D the relation also is linear and the measured stiffness is equal to the measured stiffness of an identical sheet containing a saw cut of the same length as the fatigue crack. Between points B and C the curvature $d^2S/d\delta^2$ is negative. Because plastic behavior of the material would produce a positive curvature on unloading, the only possible cause for a negative curvature is a change in configuration which increases the stiffness for decreasing loads. This change of configuration can be explained by crack closure only. From these considerations, the conclusion is reached that the crack is fully open between points D and C during unloading. The crack closes gradually between points C and B and is closed between points B and A.

Figure 6 shows a relationship between stress and displacement recorded at the crack tip of the same specimen under the same loading conditions. The behavior measured at that point is not fully elastic but has similarities with the behavior shown in Fig. 5. In Fig. 6 the relation has a plastic deformation effect superimposed on the configuration change effect. Between points A and
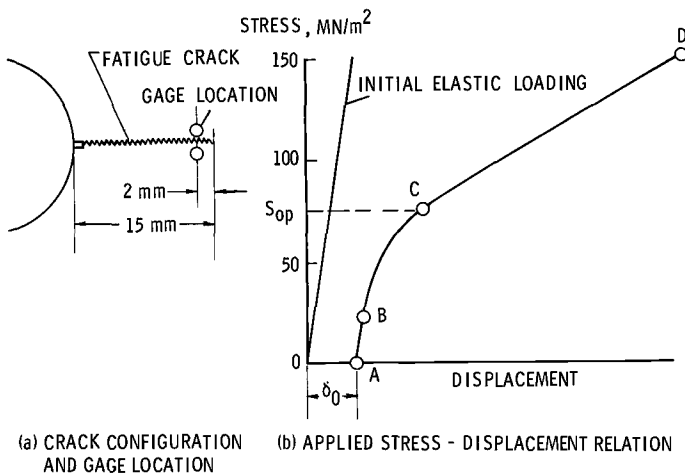

(a) CRACK CONFIGURATION   (b) APPLIED STRESS - DISPLACEMENT RELATION
    AND GAGE LOCATION

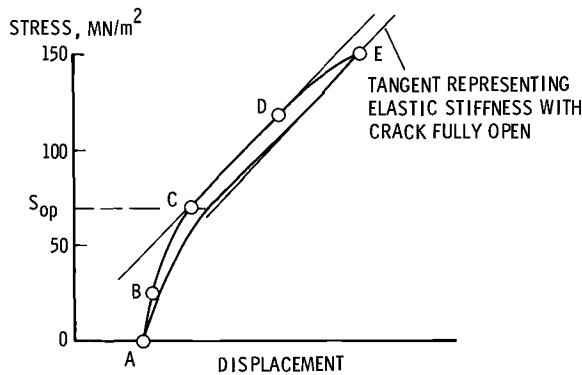FIG. 5—*Crack configuration and applied stress-displacement relationship.*

FIG. 6—*Relationship between applied stress and gage displacement at the crack tip.*

B the relation is linear, showing that the crack is closed; between points B and C the negative curvature indicates that the crack is opening; between points C and D the curve is linear; and between points D and E the curve again has a negative curvature. Since plastic tensile deformations can occur only after the crack is fully open, the curvature between B and C is due entirely to crack opening and the curvature between D and E is due entirely to plastic deformations in the plastic zone. In some cases the length between C and D is relatively short compared to the total length of the curve, and a straight line portion cannot be identified. Nevertheless, there must be a stress level at which the crack is fully open and at which the stiffness corresponds to the elastic stiffness of the fully open crack. This stiffness is obtained as the slope of the unloading branch at the maximum load of the previous cycle, where the crack is fully open and the material behaves elastically. A line with this slope can be used as a tangent to the loading branch to determine the crack opening load. When the tangency condition exists for some length of curve, the crack opening load is given by the lowest stress level satisfying the tangency condition. This is shown in Fig. 6, where C represents the lowest tangency point.

As further elucidation of the curvatures of the relation between applied stress and gage displacement, Fig. 7 contains the interpretations of curvatures for loading and unloading conditions.

Effects of Crack Closure

Constant Amplitude Loading

Concepts—Crack propagation can occur only during that portion of the loading cycle in which the crack is fully open at the crack tip; therefore, in attempting to predict analytically crack propagation rates it seems reasonable that the crack opening stress level should be used as a reference stress

level from which an effective stress range is obtained. The effective stress range is defined therefore as

$$\Delta S_{eff} = S_{max} - S_{op}$$

where S_{op} is the crack opening stress. An effective stress range ratio is then defined as

$$U = \frac{(S_{max} - S_{op})}{(S_{max} - S_{min})} = \frac{\Delta S_{eff}}{\Delta S}$$

It generally has been accepted that crack propagation rate is a function of ΔK, the stress intensity range during a cycle. Based on the above, it seems reasonable to expect that a better analysis of crack propagation rates might utilize the effective stress intensity range concept. The following functional form of the crack propagation equation will be tested:

$$da/dN = C(\Delta K_{eff})^n = C(U\Delta K)^n \ldots \ldots \ldots \ldots \ldots (1)$$

Experimental Work—The materials, specimens, and equipment were the same as those used in the experiments described in the previous section of this paper. Two loading frequencies were used, a high frequency of 30 Hz for crack propagation and a low frequency of 1 Hz for observation of the crack opening displacement.

A series of constant amplitude tests were performed to establish the crack opening load under various conditions of stress intensity range, load ratio, and crack length. The stress intensity was varied over the range $13 < \Delta K < 40$ MN/m$^{3/2}$ and the stress ratio was varied over the range $-0.1 < R < 0.7$. Antibuckling guides were used when compressive loads were applied.

	$\dfrac{d^2P}{d\delta^2}$	Shape	Loading	Unloading
I	>0		Generally impossible for metals	1) Plastic behavior 2) Plastic behavior > configuration change
II	<0		1) Configuration change 2) Plastic behavior	1) Configuration change 2) Configuration change > plastic behavior
III	≈0		Elastic behavior at constant configuration	1) Elastic behavior at constant configuration 2) Plastic behavior = configuration change
IV	→0		Transition from changing configuration to constant configuration	Transition to configuration change > plastic behavior

FIG. 7—*Curvature effects in the load-displacement relationship.*

Results and Discussion—Constant amplitude loading tests were conducted to establish the relationship between U and three variables which were anticipated to have a significant effect on U, namely, stress intensity range, crack length, and stress ratio.

The results are shown in Fig. 8. For the given range of testing conditions only the stress ratio R is a significant variable. The relation between U and R is linear and can be expressed as

$$U = 0.5 + 0.4R, \text{ where } -0.1 < R < 0.7 \ldots\ldots\ldots\ldots(2)$$

for 2024-T3 aluminum alloy.

With the substitution of Eq 2 for U in terms of the known quantity R, Eq 1 becomes

$$da/dN = C[(0.5 + 0.4R)\Delta K]^n$$

for this material. A least squares fit of this equation was performed to the data reported by Hudson [7]. The parameters were found to be

$$C = 1.21 \times 10^{-9}$$

$$n = 3.62$$

when ΔK has units of $MN/m^{3/2}$ and da/dN has units of m/cycle. This relation is shown in Fig. 9. For comparison of the least squares fit of this equation and the equations of Forman [3] and Erdogan [4], the sums of squares of residuals have been computed. These are listed in the accompanying table

Equation	Sum of Squares of Residuals
Forman	28
Erdogan	27
Crack closure	21

The correlation of the data was found to be best for the crack closure equation of this work.

Variable Amplitude Loading

Concepts—One of the most important problems in aircraft structures is the inablity to predict accurately the rate of fatigue crack propagation under variable amplitude loading. Attempts to calculate these crack rates on the basis of constant amplitude data usually ignore interaction effects and lead to errors of significant magnitude.

Crack closure may be a significant factor in causing these interaction effects. This can be shown by the following example: Assume a crack in 2024-T3 aluminum alloy is propagating under the conditions $R = 0$ and $K_{max} = 20 \text{ MN/m}^{3/2}$. Under these conditions the crack opening level is at

$K_{op} = 10$ MN/m$^{3/2}$. If the stress intensity range suddenly is halved, the new conditions are $K_{max} = 10$ MN/m$^{3/2}$ and $R = 0$. The crack opening level, however, is still at $K_{op} = 10$ MN/m$^{3/2}$, equal to the new peak stress intensity, so the crack does not open. Therefore, the crack does not propagate until the crack opening level changes. The behavior of the crack opening stress level under variable amplitude loading must therefore be investigated.
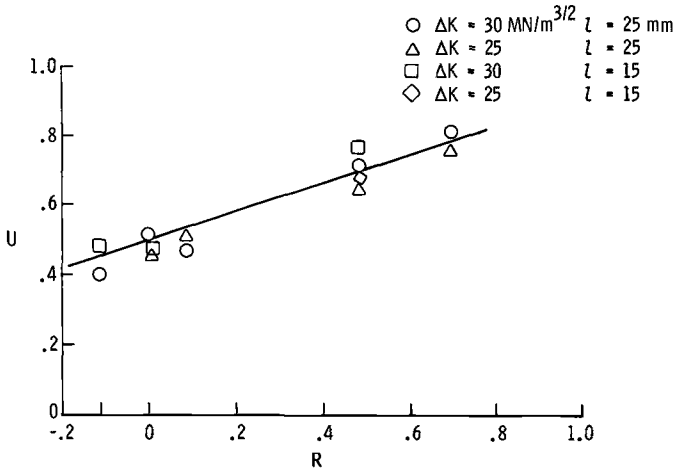

FIG. 8—*Relationship between effective stress range ratio and stress ratio for 2023-T3 aluminum alloy.*
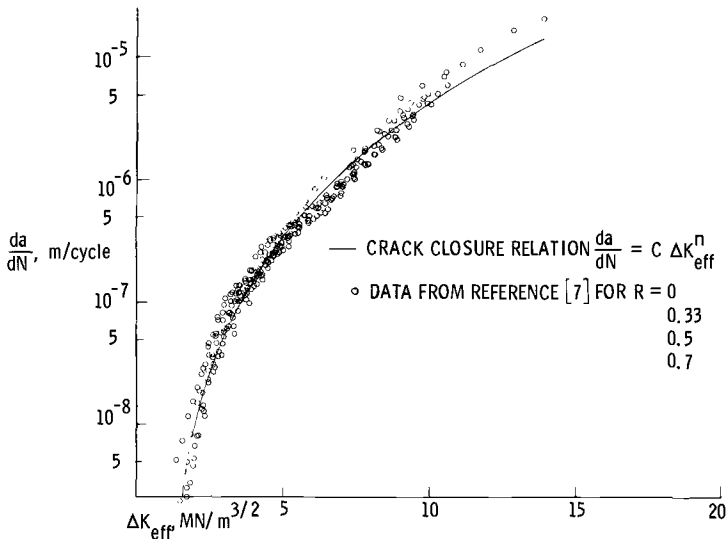

FIG. 9—*Relationship between crack propagation rate and effective stress intensity range.*

For these experiments, the same equipment and specimens were used as in the previous experiments. A crack was grown to a length of 4 mm at a stress level of 100 MN/m². The stress sequence shown in Fig. 10a, containing a single high load, was then applied to the specimen. The gage was located 0.1 mm ahead of the crack tip, and crack opening displacement records were taken during the last cycle before the high load, during the high-load cycle, and at intervals after the high-load cycle.

A second experiment was performed with a stepped program load. As in the previous experiment, a 4-mm-long crack was grown at a stress level of 100 MN/m² and the stress level was then changed to 180 MN/m²; during and after the stress level step, records of the crack opening displacement were taken. The stress program is shown in Fig. 11a.

Results and Discussion—Figure 10b shows the stress-displacement record for the single high-load sequence. The stress-time record shows the high-load cycle and the two load cycles before and after the high-load cycle. In addition, it shows the 1000th load cycle after the high-load cycle. The stress-displacement record shows the gage displacements during these cycles. In the first cycle, no hysteresis is registered, so loading and unloading curves are colinear; hence, the crack opening stress can be obtained as the stress at which the curve deviates from the linear portion of the curve through the point $\bar{1}$. This shows that U is approximately 0.5. For the loading $(2-\bar{2})$ the crack opening stress is the same, so $U = 0.25$. This high load produces a residual displacement which is larger than the displacement at which the crack previously opened; hence, at point 3 the crack cannot be closed over the previous fracture surfaces.
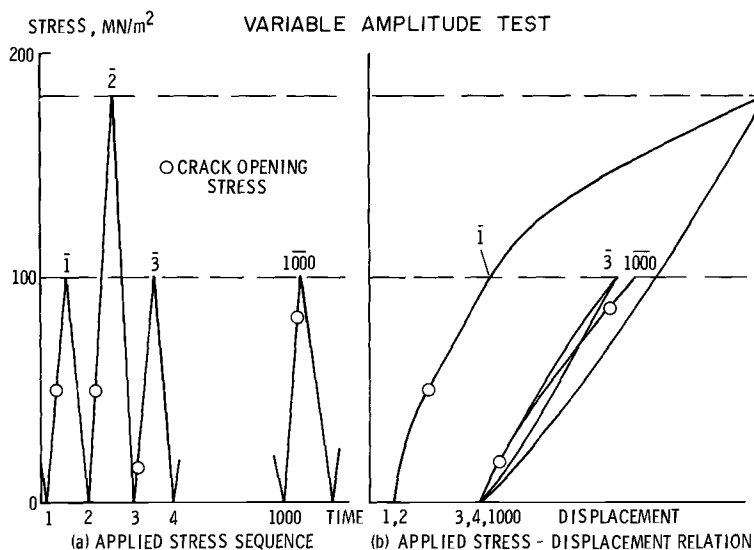

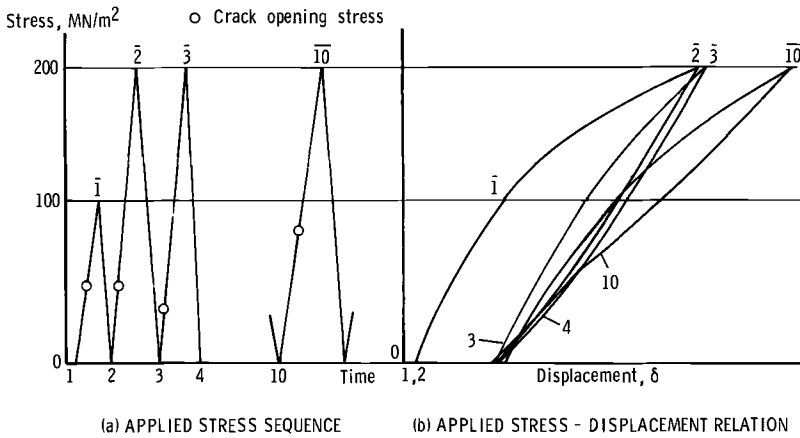FIG. 10—*Variation of crack opening stress caused by a single high load.*

(a) APPLIED STRESS SEQUENCE   (b) APPLIED STRESS - DISPLACEMENT RELATION

FIG. 11—*Variation of crack opening stress caused by a program step.*

The loading curve (3–$\bar{3}$) is nonlinear and, if the tangent from the unloading curve at $\bar{2}$ is drawn through 3–$\bar{3}$, the lowest stress satisfying tangency is approximately 30 MN/m², making $U = 0.7$. This implies that the crack has closed only over the single striation produced by the high load. After 1000 load cycles the crack has propagated approximately 0.3 mm, and the loading branch (1000–$\overline{1000}$) shows that the crack is almost continuously closed with U at approximately 0.1.

Observation of the crack propagation rate showed that the crack propagated by one large step during the high-load cycle where the effective stress intensity range was largest. The crack continued to grow at a decreasing rate during the next 150 cycles and the effective stress intensity range dropped to zero. The crack then became stationary and no further change in the stress-displacement relation could be observed. The test was discontinued at that point.

The fact that a crack will continue to grow for some time after some high loads had been observed previously by Schijve [8] and had been termed "delayed retardation." The delayed retardation of crack growth after a single high load can be explained by examining the behavior of the large plastic zone left by the high-load cycle ahead of the crack tip. The elastic material surrounding this plastic zone acts like a clamp on this zone, causing the compressive residual stresses. As long as this plastic zone is ahead of the crack tip, this clamping action does not influence the crack opening. As the crack propagates into the plastic zone, the clamping action will act on the new fracture surfaces. This clamping action, which builds up as the crack propagates into the plastic zone, requires a larger, externally applied stress to open the crack; hence, the crack will propagate at a decreasing rate into this zone and may come to a standstill.

Schijve [8] and others have presumed that the retardation was caused by the action of residual stresses ahead of the crack tip. The results of the experiments here suggest that the retardation is caused by the residual deformations appearing behind the crack tip, as the crack propagates into the plastic zone.

In the second experiment a crack was propagated under the same initial conditions. Instead of dropping back to the low stress level after one cycle, the high-stress cycles were continued (Fig. 11a). The crack opening stresses in cycles (1–1), (2–2), and (3–3) are determined from Fig. 11b. These stresses are identical to the crack opening stresses in Fig. 10b. Under the continued high-load cycling, the crack opening stress level rises and reaches the new equilibrium level for the high-load cycle after 10 cycles. The first cycles have a greater effective stress intensity range than the tenth cycle, causing an initial crack propagation rate larger than the final equilibrium rate. This phenomenon has been observed previously by fractographic methods. A typical fractograph representing this phenomenon can be found in Ref 9.

Conclusions

The results of a study to determine the significance of fatigue crack closure on crack propagation in 2024-T3 aluminum alloy sheet have been presented. From this study, the following were concluded:

1. Fatigue cracks are closed for a significant portion of the tensile load cycle.

2. Under constant amplitude loading, an expression was derived for the rate of crack propagation in terms of an effective stress intensity range. This expression provides a good fit to existing data.

3. Under variable amplitude loading the crack closure phenomenon accounts for acceleration and retardation effects in crack propagation.

References

[1] Elber, W., "Fatigue Crack Propagation," Ph.D. thesis, University of New South Wales, Australia, 1968.
[2] Elber, W. in *Engineering Fracture Mechanics*, Vol. II, No. 1, Pergamon Press, July 1970.
[3] Forman, R. G., Kearney, V. E., and Engle, R. M., *Journal of Basic Engineering, ASME Transactions*, Series D, JBAEA, Vol. 89, No. 3, Sept. 1967, pp. 459–464.
[4] Erdogan, Fazil, "Crack Propagation Theories," NASA CR 901, National Aeronautics and Space Administration, 1967.
[5] Rice, J. R. in *Fatigue Crack Propagation, ASTM STP 415*, American Society for Testing and Materials, 1967, p. 247.
[6] Jacoby, G., *Fortschritt-berichte VDI-2*, FBVBA, Reihe 5, Nr. 7, April 1969.
[7] Hudson, C. M., "Effect of Stress Ratio on Fatigue-Crack Growth in 7075-T6 and 2024-T3 Aluminum-Alloy Specimens," NASA TN D-5390, National Aeronautics and Space Administration, 1969.
[8] Schijve, J., "Fatigue Crack Propagation in Light Alloy Sheet Material and Structures," Rep. MP 195, National Luchtvaart Laboratorium, Amsterdam, Aug. 1960.
[9] McMillan, J. C. and Pelloux, R. M. N. in *Fatigue Crack Propagation, ASTM STP 415*, American Society for Testing and Materials, 1967, p. 516.

M. J. Rich[1]

Crack Propagation in Helicopter Rotor Blades

ABSTRACT: Design criteria are presented for the residual strength and life of fatigue loaded helicopter structures. The crack propagation rate methods and data are reviewed, and a bilinear semilog method is shown to be most accurate for predicting residual life. The methods developed are compared with full scale rotor blade fatigue data. The good correlation with test data demonstrates the value of fracture mechanics analysis for fail-safe design.

KEY WORDS: aircraft, helicopters, damage, rotary wings, components, cracking (fracturing), crack propagation, loads (forces), cyclic loads, residual stress, plastic properties, fracture properties

Nomenclature

a — Half crack length, in.

$d(2a)/dN$ — Crack propagation rate, in./cycle

$d(2a)^*/dN$ — Crack propagation rate at intersection of two-range approximation

K — Stress intensity factor, $\text{psi}\sqrt{\text{in.}}$

ΔK — Stress intensity range, $K_{\max} - K_{\min}$

ΔK^* — Stress intensity at intersection of two-range approximation

$\bar{K}$ — Mean stress intensity

K_{Ic}, K_c — Plane strain and plane stress fracture toughness

n_1, n_2 — Slope of two-range linear semilog crack propagation

N — Cycles of loading

R_s — Residual strength of damaged plate, fraction of ultimate strength

S_{ult} — Ultimate strength of plate without damage, psi

S_{ys} — Yield stress, psi

ΔS — Stress range, $S_{\max} - S_{\min}$

W — Plate width, in.

x — Damage, fraction of plate width

x_n — Crack size fraction at any subsequent time, $(2a)_n/W$

[1] Chief, Structures Technology, Sikorsky Aircraft, Division of United Aircraft Corp., Stratford, Conn. 06602.

x_0 Initial crack size fraction, $(2a)_0/W$

γ Ratio of mean to range of stress intensity, $\bar{K}/\Delta K$

α Compliance factor for finite width effects

The dynamic components of a helicopter are subject to a wide variety of both static and cyclic loads. Many of these types of components are not redundant, and, therefore, their safety and reliability must depend on the fatigue resistance of the specific design. However, a basic problem arises in that the safety of these structures depends upon the adequacy of timely inspection for any fatigue or service damage to preclude that such damage does not increase to a point of failure.

The initial requirements for the design of helicopter dynamic components are to provide a factor of safety of 1.5 for the peak anticipated operating loads and conservative fatigue allowables to ensure that crack initiation is extremely remote. While the latter concept has resulted in a high degree of reliability, the amount of testing involved to assure the necessary statistical data becomes staggering. A review of helicopter structures [1][2] points out the large amount of testing required and the low permissive fatigue strength that is necessary to achieve a low probability of fatigue failure for a fleet of aircraft. Using the crack initiation concept, the design concepts can preclude maintenance from being a major problem; nonetheless, for the safety of the structure it is necessary to go much further and to build in some means of inspection to prevent any premature fatigue cracks from causing catastrophic failure.

The helicopter rotor blade is a prime example of a fatigue loaded structure wherein inspection is the key to safety. Sikorsky Aircraft has developed a blade crack detection system that has been eminently successful. The blade spar is a hollow aluminum extrusion which is pressurized when put into service. A pressure gage that will show up any leakage is attached at the root end, thus acting as a crack indicator. This concept has an advantage in safety in providing a method of early crack detection and, therefore, includes all environmental conditions that can precipitate a failure in service. The economic advantage is in not having to discard blade structures which may be perfectly capable of further service. While the crack initiation concept is necessary to preclude many service problems, it is, by necessity, a wasteful procedure. This is due to the fact that a substantial reduction factor from the mean fatigue behavior is taken, thus assuring that the poorest of the lot is retired. This reduction results in discarding most blades without any significant fatigue damage. Even with this conservative approach, there is the statistical probability that there will be a structure having less fatigue life than the specified safe-life replacement time.

---

[2] Italic numbers in brackets refer to the list of references at the end of this paper.

A preferable approach (fail-safe) consists of providing an inspection system which detects damage in sufficient time to replace the part before such damage becomes critical. This requires the consideration of crack propagation and fracture mechanics in the design concept. This approach has the additional advantage of including damage resulting from imperfections in manufacturing and that incurred in service.

Design Criteria

In designing for crack propagation the criteria must encompass both the static residual strength and the crack propagation time for the fatigue or service damaged blade; therefore, the residual strength for the cracked rotor blade should first be determined. Figure 1 illustrates the relationship between the residual strength and the crack size. In general, rotor blades are designed by the fatigue loadings and as a result have a considerably greater factor of safety than the usual 1.5 for static strength. As illustrated in the figure, the critical crack size is that at which the cracked structure cannot safely withstand the design loading limit. Thus, the residual strength criterion becomes important, since it is the limit on the acceptable crack size for fatigue crack propagation.

As shown in Fig. 2, the crack growth time to failure depends upon the size of the initial crack. For example, in this figure, if the initial crack were larger, the time to failure would be foreshortened on the same diagram. Therefore, it is most important that the detection method provide early warning. To ensure the reliability of the system, the inspection period must be considerably less than the total mean crack time, that is, the time between detection and critical size.
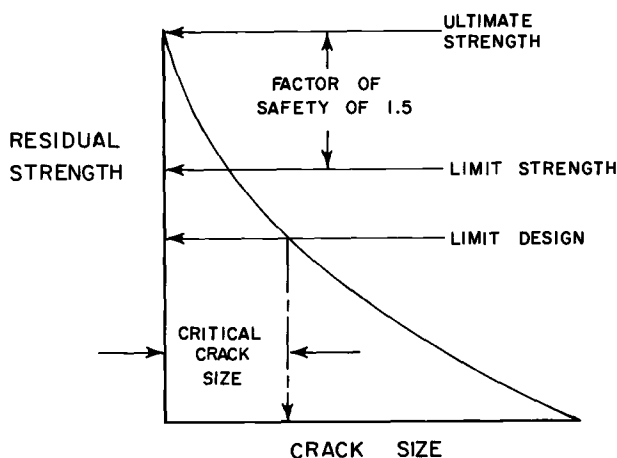

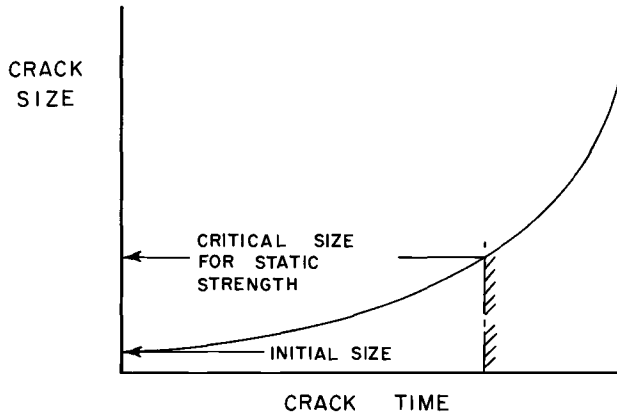
FIG. 1—*Residual strength criteria.*

FIG. 2—*Residual life criteria.*

These criteria have been proposed [2] in other investigations of fail-safe criteria and are simple to apply for any structural design. The problem actually is more complex than considering a single vibratory stress amplitude for the residual life portion. In service there is a spectrum of loads which may affect considerably the crack growth time. However, if we can determine the growth time for the variable loadings, the criteria specified will then encompass both the residual strength and the life of the blade structure. One aspect is clear though—the fail-safe and safe-life concepts are both "life" problems. In using the residual life approach we are utilizing a safe-life of the cracked structure. The real difference in the two concepts is that for fail-safe we are adding an inspection period interval and relating it to the crack propagation time. More important is the fact that the residual life concept is an active procedure requiring action related to service use, whereas the safe-life crack initiation approach is a passive method which trusts nothing will happen prior to replacement of the structure.

Analytical Methods

Crack Propagation

One simple crack rate relationship [3] is of the form

$$d(2a)/dN = C(\Delta K)^n \dotfill (1)$$

where

$$2a = \text{the crack length,}$$
$$C \text{ and } n = \text{empirical constants,}$$
$$\Delta K = \text{the stress intensity range, and}$$
$$N = \text{the cycles of stress.}$$

This crack rate relationship gives a simple, direct insight into how vibratory loadings propagate a crack in a rotor blade. As a first estimate, Eq 1 is useful in determining a preliminary value for the residual life. However, since the effect of mean stress does not appear explicitly, the designer, in using the results of crack propagation tests, must presume that any difference in mean stress will not affect appreciably his estimates of residual life.

A further extension of crack rate analysis [4] considers the effects of mean stress. These results can be put into the following form:

$$d(2a)/dN = B(1 + 2\gamma)^m \Delta K^n \dots \dots \dots \dots \dots (2)$$

where

B = an empirical constant for a material and
γ = the ratio of the mean to range stress intensity values, $\bar{K}/\Delta K$.

For aluminum alloys, such as 2024-T3 and 7075-T6, $m = 2$ and $n = 4$ appear to cover the test ranges. A simple linear analysis can be obtained by integrating Eq 2, which thus results in

$$\Delta N = \frac{1}{B(1 + 2\gamma)^m W^{(n-1)/2}} \int_{x_0}^{x_n} [\tan (\pi/2)x]^{n/2} dx \dots \dots \dots (3)$$

where

x_0 = the initial fractional crack size, $2a/W$,
x_n = the fractional crack size at any subsequent time,
ΔN = the cycle count from initial to a given fractional crack size, and
W = the plate width.

For $m = 2$ and $n = 4$ Eq 2 yields

$$\Delta N = \frac{2}{\pi B(1 + 2\gamma)^2 W} [\cot (\pi/2)x_0 - \cot (\pi/2)x_n - (x_n - x_0)] \dots (4)$$

Both methods shown in Eqs 1 and 2 presume a linear relationship of the log of stress intensity range with the log of crack rate; however, comparisons have been made [5] that show that a two-range semilog relationship is significantly more precise in determining crack propagation time. The bilinear relationship is illustrated in Fig. 3. Data [5] for the bilinear approximation are shown in Table 1 and plotted in Fig. 4.

A comparison [5] was made between test data determined by the previous methods; it illustrated that the bilinear procedure results in significantly greater accuracy. The results of the comparison are shown in Table 2.
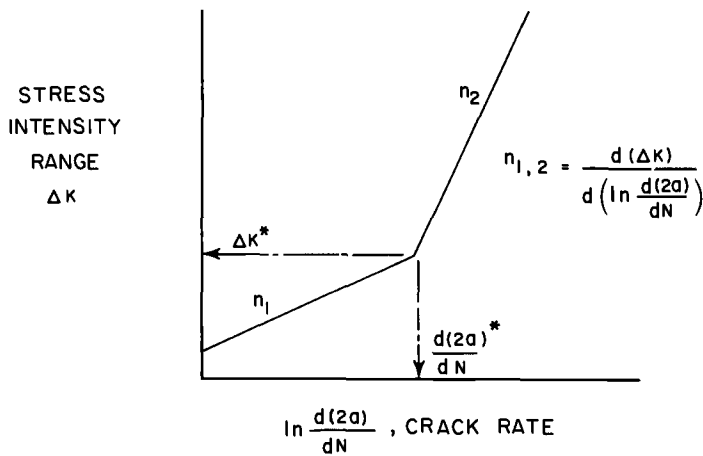
FIG. 3—*Bilinear semilog approximation.*

TABLE 1—*Crack propagation data constants.*

Material	$\Delta K/\bar{K}$	$n_1{}^a$	$n_2{}^a$	$\Delta K^*,$ ksi $\sqrt{\text{in.}}$	$d(2a)^*/dN,$ in./cycle
6061-T6	1.5	0.45	10.8	12.1	5.3×10^{-6}
2024-T3	0.42	3.7	7.1	6.8	6.4
	1.77	3.4	14.2	8.2	4.8
7075-T6	0.42	4.5	8.2	13.5	780
	1.77	9.6	16.6	25.6	760
Ti-6-4(AN)	2.0	6.1	51.0	17.5	42
Ti-8-1-1 . . . . (duplex AN)	2.0	3.2	23.7	9.6	5
4340 (175 ksi)	2.0	14.5	49.0	30	15

^{a} $n = [d(\Delta K)/[d \ln d(2a)/dN] = $ constant in range 1 or 2.

TABLE 2—*Comparison of crack growth times.*

7075-T6 Bare Sheet	Test Cycles [6]	Calculated Results, cycles	
		From Eq 4	Bilinear Semilog Method
High crack growth case:			
$x_0 = 0.125, x_n = 0.50,$ $\Delta S = 6280$ psi	64 000 ($\gamma = 1.91$)	12 900 ($\gamma = 1.91$)	66 400 ($\gamma = 1.89$ to 2.08)
Low crack growth case:			
$x_0 = 0.163, x_n = 0.50,$ $\Delta S = 2040$ psi	1 200 000 ($\gamma = 1.89$)	396 000 ($\gamma = 1.89$)	1 470 000 ($\gamma = 1.89$ to 2.08)

Formulation of a Strength Relationship

As specified in the design criteria, the limiting factor in the crack propagation time will be the crack size for the peak static loadings. Using the fracture mechanics method, wherein the stress intensity factor is related to the gross stress, the crack size, and the geometry of the plate, a strength relationship can be formulated readily. The following residual strength formula includes correction for the plastic zone at the crack:

$$R_s = \frac{K_{Ic} \text{ (or } K_c)}{S_{ult}\{W \tan [\pi x/2 + (K_{Ic}/S_{ys})^2/2W]\}^{1/2}} \dots\dots\dots\dots(5)$$

where R_s = residual strength of damaged plate, fraction of ultimate strength.
It should be noted that an alternate form would be

$$R_s = \frac{K_{Ic} \text{ (or } K_c)}{S_{ult} \, \alpha\sqrt{\pi a}} \dots\dots\dots\dots\dots\dots(6)$$

For Eq 5 the compliance factor α is

$$\alpha = \{(W/\pi a) \tan [\pi a/w + (K_{Ic}/S_{ys})^2/2W]\}^{1/2} \dots\dots\dots(7)$$

A more recent [7] form is

$$\alpha = 1 - 0.1(2a/W) + (2a/W)^2 \dots\dots\dots\dots(8)$$

and a plasticity correction would be added as applicable. The experimental data were generated using the form of Eq 5, and the differences between compliance terms are small, since in actual practice the critical damage size usually is much less than 50 percent of the plate width.
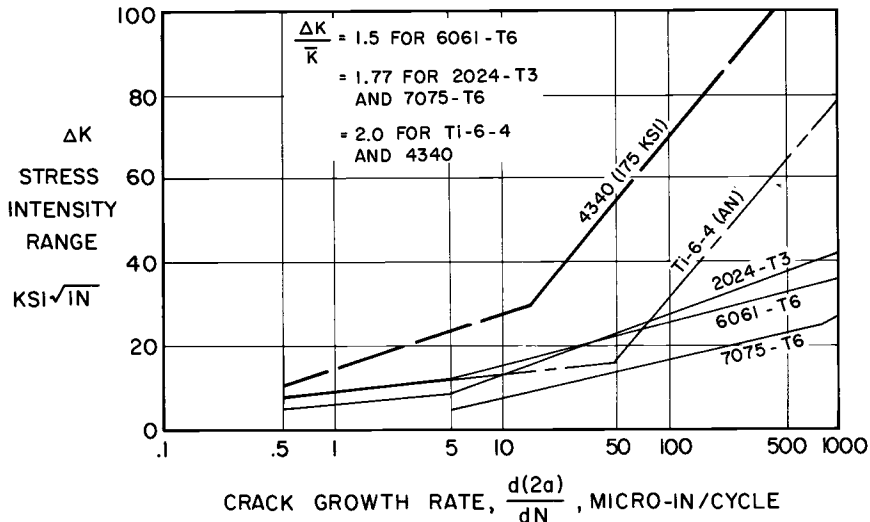

FIG. 4—*Bilinear semilog crack rate data.*

K_{Ic} is selected as being most nearly representative of the types of structures involved with rotary wing dynamic components. For thin sheet material K_c (plane stress) would, of course, be used as it results in a higher fracture toughness value depending on the thickness involved. To be more exact, the fracture toughness value for the specific material and plate thickness should be used.

Equation 5 appears to be quite accurate in the range of cracks measuring about 25 to 50 percent of the plate width but results in conservative values for the smaller crack sizes. It should be noted that Eq 5 is based on brittle fracture. For materials such as 6061-T6 aluminum alloy with a high fracture toughness to yield ratio, the design residual strength should be based on values not greater than the product of the net section and the ultimate stress of the material.

Correlation with Test Results

The spar section shown in Fig. 5 is the primary load carrying member for current Sikorsky Aircraft main and tail rotor blades. It is an extruded hollow section made from 6061-T6 aluminum alloy. Spar test specimens were fatigue tested with steady, axial tensile loading to represent the centrifugal blade forces and with vibratory loading to simulate the cyclic stresses in flight. Both steady and vibratory loadings were maintained throughout the testing, rather than amplitude conditions, to assure that the results were representative of actual operating conditions.

The test specimens were pressurized, and both the time to crack initiation and the time from crack detection (indicated by initial loss of pressure) to fracture were measured. The majority of the 300 specimens were tested at 200 cpm (for the main rotor blades) and at 600 cpm (for the tail rotor blades). As a further check, some additional testing was conducted at 1000 cpm for the main rotor blades. The test results indicated no strain sensitivity in fatigue for 6061-T6 alloy, since the testing speed did not alter either the crack initiation or crack rate times. Nevertheless, this is a point that should be checked when using other alloys, and the data of Table 2 should be modified depending on the strain sensitivity of the alloy in crack propagation.

The results of the fatigue testing are shown in Fig. 6 as *S-N* diagrams. The upper curve represents the time to crack initiation. The stress levels were then reduced to obtain the time from crack initiation to fracture. The method of analysis was to integrate numerically the crack rate data using the bilinear semilog data of Table 2 for 6061-T6 alloy. The analytical results, in terms of vibratory stress, are within 15 percent of the test data range of 10,000 to 10,000,000 cycles. It should be noted that the analytical results are conservative throughout the entire cyclic range. This consistent trend lends considerable confidence to the use of the methods described as a tool for fail-safe design.
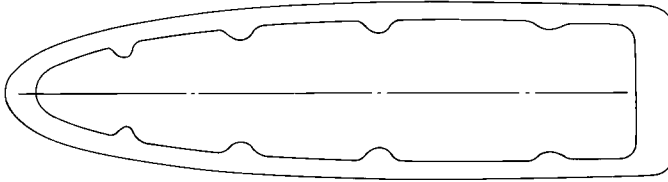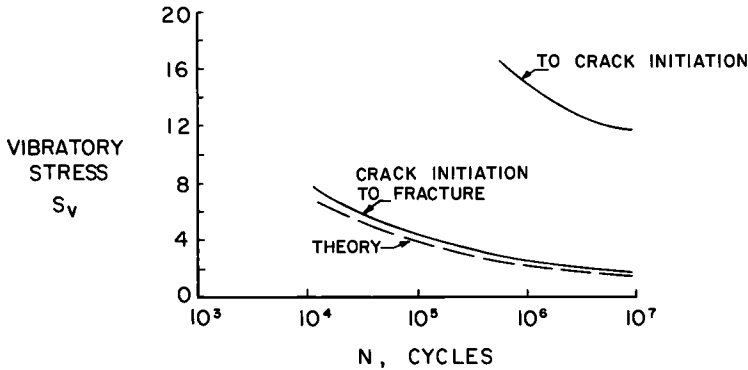
FIG. 5—*Blade spar section.*

FIG. 6—*Blade spar* S-N *diagrams.*

Conclusions

The use of fracture mechanics provides a valuable design method in predicting residual strength and life of fatigue cracked structures. A bilinear semilog crack rate method appears to be more accurate than simplified linear methods. The results of analysis on blade spars correlate very well with full scale tests.

There are further problems to be explored, such as the effects of spectrum loadings, correction of strain rates for strain rate sensitive materials, and the effect of environment on crack rate growth. Yet, it appears that crack propagation and fracture strength methods provide a good tool for fail-safe design.

References

[1] Jensen, H. T. in *Fatigue Design Procedures*, Proceedings of the 4th Symposium of the International Committee on Aeronautical Fatigue.
[2] Rich, M. J., *Journal of Aircraft*, JAIRA, Vol. 6, No. 6, Nov.–Dec. 1969, pp. 574–576.
[3] Paris, P. C. in *Proceedings of the 10th Sagamore Army Materials Research Conference*, Syracuse University Press, Syracuse, New York, 1964.
[4] Roberts, R. and Erdogan, *Journal of Basic Engineering*, *ASME Transactions*, Series D, JBAEA, Vol. 98, 1967, pp. 885–892.
[5] Rich, M. J., "Vulnerability Considerations in the Design of Rotary Wing Aircraft Structures," Proceedings of Air Force Conference on Fatigue and Fracture of Aircraft Structures and Materials, Miami Beach, Fla., 1969.
[6] Smith, S. H. in *Structural Fatigue in Aircraft*, *ASTM STP 404*, American Society for Testing and Materials, 1965, pp. 74–100.
[7] Brown, W. F. and Srawley, J. E., *Plane Strain Crack Toughness Testing of High Strength Metallic Materials*, *ASTM STP 410*, American Society for Testing and Materials, 1966.